Measuring properties of accreting black holes with X-ray reverberation

Mastroserio, G.

Publication date
2019
Document Version
Final published version
License
Other

Link to publication

Citation for published version (APA):
Mastroserio, G. (2019). *Measuring properties of accreting black holes with X-ray reverberation*. [Thesis, fully internal, Universiteit van Amsterdam].

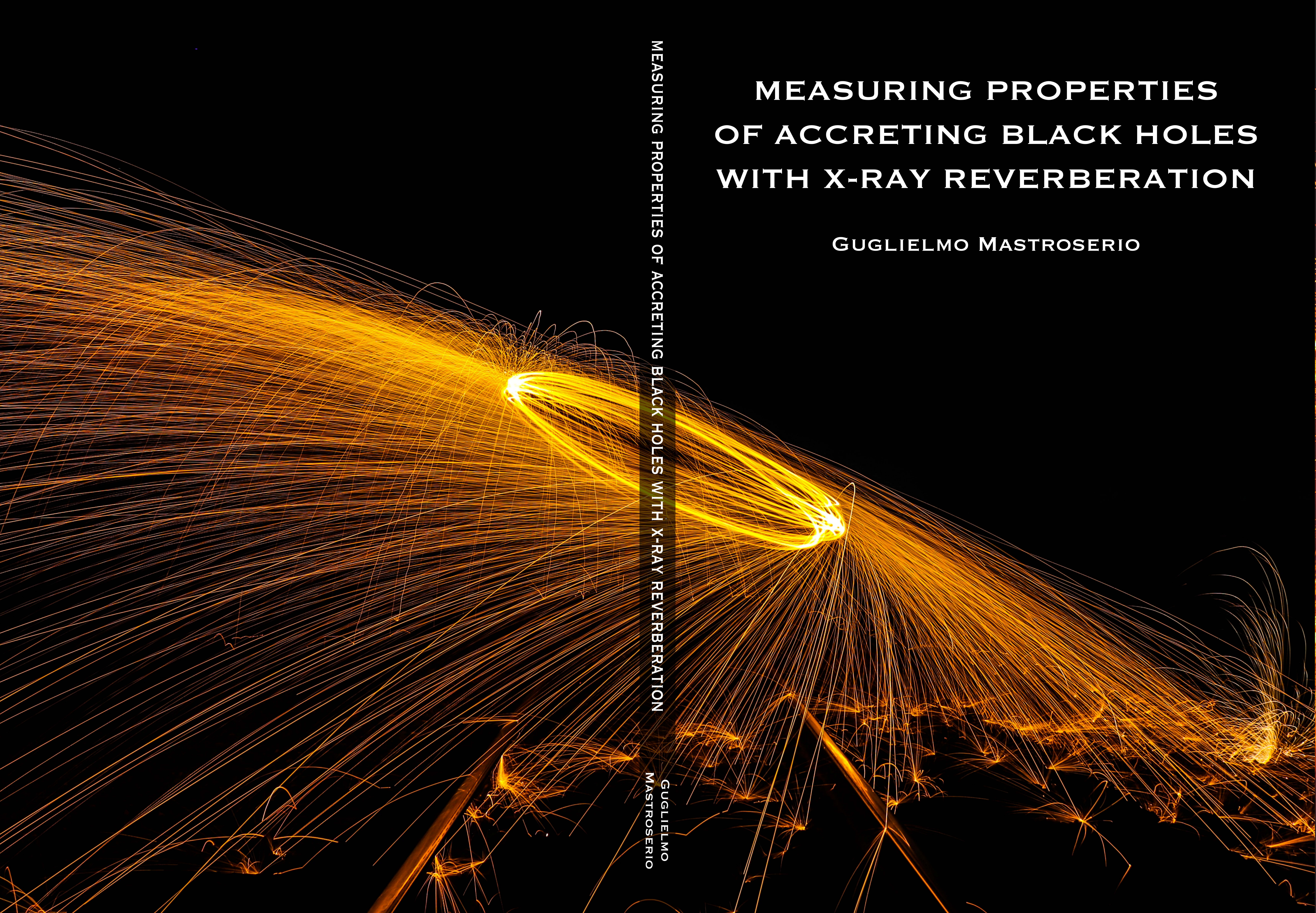

MEASURING PROPERTIES OF ACCRETING BLACK HOLES WITH X-RAY REVERBERATION

Guglielmo Mastroserio

MEASURING PROPERTIES OF ACCRETING BLACK HOLES WITH X-RAY REVERBERATION
Guglielmo
Mastroserio

Measuring properties of accreting black holes with X-ray reverberation

ACADEMISCH PROEFSCHRIFT

ter verkrijging van de graad van doctor
aan de Universiteit van Amsterdam
op gezag van de Rector Magnificus
prof. dr. K. I. J. Maex
ten overstaan van een door het College voor Promoties ingestelde
commissie, in het openbaar te verdedigen in de Agnietenkapel
op donderdag 14 november 2019, te 12:00 uur

door

Guglielmo Mastroserio

geboren te Milaan

Promotiecommissie:

Promotor:	prof. dr. M.B.M. van der Klis	Universiteit van Amsterdam
Copromotor:	dr. A. Ingram	University of Oxford
Overige leden:	prof. dr. C. Done	University of Durham
	prof. dr. R. A. M. J. Wijers	Universiteit van Amsterdam
	prof. dr. R. A. D. Wijnands	Universiteit van Amsterdam
	prof. dr. W. Hermsen	Universiteit van Amsterdam
	dr. B. De Marco	Nicolaus Copernicus Astronomical Center
	dr. J. García	California Institute of Technology
	dr. P. Uttley	Universiteit van Amsterdam

Faculteit der Natuurwetenschappen, Wiskunde en Informatica

The research described in this thesis was supported by the Netherlands Organisation for Scientific Research (NWO) Top-Grant and carried out at the Anton Pannekoek Institute for Astronomy (API), University of Amsterdam. A 3 month period spent at Oxford University was supported by the UvA385 Grant created in cooperation between the University of Amsterdam and Amsterdam University Fund (AUF). Some travel support was provided by the NWO Spinoza grant and Leids Kerkhoven-Bosscha Fonds (LKBF).

Alla mia famiglia

All our knowledge begins with the senses, proceeds then to the understanding, and ends with reason. There is nothing higher than reason.

Immanuel Kant, Critique of Pure Reason

Contents

1

Introduction

Black holes are the most extreme objects in the Universe. Although direct evidence of the their existence was obtained only in the second half of the 20th century, the concept of ‘invisible bodies’ had been advanced already in the 18th century by John Michell and Pierre-Simon Laplace (Montgomery et al. 2009). From a purely mathematical point of view, a black hole can be seen as the vacuum solution of Einstein’s field equations, with all the mass of the object concentrated in a central singularity. According to the ‘No-hair Theorem’ this solution is characterised by only three parameters: the mass (M), the angular momentum, and the electrical charge. This singularity is hidden behind the *event horizon*, a surface from within which nothing can escape, not even light.

As the interior is unobservable, astrophysical black holes can be defined based on the properties of the region down to the event horizon, including the event horizon as a one-way membrane. For a non-spinning black hole the event horizon is a sphere with radius $R = 2GM/c^2$. In the case of spinning black hole the radius of the event horizon is $r_h = 1 + \sqrt{1 - a^2}$, where r_h is expressed in units of gravitational radii ($R_g = GM/c^2$) and where the black hole angular momentum is aGM^2/c. The spin parameter a has an allowed absolute range from 0 (non-spinning) to just below 1 (maximally spinning; Thorne 1974). Astrophysical black holes formed from gravitational collapse are expected to be nearly neutral, since any significant electric charge would be neutralized by attracting particles of opposite charge from the surrounding plasma. Thus they are characterized by only two numbers: the mass, and the spin. General Relativity defines a radius inside which there are no stable circular orbits. This is called the innermost stable circular orbit (ISCO) and depends on black hole spin, which can take values from $R_{\rm ISCO} = R_g$ for $a = 1$ via $R_{\rm ISCO} = 6\ R_g$ for $a = 0$

(Schwarzschild) to $R_{\rm ISCO} = 9\ R_g$ for $a = -1$ (maximally retrograde; negative values of the spin are used to indicate retrograde orbits).

Black holes as we observe them in the Universe are classified according to their mass. Stellar mass black holes range from a few to several tens of Solar masses and can be discovered orbiting a companion in a binary system. The other category of black holes is much more massive: typically $10^6 - 10^9$ Solar masses. These supermassive black holes are observed in the nuclei of galaxies including our own Milky Way galaxy. The discovery of gravitational waves brought evidence of binary black hole systems whereby two stellar mass black holes merge to form a single (probably isolated) black hole.

The black hole systems discussed in this thesis are all powered by accretion. The material around the black hole, either coming from a binary companion star (in black hole binaries or BHB) or from the gas of the host galaxy (in active galactic nuclei or AGN), is dragged into the black hole by its gravitational attraction. If the infalling matter carries angular momentum relative to the black hole, it will form an accretion disc, which can be extremely efficient in converting gravitational potential energy into emitted radiation. In the Newtonian approximation, a test mass m orbiting a black hole of mass M at radius R has gravitational potential energy $-GMm/R$ and kinetic energy $(1/2)GMm/R$. Therefore, if material drifts toward the black hole with radial velocity $v_r << v_\phi$, half the gravitational potential energy lost is converted to kinetic energy with the rest in principle free to be radiated. In the same approximation, an accretion disc extending from $R = \infty$ to $R = R_{\rm in}$ with mass accretion rate $\dot{M}$ will radiate a luminosity $L_{\rm disc} = GM\dot{M}/(2R_{\rm in}) = c^2\dot{M}/(2r_{\rm in})$, where $r_{\rm in} \equiv R_{\rm in}/R_g$. Therefore the luminosity of an accretion disc that extends down to the ISCO depends only on the mass accretion rate $\dot{M}$ and the spin of the black hole, and in principle nearly half of the rest mass energy of the disc can be converted to radiation. A useful mass accretion rate scale is provided by defining the Eddington luminosity $L_{\rm Edd} \approx 1.26 \times 10^{38}(M/M_\odot)$ erg s^{-1}, which is the limiting luminosity for a steady, spherically symmetric flow where the radiation pressure is balanced by the gravitational force. The accretion can be unstable and/or asymmetric and then may exceed the Eddington limit. However, as the limiting luminosity scales linearly with black hole mass, it is clear that AGN can be much more luminous than black hole binaries.

Characterizing black holes (measuring their mass and spin) by studying the accretion processes is important for understanding the formation mechanisms and the evolution of the black holes and their host systems. Stellar mass black holes are a fundamental ingredient in the study of the evolution of their stellar progenitors. When massive stars[1] ($\gtrsim 20M_\odot$) come to the end of their nuclear (fusion) fuel, the radiation pressure in the star's interior can no longer match gravity, and gravitational collapse

---

[1] Although the possibility of black hole formation for lower mass has been discussed in the literature (e.g. O'Connor & Ott 2011)

ensues. Simulations of what happens after depletion of the nuclear fuel (e.g., whether there is a supernova explosion or not) can be constrained using the characteristics of the final product (Janka 2012 and references therein). Black hole mass can also be used to estimate the importance of mass loss processes of the stellar progenitor, such as winds, in particular in the final stages of its evolution (e.g. Belczynski et al. 2010). The black hole spin derives from the angular momentum of the progenitor star and the gravitational collapse / supernova explosion, so these processes can be constrained by measuring the spin (Chan et al. 2018). Supermassive black holes, on the other hand, preserve information on how the host galaxy grew (e.g. Salpeter 1964), and what its dynamic evolution was (e.g. Rees 1984). The growth mechanism of the a supermassive black hole involves the radiative accretion efficiency and thus its spin (King & Pringle 2006; King et al. 2008). The formation and evolution of galaxies and galaxy clusters have implications for cosmological theories.

Accreting black holes can also serve as a laboratory to study General Relativity in the "strong field regime". According to Einstein's theory the spacetime around a spinning black hole is described by the Kerr metric. This leads to very specific predictions for the trajectories and energy shifts of the photons produced in the accretion process, so that by analyzing the electromagnetic radiation it is possible to study this metric and look for possible deviations from the theory's predictions (e.g., Bambi 2017).

1.1 Spectral Emission

The energy spectrum of a source is its flux per unit photon energy as a function of photon energy. The flux can be expressed either as specific photon flux (dN/dE) or as specific energy flux ($E\,dN/dE$). In this section I will refer to the flux as the specific photon flux (if not specified). The energy spectrum is an important tool to identify the various radiative processes that contribute to the total flux, and to characterise the physical circumstances in the emitting regions. The emission of accreting black holes covers the entire electromagnetic spectrum, but the work in this thesis focuses on the X-ray emission around $0.5-30$ keV. The radiation in this energy range is emitted by the regions very close to the black hole where its impact is stronger.

1.1.1 Disc Emission

From simple considerations in Newtonian gravity similar to those used in the previous section, the material of the accretion disc accreting from $R+dR$ to R with mass accretion rate $\dot{M}$ loses potential energy, and the luminosity free to be radiated is $dL(R) = GM\dot{M}/2R^2 \times dR$. Since the disc is optically thick, any photon that escapes to reach an observer at infinity must have had many interactions within the disc and therefore the locally radiated spectrum is a blackbody, so $dL(R) = dA\sigma_{\rm SB}T^4$. As the area of the emitting region is $dA = 2{\times}2\pi R{\times}dR$, where the factor 2 is because the emission happens on both surfaces of the disc, it follows that $T^4(R) = GM\dot{M}/(8\pi R^3 \sigma_{\rm SB})$. Shakura & Sunyaev (1973) derived that the temperature profile has an extra factor $3\,(1 - (R_{\rm in}/R)^{1/2})$ if zero stress at the disc inner radius $R_{\rm in}$ is assumed. This factor therefore derives from the inner boundary condition. Novikov & Thorne (1973) calculated all the relativistic corrections. So, the maximum temperature is approximately $T^4_{\rm max} \propto GM\dot{M}/(8\pi R^3_{\rm in}\sigma_{\rm SB})$, where the precise radius where $T_{\rm max}$ is attained and the constant of proportionality depends on the inner boundary condition. In the previous section I derived that the disc luminosity is $L = c^2\dot{M}/(2r_{\rm in})$. Therefore a disc with a given inner boundary condition and a given inner radius in units of R_g (e.g. the ISCO) accreting at a given fraction of the Eddington limit, will have a peak temperature that scales with black hole mass as $T^4_{\rm max} \propto 1/M$. If a $10M_\odot$ black hole has peak disc temperature 1 keV, then a $10^8 M_\odot$ black hole has peak disc temperature $T_{\rm max} = 10^{-7/4}$keV $= 0.0178$ keV, which is in the UV. In both types of black hole system, this theoretically derived radiation has been observed. Stellar mass black holes show a thermal state where a thermal component dominates the energy spectrum (Remillard & McClintock 2006). It has been shown that this component is well fitted using the multi-temperature accretion disc model (Mitsuda et al. 1984; Makishima et al. 1986; Kubota et al. 2005). The spectral energy distribution of AGN shows thermal emission from UV to optical region, known as “the big blue bump”, which is thought to be emitted from the optically thick accretion disc feeding the black hole (Shields 1978; Malkan 1983). Laor (1990) showed that in several AGN the optical-UV continuum is consistent with thin accretion disc models.

1.1.2 Comptonized Emission

From an observational point of view the X-ray energy spectrum of accreting black holes shows evidence of a hard excess. Seyfert galaxies, which are relatively nearby AGN that show broad and narrow emission lines (Peterson 1997), always show this component which is approximately constant over timescales of days or weeks. In black hole binaries, instead, the contribution of the spectral components changes as the source transitions from the ‘hard’ state to the ‘soft’ state over days or weeks (see Done et al. 2007 for a review). These two states are respectively described by an energy spectrum dominated by hard emission, with disc emission below 1 keV (hard state), and a disc emission dominated energy spectrum, with just a small hard tail (soft state). In this thesis I focus on the hard state and do not investigate the details of this transition. However, it is worth noting that in AGN it is not possible to detect this type of long time scale variability because the timescales are much longer due to the bigger size of the systems.

In this section I focus on the spectral component that describes the hard part of the X-ray energy spectrum which is thought to be due to inverse Compton emission for both BHBs and AGN. This emission is due to seed photons from the disc that illuminate a region of optically thin ($\tau \sim 1$) hot electrons, usually referred to as the *corona*, where they are up-scattered (inverse Compton effect). The geometry of this region is not clear (see Section 1.1.4), however, it is part of the accretion process and therefore connected to the disc sharing the accretion energy. The spectral shape of the Comptonized radiation depends on the number of scatterings that the seed photons have with the electrons and how much energy the photons gain per scattering. The probability for a photon to interact with an electron when passing a distance R through a medium containing n electrons per unit volume, each with an interaction cross-section σ, is set by the optical depth $\tau = n\sigma R$, which is the number of electrons in the volume σR. The probability for a photon to escape without undergoing any scatterings is $\mathrm{e}^{-\tau}$, and therefore a fraction $1 - \mathrm{e}^{-\tau}$ of the seed photons experience at least one scattering. For $\tau << 1$, this becomes $1 - \mathrm{e}^{-\tau} \sim \tau$. Of these scattered photons, a fraction $\sim \tau$ will have at least one more interaction, therefore a fraction $\sim \tau^2$ of the seed photons will interact at least twice, and so on. For a thermal population of electrons, the fractional gain in photon energy per scattering is $A \approx 1 + 4\Theta + 16\Theta^2$ (Blumenthal & Gould 1970; Rybicki & Lightman 1979; Done 2010) where $\Theta = kT_e/m_ec^2$ is the normalized electron temperature, defined as the energy of the peak of the thermal electron distribution as a fraction of the electron rest mass energy. Fig 1.1 demonstrates how the sum of multiple scatterings leads to a power-law spectrum (specific photon flux), $F(x) \sim x^{-\Gamma}$, where x is defined as $x = h\nu/m_ec^2$. Since each scattering order has a lower photon number than the last by the same fraction $\sim \tau$ and a higher energy than the last by the same fraction A, it is simple to see that $\log F(x)$ is a linear function of $\log x$, and $\Gamma \sim \log\tau/\log A$.

This power-law description is valid until the characteristic normalized photon energy of a scattering order becomes $x \sim 3\Theta$, at which point photons no longer gain energy from collisions. This leads to a high energy cut-off in the spectrum that can be roughly modeled with an exponential, $F(x) \sim x^{-\Gamma}\mathrm{e}^{-x/(3\Theta)}$, although the cut-off for a self-consistently calculated thermal Comptonised spectrum is sharper (e.g. the model NTHCOMP; Zdziarski et al. 1996). Thus the slope is determined by the optical depth and the temperature of the hot electrons, whereas the high energy cut-off depends only on the electron temperature.

The power-law description of the spectral shape is a good approximation only when there is overlap between the scatterings; if τ is too small or Θ is too large then Comptonization produces a more irregular spectrum with a 'jump' for every scattering. Other models have been developed to treat the cases where a phenomenological power-law is not sufficient, for example COMPTT (Titarchuk 1994) and EQPAIR (Coppi 1999). Although we may expect some sources to deviate from a smooth power-law behaviour, the observed hard X-ray emission is almost always well described by this phenomenological model. This is naturally explained if the corona is slightly inhomogeneous in e.g. temperature and optical depth.

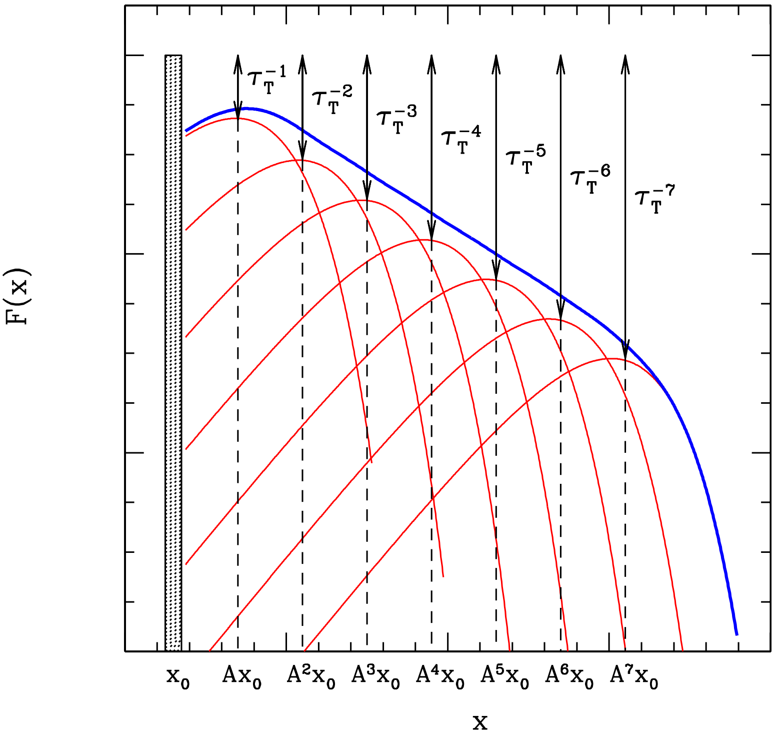

Figure 1.1: Emission energy spectrum for multiple Compton scattering events in the case of $\tau << 1$. The incident photons have energy x_0. A fraction τ of them experiences at least one scattering, τ^2 at least two scatterings and so on. The fractional energy gain per scattering is A. When the energy of the photons equals the typical electron energy, 3Θ, the following scatterings do not increase their energy, leading to a cut-off in the spectrum. The plot is in logarithmic scale. Image adapted from Ghisellini (2013).

1.1.3 Reflected Emission

Some of the radiation from the corona is seen directly by the observer, and this represents the *continuum* component in the spectrum. Some of the radiation, instead, illuminates the accretion disc where it is re-emitted with a specific spectral shape. This spectral component is called *reflection*, even though this term could be misleading because the illuminating spectrum is actually reprocessed rather than reflected. The reflection spectrum was studied for the first time in X-ray binaries in the case of Her X-1, where Basko et al. (1974) considered the reprocessing of radiation from the accretion disc by the atmosphere of the companion star. Guilbert & Rees (1988) and Lightman & White (1988) argued that similar reprocessing could occur in the atmosphere of the accretion disc. There are two main processes that contribute to shape the reflection spectrum: photo-electric absorption and electron scattering. The former dominates at low energies where the cross-section of the heavy elements is larger than the electron scattering cross-section. Photons in this low energy regime, upon interacting with bound atoms in the disc, are most likely to excite an electron from the K-shell ($n = 1$). This imprints absorption edges on the reflection spectrum. The resulting ion is unstable, so an electron from a higher energy shell, most likely the L-shell ($n = 2$), decays to fill the gap in the less energetic K-shell. During this transition, either a photon is emitted, imprinting a *fluorescence* line on the reflection spectrum, or an outer shell electron is ejected via Auger ionisation. The latter has higher probability for low atomic number elements, and thus lines at low energy are more suppressed than those at higher energies from heavier elements. Since iron is the heaviest astrophysically abundant element, its fluorescence line features are the most prominent, in particular the Kα emission line, which corresponds to the transition from the L to the K shell. The photo-electric cross-section decreases as E^{-3} and at around 10 keV is equal to the electron scattering cross-section. Above this energy, the scattering process dominates, increasing the number of photons that are reflected. The highest energy photons are still scattered, but they *lose* energy, which introduces a high energy cut-off to the reflection spectrum (similar to that described in the previous section). The combination of the iron K edge at 7.1 keV and this high energy turn over leads to the characteristic *Compton hump* between $20 - 50$ keV. Fig. 1.2 shows a typical reflection spectrum produced by a layer of neutral gas with Solar abundances (black line).

The shape of the reflection spectrum is dependent on the ionisation state of the reflecting material, which is usually described by the *ionisation parameter*

$$\xi = \frac{4\pi F_x}{n_e}, \tag{1.1}$$

where F_x and n_e are respectively the illuminating 13.6 eV to 13.6 keV flux and the electron number density in the disc. This can be understood as setting the probability of a photon interacting with an ion instead of a bound atom that has had time to recombine since its last interaction. Since the photo-electric absorption cross-section is anti-correlated with the ionisation state, increasing the ionisation parameter increases the reflection continuum (see Figure 1.2, blue and red lines). Moreover at very high ionisation, even the emission lines of the heavy elements become faint (see Figure 1.2, green line). One of the most advanced models to compute the reflection spectrum emerging from an X-ray illuminated accretion disc is XILLVER (García & Kallman 2010; García et al. 2013a). This model simultaneously solves the equations of radiative transfer, energy balance, and ionisation equilibrium in a Compton-thick, plane-parallel medium. Most reflection models to date have assumed ξ to be constant with disc radius, which is unlikely to be the case in reality. Assuming a specific geometry for the illuminating region and a radial density profile in the disc, it is possible to self-consistently calculate the ionisation parameter as a function of radius.

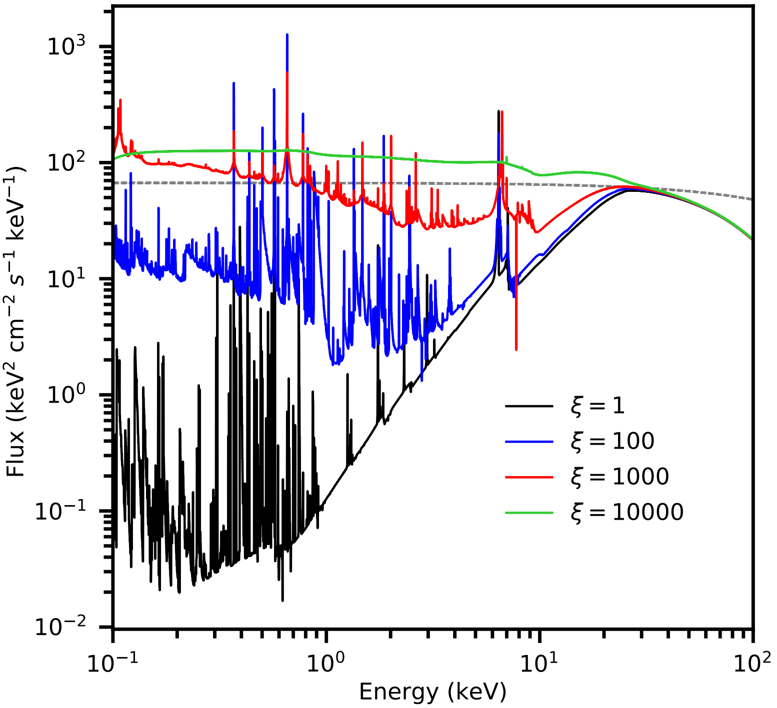

Figure 1.2: Dashed line: incident energy spectrum. Solid lines: restframe reflection energy spectra from solar abundance gas. The different colors are for different ionisation levels of the gas, from neutral (black line) to completely ionised (green line). The energy spectra are computed with the XILLVER model.

In this thesis, I explore some of the effects of including a self-consistently calculated ionisation profile in reflection models.

However, this is not the final reflection spectrum of an accretion disc around a black hole. The emission conveys several dynamic effects that skew in particular the emission lines. Fig. 1.3 shows an overview of the effects that modify the emission line profile and all of them depend on the distance of the emission point from the black hole. In a rotating disc the line splits into a double peak profile due to Doppler shifts, even in a non-relativistic limit. The energy of the photons emitted by the disc patches moving towards the observer is blueshifted in the spectrum, whereas the photons from the portion of the disc moving away from the observer are redshifted. This effect is stronger closer to the center of the disc because the orbital velocity is higher there. Close to the black hole, relativistic alterations dominate the line profile. Special relativity causes the beaming of the blueshifted photons, increasing the flux that arrives to the observer. On the other side the redshifted photons experience the opposite

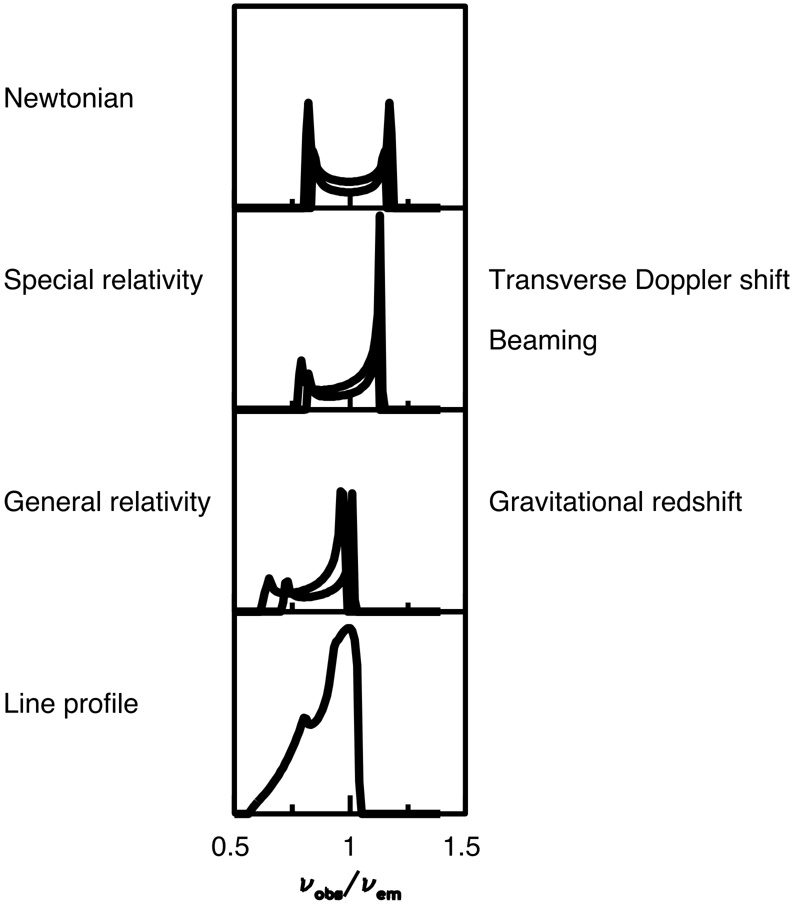

Figure 1.3: Sketch of how a delta line emitted at ν_{em} is distorted by the dynamic and relativistic effects. From the top to the bottom panel it is shown the Newtonian Doppler shift, the relativistic Doppler shift that accounts for time dilation and the relativistic beaming of the blue peak and the redshift due to General Relativity. The bottom panel illustrates an example of the final line profile emitted by the accretion disc. Image adapted from Fabian et al. (2000).

effect, decreasing their flux. This produces an asymmetry of the line. Special relativistic *transverse Doppler shifts* and general relativistic *gravitational redshifts* shift the entire profile towards the lower-energy ('red') part of the spectrum. This forms a characteristic tail of the emission line called the 'red wing', which is more prominent the closer the emission comes from the black hole. In the time-averaged energy spectrum, the emission line is the average of all these effects, leading to a broadened and skewed line profile (bottom panel in Fig. 1.3). Since the contributions to the line depend on radius, the average is weighted by the radial profile of flux irradiating the disc. This is usually proportional to $R^{-\beta}$ with β either calculated assuming a certain geometry of the illuminating corona or considered as a free parameter in the model and set by the observations. Another very important parameter is the extent of the disc, in particular the location of its inner radius. The shape of the line profile provides a diagnostic for this radius, and therefore the black hole spin parameter if $R_{\rm in} = R_{\rm ISCO}$. The final spectral shape of the reflection component is the convolution of the restframe reflection spectrum with the line profile if the intrinsic spectrum is a delta line, where all the features are distorted by the dynamical and relativistic effects.

1.1.4 Coronal Geometry

The literature presents an extensive debate about the geometry of the corona, which is thought to be similar for AGN and hard state BHBs. The structure of this region is important to determine the contribution of the different spectral components. The disc and corona interact, in that the disc is thought to be the source of seed photons for the corona, and the up-scattered photons illuminate the disc to produce the reflection component. Thus, the geometry 'disc + corona' has been developed in different flavours to justify both the spectral shape and the variability observed. I list here a few of the most common geometry models in the literature (see Fig. 1.4):

Sandwich corona The hot corona embeds a colder accretion disc. Haardt & Maraschi (1993) studied the radiative transfer in this geometry and showed that soft thermal photons emitted by the cold layer are the source of cooling for the hot electrons in the corona. On the other hand, half of the high-energy photons heat the underlying layer of the disc. The electrons are confined close to the accretion disc by the magnetic field in analogy to the corona of the Sun (Field & Rogers 1993). This model produces the observed spectrum of Seyfert galaxies only when all the gravitational potential energy is dissipated in the corona (Poutanen 1998). Similar caveats have been found applying this geometry to BHBs (Dove et al. 1997).

Patchy corona This is an irregular corona composed of multiple regions spread around the accretion disc (Haardt et al. 1994). The clumpy corona does not completely cover the disc, so that the cooling by the thermal disc photons is less efficient than with a total covering corona. Thus, it is easier to emit hard spectra. The coronal patches, active regions with geometries such as hemispheres, can be produced by flares or coronal loops (Stern et al. 1995).

Inner flow The disc is divided into two regions: an inner hot geometrically thick optically thin zone and an outer cold geometrically thin optically thick zone (Shapiro et al. 1976). The outer part of the disc produces the thermalized photons that are Comptonized by the inner flow. The reason for the transition between the two zones

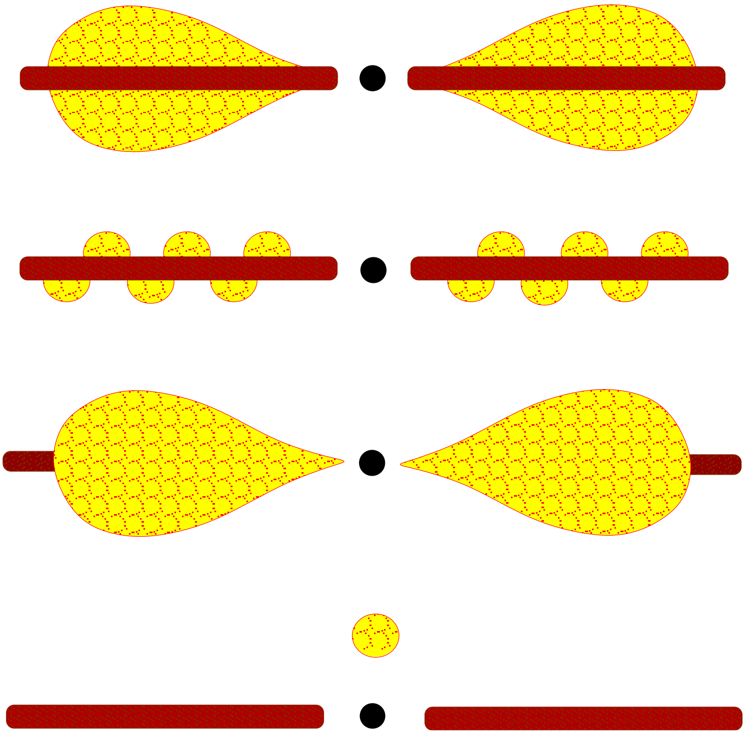

Figure 1.4: Sketch of possible geometries for the disc + corona system. From the top, *Sandwich corona*: the accretion disc is embedded in the corona; *Patchy corona*: the corona is formed by active regions which do not completely cover the disc; *Inner flow*: the corona is a geometrically thick extension of the disc; *Lamppost corona*: the ultra-compact corona is placed on the disc symmetry axis above the black hole. Image adapted from (Reynolds & Nowak 2003).

is not clear, but has been proposed to involve disc evaporation (Meyer & Meyer-Hofmeister 1994) or other instabilities (e.g. Potter & Balbus 2017). In this configuration only a portion of the thermal radiation would reach the internal corona leading to less drastic cooling than with the sandwich geometry.

Lamppost corona In this case the corona is a point-like source placed above the disc on its symmetry axis (Matt et al. 1991, 1992). This geometry still considers seed photons from the accretion disc, but their cooling effect is less because of the smaller corona, making it possible to reproduce the observed hard spectra (e.g. Duro et al. 2011). For an illuminating point-like source it is possible to self-consistently calculate the radial emissivity profile of the accretion disc. Due to relativistic effects, this is steeper than r^{-3}, as is required by observations (Fabian et al. 2004; Wilkins & Fabian 2011; Miller et al. 2013). I will employ the lamppost geometry for much of this thesis, because it is simple enough to be computationally tractable. Physically, such a compact corona may take the form of an over-density at the base of the outflowing jet (Markoff et al. 2005; Kara et al. 2019), which we see downstream far from the black hole via radio emission (e.g. Fender 2010).

Spectral analysis is used to measure the parameters of accreting black holes; e.g. black hole spin, inclination and iron abundance of the disc. However, it is difficult to measure the mass of the central black hole. The only spectral component sensitive to the mass is the multi-temperature blackbody, but for this component the mass is degenerate with $r_{\rm in}$, the distance to the source and the inclination angle. The reflection component depends on distances in units of the gravitational radius, which scales with the mass of the black hole. Therefore the only way to measure the mass using this component is by calibrating the physical length of the gravitational radius. The X-ray timing characteristics of these systems, on the other hand, depend directly on the physical size of the system. Hence considering the spectral and timing properties together can provide the calibration of the gravitational radius required to measure the mass using the X-ray signal.

1.2 Timing Properties

Another technique to study accreting black holes involves considering the time variability of the emitted radiation. In spectral analysis, the flux variations of the light curve are averaged over the length of the observation. However, the count rate detected by the telescope is not constant, but varies down to relatively short timescales, $\sim (0.01 - 10) M/M_{\odot}$ s. This rapid variability most likely originates in the regions close to the black hole, and therefore is a fundamental piece of information to probe the physical properties of the black hole and the accretion disc.

Fourier analysis of X-ray time-series is a convenient tool to study this variability. In the frequency domain accessed by such Fourier analysis, it is easier to disentangle the different processes that contribute to the total variability. Even though Fourier techniques suffer from some artifacts such as aliasing and windowing effects, they make it possible to decompose the data in terms of variations on different timescales. In the next section I describe the Fourier cross-spectrum technique, which is particularly useful to compare the variability simultaneously taking place in different energy bands. With this technique it is possible to reconstruct how the energy spectrum varies on short time scales.

1.2.1 Cross-Spectrum

Let us divide an observed light curve $x(t)$ into adjacent time-series of identical length. A single time-series is defined as x_k, expressed in counts per unit time, with N time bins of width dt with $k = 1, ..., N$. The discrete Fourier transform is defined as

$$X_j = \frac{1}{N} \sum_{k=1}^{N} x_k e^{i\,2\pi\,jk/N} \tag{1.2}$$

where X_j is evaluated at each Fourier frequency $\nu_j = j/(N\,dt)$ and $j = -N/2 + 1, ..., N/2$. Low Fourier frequencies correspond to long timescale variability, whilst high Fourier frequencies correspond to short timescale variability. The length of the time-series ($T = N\,dt$) determines the lowest Fourier frequency that this technique can probe. The highest frequency is called the Nyquist frequency and it is set by the time resolution (dt) of the time series as $\nu_{\mathrm{Ny}} = 1/(2\,dt)$.

The Fourier cross-spectrum technique compares two time-series (x_k y_k), which are two of the segments of the observed light curves ($x(t)$ $y(t)$), and finds the timescales where they vary together: the cross-spectrum measures the level of variability *correlation* between two light curves and the time lag between these variations. Using this technique to study the variability in two simultaneous light curves in different energy bands will tell if there are timescales that are connected between the two light curves and how they are correlated. The cross-spectrum is defined in the Fourier domain, as

$$C_j = X_j Y_j^* \tag{1.3}$$

where the upper case letters are the Fourier transform of the light curves and the * denotes the complex conjugate. C_j is a complex quantity, therefore, it defines amplitudes and phases as a function of Fourier frequency. It turns out that black hole rapid variability is a stochastic process, so it is more relevant to study the average properties than a single realization. Therefore the ensemble of cross-spectra calculated from the adjacent segments of the two initial light curves are averaged together to obtain a single cross-spectrum of the process. It is also possible to average further the cross-spectrum over a range of Fourier frequencies. Statistically there is no difference between the two averages, since the adjacent Fourier frequencies are statistically independent one another as well as the adjacent light curve segments.

The amplitude of the averaged cross-spectrum is $A(\nu) = \sqrt{(\mathrm{Re}[C(\nu)])^2 + (\mathrm{Im}[C(\nu)])^2}$ where Re[] and Im[] denote real and imaginary part. It represents the amount of correlated variability at each Fourier frequency. The amplitude due to any uncorrelated contributions to the signal in the two light curves, such as the Poisson noise due to counting statistics, tends to zero. The phase difference between two light curves as a function of Fourier frequency is $\phi(\nu) = \arctan[\mathrm{Im}[C(\nu)]/\mathrm{Re}[C(\nu)]]$. The phase lags can be converted to 'time lags', $\mu(\nu)$, by dividing by frequency $\mu(\nu_j) = \phi(\nu_j)/(2\pi\nu_j)$ for an easier interpretation of the data. However, the phase lag is limited to the range $-\pi$ to π, so for true physical time lags exceeding $\pm 1/(2\nu_j)$, care should be taken in the interpretation of μ. In particular, when the value is close to these limits, the phase lag, and hence the μ calculated from it can flip from positive to negative (or vice versa). This arises because there is no difference between two periodic waves that are shifted by half a period, either backwards or forwards. Therefore, when the true time lag at a specific Fourier frequency (ν_0) increases from just less to just more than half a cycle, $1/(2\nu_0)$, or vv., the calculated time lag μ shows a large jump and changes sign in an unphysical way. The process repeats at values of the true time lag that are exactly an integer number of cycles larger or smaller, so multiple jumps can be observed. This effect is called phase-wrapping and it is an artifact that arises due to the periodic nature of the sinusoids used to decompose the signal in Fourier analysis, similar to car wheels appearing to rotate backwards when viewed over lower frequency frame rate.

1.2.2 Time Lags

In this Section I describe the time lags in accreting black holes starting from what is expected in terms of the geometry that I outlined above. According to the geometry of the system the X-ray continuum photons reflected by the disc towards the observer have a longer path than the inverse Compton photons that travel directly to the observer. This should produce a time lag between the light curves in the energy bands dominated by the reflected emission and light curves dominated by the continuum emission. The first studies of the X-ray variability in terms of the cross-spectrum were on X-ray binaries (GX 5-1 and Cyg X-2; van der Klis et al. 1987). Miyamoto et al. (1988) first found that in the black hole binary Cygnus X-1 ‘hard’ light curves (extracted from high energy X-rays) lag behind the ‘soft’ light curves (extracted from low energy X-rays). These *positive* lags (also called hard lags) are much larger than what is expected from the reverberation mechanism unless the distance between the disc and the corona is thousands of R_g (Kotov et al. 2001). Lyubarskii (1997) proposed that these lags are instead due to propagating mass accretion rate fluctuations. In this mechanism, independent viscosity fluctuations are produced at different radii in the disc, where they trigger fluctuations in the mass accretion rate, and therefore in the luminosity. The timescale of the fluctuations depends on the viscous timescale which is a function of radius, with longer timescales at larger radii and shorter timescales closer to the black hole. Since the matter in the accretion disc is accreting, these fluctuations propagate towards the center, thus the variability at at each radius is the product of the mass accretion rate fluctuations produced locally and the fluctuations propagated from radii further out. This means that the high energy emission coming from the the inner part of the accretion disc is characterized by both short timescale and long timescale variability, the latter lagging the same variability observed from the outer regions of the disc by the time it takes for the long timescale fluctuations to propagate in. This type of lag has been observed in both stellar mass black holes (e.g. Nowak et al. 1999) and supermassive black holes (Papadakis et al. 2001; McHardy et al. 2004). Following Lyubarskii (1997), detailed models have been developed to reproduce light curves caused by propagating mass accretion rate fluctuations (Kotov et al. 2001; Arévalo & Uttley 2006; Ingram & van der Klis 2013). These models are computationally time consuming because they have to simulate the radial disc structure and propagate the fluctuations at the viscous timescales. However, Ingram & van der Klis (2013) calculate the asymptotic result of averaging an infinite number of realizations analytically, making it possible to fit to the data (Rapisarda et al. 2016, 2017a,b).

The first hint of reverberation lags was found by McHardy et al. (2007) who discovered evidence for two components in the lag vs frequency spectrum of Ark 564. This result was confirmed by the clear detection of negative lags in 1H0707-495 (Fabian et al. 2009). The upper panel of Figure 1.5 shows the lag of the soft energy band relative to the hard energy band as a function of frequency in Ark 564 (Kara et al. 2013a). The lag is positive (hard lags soft) at low frequencies and negative (soft lags hard) at high frequencies. This type of lag must come from a different process than mass accretion rate propagating fluctuations. Since one of the interpretations of the soft excess in the AGN spectra is connected to the reflected emission, it was immediately suggested that negative lags were due to the reverberation process involving the light crossing time between reflected photons and direct photons (Fabian et al. 2009). At long timescales the lags are dominated by the intrinsic variability of the accretion flow, but this variability is weaker at short timescales allowing the reverberation to show up. This behaviour of the lag as a function of frequency has been observed in several AGN (De Marco et al. 2013a), revealing a correlation between the magnitude of the negative lag and the mass of the black hole. This correlation is naturally explained by the reverberation process since the size of the system scales with the mass.

Further investigations into the nature of these lags include the analysis of the lag as a function of energy. This analysis involves computing the cross-spectrum of light curves from multiple energy bands with the same reference band. This is usually the light curve of the total energy range from which the subject light curve has been subtracted in order to avoid the zero-lag component due to the trivial correlation of the subject *Poisson noise* band with itself, which would dilute the lag (for the step-by-step procedure see Uttley et al. 2014). The lag energy spectrum was first studied for both the hard lag and the soft lag frequency regime in AGN. Zoghbi et al. (2012) were the first to discover the iron Kα line feature in the lag energy spectrum of NGC 4151. Furthermore in the same observation they found that the core of the line lags behind the red wing of the line as expected from the reflection response of the disc. The relativisticly broadened part of the line is emitted from the inner part of the disc whereas its narrow core comes from the outer regions. The bottom panels of Figure 1.5 show the lag energy spectra of Ark 564 in two frequency ranges. The reflection feature appears only at high frequencies, whereas at low frequencies the lag

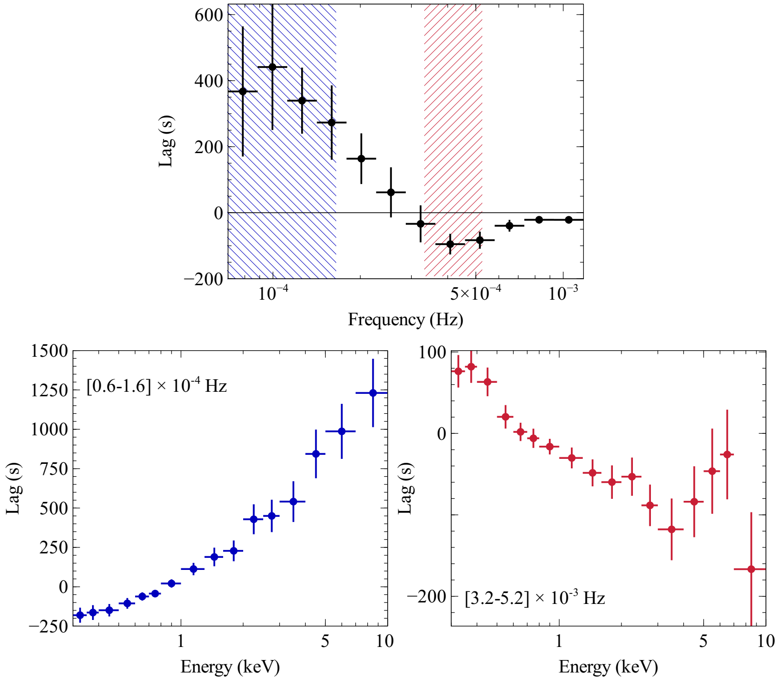

Figure 1.5: Evolution of the lags as a function of frequency and energy in Ark 564. Top panel: lag vs frequency between $1.2-4$ keV and $0.3-1$ keV. The lag starts positive at low frequencies and becomes negative at high frequencies, suggesting two different processes. Bottom panels: lag vs energy in the low frequency range (blue, left) and in the high frequency range (red, right), the ranges are highlighted in the top panel. The low-frequency spectrum shows a featureless lag, whereas the Fe Kα signature of a reflection spectrum shows up in the high-frequency spectrum indicating it is caused by the reverberation. This confirms the two different origins of the lags. Image adapted from Kara et al. (2013a).

energy spectrum is featureless and with a monotonic shape. This is an additional confirmation that the two types of lag are caused by to two different processes which need specific modelling. The iron line in the lag energy spectrum has been detected in several Seyfery galaxies (Kara et al. 2016). Alternative explanations have also been put forward for the soft lag. Miller et al. (2010) proposed that the X-ray source is partially covered by distant optically thick clouds. The reverberation from material up to a few light-hours from the central source produces the observed lags. However, this model has difficulties to explain the Fe Kα feature in the lag spectrum. More recently Mizumoto et al. (2018) proposed that the Fe-K lags could be produced by a fast ($0.2\,c$) outflowing, highly ionised wind.

In view of the expectation of similar geometry of the accretion flows onto stellar mass black holes and supermassive black holes, they should show the same behaviour, but at different timescales. The Fourier frequencies of the processes scale inversely with the mass. So the high frequencies where the reverberation lag is expected ($\sim 300 M_\odot/M$ Hz) in stellar mass black holes are very challenging to probe even with most of the current instruments due to the high time resolution required. Nevertheless the energy dependence of the variability has been studied analyzing the variability amplitude. Revnivtsev et al. (1999) showed how the iron line becomes weaker at shorter timescales because the fastest continuum variability is washed out in the reflected emission by the finite size of the reflector. Kotov et al. (2001) noticed a structure around the iron line energy in the lag energy spectrum of Cygnus X-1, although it resembles an absorption-like feature. De Marco et al. (2017) analyzed *XMM-Newton* data of GX 339–4 finding hints of Fe Kα reverberation, although the poor signal to noise at high frequency did not allow a strong claim. The first evidence of the reverberation signature in stellar mass black holes was therefore found in the thermal reprocessing of the incident radiation by the disc. Again in GX 339–4 Uttley et al. (2011) found that the soft (below 1 keV) photons, whose variability is linked to the variability in the disc, lag the power-law photons with time lags of milliseconds. This happens *only* at frequencies above 1 Hz. This picture is consistent with fluctuations propagating through the disc to the inner corona on the viscous timescales and photons from the corona being thermally reprocessed by the disc with delays equal to the light travel time. De Marco et al. (2015) confirmed this result in in GX 339–4 and H1743–322 and found that the reverberation lag decreases as the luminosity of the source increases, implying that either the reprocessing region or the illuminating region moves gradually closer the black hole. It is worth noting that the thermal reprocessing time may not be negligible due to the many scattering events needed to thermalise the radiation. This would contribute to the observed lag, which is then not only caused by the light crossing time. The reprocessing of the reflected emission to create the reflection features involves fewer scatterings therefore it is less likely to be an important factor in the lags.

In June 2017 the *Neutron star Interior Composition Explorer* (*NICER* Gendreau et al. 2016) was launched with the X-ray Timing Instrument on board, which has an unprecedentedly high time resolution (40 ns). Together with the capability of collecting large numbers of photons and a very good telemetry rate, this instrument is able to access the very short timescales of the reverberation lags with good spectral resolution and high signal to noise. In early 2019 Kara et al. (2019) found a clear detection of the iron Kα line in the lag energy spectrum of MAXI J1820+070. Figure 1.6 shows that the iron line feature emerges at the frequencies corresponding to the negative lag in the lag vs frequency spectrum for different observations (different colors). It is worth noting that the lag vs energy spectra also show the feature of the thermal reverberation below 1 keV. So far the behaviour in black hole binaries seems remarkably similar to that which has been observed in AGN.

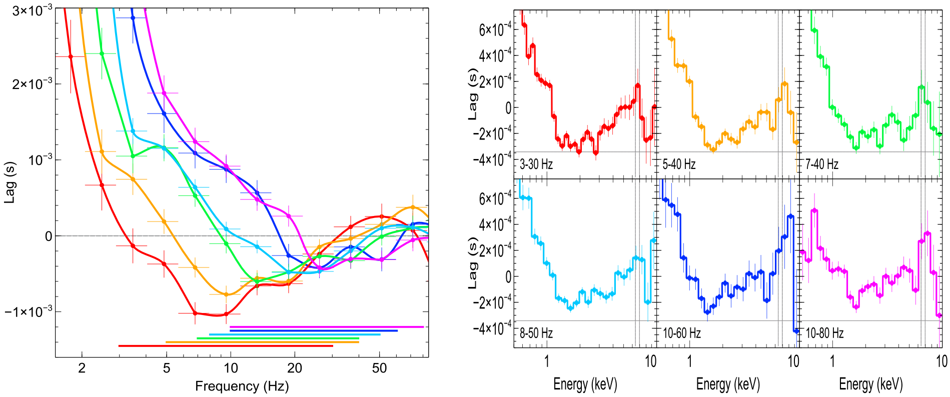

Figure 1.6: Evolution of lags as a function of frequency and energy in MAXI J1820+070. Left panel: lag vs frequency spectrum between $0.5 - 1$ keV and $1 - 10$ keV energy bands in six subsequent observations during the 2018 outburst (the colors code the increasing hardness ratio from red to fuchsia). The points are connected with a Bezier join to guide the eye. Positive lags (hard band follows the soft band) dominate at lower frequencies, negative lags at high frequencies. Right panels: lag vs energy in the frequency ranges indicated by the horizontal lines in the left panel (only negative lag frequencies are considered). All six observations show an Fe Kα lag due to reverberation. The horizontal line indicates the minimum lag of the first observation. Images from Kara et al. (2019).

1.2.3 Modelling

In the previous section I presented the phenomenology of the lags observed in stellar mass and supermassive black holes. Even though it seems clear that there are two distinct types of lags which dominate in two different time scale regimes, they probably both contribute in both regimes and certainly the transition is not sharp. Therefore, in order to constrain the characteristics of these systems we model the intrinsic lags of the continuum emission together with the reverberation lags. The following chapters in thesis present the RELTRANS model which is able to account for both types of variability. In this section I introduce the concept of the model and the technique that has been used to developed it. Combining mass accretion rate fluctuations propagating through the accretion flow and the reverberation process, accounting self-consistently for the energy and timing emission is extremely challenging in terms of computing time. The idea behind RELTRANS is to use a simple analytic prescription to account for the hard lag. In previous work, the variability of the inverse Compton component has been described as a variability of the normalisation at constant spectral slope. However, if the slope of this component fluctuates as well as the normalisation, this can produce an intrinsic lag (see Chapter 2) with the characteristics of the hard lags observed in the data. Furthermore every patch of the disc sees a slightly different inclination of the illuminating continuum causing non-linear effects both in the time-averaged energy spectrum and in the lag energy spectrum. The *pivoting* of the continuum component is due to the heating and cooling of the corona caused by fluctuations in the mass accretion rate and the Compton cooling in the corona, the former caused by the propagating fluctuations in the disc that eventually reach the corona, the latter by photons coming directly from the ‘cold’ outer disc.

The best way to account for the variations in the disc in response to these slope variations is through the transfer function. This is the Fourier transform of the time-energy response function, which itself is the dependence on time and energy of the radiation emitted by the disc in response to a delta-function flash of the incident high energy cut-off power-law radiation from the illuminating source. So, this technique combines the time-dependent response of the disc with its energy-dependent response. The former accounts for the energy-averaged response of an accretion disc to a flash of illuminating radiation, computing the geodesics of the photons from continuum source to each patch of the disc and from there to the observer. The latter is the time-averaged spectral response of the disc that accounts for the emission line profile of each patch of the disc, resulting in the relativistically broadened line profile studied in Section 1.1.3. The inner part of the disc responds before the outer part and the emitted line profile is broader because of the stronger relativistic effects. The response of the outer part comes later and the line profile is narrower. Hence, at low Fourier frequencies we see the response of all the disc, while at high Fourier frequencies we look at the inner parts of the disc and the outer parts are filtered out. Cackett et al. (2014) studied the detailed response of the iron Kα line as a function of frequency. The shape of the transfer function depends on the characteristic parameters of the system such as the mass and spin of the black hole and the geometry of the accretion disc. In this thesis we use this mathematical tool to describe analytically how our prescription for the hard lags affects the time and the energy dependence of the reflection component. The time dependence of the observed reflection spectrum is expressed in terms of a convolution, which becomes a multiplication in the Fourier domain. Moreover, Taylor expanding both continuum and reflection components keeps the mathematical expression of the emitting radiation as a function of energy and time linear and makes it possible to describe the pivoting effect in terms of a sum of transfer functions. This procedure is mathematically described in the following chapters and it has the advantage of maintaining an analytic description of the model.

1.3 Thesis Outline

The scope of this thesis is to improve our current understanding of accreting black holes using spectral timing analysis of the X-ray reflection. In the following chapters I describe how we pursued this objective, particularly focusing on X-ray reverberation, which allows parameters of the system to be measured such as the mass of the black hole.

Chapter 2 presents the mathematical prescription to account for the pivoting hardness of the continuum emission and shows how it can produce the hard lags observed in Cygnus X-1. Furthermore, it demonstrates how these hardness fluctuations affect the reverberation lags. The proof-of-principle fit to the observed Cygnus X-1 correlated variability shows good agreement between the data and the model, although some residual structures are still present.

Chapter 3 presents the fully relativistic RELTRANS model, which calculates the reverberation lags and correlated variability amplitudes in an arbitrary Fourier frequency range. The model includes a self-consistently calculated radial ionisation profile of the disc and accounts for a different emission angle and high energy cut-off in every patch of the disc. It also includes a proper treatment of the telescope response matrix and the Galactic absorption which can affect particularly the soft part of the time lag spectrum.

Chapter 4 presents a mass measurement of the Cygnus X-1 black hole using the X-ray reverberation modelled with RELTRANS. The model includes the non-linear effects due to the power-law pivoting in order to make it possible to fit a wider range of Fourier frequencies. The best fit favours the model with the more physical assumption of a radial ionisation profile instead of constant ionisation in the disc. The fit constrains the black hole mass for different assumptions made on the radial ionisation profile and all the values are compatible with the dynamical measurement within 3 σ. Setting a realistic upper limit on the ionisation peak based on the illuminating flux and the density of the disc leads to mass values that are closer to the dynamical measurement.

Chapter 5 presents a RELTRANS analysis of Mrk 335. We first model the reverberation lag and the time-averaged spectrum simultaneously, which we show can constrain the mass of the central supermassive black hole. The model favours a lower mass (a few million Solar masses) than what has been measured with other techniques (such as optical reverberation mapping). However, when we also consider the correlated variability amplitudes the model is unable to fit the characteristic reverberation features that show up in the data, and can not constrain the black hole mass. In order to solve this issue we plan to experiment with more realistic geometries in future versions of the model.

2

Multi-timescale X-ray reverberation mapping of accreting black holes

Guglielmo Mastroserio, Adam Ingram & Michiel van der Klis

Monthly Notices of the Royal Astronomical Society, 2018, 475, 4027-4042

Abstract

Accreting black holes show characteristic reflection features in their X-ray spectrum, including an iron Kα line, resulting from hard X-ray continuum photons illuminating the accretion disk. The reverberation lag resulting from the path length difference between direct and reflected emission provides a powerful tool to probe the innermost regions around both stellar-mass and supermassive black holes. Here, we present for the first time a reverberation mapping formalism that enables modeling of energy dependent time lags and variability amplitude for a wide range of variability timescales, taking the complete information of the cross-spectrum into account. We use a pivoting power-law model to account for the spectral variability of the continuum that dominates over the reverberation lags for longer time scale variability. We use an analytic approximation to self-consistently account for the non-linear effects caused by this continuum spectral variability, which have been ignored by all previous reverberation studies. We find that ignoring these non-linear effects can bias measurements of the reverberation lags, particularly at low frequencies. Since our model is analytic, we are able to fit simultaneously for a wide range of Fourier frequencies without prohibitive computational expense. We also introduce a formalism of fitting to real and imaginary parts of our cross-spectrum statistic, which naturally avoids some mistakes/inaccuracies previously common in the literature. We perform proof-of-principle fits to *Rossi X-ray Timing Explorer* data of Cygnus X-1.

2.1 Introduction

In black hole X-ray binaries (BHBs) and active galactic nuclei (AGN), the central black hole is thought to be fed, at least in part, by an optically thick accretion disc that radiates a multi-temperature blackbody spectrum (Shakura & Sunyaev 1973). This disc emission peaks in soft X-rays for BHBs and optical soft X-rays for AGN. In both cases, a different component dominates the hard X-ray radiation, which is often described by a cut-off power-law. This *continuum* emission is thought to originate from the Compton up-scattering of comparatively cool photons by hot electrons located in an optically thin ($\tau \sim 1$) region close to the black hole, often referred to as the corona (Eardley et al. 1975; Thorne & Price 1975). Some fraction of these continuum photons illuminate the disc to be scattered into our line-of-sight, giving rise to a characteristic *reflection* spectrum that imprints features onto the observed spectrum including a prominent iron Kα fluorescence line at $\sim$ 6.4 keV and a reflection hump peaking at $\sim$ 30 keV. This reflection spectrum provides a powerful diagnostic for the dynamics of the accretion disc, since it is distorted by the gravitational pull of the black hole and Doppler shifts from rapid orbital motion (Fabian et al. 1989). Rapid variability of the system provides another powerful diagnostic, particularly because any fluctuations in the continuum should be followed, after a light-crossing delay, by similar fluctuations in the reflection spectrum. Characterization of these reverberation lags provides another tool to map the accretion disc.

Reverberation lags can be probed by studying the Fourier frequency dependent time lags between different energy bands, since bands with a greater contribution from reflection should slightly lag those dominated by the continuum. The time lags can be calculated from the argument of the cross-spectrum between each energy channel and a common reference band (Uttley et al. 2014). It has long been known that hard photons lag soft photons for comparatively low Fourier frequencies (below $\sim 300[M_\odot/M]$ Hz), both in BHBs (e.g. Miyamoto & Kitamoto 1989; Nowak et al. 1999) and AGN (e.g. Papadakis et al. 2001; McHardy et al. 2004; Epitropakis & Papadakis 2017). However, these lags do not show any reflection features in the lag-energy spectrum and for this reason they are thought to be associated with intrinsic variation of the continuum spectral shape. This is commonly interpreted as propagation of mass accretion rate fluctuations towards the black hole on a viscous timescale (Lyubarskii 1997; Kotov et al. 2001; Arévalo & Uttley 2006; Ingram & van der Klis 2013; Rapisarda et al. 2016). This intrinsic continuum lag reduces with increasing Fourier frequency, leaving the opportunity to detect a reverberation signature at high frequencies. Such lags have been detected for AGN, first in the form of soft-excess emission ($\sim 0.2-0.9$ keV) lagging the continuum dominated band ($\sim 1-4$ keV) (Fabian et al. 2009), and later in the form of an iron K feature in the lag-energy spectrum at $\sim$ 6.4 keV (Zoghbi et al. 2012; Kara et al. 2016). The latter is the cleanest measurement, since the proposed reflection origin of the soft X-ray excess in AGN is not universally accepted, with alternative models invoking an extra Compton up-scattering component (Page et al. 2004; Done et al. 2012), while it is very difficult to reproduce the iron K feature in the lag-energy spectrum without using the reflection mechanism. Reverberation lags have not yet been clearly detected for BHBs (even though De Marco et al. 2017, recently found hints of FeK reverberation), since the smaller size of these systems leads to the lags being shorter ($\sim$ millisecond) and only dominant over the continuum lags for higher Fourier frequencies. However, Uttley et al. (2011) and De Marco et al. (2015); De Marco & Ponti (2016) found that the disc blackbody emission lags the continuum emission in GX 339$-$4 and H1743$-$322 by a few milliseconds, which they attribute to reprocessed photons being re-emitted as thermalised radiation.

The reverberation signature also depends on Fourier frequency, since fast variations in the driving continuum are washed out in the reflected emission by path length differences between photons reflecting from different parts of the disc. This means that the iron K feature in the lag-energy spectrum should be broader at higher Fourier frequencies, since rapid variability is washed out for reflection from all but the smallest, most rapidly rotating and gravitationally redshifted disc radii. Indeed, Zoghbi et al. (2012) found just this for the iron K lags in NGC 4151. Further information is contained in the variability amplitude of the reflected emission relative to the continuum. Revnivtsev et al. (1999) and Gilfanov et al. (2000) found that the relative variability amplitude of the reflected emission in Cygnus X-1 decreases at higher Fourier frequencies, as expected (see Section 2.4).

An elegant way to model reverberation is to calculate a *response function*, defined as the energy and time dependent reflected emission resulting from a $\delta-$function flash in the driving continuum (e.g. Campana & Stella 1995; Reynolds et al. 1999; Kotov et al. 2001). If the disc properties are approximately independent of the irradiating flux, the reflected flux responding to an arbitrary driving continuum signal is given by a convolution between the driving signal and the response function. The convolution theorem therefore means it is most convenient to consider the Fourier transform of the response function, referred to here as the *transfer function* (e.g. Oppenheim & Schafer 1975). This function, which can in principle be constrained from energy and Fourier frequency dependent amplitude and phase of the observed cross-spectrum, contains information about the accretion geometry. However, the dominance of continuum lags at low frequencies makes this challenging. Authors have therefore previously modelled the lags only at high Fourier frequencies (e.g. Cackett et al. 2014), used an *ad hoc* prescription to account for the continuum lags (Emmanoulopoulos et al. 2014; Epitropakis et al. 2016), or only considered amplitude and not phase (Gilfanov et al. 2000). Progress has been made in modelling the intrinsic continuum lag with propagating fluctuations and taking account of reverberation lags in specific geometries (Wilkins & Fabian 2013; Wilkins et al. 2016; Chainakun & Young 2017). However this is computationally expensive, particularly for the purpose of fitting lag-energy spectra for a large range of Fourier frequencies. Here, we present a simple analytic way to model the continuum lags, and self-consistently take into account the impact of those lags on the reverberation signal. We model the continuum lags as perturbations in the continuum power-law index and account for the changes in the reflection spectrum caused by these perturbations with a first order Taylor expansion. A similar pivoting power-law model was considered by Poutanen (2002), but he assumed the energy dependent reflection to continuum ratio to be *independent* of the illuminated continuum. Our formalism allows us to fit to data, considering lags and amplitude for a large range of Fourier frequencies without prohibitive computational cost.

In Section 2.2 we introduce the cross-spectral method that we use to compute the model and analyse the data. We highlight some common inaccuracies that can occur with similar techniques, and show that such inaccuracies can be easily avoided by modelling real and imaginary parts of the cross-spectrum rather than the amplitude and phase. In Section 2.3, we present our model formalism. In Section 2.4, we explore our model parameters, focusing on the importance of the non-linear effects resulting from variations in the energy dependence of the reflection disc caused by variations in the hardness of the driving continuum. In Section 2.5, we perform proof of principle fits to Cygnus X-1 data.

2.2 Cross-Spectrum Method

This Section briefly reviews the spectral timing techniques previously used, before describing our technique that allows amplitude and phase as a function of energy and frequency to be modelled. We also describe how our method naturally corrects some mathematical inaccuracies often encountered in the literature.

First we define a set of complex cross-spectra $\langle C\left(E,\nu\right)\rangle$ as a function of energy and frequency

$$\langle C\left(E,\nu\right)\rangle = \langle S\left(E,\nu\right)\ F^{*}\left(\nu\right)\rangle, \tag{2.1}$$

where $S\left(E,\nu\right)$ is a set of Fourier transforms of the signal light curve in different energies E, and $F\left(\nu\right)$ is the Fourier transform of the signal in an arbitrary reference band. Starred quantities and angle brackets denote the complex conjugate and ensemble averaging respectively. The phase lag for each energy band relative to the reference band is

$$\phi(E,\nu) = \arg\left[\langle C\left(E,\nu\right)\rangle\right]. \tag{2.2}$$

Many works have focused on analysing the phase-lag with reverberation models (Kotov et al. 2001; Poutanen 2002; Zoghbi et al. 2011; Emmanoulopoulos et al. 2014; Wilkins et al. 2016; Chainakun & Young 2017). Although these studies constrain model parameters by fitting either lag-frequency or lag-energy spectra (sometimes both), they all neglect the information included in the cross-amplitude.

With a suitable choice of normalization, the variability amplitude (in units of absolute rms) as a function of energy and frequency, $\sqrt{\langle |S\,(E,\nu)\,|^2\rangle}$, can be calculated directly (Revnivtsev et al. 1999) by measuring the power spectrum averaged over the frequency range Δ for each energy channel

$$\sqrt{\langle |S\,(E,\nu)\,|^2\rangle} = \sqrt{\left[\langle P\,(E,\nu)\rangle - P_{\mathrm{noise}}\,(E)\right]\,\Delta} \tag{2.3}$$

where the $P\,(E,\nu)$ and $P_{\mathrm{noise}}\,(E)$ are respectively the power spectra and Poisson noise measured for each energy channel (see e.g. van der Klis 1989; Uttley et al. 2014). The correlated variability amplitude, a related quantity, can be calculated with higher signal-to-noise using the covariance spectrum (Wilkinson & Uttley 2009; Uttley et al. 2014)

$$|\langle G(E,\nu)\rangle| = \frac{\sqrt{\Delta}\,|\langle C\,(E,\nu)\rangle|}{\sqrt{\langle P(\nu)\rangle - P_{\mathrm{noise}}}} = \gamma_{\mathrm{c}}(E,\nu)\sqrt{\langle |S\,(E,\nu)\,|^2\rangle}, \tag{2.4}$$

where $\gamma_{\mathrm{c}}(E,\nu)$ is the coherence between each energy channel and the reference band, and $\langle P(\nu)\rangle$ and P_{noise} are respectively the power spectrum and Poisson noise contribution for the reference band (in units of absolute RMS squared per Hz) [1]. So, the covariance is the correlated variability amplitude, which is related to the variability amplitude through the coherence function (Vaughan & Nowak 1997). Since the coherence function is often close to unity for accreting compact objects (e.g. Nowak et al. 1999), the covariance gives a good estimate of the variability amplitude, and its error bars are smaller if a high count rate reference band is chosen (Wilkinson & Uttley 2009).

Many authors have modelled the variability amplitude as a function of energy and frequency (*frequency resolved spectroscopy*: e.g. Gilfanov et al. 2000; Axelsson et al. 2013), either using the power spectrum or the covariance. This approach, as with the lag modelling, provides strong constraints, but now neglects the information contained in the phase lags. Although past works have discussed both amplitude and phase together in the context of reverberation (e.g. Uttley et al. 2011; Kara et al. 2013b), none so far have used quantitative fitting of models for the energy and frequency dependent amplitude and phase to data.

We consider both the amplitude and phase jointly by considering the *complex covariance*, defined as

$$\langle G\,(E,\nu)\rangle = \frac{\sqrt{\Delta}\,\langle C(E,\nu)\rangle}{\sqrt{\langle P\,(\nu)\rangle - P_{\mathrm{noise}}}}. \tag{2.5}$$

We fit models to data for the real and imaginary parts of $\langle G\,(E,\nu)\rangle$ as a function of energy, for a number of discrete frequency ranges (following Rapisarda et al. 2016;

---

[1] P_{noise} does not have the angle brackets because it is estimated theoretically from the assumption of pure Poissonian counting noise.

Ingram et al. 2016). Fitting for real and imaginary parts rather than amplitude and phase naturally avoids some mistakes and inaccuracies commonly found in the literature. This is because the linearity inherent in the Fourier transform operation is preserved. For instance, in order to fit to data, the model must be adjusted for the instrument response. This is a trivial operation in our case, involving simply convolving real and imaginary parts of the model complex covariance with the instrument response, meaning that the model can simply be loaded into e.g. XSPEC as if it were a spectral model (in order to do this correctly it is important to choose a normalization such that the modulus of the Fourier coefficients is in units of absolute rms). For the amplitude and phase it is not possible to apply the same procedure. In particular with the amplitude, it has become commonplace in the literature to account for the instrument response by convolving the model for $\sqrt{\langle |S\,(E,\nu)\,|^2\rangle}$ with the instrument response. We show in Appendix A.1 that this is mathematically incorrect, unless $\phi(E,\nu)=0$ (which is often approximately true, but non-zero phase lags are of physical interest and can in practice be as large as 180° e.g. Cygnus X-2: Mitsuda & Dotani 1989). If there would be a need to fit directly for phase and/or amplitude, the correct procedure would be to convolve real and imaginary parts of the complex covariance (or cross-spectrum) with the instrument response and *then* compare the modulus and the argument of this 'folded' complex covariance (or cross-spectrum) to amplitude and phase measured from the observed data.

Another advantage of our method is that $\langle G\,(E,\nu)\rangle$ can be easily modelled as the sum of multiple spectral components. Although it has become commonplace in the literature to model $\langle |S\,(E,\nu)\,|\rangle$ as a sum of components, this is not mathematically correct in general, since the components should really be complex quantities summed as vectors on the complex plane (see Appendix A.1). Therefore summing spectral components of the amplitude is only appropriate if the phase difference between all complex components is zero. Kotov et al. (2001) point out that the error is small if one component is small compared with the other, but this is often not the case. Similarly, multiple components are often required to model the observed lags. For example, one component may contribute the continuum lags and the other the reverberation lags. We note that it is mathematically incorrect to simply add the lags of two different spectral components, even in a small angle approximation. There are many instances in the literature where it is not clear whether or not this mistake has been made (e.g. Poutanen 2002; Zoghbi et al. 2011; Emmanoulopoulos et al. 2014); although Epitropakis et al. (2016) explicitly show that their treatment is mathematically correct in the framework of the linear transfer function model they employ (lags associated with separate additive spectral components, as defined in Appendix A.1, are not calculated in their treatment). These difficulties are naturally avoided for our method (see also Rapisarda et al. 2016; Ingram et al. 2016).

2.3 Model Formalism

We consider emission from two main components: a continuum cut-off power-law spectrum emitted by a point-like source (this could approximately represent a spectrum due to inverse-Compton scattering), and the same radiation reflected from the disc (or rather scattered in the disc atmosphere). We do not consider intrinsic thermal disc emission, under the assumption that this peaks outside of our considered energy range ($>$ 3 keV). We first describe the two components separately and then we consider them together to probe the non-linear effects resulting from variability of the continuum shape. In this section we define the theoretical model we use to describe the data. Therefore we drop the angle brackets and we can write $|S\left(E,\nu\right)|$ as a prediction of $\sqrt{\langle|S\left(E,\nu\right)|^2\rangle}$. In the whole paper E refers to the photon energy seen by the observer and $E_{\rm em}$ to the energy emitted in the local frame co-moving with the disc plasma.

2.3.1 Continuum

The continuum emission is due to photons that are Compton up-scattered by hot electrons. In the case of the continuum emission we consider $E = E_{\rm em}$. This is a relatively crude approximation that is routinely made in the literature, since the continuum is almost featureless (apart from the high energy cut-off) and therefore the energy shifts are less important than the reflection spectrum (although see Niedźwiecki et al. 2016, for a discussion on this point). The spectrum of this emission can be described as a power-law, cut off at energy $E_{\rm cut}$, that varies in time as

$$D\left(E,t\right) = A\left(t\right) E^{-\Gamma+\beta(t)} \mathrm{e}^{-E/E_{\rm cut}}. \tag{2.6}$$

D expresses the specific photon flux of the continuum at the observer, and we consider the normalization $A\left(t\right)$ and the power-law index $-\Gamma+\beta\left(t\right)$ to both be time dependent. $E_{\rm cut}$ could also be variable in general, but for simplicity we assume this to be constant. We also note that Eq. 2.6 differs somewhat at high energies from the true shape of a spectrum generated through Compton up-scattering of photons by a thermal population of electrons (e.g. Zdziarski et al. 2003), but will suffice for our purposes.

Fluctuations in the normalization and the power-law index could be due to, e.g. fluctuations of the mass accretion rate in the disc, or variation in the temperature of the Comptonising region. Another way to produce these fluctuations is through the rising of compact magnetic flares from the accretion disc (Poutanen & Fabian 1999), although the observed linear rms-flux relation rules out a simple model in which these flares are statistically independent (Uttley et al. 2005).

Here, we simply use Eq. 2.6 as a mathematical model to describe what varies with time in the continuum emission. This model was briefly considered by Kotov et al. (2001) who noted the observed phase lags (in Cygnus X-1) are not consistent with a simple scenario in which $\beta(t) \propto A(t)$; instead there must be a delay between $\beta(t)$ and $A(t)$ oscillations and this was explored in more detail by Körding & Falcke (2004) (also see Shaposhnikov 2012; Misra & Mandal 2013, for similar models applied with different purpose).

We use the lamppost geometry (Matt et al. 1992) in which the continuum is emitted isotropically by a point source situated on the black hole spin axis and with a stationary, cylindrically symmetric thin prograde disc in the equatorial plane. This drastically simplifies our calculations.

2.3.2 Reverberation

Some fraction of the continuum photons are reflected from the disc into our line of sight. Suppose the ionization structure of the disc does not change much on short timescales. Then the reflection spectrum observed from a patch of the disc of area subtending a solid angle according to the observer of $\mathrm{d}\Omega\,(r,\phi)$, where coordinates (r,ϕ) are respectively disc radius and azimuth, is

$$\begin{aligned} dR(E,t|r,\phi) = &\varepsilon\,(r)\, g^3\,(r,\phi)\, A\big(t-\tau(r,\phi)\big) \\ &\mathscr{R}\big(E/g(r,\phi)|\Gamma-\beta\,(t-\tau(r,\phi))\,\big)\mathrm{d}\Omega. \end{aligned} \tag{2.7}$$

The reflection energy spectrum varies with time because the incident continuum radiation does. In Eq. 2.7, $\mathscr{R}\,(E/g|\Gamma-\beta)$ represents the plasma restframe reflection energy spectrum (in units of specific flux) emerging from the X-ray illuminated disc at coordinate (r,ϕ) and $g\,(r,\phi) \equiv E/E_{\mathrm{em}}$ is the blue shift resulting from Doppler & relativistic effects. The factor $g^3\,(r,\phi)$ accounts for Doppler boosting, and gravitational redshift of photons travelling from disc to observer, while $\varepsilon\,(r)$ is the geometrical correction for the flux of photons travelling from source to disc (both g and ε are defined in the Appendix A.2). In Eq. 2.7, and throughout this paper, we express distances in units of $R_{\mathrm{g}} = GM/c^2$. The observed variations of the normalization and the power-law index of the continuum radiation are delayed by an interval $\tau\,(r,\phi)$. This is the time difference between the reflected and the direct signals reaching the observer (see Appendix A.2). A given value of τ defines iso-delay curves on the disc that the observer sees to be simultaneously illuminated with the same continuum normalization A and power-law index $-\Gamma+\beta$. This is the only correction we apply to the incident emission, so we ignore that every radius of the disc sees a different energy shift in the continuum energy spectrum due to gravitational redshift or blueshift, causing a different incident flux and power-law cut-off for every radius of the disc. We use the model XILLVER (García & Kallman 2010; García et al. 2013a) to calculate $\mathscr{R}$. This model calculates the reflection spectrum by solving the equations of radiative transfer, energy balance, and ionization equilibrium in a Compton-thick, plane-parallel medium, being irradiated by a cut-off power-law spectrum.

The observed reflection spectrum can be calculated by integrating Eq. 2.7 over the entire disc surface. This can be simplified greatly by ignoring variations in the power-law index, i.e. setting $\beta = 0$. In this case, the variations in both the continuum and reflected radiation are *linear* and we can therefore calculate the observed reflection spectrum time series by convolving the restframe spectrum time series with the response function. In this case, we can write

$$R\left(E,t\right) = A\left(t\right) \otimes w\left(E,t\right), \tag{2.8}$$

where the operation $\otimes$ denotes a convolution in the time domain (see Appendix A.3 for the definition) and $w(E,t)$ is the response function. Here, we use a simplified calculation of the response function employing the Kerr metric to calculate the energy shift as a function of r and ϕ, but using a flat spacetime for calculating the light travel time of both continuum and reflection photons. In this case, $\mathrm{d}\Omega = r\,\mathrm{d}r\,\mathrm{d}\phi \cos\left(i\right)/D^2$, where i is the inclination angle (defined as the angle between the observer's line-of-sight and the disk normal) and D is the distance to the observer. We can therefore write

$$\begin{aligned} w\left(E,t\right) = \int_0^{2\pi} \int_{r_{\mathrm{in}}}^{r_{\mathrm{out}}} & K\left(r\right) g^3\left(r,\phi\right) \delta\left(t - \tau\left(r,\phi\right)\right) \\ & \mathscr{R}\left(E/g(r,\phi)|\Gamma\right) r\,\mathrm{d}r\,\mathrm{d}\phi, \end{aligned} \tag{2.9}$$

where $K\left(r\right) \equiv \epsilon\left(r\right)\cos\left(i\right)/D^2$. A simple example of such a response function is reported in Fig. 2.1, where $\mathscr{R}$ is a $\delta-$function at 6.4 keV. Although this is an over-simplification of the restframe spectrum, it allows us to see the modifications to a narrow emission line as a function of time and energy. A more realistic scenario (Fig. 2.2) is when $\mathscr{R}$ is calculated using XILLVER. The response function is drawn in the central panels of both the two figures, while the sides panels represent the *time averaged spectrum* (right side panels) and *impulse-response function* i.e. the response function integrated over energy (bottom panels). We will describe these plots in detail with all the parameters used to compute $w\left(E,t\right)$ in Section 2.4.

With the response function formalism we are able to write the time dependence of the observed reflection spectrum in terms of a convolution, which by the convolution theorem corresponds to a multiplication in the Fourier domain. The time dependence of the reflection spectral shape arises entirely due to the response function which provides the corrections to the restframe energy spectrum. The linearity assumption (i.e. $\beta = 0$) has been used for most previous reverberation mapping studies (e.g. Cackett et al. 2014; Emmanoulopoulos et al. 2014; Epitropakis et al. 2016). In the following section, we introduce for the first time a non-linear effect (i.e. $\beta \neq 0$).

2.3.3 Non-linear effects

In the previous Section we set $\beta = 0$ as has been done in the literature. This means that the response function has been calculated assuming there are no phase lags asso-

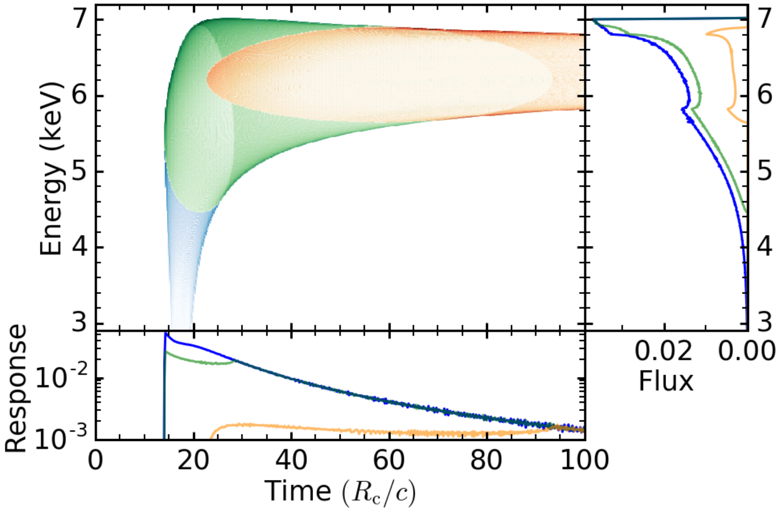

Figure 2.1: Central panel: Response function calculated for three different values of $r_{\rm in}$ of the disc: $1.2\,R_{\rm g}$ (blue), $10\,R_{\rm g}$ (green), and $50\,R_{\rm g}$ (red). For all three functions we consider a disc with $i = 45°$ and $r_{\rm out} = 10^6\,R_{\rm g}$ illuminated by a flash of emission from a point like source at height $h = 10\,r_{\rm g}$ above a black hole with spin $a = 0.998$. Here $\mathscr{R} = \delta\,(E - 6.4~{\rm keV})$. Right panel: Time integrated spectrum (i.e. line profile). Bottom panel: Energy integrated flux (i.e. impulse response function).

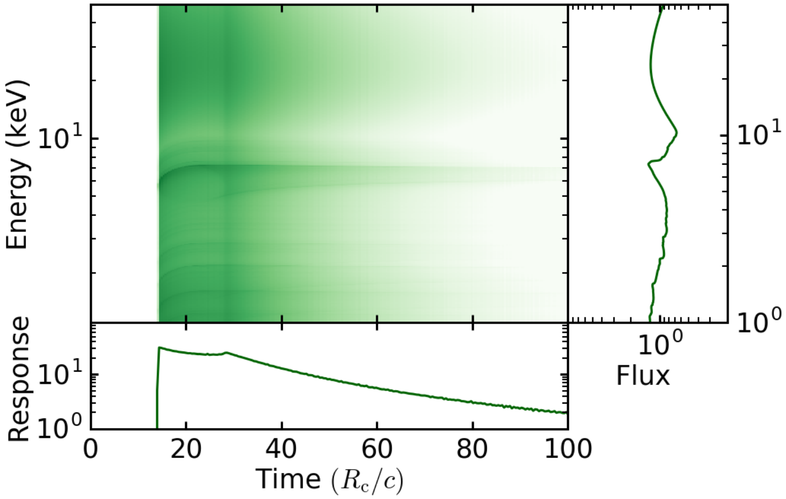

Figure 2.2: Central panel: Response function for a disc with $i = 45°$, $r_{\rm in} = 10\,r_{\rm g}$, and $r_{\rm out} = 10^6\,R_{\rm g}$ illuminated by a flash from a point like source at height $h = 10\,R_{\rm g}$ above a black hole with spin $a = 0.998$. Here $\mathscr{R}$ is calculated using XILLVER with the parameters specified in the text. Right panel: Time integrated spectrum (i.e. energy spectrum). Bottom panel: energy integrated flux (i.e. impulse-response function).

ciated with the continuum. However, neither AGN nor BHBs show any feature in the lag spectrum indicative of reverberation lags for frequencies below $\sim 300[M_\odot/M]\,\mathrm{Hz}$, with the lag spectrum instead *dominated* by featureless continuum lags (e.g. Kotov et al. 2001; Walton et al. 2013).

We model non-linear variation of the continuum spectrum with a variation of the power-law index; i.e. $\beta \neq 0$. We can see from Eq. 2.7 that the shape of the reflection spectrum now depends on time not just because of the response function, but also because it depends on the variable power-law index. Therefore Eq. 2.7 becomes *non-linear* for $\beta \neq 0$ and the simple transfer function formalism is not useful any more. We can, however, linearise. Following Kotov et al. (2001), we can Taylor expand the continuum spectrum to get

$$D\left(E,t\right) \simeq A\left(t\right) E^{-\Gamma} \mathrm{e}^{-E/E_{\mathrm{cut}}} \left[1 + \beta\left(t\right) \ln E\right], \tag{2.10}$$

where we keep terms up to first order. We can take this further, and also Taylor expand the restframe reflection spectrum

$$\mathscr{R}\left(\Gamma - \beta\left(t\right)|E\right) \simeq \mathscr{R}\left(E|\Gamma\right) - \beta\left(t\right) \frac{\partial \mathscr{R}\left(E|\Gamma\right)}{\partial \Gamma}, \tag{2.11}$$

where we compute $\partial\mathscr{R}/\partial\Gamma$ numerically. We explicitly test if it is reasonable to ignore higher order terms in the Taylor expansion in Appendix A.3. Since these expressions are both linear, we can once again employ the response function formalism using Eq. 2.11 to obtain a second response function (i.e. first order approximation whereas w is the zero-order approximation):

$$\begin{aligned} w_1\left(E,t\right) = &\int_0^{2\pi} \int_{r_{\mathrm{in}}}^{r_{\mathrm{out}}} K\left(r\right) g^3\left(r,\phi\right) \delta\left(t - \tau\left(r,\phi\right)\right) \\ &\frac{\mathscr{R}\left(E/g(r,\phi)|\Gamma_2\right) - \mathscr{R}\left(E/g(r,\phi)|\Gamma_1\right)}{\Gamma_2 - \Gamma_1} r\,\mathrm{d}r\,\mathrm{d}\phi, \end{aligned} \tag{2.12}$$

where $\Gamma_2 = \Gamma + {}^{\Delta\Gamma}\!/_2$, $\Gamma_1 = \Gamma - {}^{\Delta\Gamma}\!/_2$ and $\Delta\Gamma$ sets the Γ range where the variation of the restframe reflection spectrum as a function of Γ is supposed to be linear. To keep the linearity even after the Fourier transform we define $B\left(t\right) = A\left(t\right)\beta\left(t\right)$. Since β is arbitrary, we are free to introduce the more useful arbitrary variable B. The total emitted spectrum is simply $S(E,t) = D(E,t) + R(E,t)$ and its Fourier transform after the linearization can be written as

$$\begin{aligned} S\left(E,\nu\right) = &A\left(\nu\right)\left[E^{-\Gamma}\mathrm{e}^{-E/E_{\mathrm{cut}}} + W\left(E,\nu\right)\right] \\ &+ B\left(\nu\right)\left[E^{-\Gamma}\mathrm{e}^{-E/E_{\mathrm{cut}}}\ln E - W_1\left(E,\nu\right)\right]. \end{aligned} \tag{2.13}$$

Here, W and W_1 are the *transfer functions* i.e. Fourier transform of the response function. Since the equation is linear in time the convolution converts into a multiplication in the frequency domain. We see the light-crossing lags are accounted for in Eq. 2.13 by the transfer functions, and the phase difference between A and B at each frequency introduces a continuum lag (the explicit derivation of Eq. 2.13 is in Appendix A.3). We calculate the model complex covariance $G(E,\nu)$ by multiplying $S(E,\nu)$ (Eq. 2.13) with the complex conjugate of the Fourier transform $F(\nu)$ of an arbitrary reference band and dividing by its modulus. In the final expression of the complex covariance, we define the phase angles $\phi_A(\nu) = \arg[A(\nu)F^*(\nu)]$ and $\phi_B(\nu) = \arg[B(\nu)F^*(\nu)]$. We also define $\alpha(\nu) = \sqrt{\Delta}|A(\nu)|$ and $\gamma\left(\nu\right) = \left|B\left(\nu\right)\right|/\left|A\left(\nu\right)\right|$. The model complex covariance then becomes

$$G\left(E,\nu\right) = \alpha\left(\nu\right)\Bigg[\mathrm{e}^{i\phi_A(\nu)}\Big[E^{-\Gamma}\mathrm{e}^{-E/E_{\mathrm{cut}}} + W\left(E,\nu\right)\Big] + \gamma\left(\nu\right)\mathrm{e}^{i\phi_B(\nu)}\Big[E^{-\Gamma}\mathrm{e}^{-E/E_{\mathrm{cut}}}\ln E - W_1\left(E,\nu\right)\Big]\Bigg]. \tag{2.14}$$

Therefore, for each Fourier frequency considered, we model the continuum variation with four arbitrary parameters: $\alpha\left(\nu\right)$, $\gamma\left(\nu\right)$, $\phi_A\left(\nu\right)$ and $\phi_B\left(\nu\right)$. In the fits, these parameters are constrained by the data, but due to their arbitrary nature they do not constrain any of the physical parameters in our model. This does not affect our conclusions on the reflection parameters, which are constrained by the spectral correlations in the data described by our model. In principle, we could recover from these parameters the Fourier transform of $\beta\left(t\right)$. However, in practice this involves a deconvolution ($B(\nu) = A(\nu) \otimes \beta(\nu)$), which requires knowledge of the higher order variability properties of $A(\nu)$ and $B(\nu)$ (Körding & Falcke 2004), which we do not constrain in our modelling. Since this is simply a mathematical model however, $\beta(t)$ is of no more physical interest than $\gamma(\nu)$, which can easily be constrained from data. To fit to the data Eq. 2.14 should be convolved with the instrument response matrix converting energies E into channel numbers I. Therefore the final expression of the complex covariance model is

$$G(I,\nu) = \alpha(\nu)\left[\mathrm{e}^{i\phi_A(\nu)}Z(I,\nu) + \gamma(\nu)\mathrm{e}^{i\phi_B(\nu)}Z_1(I,\nu)\right], \tag{2.15}$$

where $Z(I,\nu)$ and $Z_1(I,\nu)$ are respectively the convolution of $Z(E,\nu) = E^{-\Gamma}\mathrm{e}^{-E/E_{\mathrm{cut}}} + W(E,\nu)$ and $Z_1(E,\nu) = E^{-\Gamma}\mathrm{e}^{-E/E_{\mathrm{cut}}}\ln E - W_1(E,\nu)$ with the instrument response (see Appendix A.4 for a demonstration that convolving the complex covariance with the response is equivalent to the actual process where we cross Fourier transforms of the convolved time series). Note that any additive/multiplicative model (such as line-of-sight absorption) should be applied before the convolution operation, as shown in the previous section and in Appendix A.1. We implement this by multiplying the real and imaginary part of the complex covariance with the absorption component directly and then convolving with the instrument response.

2.4 Model Parameter Exploration

In this Section we explore the parameter space of our model. Although in the following Section we will use real and imaginary parts of the complex covariance to fit to data, here we consider time lags and variability amplitude to explore the parameter space, since these are more intuitive. We can consider two main groups of model parameters: those that govern the response function and therefore the reverberation lags, and those that govern the continuum lags. Further parameters govern the restframe reflection spectrum, which we only briefly discuss but refer the interested reader to García et al. (2013a). Here, we first summarise the response function parameter dependencies and then concentrate on the continuum parameters. We then analyse the importance of accounting for the non-linear effects caused by fluctuations in the reflection energy spectrum.

2.4.1 Response function

The response function for a lamppost geometry depends on the height h of the point source, the inclination angle i, the inner (r_{in}) and the outer (r_{out}) radius of the disc, the dimensionless spin parameter a and the mass M of the black hole. The parameter dependencies of such a response function have already been extensively explored in the literature (Cackett et al. 2014; Emmanoulopoulos et al. 2014). Therefore, here we only briefly explore the transfer function and refer the interested reader to previous papers for more detail. In Fig. 2.1, we show the response function assuming that the restframe reflection spectrum is simply a $\delta-$function iron line at 6.4 keV. In Fig. 2.2 we instead use XILLVER to calculate the restframe reflection spectrum, setting the iron abundance $A_{\mathrm{Fe}} = 1$, ionisation parameter $\log \xi = 3.1$, cut-off energy of the incident power-law $E_{\mathrm{cut}} = 300$ keV and reflection fraction to 1.0.

For both figures, we set $i = 45^{\circ}$, $h = 10$, $r_{\mathrm{out}} = 10^{6}$ and $a = 0.998$. Since we represent time in units of R_{g}/c, Fig. 2.1 and Fig. 2.2 are independent of black hole mass. In Fig. 2.1 blue, green and orange represent an inner radius of $r_{\mathrm{in}} = 1.2$, 10 and 50 respectively, while Fig. 2.2 shows the $r_{\mathrm{in}} = 10$ case only. The central panels show the response function (with shades representing flux), the bottom panels show the impulse response function, and the right hand panel shows the time-averaged line profile. The time axis is defined such that the $\delta-$function flash in the continuum reaches the observer at a time of zero R_{g}/c. After the continuum flash, the next photons to reach the observer are those that reflect from the front of the disc (as seen by the observer), at a radius that depends on h and i. For $i = 45^{\circ}$ and $h = 10$ this radius is $10R_{\mathrm{g}}$. The initial sharp rise in the blue and green curves in Fig. 2.1 therefore occurs at the same time because the inner disc radius for both cases is $\leqslant 10R_{\mathrm{g}}$. The secondary peak in the impulse response function indicates when we see the first photons that reflect from the back of the disc. For a small r_{in}, the broadest iron line is seen shortly after the continuum flash ($\sim 15R_\mathrm{g}/c$ for $r_\mathrm{in} = 1.2$), whereas for $r_\mathrm{in} = 50$ the iron line is initially narrow with its width peaking at $\sim 60R_\mathrm{g}/c$. This is because gravitational redshift is important for small radii, whereas Doppler broadening is dominant for larger radii. This can also be seen in the time-averaged line profile, which is smeared and skewed when the inner radius is small (e.g. blue line $r_\mathrm{in} = 1.2$), while it has the characteristic double horn profile primarily due to Doppler shifts when the disc is far from the black hole (e.g. orange-red line $r_\mathrm{in} = 50$). If we compare Fig. 2.1 with Fig. 2.2, we see the response functions and line profiles are very different because we used a different restframe reflection spectrum (we must compare the green lines because they have the same radius). In contrast, the restframe reflection spectrum makes little difference to the impulse response function, since this is the integral of the response function over all energies.

2.4.2 Continuum Variability

The continuum emission depends on the power-law index Γ and cut-off energy E_cut. We see from Eq. 2.14 that the continuum variations in a frequency range $\nu - \Delta/2$ to $\nu + \Delta/2$ are governed by the parameters $\alpha(\nu)$, $\gamma(\nu)$, $\phi_A(\nu)$ and $\phi_B(\nu)$. $\alpha(\nu)$ is simply a normalization of the variability amplitude for each frequency; i.e. it does not affect the phase lags at all and does not affect the energy dependence of the variability amplitude. Together, the other three parameters govern the energy and frequency dependence of the phase lags. We note that the four continuum variability parameters are not independent and one of them can in principle be derived from the other three using the definition of the reference band (see Appendix A.5). For the illustrative examples presented in this Section, we always use $\phi_A(\nu) = 0$. This would, for example, be the case if there were no contributions from reflection and the reference band were chosen to be at 1 keV.

To explore the continuum parameters, we set the black hole mass to $10M_\odot$ and fix the reflection parameters to those used for Fig. 2.2. In Figs. 2.3 and 2.4, we show the time lag (a) and variability amplitude (b) as a function of energy for a frequency range $1-2$ Hz. Here, amplitude is *absolute* amplitude in units of energy flux, not fractional amplitude. In Fig. 2.3, we fix $\phi_B(\nu) = 0.2$ rad and different lines correspond to different values of $\gamma(\nu)$, which controls the amplitude of the power-law index oscillation. We see that increasing $\gamma(\nu)$ gives a larger absolute value of the lag. We can see from Eq. 2.14 that setting $\gamma(\nu) = 0$ leads to no continuum lag at all. Fig. 2.3b shows that the amplitude spectrum becomes harder when γ is increased. We can partially understand this by imagining a power-law pivoting around some energy E_0, such that the flux at E_0 remains constant and the variations for $E > E_0$ are in anti-phase with the variations for $E < E_0$. In this case, the variability amplitude increases with $|E - E_0|$. For a more realistic case in which the power-law index *and* the normalisation are varying (with a general phase difference between the variations

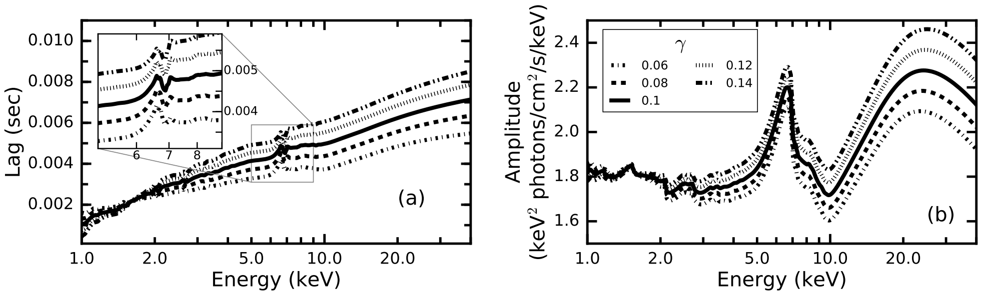

Figure 2.3: Predicted time lags (a) and absolute variability amplitude (b) as a function of energy for the frequency range $1 - 2\,\mathrm{Hz}$. For both panels, $\phi_A = 0\,\mathrm{rad}$ and $\phi_B = 0.2\,\mathrm{rad}$. The curves have different values of γ: 0.02 solid line, 0.04 dashed line, 0.06 dotted dashed line, 0.08 dotted line, 0.1 dashed double dotted line. In both panels we use the parameters: $\Gamma = 2$, $i = 45°$, $r_{\mathrm{in}} = 10$, $r_{\mathrm{out}} = 10^6$, $h = 10\,R_{\mathrm{g}}$, $a = 0.998$, $M = 10M_{\odot}$, $\log_{10}\xi = 3.1$, $A_{\mathrm{Fe}} = 1$ (respectively ionization and iron abundance in XILLVER).

in power-law index and normalisation), there can be no energy at which there is *zero* variability amplitude, but there will be an energy at which the amplitude reaches a *minimum*. The phase lags will also be anti-symmetric about this energy. We will call this the pivot energy, $E_0(\nu)$. Note that the pivot energy can be a function of frequency. Since the amplitude increases with energy in Fig. 2.3, the pivot energy for this example is $E_0(\nu) < 1$ keV. It is worth noting however that extra complication occurs when a realistic spectral model including photoelectric absorption and a low energy cut-off are considered.

In Fig 2.4, we fix $\gamma(\nu) = 0.1$ and vary $\phi_B(\nu)$. We see that increasing $\phi_B(\nu)$ also increases the lags. Panel (b) shows that increasing $\phi_B(\nu)$ makes the amplitude spectrum softer. This can be understood partially as the pivot energy increasing as $\phi_B(\nu)$ is increased. Figs. 2.3a and 2.4a show features around the iron line in the lag-energy spectrum, which are highlighted with a zoom-in. These result from the combination of reverberation lags and continuum lags, and also non-linear effects. The simplest effect comes from the reverberation lag simply being a different value from the continuum lag. In this case, the total energy spectrum is continuum plus reflection and so we expect a dip in the lags at the iron line if the reverberation lag is smaller than the continuum lag, and a peak for the opposite case, since the reflection dominates the energy spectrum at the iron line energy band. Non-linear effects further contribute to these features, with the variations in continuum power-law index causing changes in the shape of the disc reflection energy spectrum. This combination of effects leads to the dependence of the lag around the iron line on $\gamma(\nu)$ and $\phi_B(\nu)$ being subtle.

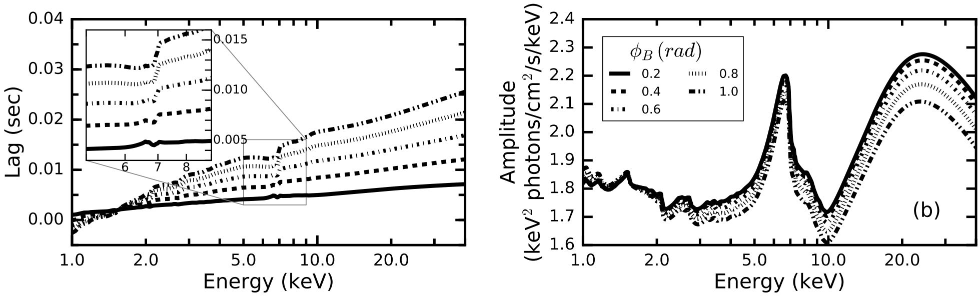

Figure 2.4: Predicted time lags (a) and absolute variability amplitude (b) as a function of energy for the frequency range $1-2\,\mathrm{Hz}$. For both panels, $\phi_A = 0\,\mathrm{rad}$ and $\gamma = 0.1$. The curves have different values of ϕ_B: $0.2\,\mathrm{rad}$ solid line, $0.4\,\mathrm{rad}$ dashed line, $0.6\,\mathrm{rad}$ dotted dashed line, $0.8\,\mathrm{rad}$ dotted line, $1\,\mathrm{rad}$ dashed double dotted line. In both panels we use the parameters: $\Gamma = 2$, $i = 45°$, $r_{\mathrm{in}} = 10$, $r_{\mathrm{out}} = 10^6$, $h = 10\,R_{\mathrm{g}}$, $a = 0.998$, $M = 10M_{\odot}$, $log_{10}\xi = 3.1$, $A_{\mathrm{Fe}} = 1$ (respectively ionization and iron abundance in XILLVER).

2.4.3 The Importance of Non-Linear Effects

Fig. 2.5 shows the lag spectrum for different frequency ranges. The solid lines are produced with the complete model (both continuum and reverberation lags), while the dashed lines only include the reverberation lag (there is no variation of the continuum power-law index). For the dashed dotted lines, we instead calculate the continuum lags using our pivoting power-law model, but naively do not account for the variations in continuum power-law index when calculating the reflection spectrum (i.e. we set $W_1 = 0$ artificially). This allows us to assess the bias caused by not self-consistently accounting for the non-linear nature of the continuum variations. Here, we fix $\gamma(\nu)$, $\phi_A(\nu)$ and $\phi_B(\nu)$ to be constant with frequency (see the figure caption for all parameter values) and assume the same reflection parameters as those used for the previous sub-section. We see that, consistent with observational data, the continuum lags dominate over the reverberation lags for low frequencies, and the decrease of the continuum lag with frequency allows the reverberation lag to dominate at the highest frequencies. For low frequencies, the full model does differ quite significantly from the naive treatment, particularly below ~ 2 keV for which the full model predicts a steep break in the lag-energy spectrum. Therefore, ignoring non-linear effects could bias measurements of the reverberation lags. At high frequencies the models converge, since the lags are dominated by reverberation lags.

Fig. 2.6 shows the modulus of the complex covariance for a range of Fourier frequencies for the linear model (i.e. $\gamma = 0$, meaning there are no continuum lags) and the full model ($\gamma = 0.1$, meaning there are now continuum lags), represented respectively by the dots and the hatching. We see that, for both cases, the iron line feature is stronger for low frequencies (top lines) than for high frequencies (bottom lines). This is a result of the finite size of the reflector. Whereas the continuum can vary on arbitrarily short timescales, the fastest variability is washed out in the reflected emission by path length differences between rays that reflected from different parts of the disc (Gilfanov et al. 2000; Cackett et al. 2014). We also see that in terms of amplitude there is little difference between the two models, aside from the higher overall variability amplitude for the full model introduced by fluctuations in the continuum power-law index. The non-linear effects considered here therefore influence the predicted lags more than the amplitude and could therefore easily be missed when ignoring the lags.

2.5 Example fits to Cygnus X-1 data

As a proof of principle of our method, we fit the complex covariance for a few hard state observations of Cygnus X-1 for multiple Fourier frequencies. The data analysis presented here is intended primarily to show the feasibility of jointly describing the non-linear continuum and resulting reflection variability using the methods outlined above. As the model does not contain a description of the relativistic light bending, the fit results should be interpreted with caution, in particular if they require a corona/disc geometry close to the black hole. Cygnus X-1 is one of the first black hole X-ray binaries observed and has been studied extensively during the past decades, in particular with *the Rossi X-ray Timing Explorer* (*RXTE*). Another motivation to select this source is the absence of strong low frequency QPOs, which are routinely seen in many other black hole X-ray binaries. Since there is good evidence that these signals are due to precession of the inner accretion flow (Ingram et al. 2016), or at least geometrical in origin (e.g. Heil et al. 2015; Motta et al. 2015; van den Eijnden et al. 2017), they complicate the situation somewhat. In particular, transfer modelling assumes a stationary geometry, and so it is convenient to avoid observations with strong QPOs. Following Revnivtsev et al. (1999); Kotov et al. (2001), we use *RXTE* observations P10238 recorded between March 26$^{\text{th}}$ and 31$^{\text{st}}$ 1996 by the proportional counter array (PCA). In all, this consists of seven observations[2]. However, since the two first observations[3] have a slightly different spectral slope we only consider these last five.

The timing data are in the 'Generic Binned' mode `B_16ms_64M_0_249`, which has 1/64 s time resolution in 64 energy channels covering the whole PCA energy band. We apply standard *RXTE* good time selections (elevation greater than 10° and offset less than 0.02°) and additionally select times when 5 proportional counter units (PCUs) were switched on, using FTOOLS from the HEASOFT 6.19 package. This gives a total exposure time of 56.2 ks (after sorting into segments of contiguous data, the remaining useful exposure is 46.6 ks). Following the procedure outlined in Section 2.2,

---

[2] Observation IDs: 10238-01-05-00, 10238-01-05-000, 10238-01-06-00, 10238-01-07-00, 10238-01-07-000, 10238-01-08-00, 10238-01-08-000.

[3] Observation IDs: 10238-01-05-00,10238-01-05-000.

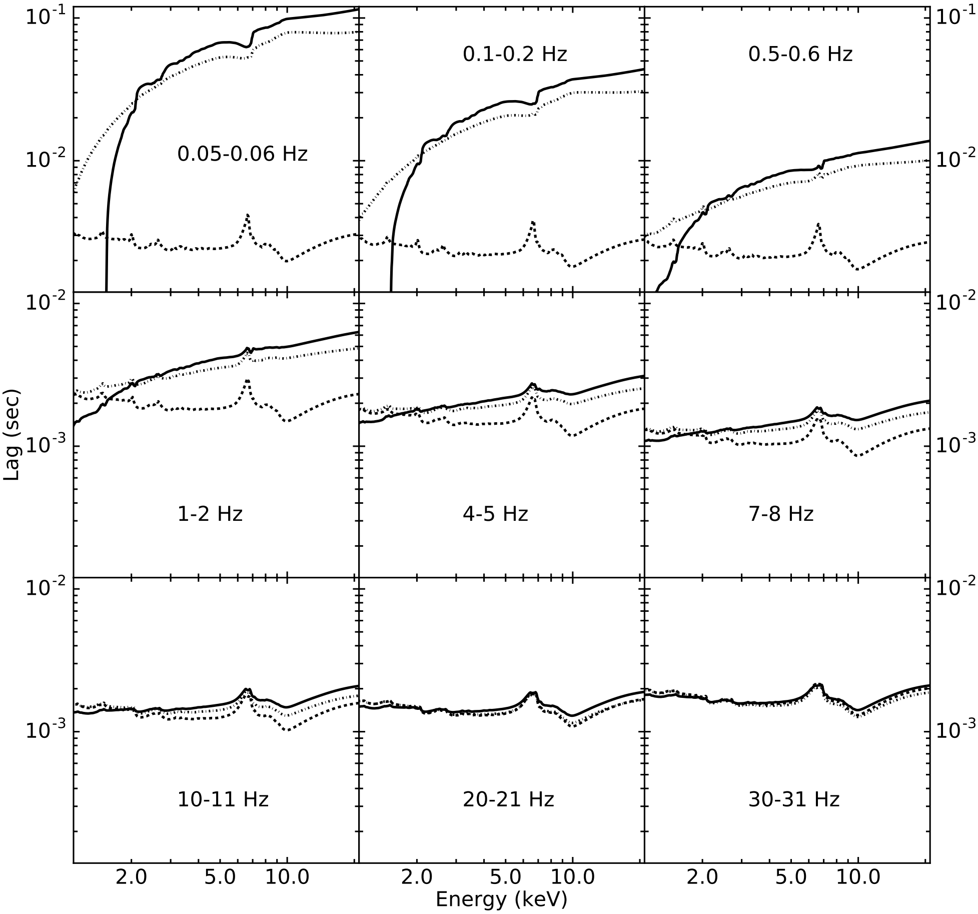

Figure 2.5: Time lag as a function of energy for different frequency ranges. The solid lines represent the lag calculated with the complete model: pivoting power-law in the continuum emission and contribution of reverberation. The dashed line is the lag only due to the reverberation (no pivoting power-law in the continuum emission). The dash-dotted line is the lag calculated considering the non-linear effect in the continuum emission (pivoting power-law) but naively ignoring this effect in the reverberation lag. The other parameters are $\phi_A = 0\,\mathrm{rad}$, $\phi_B = 0.2\,\mathrm{rad}$, $\Gamma = 2$, $i = 45°$, $r_{\mathrm{in}} = 10$, $r_{\mathrm{out}} = 10^6$, $h = 10$, $a = 0.998$, $M = 10M_{\odot}$, $\log_{10}\xi = 3.1$, $A_{\mathrm{Fe}} = 1$.

we calculate the complex covariance for 8 frequency ranges between 0.017 and 32 Hz. We assume unity coherence for this observation, which is a good assumption for the hard state of Cygnus X-1 (Nowak et al. 1999; Grinberg et al. 2014). The reference band is always $2.84-3.74$ keV and we consider the energy range $4-25$ keV for fitting. The choice of the reference band is discussed in Appendix A.5.

We use XSPEC version 12.9 (Arnaud 1996) to fit real and imaginary parts of the complex covariance as a function of energy, simultaneously for all 8 frequency ranges

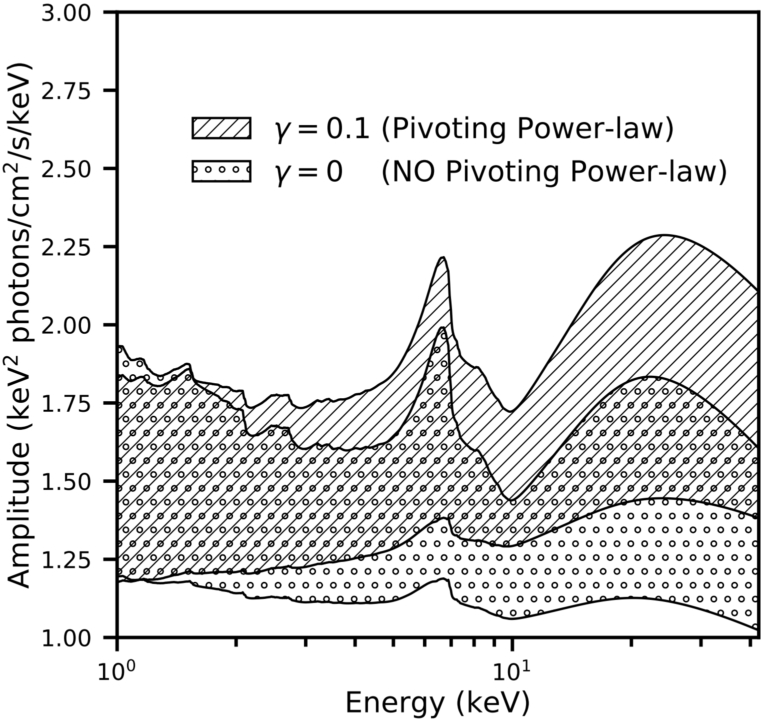

Figure 2.6: Covariance amplitude as a function of energy. The two regions represent frequency ranges from 0.02 Hz (the two highest curves) to 50 Hz (the two lowest curves). For the hatched region, we use the full model (pivoting power-law) and for the dotted region we do not include any continuum lags (NO pivoting model). All the parameters are equal to the ones in Fig. 2.5.

considered. We created an XSPEC local model for the complex covariance following the procedure explained in Section 2.3 using a cut off power-law for the continuum spectrum and XILLVER for the rest-frame reflection spectrum. We additionally fit the time-averaged energy spectrum with the DC component of the covariance model, meaning that we simultaneously fit accross 17 spectra. The energy spectrum is computed adding the PCA standard 2 data of the considered observations with the ftool *addspec* and adding in quadrature 0.1% systematic error [4].

For each of these 17 spectra, absorption is accounted for using the multiplicative model TBABS, assuming the abundances of Wilms et al. (2000). All parameters are tied to be the same for real and imaginary parts of a given frequency range. The parameters governing the continuum variations, $\phi_A(\nu)$, $\gamma(\nu)$ and $\phi_B(\nu)$, are allowed to vary freely with frequency. For the time-averaged spectrum, $\phi_A = \phi_B = \gamma = 0$,

---

[4] We add systematic errors only in the time-average energy spectrum. The complex covariance spectra are dominated by statistical errors so that no systematic errors are needed.

whereas $\alpha(\nu)$ is a free normalisation parameter. All remaining model parameters are tied to be the same for all 17 spectra. We fix the mass of the black hole to 14.8 $M_\odot$ (Orosz et al. 2011). It is important to note that this analysis is sensitive to black hole mass and can therefore in future be used as a new method to estimate the mass. However, that is beyond the scope of this current paper.

We achieved a reduced $\chi^2 = 480.64/460$ with the physical parameters in Table 2.1. For the best fitting model, $r_{\rm in}$ is pegged at its lowest allowed value (1.5). This means that the model is not able to fully reproduce the shape and normalisation of the iron line simultaneously over the full range of frequencies considered. The source height is very close to the black hole (2.4 ± 0.5). As noted above, the values of these two parameters suggest caution in interpreting our results, as we explore a region close to the black hole without accounting for all the relevant physics (in particular, light bending).

To simplify the explored parameter space and to mimic an oblate geometry of the illuminating corona, we additionally tried tying the inner radius of the disc to be twice the height of the point source. In this case, the best fit has a χ^2/d.o.f. = 484.43/461, the height of the source is pegged to the lowest value. An F-test favours the first of the two models. The hydrogen column density is a free parameter in our best fitting model, with the best fit value giving a significantly better χ^2 than fixing $N_{\rm H} = 0.6 \times 10^{21}{\rm cm}^{-2}$ following Gilfanov et al. (2000). From Table 2.1 it could be noted that our fit requires a strongly super-solar iron abundance $A_{\rm Fe} = 4.0 \pm 0.1$ as has previously been found in this source (e.g. Duro et al. 2016) [5] and other BHBs (e.g. GX 339–4: García et al. 2015) [6]. The high energy cut-off in our fit is compatible with what Wilms et al. (2006) found for the hard state of Cygnus X-1. We notice our value is slightly higher than their average, but the authors used a different model to fit the spectrum, for example accounting for the reflection with a Gaussian curve. We find a high reflection fraction compared to e.g. Parker et al. (2015) and Basak et al. (2017). We expect this result to be highly biased by the absence of light bending in our model.

The best fitting continuum parameters are plotted in Fig. 2.7. Here, the black and blue points (ϕ_A and γ respectively) correspond to y-axis scale on the left, while the red points (ϕ_B) correspond to the y-axis scale on the right. ϕ_A and ϕ_B are in units of radians, whereas γ is dimensionless. We see that all 3 parameters reduce with frequency. Since our continuum lag model is simply empirical, the direct physical meaning of these parameters is not immediately clear. It is still interesting to compare the results in Fig. 2.7 with more physical models.

---

[5] Analyzing Cygnus X-1 soft state Tomsick et al. (2014) also found evidence of super-solar abundance although still much lower than our result.

[6] Although the empirical evidence for these super-solar iron abundances is now very strong, the physical cause is still unknown. It could result from radiative levitation of the iron atoms in the inner disc, or perhaps is merely an artifact of some missing physics in the current state-of-the-art reflection models.

Figs. 2.8 and 2.9 show the data and best fitting model for 7 of the 8 frequency ranges considered (the lowest frequency range is very noisy). In Fig. 2.8, we show real (a) and imaginary (b) parts of the complex covariance, and plot the model with a higher energy resolution than the data for clarity. We additionally show fit residuals in the bottom panels. In Fig.2.9, we instead represent the data and model as time lag (a) and variability amplitude (b). In the lags, we see the characteristic dip at ~ 6.4 keV for both data and model, which becomes less prominent for higher frequencies. This occurs mainly because the continuum lags are greater than the reverberation lags, and so at the iron line the greater contribution from reflection dilutes the overall time lag. For higher frequencies, the difference between continuum and reverberation lags reduces and so the dip becomes less prominent. For even higher frequencies, we expect to see an emission-like feature at the iron line, but unfortunately the maximum possible Nyquist frequency for this data mode is 32 Hz. For the amplitude, we see the iron line becomes less prominent for higher frequencies, which is due to the finite size of the reflector as discussed in Section 2.4.

Fig. 2.8 shows that there are some systematic residuals in the real part of the complex covariance around the iron line. This seems to be because the amplitude of the iron line reduces more steeply with frequency in the data compared with the model. In the model, the accretion geometry (i.e. the source height and disc inner radius) sets both the frequency dependence of the iron line amplitude *and* the width of the iron line. For a smaller inner disc radius, the iron line is broader and the variability amplitude of reflection drops-off less steeply with frequency. Therefore, it appears that our small best-fitting inner radius of $r_{\rm in} \approx 1.5$ reproduces the broad iron line seen in the complex covariance and time-averaged spectrum, but predicts a slower drop-off in reflection variability amplitude with frequency than is observed. Since the data constrain the broadness of the iron line at all frequencies better than they constrain the drop off of the line amplitude at high frequencies, our fit returns a small value for inner radius. These residuals may be fixed in future by considering light bending, since this would give 1) longer reverberation lags for a given disc inner radius due to longer path lengths of rays close to the black hole, and 2) a broader iron line for a given disc inner radius due to the steeper emissivity profile resulting from focusing of rays close to the black hole.

2.6 Discussion

In this paper we have introduced a formalism to fully utilize X-ray reverberation mapping as a tool to measure the geometry of accreting black holes, and ultimately to provide a new means of measuring black hole mass and inner radius of the disc. The main innovation is that we fit a reverberation model that considers phase lags and variability amplitude jointly for a wide range of Fourier frequencies for the first

Table 2.1: Best fitting disc parameters obtained from our simultaneous fit to the complex covariance in 8 frequency ranges (0.017 – 32 Hz) and the time-average spectrum. The χ^2 is 480.64 with 460 degrees of freedom. We report 1 σ errors for each parameter value.

$N_{\rm H}$ $\left(10^{22}\ {\rm cm}^{-2}\right)$	Γ	h ($R_{\rm g}$)	$r_{\rm in}$ ($R_{\rm g}$)[a]	Incl (deg)
$0.2\pm^{0.2}_{0.1}$	$1.603\pm^{0.004}_{0.003}$	$2.4\pm^{0.5}_{0.5}$	$1.5\pm^{0.6}_{0}$	$35.7\pm^{1.2}_{1.3}$

$A_{\rm Fe}$	$E_{\rm cut}$ (keV)	$\log\xi$	Reflection Fraction[b]
$4.0\pm^{0.1}_{0.1}$	$241\pm^{10}_{5}$	$3.08\pm^{0.01}_{0.01}$	$-0.93\pm^{0.02}_{0.02}$

[a] The parameter is pegged at its minimum allowed value.

[b] In XILLVER a negative reflection fractions means the model represents only the reflection spectrum without the continuum.

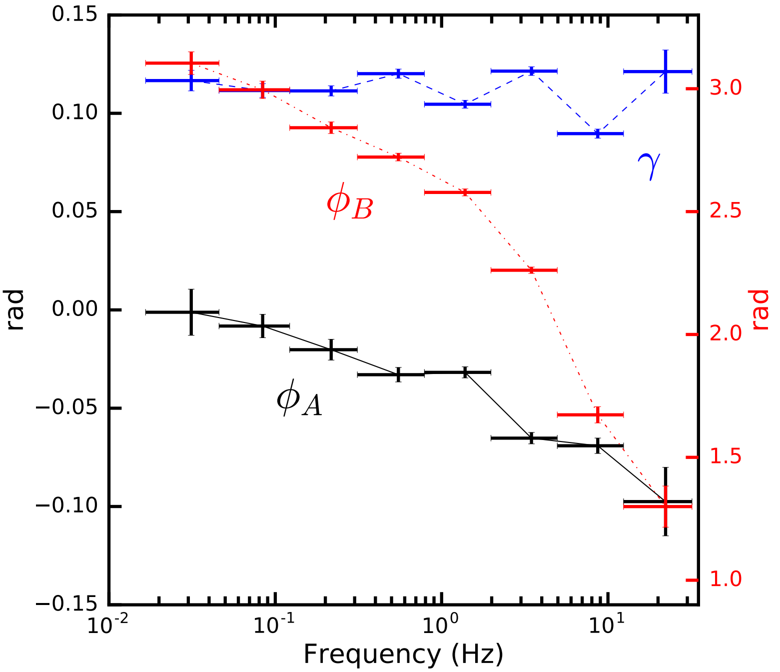

Figure 2.7: Continuum variability parameters as function of Fourier frequency. The black solid and blue dashed curves refer to the left y-axis, while the red dotted curve refers to the right y-axis. The x-errorbars represent the range of frequency used to fit the complex covariance as a function of energy. The points with the same frequency range are computed from the same fit.

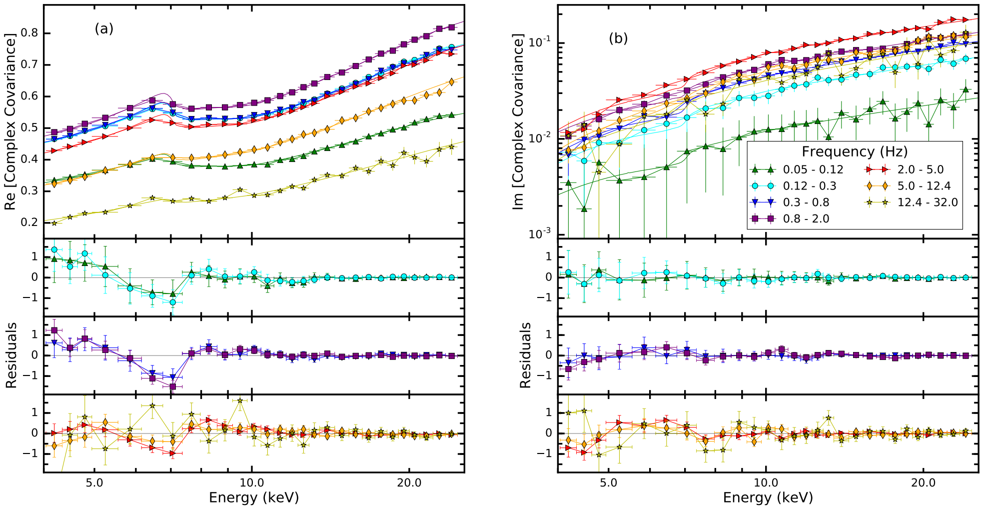

Figure 2.8: Fit of the real (a) and imaginary (b) part of Cygnus X-1 complex covariance spectrum for different Fourier frequency ranges. The dots are the data, the solid line is the model with a better energy resolution. Both the bottom panels show the data minus the folded model in units of normalised counts per second per keV (command residuals in XSPEC). The residuals around the iron line are discussed in the text.

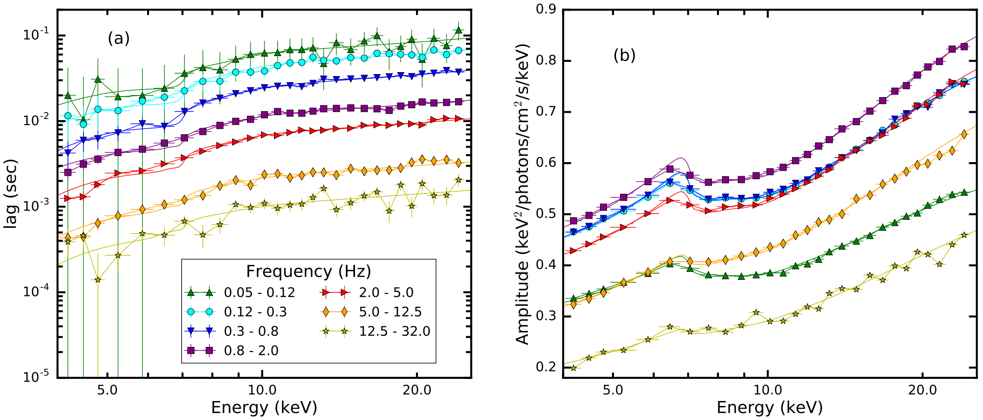

Figure 2.9: Lag (a) and variability amplitude (b) as a function of energy for different Fourier frequency ranges. Both data and model have been derived from the fit of real and imaginary part of the complex covariance spectrum (Fig. 2.8).

time. In order to do this, we introduce the complex covariance, and show that it is statistically more convenient to fit for the real and imaginary parts of the complex covariance than fitting directly for the amplitude and phase lags, which has led to some previous inaccuracies in the literature (it is still possible to compute the amplitude and phase lags, which are more physically intuitive, and compare them with other works). In order to fit for the full range of Fourier frequencies (determined by the duration and time resolution of the observation) we need to account for the continuum lags that dominate at low frequencies. We introduce a simple variation in the slope of the continuum emission (pivoting power-law model), and use a Taylor expansion to calculate the model analytically whilst still accounting for the variations in disc reflection spectrum shape caused by fluctuations in the illuminating power-law index. As noted by Kotov et al. (2001); Körding & Falcke (2004), a pivoting power-law model is fairly attractive, since it naturally produces time lags with a log-linear energy dependence, as is regularly observed.

The continuum lags are often assumed to result from propagating mass accretion rate fluctuations, with perturbations far from the black hole propagating inwards and modulating new fluctuations generated closer to the black hole (Lyubarskii 1997; Kotov et al. 2001; Arévalo & Uttley 2006). We note that, if the power-law emitting region is small compared with the disc inner radius, our adopted lamppost geometry still provides a good approximation to propagating fluctuations models. However, our treatment is at odds with sandwich models that consider propagation in a coronal layer above and below the disc. It could be that propagating fluctuations *cause* fluctuations in power-law index, through, for example, accretion rate fluctuations in the disc giving rise to fluctuations in the luminosity of seed photons (Uttley et al. 2014, Uttley & Malzac in prep). The fluctuations in power-law index could also result from fluctuations in electron temperature, seed photon luminosity and/or optical depth of the Comptonising region.

A few authors have made progress on integrating a propagating fluctuation model with reverberation modelling. Wilkins & Fabian (2013) consider fluctuations propagating through the corona with different geometries, and calculate reflection from each region of the corona. This is perhaps the most physically self-consistent treatment in the literature, but requires many response functions and so is computationally expensive. It will therefore be challenging to attempt the multi-frequency fits that we present here with such a model. Chainakun et al. (2016a) and Chainakun & Young (2017) instead explore a 'two blobs' model, consisting of two lamppost sources with different heights and different intrinsic spectra, with the propagation time between the two sources set as a model parameter. This is of comparable simplicity to our treatment, indeed both of our formalisms require only two response functions. It therefore should be possible to also fit this model for the full range of Fourier frequencies, and comparison of our two different formalisms may provide information on the physical origin of the continuum lags.

An interesting result we find here is that the low frequency lag spectrum is predicted to dip dramatically at ~ 2 keV (see top left of Fig. 2.5), which Uttley et al. (2011) see for GX 339–4. They attribute it to fluctuations propagating in from the disc, which could well be the case because of the shape of the covariance spectrum, but it is interesting to note that we naturally expect this dip at ~ 2 keV without any disc component. This is true only if we account for the non-linear effects, indicating that ignoring them could bias the results. We note, however, that the introduction of a low energy cut-off in the continuum spectrum of our model could modify the lags at such low frequency.

Since the model is analytic, fits to data for many frequencies are feasible without prohibitive computational expense. We fit hard state Cygnus X-1 data, and find an unphysically low value for the disc inner radius in our best-fit. Moreover the fit shows some residuals in the iron line energy range of the real part of the covariance spectrum for low frequencies. In the data, the line appears to be broad, both in the time-averaged spectrum and for non-zero Fourier frequencies, implying a small disk inner radius. However, the variability amplitude of the reflection signal drops off with frequency, which in itself favours a fairly large disk inner radius (Gilfanov et al. 2000). It is this tension that is behind the residuals seen in Fig. 2.8. However, the transfer function we used to model reflection in this illustrative fit is over-simplified. In particular, including light bending should go some way to improving the fit as it both increases the light travel time of reflected X-rays and focuses them to the inner regions of the disk. In any case, the inclusion of light bending will dramatically alter the model for our best fitting parameters, and so our results from Section 2.5 should be seen only as a proof of principle of the method, with further insight delayed until all GR effects are included in the analysis.

The value of the disk inner radius of Cygnus X-1 in the hard state has long been a subject of debate in the literature. For example, reflection modelling of the same *NuSTAR* dataset gives values of $r_{\rm in}$ ranging from $\simeq 1.3R_{\rm g}$ (Parker et al. 2015) to $\simeq 13-20R_{\rm g}$ (Basak et al. 2017), depending on assumptions about the continuum. Rapisarda et al. (2017a) obtain a similar result for the inner radius $\sim 20\ R_{\rm g}$ fitting a propagating fluctuations model to a hard state observation of Cygnus X-1, although they did not account for the reverberation effects on the lags. We also note that the high resolution data used by Parker et al. (2015) reveal absorption features around the iron line which would not be detectable with *RXTE* data. Since the absorption properties of Cygnus X-1 depend on the binary orbital phase (likely due to the wind from the companion; Grinberg et al. 2015), it is not clear if such absorption features affect our data. Here, we fixed the black hole mass in our fits but note that this can be left as a free parameter in future. We also note that the same model can be used for AGN, and is also sensitive to black hole mass in this case.

Aside from including light bending, a number of other improvements can be made to our method. More realistic geometries than the lamppost model can be explored in future, albeit with the trade-off of extra complexity increasing computational expense. Our model is designed such that any transfer function can be ported into our formalism, allowing flexibility. It will also be fairly simple to include variations in cut-off energy and ionisation parameter. As with power-law index variations considered here, this can be done using a Taylor expansion, and so will not add prohibitively to computational cost. Finally, we have assumed that reflection is instantaneous, as is routinely assumed in the literature. In reality, the reflected flux will take some finite time to increase when the illuminating flux increases (on top of the light-crossing time). García et al. (2013b) showed, albeit with a very simple model, that the reflection spectrum for a stellar-mass black hole should indeed respond very quickly (~ 1 ns) to a rise in the illuminating flux, but the response to a *drop* in illuminating flux could take as long as ~ 1 ms for a very low disc density. The different timescales occur because the rise time depends on photoionisation, but the fall time depends on recombination. Therefore, this response time may be relevant for reverberation mapping.

2.7 Conclusions

We developed a formalism for X-ray reverberation mapping of accreting black holes that enables characterisation of the full range of cross-spectral properties for a wide range of Fourier frequencies. We empirically model the continuum lags that dominate at low Fourier frequencies, and self-consistently account for the effect of the continuum lags on the reverberation signal. We point out some of previous inaccuracies in the literature associated with fitting models to the observed energy dependent phase lag and variability amplitude, and employ real and imaginary parts of the complex covariance to easily circumvent such problems. As a proof of principle, we have fitted our model to an *RXTE* observation of Cygnus X-1 in the hard state. We assume an on-axis lamppost geometry, and obtain a fit with reasonable χ^2, albeit with systematic residuals around the iron line that would likely be improved by the inclusion of light bending in the reflection model. We also note that more realistic geometries will impact these results. Although here we fixed the black hole mass in our fits to 14.8 $M_\odot$ (following Orosz et al. 2011), we note that the model is sensitive to the black hole mass. This optimised model for X-ray reverberation mapping using the information of the cross variability for a wide range of Fourier frequencies can therefore be used in future as a new way to measure the mass of stellar-mass and supermassive black holes.

3

A public relativistic transfer function model for X-ray reverberation mapping of accreting black holes

Adam Ingram, Guglielmo Mastroserio, Thomas Dauser , Pieter Hovenkamp, Michiel van der Klis & Javier A. García

Monthly Notices of the Royal Astronomical Society, 2019, 488, 324-347

Abstract

We present the publicly available model RELTRANS that calculates the light-crossing delays and energy shifts experienced by X-ray photons originally emitted close to the black hole when they reflect from the accretion disc and are scattered into our line-of-sight, accounting for all general relativistic effects. Our model is fast and flexible enough to be simultaneously fit to the observed energy-dependent cross-spectrum for a large range of Fourier frequencies, as well as to the time-averaged spectrum. This not only enables better geometric constraints than only modelling the relativistically broadened reflection features in the time-averaged spectrum, but additionally enables constraints on the mass of supermassive black holes in active galactic nuclei and stellar-mass black holes in X-ray binaries. We include a self-consistently calculated radial profile of the disc ionisation parameter and properly account for the effect that the telescope response has on the predicted time lags. We find that a number of previous spectral analyses have measured artificially low source heights due to not accounting for the former effect and that timing analyses have been affected by the latter. In particular, the magnitude of the soft lags in active galactic nuclei may have been under-estimated, and the magnitude of lags attributed to thermal reverberation in X-ray binaries may have been over-estimated. We fit RELTRANS to the lag-energy spectrum of the Seyfert galaxy Mrk 335, resulting in a best fitting black hole mass that is smaller than previous optical reverberation measurements (~ 7 million compared with $\sim 14 - 26$ million $M_{\odot}$).

3.1 Introduction

Stellar-mass black holes in X-ray binary systems and supermassive black holes in active galactic nuclei (AGN) are thought to accrete via a geometrically thin, optically thick accretion disc, which radiates thermally (Shakura & Sunyaev 1973; Novikov & Thorne 1973). The hard X-ray spectrum is often dominated by a power-law component with a high energy cut off, thought to be due to Compton up-scattering of comparatively cool photons in a cloud (with optical depth $\tau \sim 1-2$) of hot electrons located close to the black hole (Thorne & Price 1975; Sunyaev & Truemper 1979). The exact geometry of this cloud is still debated, with suggested models including a standing shock at the base of the jet (Miyamoto & Kitamoto 1991; Fender et al. 1999), a coronal layer sandwiching the disc (Galeev et al. 1979; Haardt & Maraschi 1991), and evaporation of the inner disc regions to form a hot, large scale height accretion flow (*the truncated disc model*; Eardley et al. 1975; Ichimaru 1977; Done et al. 2007). In the absence of a consensus on its geometry, the Comptonising region is often simply referred to as the corona, a convention that we will employ here.

We observe Comptonized radiation that reaches us directly from the corona (the *direct* component) in addition to coronal emission that has been reprocessed and re-emitted in the upper atmosphere of the disc, conventionally called the *reflection* component. These 'reflected' photons imprint characteristic features onto the observed spectrum including a prominent iron Kα emission line at $\sim$ 6.4 keV and a so-called reflection hump peaking at $\sim 20-30$ keV (e.g. Lightman & Rybicki 1980; George & Fabian 1991; Ross & Fabian 1993; García & Kallman 2010). The iron line provides a powerful probe of the disc dynamics and geometry, since its shape is observed to be distorted by photon energy shifts caused by relativistic orbital motion of disc material and gravitational redshift (Fabian et al. 1989; Laor 1991). If the disc inner radius inferred from the line profile is sufficiently small, setting it equal to the innermost stable circular orbit (ISCO) of general relativity (GR) provides an estimate for the spin of the black hole.

Many studies have used reflection spectroscopy to probe both AGN (e.g. Tanaka et al. 1995; Reynolds & Nowak 2003; Patrick et al. 2012; Walton et al. 2013; Risaliti et al. 2013) and black hole X-ray binary (e.g. Miller 2007; Reis et al. 2009; Miller et al. 2013; Kolehmainen et al. 2014; Plant et al. 2014; García et al. 2015) accretion flows. This has yielded many measurements of high black hole spin in AGN (e.g. Reynolds 2019; Middleton 2016), although complex line-of-sight absorption can potentially introduce modelling systematics (e.g. Miller et al. 2008). For the binaries, spectral modelling studies often conclude that the inner radius moves towards the black hole as the spectrum evolves from the hard power-law dominated *hard state* to the thermal disc dominated *soft state* on timescales of ~months (Done et al. 2007; Plant et al. 2014; García et al. 2015). However, even though there is broad agreement in the *trend* in disc inner radius, the measured *values* themselves vary enormously between different studies (García et al. 2015), with potential systematics including calibration uncertainty (e.g. Done 2010) and the difficulty of disentangling the direct and reflected components (e.g. Basak et al. 2017).

The degeneracies associated with spectral modelling can be addressed by additionally modelling the light-crossing delay between variations in the direct and reflected spectral components (Campana & Stella 1995; Reynolds et al. 1999; Uttley et al. 2014). Such reverberation mapping techniques therefore promise better constraints on the disc geometry (and therefore the black hole spin), but also entirely new constraints on black hole mass (Stella 1990). This is essentially because the delays depend on physical distances, whereas the energy shifts are only sensitive to distances in units of gravitational radii ($R_g = GM/c^2$). Fourier frequency dependent time lags between energy channels can be calculated from the argument of the cross-spectrum (van der Klis et al. 1987). It is routinely found that, at low Fourier frequencies ($\nu \lesssim 1.5 \times 10^{-3} c/R_g$), hard photons lag soft, both for the binaries (Miyamoto et al. 1988; Nowak et al. 1999; Kotov et al. 2001) and AGN (e.g. Papadakis et al. 2001; McHardy et al. 2004; Epitropakis & Papadakis 2017). These *intrinsic hard lags* are thought to be caused by spectral variability of the direct component rather than reverberation, due to their large magnitude and the lack of reflection features in their energy dependence, and may originate from inward propagation of fluctuations in the mass accretion rate (Arévalo & Uttley 2006; Ingram & van der Klis 2013; Rapisarda et al. 2017a; Mahmoud & Done 2018a). Since the hard lags reduce with frequency, it has been possible to detect reverberation signatures at high frequencies in AGN, first through soft lags interpreted as the soft-excess of the reflection spectrum lagging the direct radiation (Fabian et al. 2009; De Marco et al. 2013b), and later through an iron line feature in the lag-energy spectrum (Zoghbi et al. 2012; Kara et al. 2016). A number of studies have focused on modelling these high frequency lags in AGN (Cackett et al. 2014; Emmanoulopoulos et al. 2014; Epitropakis et al. 2016; Chainakun et al. 2016b; Wilkins et al. 2016; Caballero-García et al. 2018). Discoveries of reverberation signals came a little later for the binaries, since the cross over from intrinsic to reverberation lags is at a much higher frequency (measured in Hz rather than c/R_g) for a stellar-mass black hole (due to mass scaling), and therefore the signal is harder to pick out of the Poisson noise. Still, soft lags, interpreted as reverberation of thermally reprocessed photons, have been detected (Uttley et al. 2011; De Marco et al. 2015 - although this could feasibly result from backwards propagation of accretion rate fluctuations: Mushtukov et al. 2018), and iron K lags were finally detected for MAXI J1820+070 by Kara et al. (2019) using the *Neutron star Interior Composition ExploreR* (*NICER*; Gendreau et al. 2016).

Still further information is contained in the energy and frequency dependent variability amplitude, which can also be measured from the cross-spectrum. This can provide powerful constraints, since the variability amplitude of reflected emission should be washed out at the highest frequencies due to destructive interference between rays reflected from different parts of the disc (Gilfanov et al. 2000). It is optimal to consider all of these properties simultaneously[1]. The neatest way to do this statistically is to jointly model the time-averaged spectrum and the real and imaginary parts of the energy dependent cross-spectrum (Mastroserio et al. 2018). Here we present a public XSPEC model that enables such an analysis. We define two versions of the model, RELTRANS and RELTRANSCP, which represent the direct spectral component respectively as an exponentially cut-off power-law and using the model NTHCOMP. We assume a simple lamppost geometry (Matt et al. 1991; Martocchia & Matt 1996), which allows all GR effects to be properly accounted for without prohibitive computational expense – although we note that it is simple in our formalism to consider a number of lamppost sources. Source code and usage instructions can be downloaded from `https://adingram.bitbucket.io/`.

We present a detailed derivation of our model in Section 3.2 and explore its properties in Section 3.3. Our treatment properly accounts for line-of-sight absorption and the telescope response, and the model accounts for the radial dependence of the disc ionisation parameter. In Section 3.4 we investigate the importance of these effects. In Section 3.5, we perform a proof-of-principle fit to the lag-energy spectrum of the narrow-line Seyfert 1 galaxy Mrk 335 for a single frequency range. We discuss and conclude our findings in Sections 3.6 and 3.7.

3.2 Derivation of the cross-spectrum in the lamppost geometry

Here we derive the time-dependent observed energy spectrum assuming an isotropically radiating lamppost source located on the black hole spin axis a height h above the hole, and use the Fourier transform to calculate the energy dependent cross-spectrum as a function of Fourier frequency ν. We assume that the specific (energy) flux (i.e. energy per unit time per unit area per unit photon energy) seen by a distant observer as a function of photon energy, E, and time t, both defined in the observer's restframe, is given by

$$S(E,t) = F(E,t) + R(E,t). \tag{3.1}$$

The first and second terms on the right hand side represent respectively the direct and reflected spectral components. In this paper, we ignore directly observed disc radiation, assuming it to be below our X-ray bandpass. This is appropriate for AGN, and hard state X-ray binaries in the $E \gtrsim 3$ keV bandpass.

In this section, we first go over some general considerations of radiation theory in GR (Section 3.2.1). We then derive the observed time-dependent direct spectrum

---

[1] Indeed, also considering the power spectrum additionally provides information on the coherence between energy bands (e.g. Rapisarda et al. 2016), which we ignore here.

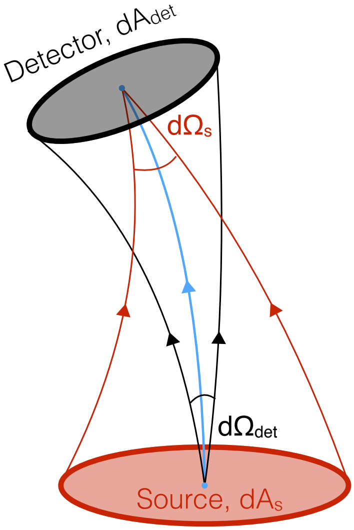

Figure 3.1: Schematic of a source and detector with surface areas (measured in their own restframes) dA_s and dA_{det} respectively. The blue line represents a photon path that emerges parallel to the source surface area vector (in the source restframe) and arrives parallel to the detector surface area vector (in the detector restframe). Only photons emerging from the source within the solid angle $d\Omega_{\text{det}}$ will eventually hit the detector. The solid angles and surface areas are related through the reciprocity theorem (equation 3.2).

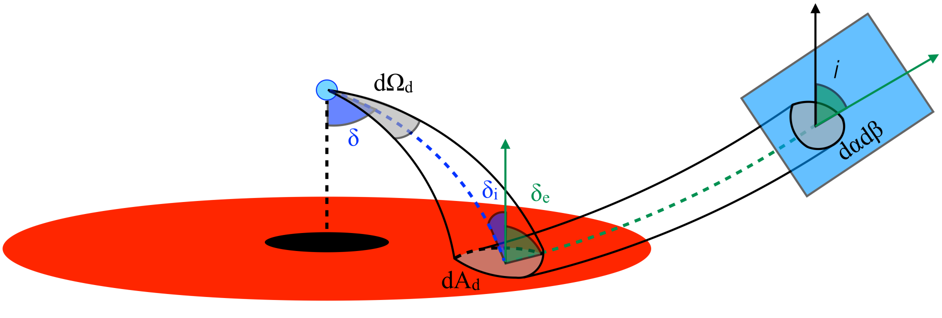

Figure 3.2: Schematic of the on-axis lamppost geometry. A disc patch with area dA_d subtends a solid angle $d\Omega_d$ according to the irradiating source. The disc patch corresponds to an area $d\alpha d\beta$ on the image plane, where α and β are respectively horizontal and vertical impact parameters at infinity. The bundle of rays within the represented solid angle are assumed to follow the trajectory (green dashed lines) defined by the initial (δ), incidence (δ_i), emission (δ_e) and inclination (i) angles.

(Section 3.2.2) and the reflection spectrum (Section 3.2.3), before deriving the transfer function that we will use for our reverberation model (Section 3.2.4), followed by the kernel used to calculate our transfer function (Section 3.2.5). Finally we will discuss the so-called reflection fraction (Section 3.2.6).

3.2.1 Reciprocity and Liouville's theorem

Fig 3.1 shows a schematic of a source with surface area dA_s in its own rest frame and a detector with surface area dA_{det} in its own rest frame. Photons travel along null geodesics, which are solutions to the geodesic equation with line element $ds^2 = g_{\mu\nu}dx^\mu dx^\nu = 0$. Here, $g_{\mu\nu}$ is the metric and dx^μ is the coordinate interval corresponding to an interval ds/c in proper time. Throughout this paper, we use the Kerr metric in Boyer-Lindquist coordinates. The position of a photon along its geodesic is described by the affine parameter λ and its trajectory described by the tangent vector $k^\mu(\lambda) = dx^\mu/d\lambda$. The blue line in Fig 3.1 represents the unique null-geodesic, $k^\mu(\lambda)$, that connects the centre of the source to the centre of the detector. For this example, the geodesic begins parallel to the source's surface area vector and ends parallel to the detector's surface area vector, but we can generalize by specifying dA_{det} and dA_s to be respectively the *projected* area of the detector and source perpendicular to k^μ in the local restframe. The black lines depict the trajectory of photons that emerge from the centre of the source and hit the edge of the detector, representing a bundle of photons that diverge from the centre of the source around $k^\mu(\lambda)$, subtending a solid angle $d\Omega_{det}$ in the source rest frame (i.e. all the photons in the bundle hit the detector and all others miss). The red lines depict the trajectory of photons that emerge from the edge of the source and hit the centre of the detector, representing a bundle of geodesics that converge onto the centre of the detector around $k^\mu(\lambda)$, subtending a solid angle $d\Omega_s$ in the detector rest frame. This is the solid angle that the source subtends on the detector's sky (i.e. all photons from the bundle hit the centre of the detector and all others miss the centre).

These four quantities are related by the general relativistic *reciprocity theorem*

$$g_{so}^2 dA_{det} d\Omega_s = dA_s d\Omega_{det}. \tag{3.2}$$

Here $g_{so} = E_o/E_s$ is the blueshift[2] experienced by photons traveling from source to detector and E_o and E_s are respectively the energy of the photon as measured in the rest frame of the detector and source (see Appendix B.2 for expressions of blueshift factors in the Kerr metric). The reciprocity theorem in GR was first derived by Etherington (1933), and a more concise presentation of the derivation can be found on pages 631-633 of Ellis (2009, this is a republication of the original 1971 proceeding). Ellis (2007) provides a useful commentary on the original Etherington paper. This

---

[2] i.e. $g_{so} > 1$ corresponds to a blueshift and $g_{so} < 1$ to a redshift. Note that $g_{so} = 1/(1 + z_{so})$, where z_{so} is redshift defined in the traditional sense of fractional change in wavelength.

is an intriguing geometrical result, showing that the curvature of spacetime does not influence the relationship between these solid angles and surface areas: the reciprocity theorem in GR is the same as that in special relativity for a given blueshift factor. We can even recover the classical reciprocity theorem by transforming $d\Omega_{det}$ into the detector frame to cancel out the g_{so}^2. The blueshift is calculated as

$$g_{so} = \frac{(k_{det})^\mu (u_{det})_\mu}{(k_s)^\nu (u_s)_\nu}, \tag{3.3}$$

where u_s and u_{det} are respectively the 4-velocity of the source and detector.

If $dN(E_s)$ photons with energies ranging from E_s to $E_s + dE_s$ are radiated isotropically from the flat source surface in its restframe, a fraction $d\Omega_{det}/\pi$ of them will cross the detector some time later[3]. Their energies will be measured to range from E_o to $E_o + dE_o$ in the detector rest frame, meaning that the number of photons crossing the detector is $dN_o(E_o) = dN(E_s) d\Omega_{det}/\pi$. The specific (energy) flux crossing the detector is therefore

$$\begin{aligned} F_o(E_o, t_o) &\equiv \frac{E_o dN_o(E_o)}{dt_o dE_o dA_{det}} \\ &= \frac{g_{so}}{\pi} \frac{E_s dN(E_s)}{dt_s dE_s dA_s} dA_s \frac{d\Omega_{det}}{dA_{det}} \\ &= \frac{g_{so}}{\pi} F_s(E_s) dA_s \frac{d\Omega_{det}}{dA_{det}}, \end{aligned} \tag{3.4}$$

where $F_s(E_s)$ is the specific flux radiated by the source, $dt_s = g_{so} dt_o$ and we have used $dE_o/dE_s = g_{so}$. Rearranging the above equation and applying the reciprocity theorem (equation 3.2) gives the rather familiar formula

$$I_o(E_o) = g_{so}^3 I_s(E_s), \tag{3.5}$$

where $I_o(E_o)$ and $I_s(E_s)$ are specific intensities: specific flux per unit solid angle (in this case $I_o(E_o) = F_o(E_o)/d\Omega_s$ and $I_s(E_s) = F_s(E_s)/\pi$). This famous result can also be derived from Liouville's theorem, which states that the number of photons per unit volume in phase space is Lorentz invariant (see e.g. Lindquist 1966; Misner et al. 1973). The derivation presented here is perhaps more intuitive. Integrating both sides over all observed energies gives the familiar expression for bolometric flux in terms of bolometric intensity

$$F_o = g_{so}^4 I_s d\Omega_s. \tag{3.6}$$

We can understand intuitively where these four factors of blue shift originate. Two come from the adjustment to solid angle in the reciprocity theorem (equation 3.2 - and

---

[3] This is because the projected area of the source is $\propto \cos\theta$ if it is viewed from inclination θ (and $d\Omega = d\cos\theta d\phi$). Therefore the fraction is $d\Omega / \int_0^{2\pi}\int_0^1 \cos\theta d\cos\theta d\phi = d\Omega/\pi$

these two factors can further be understood as special relativistic aberration in the small angle limit), one comes from the adjustment to the energy of each photon and one comes from the adjustment to time intervals (i.e. bolometric flux is $\propto EdN/dt$). Finally, all blue shifts in this paper are calculated in the Kerr metric, which is asymptotically flat and stationary and therefore does not account for cosmological redshift. An observer at cosmological redshift z will therefore measure a specific intensity

$$I(E) = \left(\frac{g_{so}}{1+z} \right)^3 I_s(E_s), \tag{3.7}$$

and will measure time intervals $\tau = (1+z)\tau_o$ (cosmological time dilation).

3.2.2 Direct spectrum

We assume a spherical X-ray source, with surface area in its own rest frame a_s, that isotropically radiates a specific flux

$$F_s(E_s, t'_o) = \frac{C(t'_o)}{a_s} f(E_s|\Gamma, E_{cut}), \tag{3.8}$$

where t'_o is time in the restframe of an observer at cosmological redshift $z = 0$. In the RELTRANS version of the model, the direct spectrum is

$$f(E|\Gamma, E_{cut}) \propto E^{1-\Gamma} \mathrm{e}^{-E/E_{cut}}, \tag{3.9}$$

where the constant of proportionality will be calculated below. The RELTRANSCP version instead uses the thermal Comptonisation model NTHCOMP (Zdziarski et al. 1996; Życki et al. 1999), with the E_{cut} parameter replaced by the electron temperature kT_e. For the purposes of this derivation, we will always use E_{cut}, on the understanding that this can be replaced with kT_e for the case of the NTHCOMP version. In order to evaluate the function $f(E)$ in these two cases, we use the model XILLVER and XILLVERCP respectively (García & Kallman 2010; García et al. 2013a), which we will also use in order to calculate the restframe reflection spectrum. Our code calls the relevant XILLVER model with the reflection fraction parameter set to zero, which returns the illuminating spectrum used for the calculation of the reflection spectrum.

In this paper, as can be seen in Equation (3.8), we will only consider *linear* variability of the source flux. That is, the shape of the direct component of the spectrum remains constant in time and only the normalisation varies. In future versions, we will extend our modelling to account for non-linear variations of the spectrum radiated by the corona using the Taylor expansion technique described in Mastroserio et al. (2018).

We assume the source is small enough to ensure that any light rays that pass by either side of it on route to the distant observer are parallel to one another (i.e. spacetime is approximately flat on the scale of the source area). The projected area of the source is therefore $dA_s = a_s/4$. Substituting this into equation 3.4 gives the observed specific flux at time t_o

$$\begin{aligned} F_o(E_o, t_o) &= \frac{g_{so}}{4\pi} F_s(E_s, t_o') a_s \frac{d\Omega_{det}}{dA_{det}} \\ &= \frac{C(t_o')}{4\pi} g_{so}^{\Gamma} f(E_o|\Gamma, g_{so}E_{cut}) \frac{d\Omega_{det}}{dA_{det}}, \end{aligned} \tag{3.10}$$

where $t_o = t_o' + \tau_{so}$ and τ_{so} is the time it takes photons to travel from source to detector, as measured in the detector frame (and assuming $z = 0$). The second line of the above equation is exact for an exponentially cut-off power-law illuminating spectrum but only approximate for an NTHCOMP spectrum. The final term on the right hand side accounts for lensing / de-lensing due to light bending. Defining the inclination angle i as the angle between the black hole spin axis and the trajectory of photons when they cross the detector (see Fig 3.2, but note that photons reach the detector both directly and via reflection) and $D = \sqrt{dA_s/d\Omega_s}$ as the distance between the source and the detector (and also, to a very good approximation, the distance between the hole and the detector, since $D \gg h$), the detector area is $dA_{det} = D^2 \sin i \; di \; d\phi$. Defining δ as the angle, measured in the source rest frame, between the spin axis and the emergent trajectory of a photon as it is radiated by the source (see Fig 3.2 for an example of a photon that reflects from the disc, but note that photons with larger δ may reach the observer directly), we can write

$$\frac{d\Omega_{det}}{dA_{det}} = \frac{1}{D^2} \left| \frac{d\cos\delta}{d\cos i} \right| = \frac{\ell}{D^2}, \tag{3.11}$$

since intervals in azimuth $d\phi$ are constant along a geodesic for an on-axis source in the Kerr metric. We calculate the lensing factor, $\ell = |d\cos\delta / d\cos i|$, numerically by tracing rays along null geodesics in the Kerr metric, calculated using the publicly available code YNOGK (Yang & Wang 2013), which is based on another publicly available code GEOKERR (Dexter & Agol 2009). The observed specific flux is therefore

$$F_o(E_o, t_o) = A(t_o') \ell g_{so}^{\Gamma} f(E_o|\Gamma, g_{so}E_{cut}), \tag{3.12}$$

where we have defined $A(t) \equiv C(t)/(4\pi D^2)$. An observer at a cosmological distance sees a specific flux

$$F(E, t) = A(t')\ell \left(\frac{g_{so}}{1+z} \right)^{\Gamma} f[E|\Gamma, g_{so}E_{cut}/(1+z)], \tag{3.13}$$

and measures a time interval $t - t' = (1+z)\tau_{so}$. In our model, for consistency with the RELXILL family of models (Dauser et al. 2013; García et al. 2014), we specify as a model parameter the cut-off energy in the *observer's* frame, $(E_{cut})_{obs} = g_{so}E_{cut}/(1+z)$. When the verbose level is set suitably high, the code prints to screen the value of the cut-off energy in the source restframe. For RELTRANSCP, we instead specify the parameter $(kT_e)_{obs} = g_{so}kT_e/(1+z)$.

3.2.3 Reflection spectrum

Fig. 3.2 illustrates the source irradiating a patch of the disc that subtends a solid angle $d\Omega_d$ in the *source* rest frame and has a surface area dA_d in the reference frame of the *disc patch*. Again using equation 3.4, the specific flux crossing the surface of the disc patch, in the restframe of the disc patch is

$$F_{d,in}(E_d, t_o') = \frac{C(t_o' - \tau_{sd})}{4\pi} g_{sd}^{\Gamma} f(E_d|\Gamma, g_{sd}E_{cut}) \frac{d\Omega_d}{dA_d}. \tag{3.14}$$

The irradiating flux is all re-processed into the reflection spectrum, which is radiated an-isotropically from the disc upper surface ($\mu_e = \cos\delta_e \geq 0$; see Fig. 3.2). The emission angle-dependent reflected specific intensity $I_{d,out}$ emergent from the disc is related to the incident flux $F_{d,in}$ as

$$\int_0^\infty F_{d,in}(E_d, t_o') dE_d = 2\pi \int_0^1 \int_0^\infty I_{d,out}(E_d, t_o'|\mu_e) \mu_e dE_d d\mu_e. \tag{3.15}$$

As alluded to in the previous section, we use XILLVER or XILLVERCP to calculate the reflected specific intensity $\mathcal{R}(E|\mu_e)$ for an illuminating specific flux $f(E|\Gamma, E_{cut})$ (we set the reflection fraction parameter to -1, where the minus sign ensures that the XILLVER model returns only the reflection spectrum rather than summing it with the incident spectrum). The XILLVER models are normalized such that

$$\begin{aligned} \frac{1}{2} \int_0^1 \int_0^\infty & \mu_e \mathcal{R}(E|\mu_e, \Gamma, E_{cut}, \log_{10}\xi) dE d\mu_e \\ &= \int_0^\infty f(E|\Gamma, E_{cut}, \log_{10}\xi) dE, \end{aligned} \tag{3.16}$$

where $\xi(r) = 4\pi F_x(r)/n_e(r)$ is the ionisation parameter, $F_x(r)$ is the 13.6 eV to 13.6 keV illuminating flux and $n_e(r)$ is the electron number density.

Inspection of equations (3.14), (3.15) and (3.16) shows

$$I_{d,out}(E_d, t_o'|\mu_e) = \frac{1}{2} \frac{C(t_o' - \tau_{sd})}{2\pi} g_{sd}^{\Gamma} \frac{d\Omega_d}{dA_d} \frac{\mathcal{R}(E_d|\mu_e, g_{sd}E_{cut})}{4\pi}. \tag{3.17}$$

Once more exploiting the symmetry of the lamppost geometry, we can consider the case whereby the disc patch is an annulus at r with width dr to find

$$\frac{d\Omega_d}{dA_d} = 2\pi \frac{|d\cos\delta/dr|}{dA_{\text{ring}}/dr}. \tag{3.18}$$

It is important to note that the angle δ in the equation is defined in the source restframe, whereas the area dA_{ring} is defined in the restframe of the disc annulus. The radial coordinate is defined in Boyer-Lindquist coordinates. We calculate $d\cos\delta/dr$ and τ_{sd} numerically using YNOGK. We calculate the area differential analytically. In

Boyer-Lindquist coordinates, the area of a disc annulus with radial extent dr is $d^2x = 2\pi\sqrt{g_{\phi\phi}g_{rr}}dr$. The area in the rest frame of the rotating annulus is $dA_{\rm ring} = \gamma^{\phi}d^2x$, where γ^{ϕ} is the Lorentz factor of the annulus (e.g. Wilkins & Fabian 2012). We present a derivation for γ^{ϕ} in Appendix B.1, pointing out some very small (largely inconsequential) errors in previous derivations (Bardeen et al. 1972; Dauser et al. 2013).

According to the stationary observer, the disc patch centered at disc coordinates r, ϕ is centered on coordinates on the observer plane α, β and subtends a solid angle $d\Omega = d\alpha d\beta/D^2$ (see Fig 3.2). Here α and β are the impact parameters at infinity. The specific flux seen from the disc patch with coordinates r, ϕ by the stationary observer viewing from an inclination angle i (with $\mu = \cos i$) is therefore $dR_o(E_o,t_o) = g_{do}^3 I_{d,out}(E_o/g_{do}, t_o-\tau)d\alpha d\beta/D^2$, giving

$$\begin{aligned} dR_o(E_o,t_o|\mu,r,\phi) &= A[t_o-\tau(r,\phi)]g_{do}^3(r,\phi)\epsilon(r) \\ \times\mathcal{R}[E_o/g_{do}(r,\phi)|\mu_e(r,\phi), g_{sd}(r)E_{cut}, &\log_{10}\xi(r)]d\alpha d\beta, \end{aligned} \tag{3.19}$$

where

$$\epsilon(r) = \frac{g_{sd}^{\Gamma}(r)}{2}\frac{|d\cos\delta/dr|}{dA_{\rm ring}/dr} \tag{3.20}$$

is the radial emissivity profile and $\tau(r,\phi) = \tau_{sd}(r) + \tau_{do}(r,\phi) - \tau_{so}$. Note that for equation 3.19 we have used equation (3.5), since $d\alpha d\beta/D^2$ is the solid angle subtended by the disc patch according to the observer in the observer's restframe. Also note that the cosine of the emission angle, μ_e, is a function of r and ϕ because bending of rays leads to photons with the same final trajectory having different initial trajectories (García et al. 2014). The total reflection spectrum seen by the stationary observer is then calculated by integrating equation (3.19) over all impact parameter values for which the corresponding geodesic intercepts the disc at radii $r_{in} < r < r_{out}$.

3.2.4 Transfer function and cross-spectrum

We can express the total reflected specific flux seen by the $z=0$ observer as $R_o(E_o,t_o) = A(t_o)\otimes w_o(E_o,t_o)$, where $\otimes$ denotes a convolution and

$$\begin{aligned} w_o(E_o,t_o) &= \int_{\alpha}\int_{\beta}\epsilon(r)g_{do}^3(r,\phi)\delta(t_o-\tau(r,\phi)) \\ \times\mathcal{R}[E_o/g_{do}(r,\phi)|\mu_e(r,\phi), g_{sd}(r)E_{cut}, &\log_{10}\xi(r)]d\alpha d\beta. \end{aligned} \tag{3.21}$$

is the *impulse-response function.* In Fourier space the convolution is a multiplication, so it is best to Fourier transform the impulse response function to get the *transfer function*

$$\begin{aligned} W_o(E_o,\nu) &= \int_{\alpha}\int_{\beta}\epsilon(r)g_{do}^3(r,\phi){\rm e}^{i2\pi\tau(r,\phi)\nu} \\ \times\mathcal{R}[E_o/g_{do}(r,\phi)|\mu_e(r,\phi), g_{sd}(r)E_{cut}, &\log_{10}\xi(r)]d\alpha d\beta. \end{aligned} \tag{3.22}$$

Setting $\nu = 0$ (The DC component, standing for direct current), gives the time-averaged spectrum. Generalising to an observer at a cosmological distance gives $R(E,\nu) = A(\nu)W(E,\nu)$, where

$$W(E,\nu) = (1+z)^{-3} \int_\alpha \int_\beta \epsilon(r) g_{do}^3(r,\phi) \mathrm{e}^{i2\pi(1+z)\tau(r,\phi)\nu} \times \mathcal{R}[E_o/g_{do}(r,\phi)|\mu_e(r,\phi), g_{sd}(r)E_{cut}, \log_{10}\xi(r)] d\alpha d\beta, \tag{3.23}$$

and we note that $A(\nu)$ is in general complex. We trace rays defined by given impact parameter values backwards from the observer plane towards the black hole along the relevant null geodesic in the Kerr metric (again calculated using YNOGK). This operation automatically accounts for lensing of rays travelling from the disc to the observer. We consider a 400×400 grid of impact parameters with $\sqrt{\alpha^2+\beta^2} \le 300\ R_g$. We additionally consider a larger grid with $300\ R_g < \sqrt{\alpha^2+\beta^2} \le r_{out}$ for which we calculate geodesics in the Minkowski metric. For rays that cross the disc mid-plane, we calculate the r, ϕ and t coordinates at the crossing point. We stop following rays after the first time they cross the mid-plane, therefore ignoring ghost images, which are likely blocked in reality by material in the vicinity of the hole. We quote the formulae for the blueshift factors and angles in Appendix B.2. We also include a 'boosting factor' to account for the likelihood that our assumption of an isotropically radiating source is inappropriate. We specify the factor $1/\mathcal{B}$ as a model parameter, such that $1/\mathcal{B} < 1$ roughly corresponds to the source being beamed towards us and away from the disc.

From the transfer function, we can calculate the energy-dependent cross-spectrum. This is a series of cross-spectra between the flux at each energy and that in a common reference band, $G(E,\nu) = S(E,\nu)F_r^*(\nu)$. In our model, this is given by

$$G(E,\nu) = \alpha(\nu)\mathrm{e}^{i\phi_A(\nu)} \left[F_{A=1}(E) + \frac{W(E,\nu)}{\mathcal{B}} \right], \tag{3.24}$$

where $\alpha(\nu)$ and $\phi_A(\nu)$ are model parameters for each frequency ν, and $F_{A=1}(E)$ is given by equation (3.13) with $A = 1$. We could equally see equation 3.24 as a formula for the *complex-covariance* (Mastroserio et al. 2018), which is simply the cross-spectrum divided through by the amplitude of the reference band, $S(E,\nu)F_r(\nu)/|F_r(\nu)|$. The only adjustment would be a slight change in the, already fairly arbitrary, meaning of the normalisation parameter $\alpha(\nu)$. Finally, line-of-sight absorption is accounted for using the multiplicative XSPEC model, TBABS (Wilms et al. 2000), such that the transmitted cross-spectrum is $G_{abs}(E,\nu) = \mathrm{TBABS}(E) \times G(E,\nu)$. For a given frequency range, our model calculates this transmitted cross-spectrum and outputs, as a function of energy, the real part of this, the imaginary part, the modulus (energy-dependent variability amplitude) or the time lag ($t_{\mathrm{lag}}(E,\nu) = \arg\{G(E,\nu)\}/[2\pi\nu]$), depending on the user-defined mode.

As discussed in Mastroserio et al. (2018), if the reference band is the sum of energy channels ranging from I_{min} to I_{max} that are all well calibrated for the instrument we are observing with, the parameter $\phi_A(\nu)$ need not be a free parameter, and can instead be expressed as

$$\tan\phi_A(\nu) = \frac{-\sum_{J=I_{min}}^{I_{max}} \Im[W(J,\nu)]/\mathcal{B}}{\sum_{I=I_{min}}^{I_{max}} F_{A=1}(I) + \Re[W(I,\nu)]/\mathcal{B}}. \tag{3.25}$$

Here, $F_{A=1}(I)$ and $W(I,\nu)$ are calculated by convolving TBABS$(E) \times F_{A=1}(E)$ and TBABS$(E) \times W(E,\nu)$ respectively with the instrument response (see Mastroserio et al. 2018 for details). Our model incorporates both a mode in which $\phi_A(\nu)$ is a free parameter and a mode in which the instrument response is read in and $\phi_A(\nu)$ is calculated self-consistently.

3.2.5 The reflection kernel

Much of the computational expense of evaluating equation (3.22) can be saved by representing it as a convolution with a kernel. The easiest case to calculate is if we assume that the shape of the rest frame reflection spectrum depends on neither r nor ϕ. This can be done by assuming that the cut-off energy seen by each disc patch is E_{cut} rather than $g_{sd}(r)E_{cut}$, that $\delta_e(r,\phi) = i$ and that the disc ionisation parameter is independent of radius. Working with $\log E$ rather than E, allows the transfer function to be represented as

$$W(\log E,\nu) = \int_0^\infty \mathcal{R}(\log E') W_\delta(\log(E/E'),\nu) \mathrm{d}\log E', \tag{3.26}$$

where

$$W_\delta(\log E,\nu) = (1+z)^{-3} \int_{\alpha,\beta} \epsilon(r) g_{do}^3(r,\phi) \mathrm{e}^{i2\pi(1+z)\tau(r,\phi)\nu} \times\delta\left[\log E - \log\left(\frac{g_{do}(r,\phi)}{1+z}\right)\right] \mathrm{d}\alpha \mathrm{d}\beta \tag{3.27}$$

is the kernel of the transfer function. It is clear that the kernel is simply the transfer function for a $\delta-$function rest frame reflection spectrum centered at 1 keV. Equation (3.26) can be recognised as a convolution in $\log E$ space, and can thus be written

$$W(\log E,\nu) = \mathcal{R}(\log E) \otimes_{\log E} W_\delta(\log E,\nu). \tag{3.28}$$

We compute the convolution using the convolution theorem (i.e. Fourier transforming both, multiplying and finally inverse transforming), which allows us to exploit the large gain in speed afforded by using the fast Fourier transform (FFT) algorithm.

In the more general case, we can quantise μ_e, g_{sd} and $\log_{10}\xi$ by defining a number of discrete bins for each and writing the transfer function as

$$W(\log E,\nu) = \sum_j \sum_k \sum_n \mathcal{R}[\log E|\mu_e(j), g_{sd}(k), \log_{10}\xi(n)] \otimes_{\log E} W_\delta(\log E,\nu|j,k,n), \tag{3.29}$$

where $W_\delta(\log E, \nu | j, k, n)$ is given by equation 3.27, except the integrand is only non-zero for disc patches with $\mu_e(r, \phi)$, $g_{sd}(r)$ and $\log_{10} \xi(r)$ in the range specified by the indices j, k and n. Computing equation 3.29 therefore requires a convolution for each permutation of j, k and n. Use of the FFT algorithm prevents the computation of so many convolutions from becoming prohibitively expensive. We will explore the effect of changing the number of convolutions on the accuracy of the model in section 3.3.3.

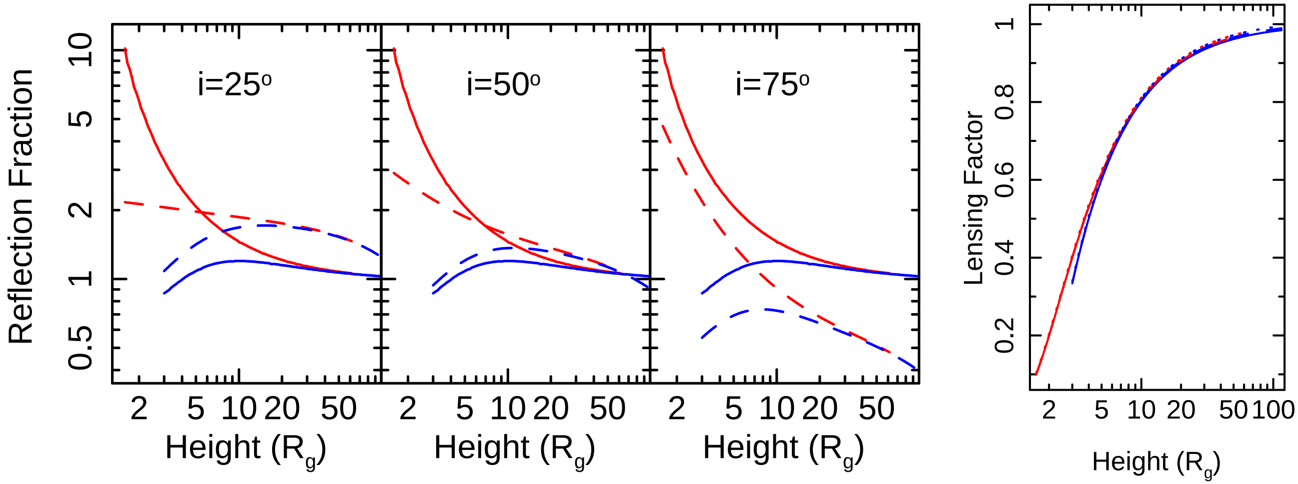

Figure 3.3: *Left:* Reflection fraction plotted against source height for three inclination angles, with the disc extending down to the ISCO for black hole spin $a = 0.998$ (red) and $a = 0$ (blue). The solid lines are ‘system’ reflection fraction as defined by Dauser et al. (2016) (see our equation 3.30) and the dashed lines are the observer’s reflection fraction as defined by our equation 3.31. The system reflection fraction does not depend on inclination angle whereas the observer’s reflection fraction does, even in the Newtonian limit. *Right:* Lensing factor, ℓ, plotted against source height for $a = 0.998$ (red) and $a = 0$ (blue) with $i = 25^\circ$ (solid), $i = 50^\circ$ (dashed) and $i = 75^\circ$ (dotted). We see that ℓ depends very strongly on h, but only weakly on a and i.

3.2.6 Reflection fraction

It is useful to define a reflection fraction that captures the ratio between reflected and direct components in the observed spectrum, specifically isolating geometric considerations from radiative transfer considerations. Here, we discuss two definitions of the reflection fraction: the *system reflection fraction*, which depends only on the geometry of the system and is independent of the observer, and the *observer's reflection fraction.*

The system reflection fraction, already used by the model RELXILLLP (Dauser et al. 2013), is

$$(f_R)_{sys} = \frac{\cos\delta_{in} - \cos\delta_{out}}{1+\cos\delta_{out}}, \tag{3.30}$$

where δ_{in} and δ_{out} are respectively the values of the angle δ for geodesics from the source that hit the inner and outer radii of the disc (Dauser et al. 2014). This definition gives the number of photons that hit the disc divided by the number that reach infinity in the hemisphere above the disc mid-plane. In the case of Newtonian gravity, $(f_R)_{sys}$ would reach a maximum of unity for a disc extending from $r_{in} = 0$ to $r_{out} = \infty$. In full GR however, $(f_R)_{sys}$ can be much larger due to focusing of photons onto the inner regions of the disc (Dauser et al. 2016).

Although the above definition is conveniently simple, it does not fully capture the relative flux of the direct and reflected spectra as seen by a given observer. We therefore additionally define an observer's reflection fraction. In order to exclude the radiative transfer calculation, we define a reflection spectrum for the case in which the disc re-emits the incident spectrum isotropically. In this case, we can define the reflection fraction as the *observed bolometric reflected flux divided by the directly observed bolometric flux.* Note that both of these fluxes are considered to be measured in the *observer's frame.* This means that the specific flux re-radiated from a disc patch is $F_{d,out}(E_d) = F_{d,in}(E_d)$ (input spectrum preserved) and the specific intensity re-radiated from the disc patch is $I_{d,out}(E_d) = F_{d,in}(E_d)/\pi$ (isotropic re-radiation). This gives

$$\begin{aligned}(f_R)_{obs} &= \frac{2}{\ell g_{so}} \int_{\alpha,\beta} g_{do}^3(r,\phi) g_{sd}(r) \frac{|d\cos\delta/dr|}{dA_{\text{ring}}/dr} d\alpha d\beta \\ &= \frac{4}{\ell g_{so}} \int_{\alpha,\beta} g_{do}^3(r,\phi) g_{sd}^{1-\Gamma}(r) \epsilon(r) d\alpha d\beta \end{aligned} \tag{3.31}$$

Applying the earlier experiment of taking the simple limiting case of an infinite slab in Newtonian gravity to equation (3.31) gives $(f_R)_{obs} = 2\cos i$. Averaging over all $\cos i$ in the hemisphere above the disc mid-plane, we find $\langle (f_R)_{obs} \rangle = 1$; i.e. source photons are either radiated into the upper hemisphere to be observed directly, or into the lower hemisphere to be observed as reflection. The angular dependence, even when isotropic radiation is assumed, results from the source being a sphere, whereas

Parameter	Units	Description	Default value
h	R_g (+ve) or R_h (-ve)	Source height	6
a		Dimensionless spin parameter	0.9
i	Degrees	Inclination angle	30
r_{in}	R_g (+ve) or ISCO (-ve)	Disc inner radius	-1
r_{out}	R_g	Disc outer radius	20000
z		Cosmological redshift	0
Γ		Photon index	2
$\log_{10}\xi$	ξ has units of erg cm/s	ionisation parameter or peak value of ionisation parameter	3 or 3.75
A_{Fe}	Solar	Relative iron abundance	1
$(E_{cut})_{obs}$	keV	Observed high energy cut-off	300
$(kT_e)_{obs}$	keV	Observed electron temperature	300
N_h	$10^{22}\mathrm{cm}^{-2}$	Hydrogen column density of material in the line-of-sight (TBABS)	0
$1/\mathcal{B}$		Boosting factor to adjust the reflection fraction from lamppost value	1
M	$M_\odot$	Black hole mass	4.6×10^7
ϕ_A	Radians	Phase norm - can be self-consistently calculated	0
ν_{min}	Hz	Minimum frequency transfer function is averaged over	1×10^{-5} or 0
ν_{max}	Hz	Maximum frequency transfer function is averaged over	2×10^{-5} or 0
`ReIm`		Sets output	$1 - 6$

Table 3.1: Model parameters for RELTRANS and RELTRANSCP. Source height and disc inner radius can be expressed in horizons and ISCOs respectively in order to avoid unphysical parameter combinations during exploration of parameters space. The chosen value of mass corresponds to NGC 4151. The model calculates the energy dependent cross-spectrum averaged over the frequency range ν_{min} to ν_{max}. The parameter `ReIm` sets the model output. The options are: 1) real part, 2) imaginary part, 3) modulus (i.e. the absolute variability amplitude), 4) time lag (the argument divided by $2\pi\nu$, where $\nu = [\nu_{min} + \nu_{max}]/2$), 5) modulus of the folded cross-spectrum, and 6) the time-lag for the folded cross-spectrum. If either ν_{min} or ν_{max} are set to zero, the time-averaged spectrum is returned.

the disc is a slab. This definition of the reflection fraction is similar, but not identical, to the ‘reflection strength’ defined by Dauser et al. (2016). In our model, we calculate both reflection fractions and print them to screen if the verbose level is set suitably high by an environment variable.

Fig 3.3 (left) shows our two definitions of reflection fraction plotted against source height for a number of parameter combinations. We see that the solid lines representing $(f_r)_{sys}$, which agree exactly with Fig 3 of Dauser et al. (2016), do not depend on viewer inclination. The dashed lines representing $(f_r)_{obs}$ do depend on viewer position. The right panel shows the contribution of the lensing factor. This is strongly dependent on source height, but only weakly dependent on spin and inclination.

3.3 Model properties

The model parameters of RELTRANS and RELTRANSCP are listed in Table 3.1. We also define a number of environment variables, listed in Appendix B.3, that are used to switch between different modes and control resolution. Each environment variable has a sensible default value, such that the model is user friendly for the beginner and flexible for the advanced user. In this section, we explore the model properties and describe the listed parameters and environment variables. For the sake of intuition we plot time lags and variability amplitudes, even though it is statistically favourable when fitting to data to consider real and imaginary parts of the cross-spectrum (Ingram et al. 2016, 2017; Rapisarda et al. 2017a; Mastroserio et al. 2018).

3.3.1 Emissivity profiles

Fig 3.4 shows the lamppost model emissivity profile and some contributing factors for a range of parameter combinations. Panel (a) shows the ratio of the area derivative in the Newtonian case to the relativistic case for three different values of spin. The difference between the three spin values results entirely from the Lorentz factor of the rotating disc element, γ^{ϕ}. This plot is very similar, but not identical, to the corresponding plot in Dauser et al. (2013) (top panel in their Fig 2). The discrepancy results from small (inconsequential as it turns out) mistakes in the expressions for γ^{ϕ} in Bardeen et al. (1972) (equation 13.12a) and Dauser et al. (2013) (equation 10). The two expressions are identical *except* the latter reference drops all $\pm$ and $\mp$ signs, meaning that they agree for prograde spin but differ slightly for retrograde spin. Upon further investigation, detailed in Appendix B.1, we found a very subtle mistake in equation (13.12a) of Bardeen et al. (1972), which is again very small and only relevant for retrograde spin. We find that, for $a = -0.99$ (which maximises the magnitude of the error), the Dauser et al. (2013) version actually gives a closer answer to our new expression than the Bardeen et al. (1972) version, although all three are very similar.

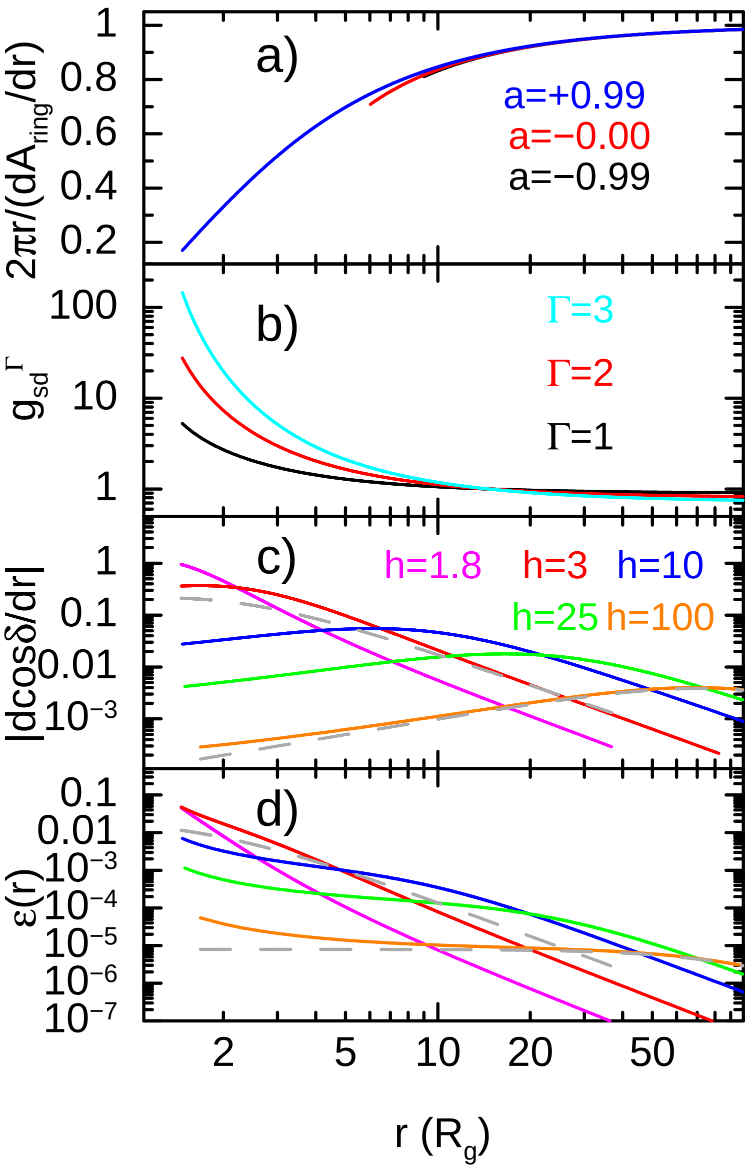

Figure 3.4: Contributions to the radial emissivity profile, designed for comparison to Fig 2 in Dauser et al (2013). *a:* Ratio of the Newtonian radial derivative to the fully relativistic version for spin as labelled. *b:* Contribution to the emissivity of the blueshift factor for $h = 10$ and $a = 0.99$. *c:* Radial derivative of $\cos\delta$ for $a = 0.99$ and h as labelled. The grey dashed lines are the Newtonian equivalent for $h = 1.8$ (to be compared with the solid magenta line) and $h = 100$ (to be compared with the solid orange line). As expected, this is a better approximation for larger source heights. *d:* Emissivity profile for $\Gamma = 2$, $a = 0.99$ and h as labelled in panel c. Again, the grey dashed lines are the Newtonian equivalent [$\epsilon(r) \propto (h^2 + r^2)^{-3/2}$] for $h = 100$ and $h = 1.8$.

Panel (b) shows the contribution of the blueshift factor for three different values of Γ, illustrating that a steeper spectrum leads to a steeper emissivity profile. Panels (c) and (d) show respectively the radial derivative of the cosine of the angle δ and the overall emissivity profile for various parameter combinations. The grey dashed lines represent the Newtonian approximations $[|d\cos\delta/dr| = hr(h^2+r^2)^{-3/2}$ and $\epsilon(r) = h(h^2+r^2)^{-3/2}/(4\pi)]$ for $h = 1.8\ R_g$ (to be compared with the magenta lines) and $h = 100\ R_g$ (to be compared with the orange lines). We see that, as expected, the full GR solution diverges dramatically from the Newtonian approximation for low source heights. Our emissivity profiles agree with those presented in Dauser et al. (2013).

3.3.2 Time-averaged spectrum

Fig 3.5 shows the direct and reflected components of the time-averaged spectrum calculated by RELTRANS (black) and the most recent version of RELXILLLP at the time of writing (red, dashed). We use the default parameters listed in Table 3.1, except we set $r_{out} = 400\ R_g$ for ease of comparison with RELXILLLP. RELXILLLP accounts for the dependence of emission angle and disc rest frame cut-off energy on disc coordinates, but assumes a single ionisation parameter. For the purposes of comparison in this plot, we therefore follow suit (although see sections 3.3.3 and 3.3.3 for further discussion on these dependencies), and use the default number of zones for both μ_e and E_{cut}. For all models, the relative normalisation of reflected and direct components is calculated self-consistently, rather than set as a model parameter. We see that RELXILLLP agrees very well with our model[4]. Besides benchmarking against RELXILLLP, we have also throughly tested our code by comparing it with outputs calculated using brute-force calculation of the transfer function (i.e. without using the kernal convolution).

3.3.3 Rest frame assumptions

In this section, we explore the impact of accounting for the coordinate dependence of the emission angle and high energy cut-off (3.3.3) and ionisation parameter (3.3.3), before comparing RELTRANS to RELTRANSCP (3.3.3).

Emission angle and cut-off energy

Fig 3.6 shows the radial dependence of the cosine of the emission angle, μ_e, for the default parameters, with the spread being for different disc azimuths. As expected, $\mu_e \approx \cos(i)$ for very large disc radii, but covers an enormous range for smaller disc

---

[4] Model versions of RELXILLLP prior to v1.2.0 have a smaller relative normalization of the reflection spectrum. This comes partly from an extra factor of $0.5\cos i$ that is applied to the XILLVER spectrum before being convolved with the smearing kernel in the older versions

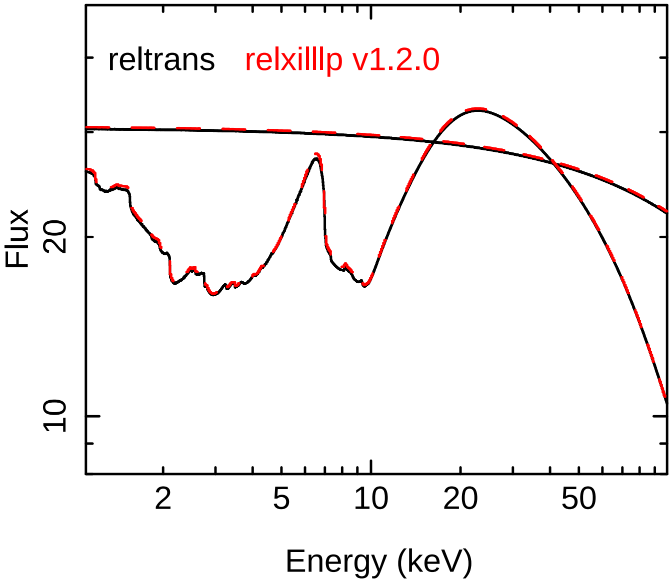

Figure 3.5: Time-averaged direct and reflected spectrum for RELTRANS (black), and the most recent version of RELXILLLP (red, dashed). We see good agreement between the two models.

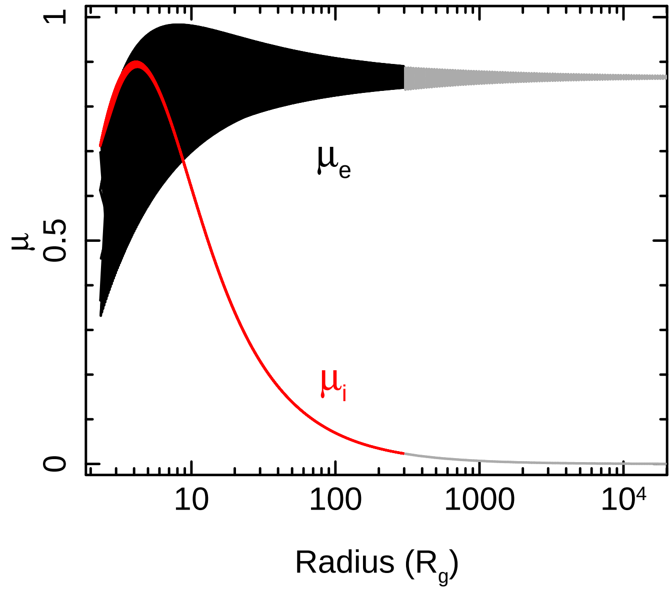

Figure 3.6: Cosine of the emission angle (black) and incidence angle (red) as a function of radius for the default parameters ($i = 30°$). We see that the emission angle depends on azimuth as well as radius, whereas the incidence angle is a monotonic function of radius. The grey points at $r \gtrsim 400\ R_g$ are computed assuming that rays travel in straight lines. The smooth joins from the full GR treatment used for $r \lesssim 400\ R_g$ demonstrate that this is a reasonable assumption.

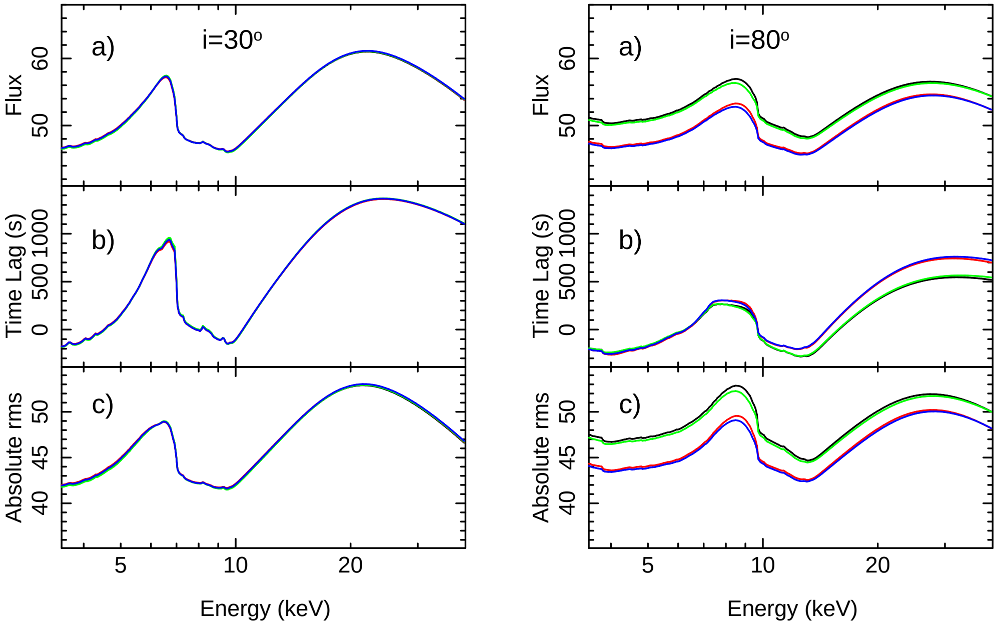

Figure 3.7: RELTRANS time-averaged spectrum (a), $1-2\times10^{-5}$ Hz time lags (b) and absolute variability amplitude (c) calculated for the default parameters. Left and right hand panels correspond to inclination angles of 30° and 80° respectively. For the black lines, we set the emission angle δ_e equal to the inclination angle i and ignore the radial dependence of E_{cut} as measured in the disc restframe. For the other lines, we account only for the disc coordinate dependence of μ_e (red), only for the E_{cut} dependence (green), and for both (blue). A single ionisation parameter is used. For the lags, ϕ_A is calculated for a $2-10$ keV *XMM-Newton* EPIC pn reference band flux.

radii. The RELXILL family of models for the time-averaged spectrum (García et al. 2014) account for this disc coordinate dependence of the emission angle, and now also for the radial dependence of apparent E_{cut} observed in the disc rest frame. Here, we investigate both effects in the context of the timing properties. Fig 3.7 shows the time-averaged spectrum (a), time lags (b) and variability amplitude (c) calculated for $i=30°$ (left) and $i=80°$ (right). The different lines account for neither effect (black), only emission angle (red), only cut-off energy (green) and both effects (blue). For the purposes of the variability amplitude calculation, we simply set $\alpha(\nu)=1$ (this in itself is unphysical, corresponding to 100% fractional variability, but as an arbitrary constant it does not have any bearing on our analysis). We see that the E_{cut} effect is always subtle, but the emission angle effect can become very large for high inclination angles (consistent with what García et al. 2014 found for the time-averaged spectrum). These figures use 10 zones to account for both effects, which we find to be comfortably enough to reach convergence for all trialled parameter combinations. Since acceptable accuracy can be achieved by using as few as 5 zones for both quantities, we set 5 as the default value for the environment variables `MU_ZONES` and `ECUT_ZONES` (see Table B.1). The user can adjust these values to test for convergence.

Ionisation profile and incidence angle

The ionisation parameter is proportional to the 13.6 eV to 13.6 keV illuminating flux, $F_x(r) \propto g_{sd}^{2-\Gamma}(r)\epsilon(r)$, divided by the disc electron density $n_e(r)$. Whereas the flux is known exactly in the lamppost model, $n_e(r)$ is more uncertain. Shakura & Sunyaev (1973) define equations for 3 disc zones, where zone A is the innermost region, in which pressure is dominated by radiation and the opacity is dominated by electron scattering. Since the emissivity is dominated by the inner regions, we first investigate the zone A density profile (equation 2.11), $n_e(r) \propto \alpha^{-1} r^{3/2}[1-(r_{in}/r)^{1/2}]^{-2}$, where α is the viscosity parameter [not to be confused with our normalisation parameter $\alpha(\nu)$]. The density profile is very different for the other zones at larger radii, but for these radii F_x is small and so the predicted ionisation is small regardless of the assumed density profile. The black solid line in Fig 3.8 shows the resulting ionisation profile for the default parameters. For simplicity, we have taken the viscosity parameter to be a constant, but we stress there is no *a priori* reason to assume this. There are other reasons to suspect an alternative density profile. For instance, the stress-free inner boundary condition may not be appropriate for a truncated disc, or there may be no zone A present when the accretion rate is a small fraction of the Eddington limit. We therefore additionally explore the simplest possible case of constant density (following Svoboda et al. 2012). The resulting ionisation profile is plotted in Fig 3.8 (black dashed line).

We normalise the ionisation profile by specifying as a model parameter the peak ionisation value, $\log_{10}\xi_{max}$. For the constant density model, the peak simply occurs at the disc inner radius. For the zone A density profile, we use $r_{peak} = (11/9)^2 r_{in}$, which is only exact for $\epsilon(r) \propto r^{-3}$, but numerical calculation of the exact r_{peak} would be fairly expensive for no real gain.

Another effect to consider is the radial dependence of the incidence angle of illuminating photons δ_i (see Fig 3.2), the cosine of which is plotted for the default parameters in Fig 3.6 (red line). The incidence angle influences the shape and normalisation of the restframe reflection spectrum (García & Kallman 2010) but, in order to save computational expense, the public XILLVER grid is tabulated only for $\delta_i = 45°$. Since the leading order effect is on the intensity of the radiation field at the disc upper boundary, $2F_x(r)/\mu_i(r)$, the radial μ_i profile can be approximately accounted for very cheaply by adjusting the ionisation profile (García & Kallman 2010; Dauser et al. 2013). The red lines in Fig 3.8 show the logarithm of the 'effective' ionisation parameter, $\xi_{eff}(r) = \xi(r)\cos(45°)/\mu_i$, that results from this adjustment. We use this effective ionisation in our model since it captures more physics for no extra computational cost.

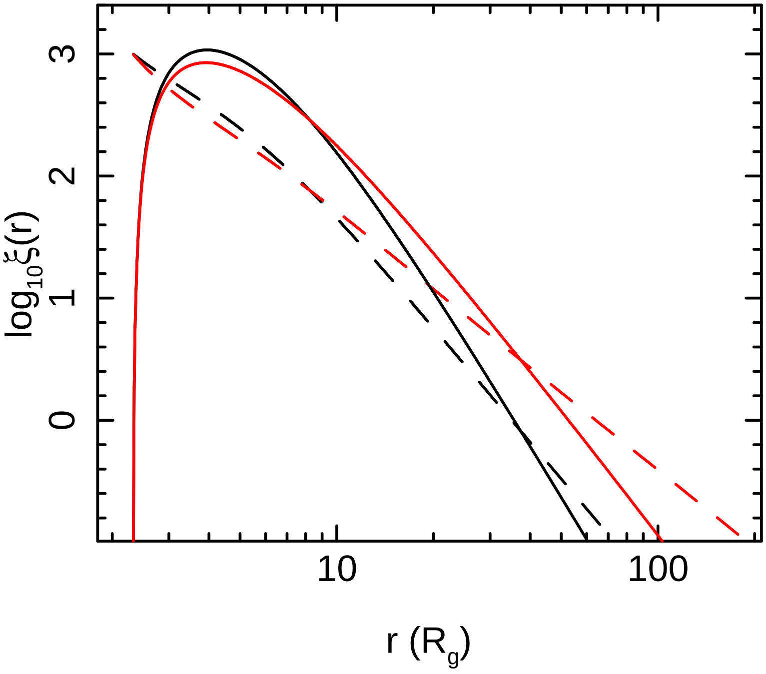

Figure 3.8: The black lines are radial ionisation profiles calculated assuming a zone A density profile (solid) and constant density (dashed). The red lines are effective ionisation profiles, which have been adjusted to account for the radial dependence of the incidence angle.

Figs 3.9 and 3.10 show the time-averaged spectrum (a), time lag (b) and amplitude (c). The thick black lines are computed for a single ionisation parameter of $\log_{10}\xi = 3$, whereas a self-consistently calculated effective ionisation profile has been used for the coloured lines. We use the zone A density profile for Fig 3.9 and constant density for Fig 3.10. From bottom to top, the red, green, blue, cyan and magenta lines are for $\log_{10}\xi_{max} = 3$, 3.5, 3.75, 4.0 and 4.25 respectively. We see that this modification to the model makes an enormous difference to all outputs. For the zone A profile, setting $\log_{10}\xi_{max} = 3.75$ (blue lines) gives the closest match to the constant ionisation model in terms of the relative peak fluxes of the time-averaged iron line and reflection hump. However, the red wing of the iron line is much more prominent for the self-consistent case. The constant density case is similar, except for $\log_{10}\xi_{max} = 4.25$. We will investigate possible biases that this may cause when fitting constant ionisation models to observational data in section 3.4.2. The effect is even greater if we also consider the timing properties. The self-consistent models have smaller iron line lags than the single ionisation model, which may perhaps be mistaken for the source height or disc inner radius being smaller. The absolute rms spectrum shows that the iron

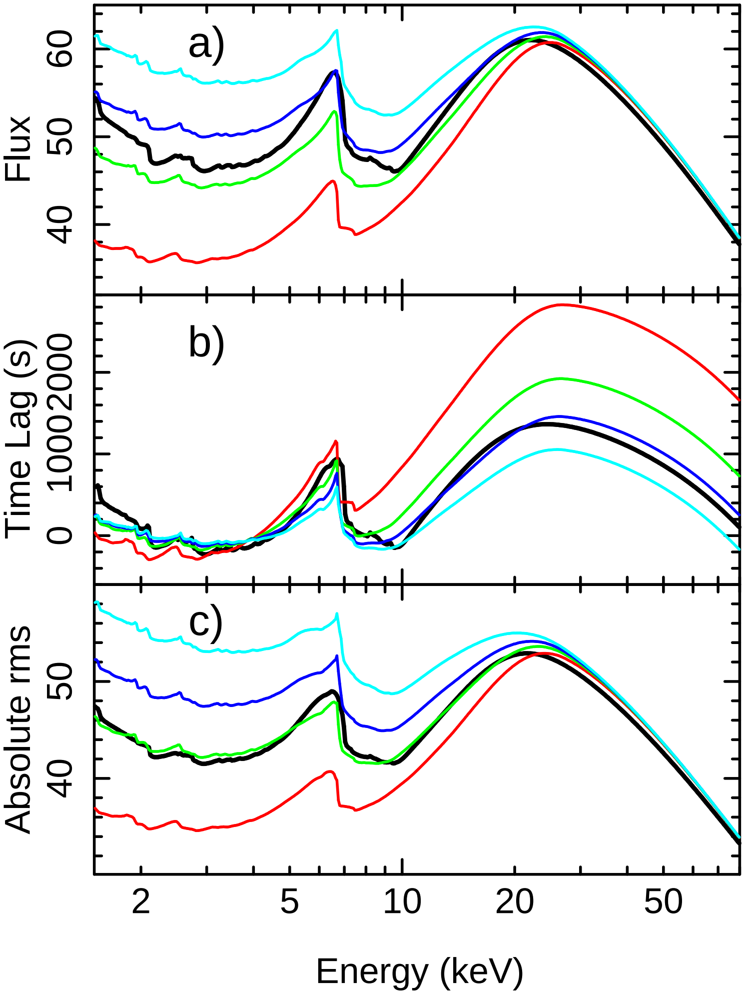

Figure 3.9: RELTRANS time-averaged spectrum (a), time lags (b) and absolute variability amplitude for different assumptions regarding the radial ionisation profile. For all lines, we assume the default parameters, and for the time lag we assume that the reference band was the $2-10$ keV EPIC-pn flux. For simplicity, we ignore the μ_e and E_{cut} dependencies explored in Fig 3.7. The thick black lines are for a constant disc ionisation parameter, $\log_{10}\xi = 3.0$. The other lines assume a radial ionisation profile self-consistently calculated from the emissivity profile and the density profile relevant to Shakura and Sunyaev's zone A. From bottom to top, the red, green, blue and cyan lines assume a 'peak' ionisation of $\log_{10}\xi$ =3, 3.5, 3.75, 4.0. We see that accounting for the radial ionisation profile makes an enormous difference to the results.

line is much more variable for the self-consistent case. As we will see in section 3.4.2, it is possible to choose a value of h that allows the single ionisation model to mimick the time-averaged spectrum of the self-consistent case, but the different effect that the ionisation gradient has on the timing properties means that considering also time lags and variability amplitude breaks the degeneracy. Both figures here are plotted using 100 zones in ionisation parameter. We find however that reasonable convergence can be achieved for 10 zones, and so we set this as the default value for the `ION_ZONES` environment variable (see Table B.1).

RELTRANSCP VS RELTRANS

Fig 3.11 demonstrates typical differences between RELTRANS (black lines) and RELTRANSCP (red lines). Whereas the former uses an exponentially cut-off power-law for the illuminating spectrum, the latter uses the model NTHCOMP (Zdziarski et al. 1996; Życki et al. 1999), which gives a much better approximation of Compton up-scattering of seed photons by a thermal population of hot electrons. We see that NTHCOMP has a low energy cut-off, which is determined by the seed photon temperature kT_{bb}. In the XILLVERCP tables, this is hardwired to 0.05 keV (assuming a multi-temperature blackbody spectrum of seed photons). The shape of the high energy cut-off is also very different for NTHCOMP. The difference between the two models is small for the lags though. Since RELTRANSCP employs a more physical emission model for little extra computational expense, we use it for the remainder of the plots in this paper.

3.3.4 Frequency dependence

Fig 3.12 demonstrates the frequency dependence of RELTRANSCP for the default parameters. Panel a shows the phase normalisation $\phi_A(\nu)$ calculated for a $2-10$ keV reference band measured by the EPIC-pn instrument onboard the *X-ray Multi-mirror Mission* (*XMM-Newton*; Jansen et al. 2001) in timing mode (calculated from equation 3.25). As noted in Mastroserio et al. (2018), we can only be confident that this function is a correct representation of the underlying spectral model if all the channels used for the reference band are considered to be well calibrated. The range $2-10$ keV demonstrated in the plot is well calibrated for *XMM-Newton*. If for any reason we wish to define our reference band from poorly calibrated channels, for instance if we wish to maximize signal to noise by collecting more photons, then a systematic error will be introduced into the calculation of $\phi_A(\nu)$ because the instrument response matrix used for the calculation does not adequately describe the true response of the telescope for all energy channels. In such a case, it may be best to leave $\phi_A(\nu)$ as a free parameter for each frequency range considered, although this will inevitably lead to larger statistical errors.

Panels b and c show respectively time lags and absolute variability amplitude as a function of energy for 10 different frequency ranges. The overall lag reduces and the

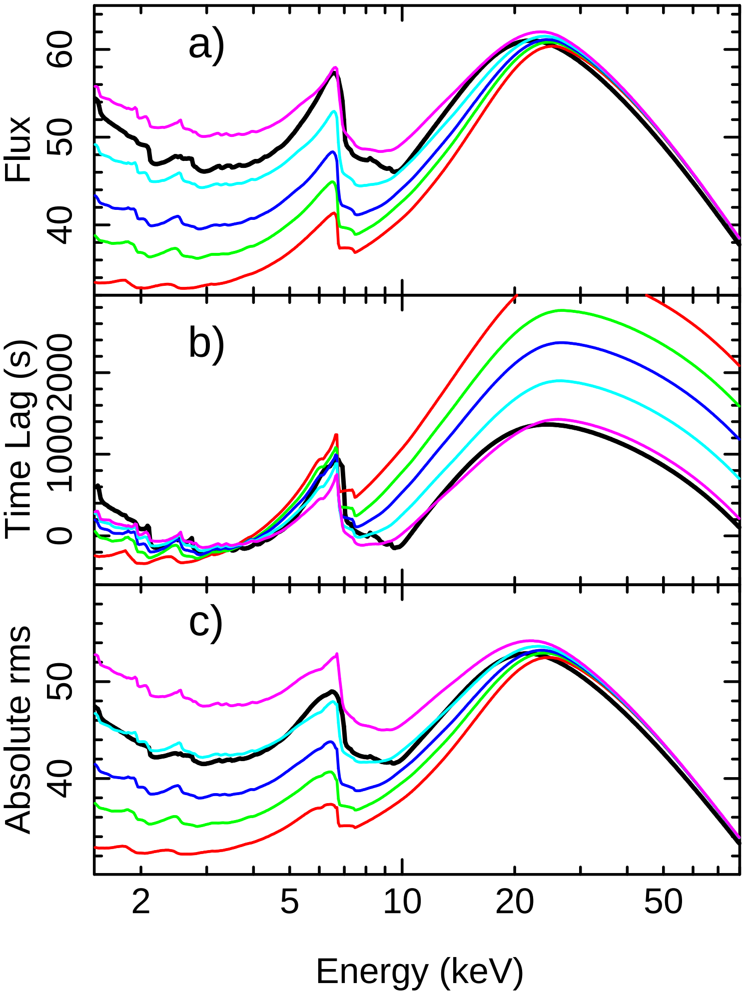

Figure 3.10: Same as Fig 3.9, except the radial ionisation profile is calculated assuming a disc with constant density. The magenta lines are for $\log\xi(r_{in}) = 4.25$. For this constant density case, the peak ionisation that most closely matches the spectrum to the constant ionisation case is slightly higher (i.e. 4.25, magenta line). We again see that the red wing of the iron line in the time-averaged spectrum (a) is exaggerated compared with the constant ionisation model (thick black lines), even though the change in shape of the line is slightly less dramatic than for Fig 3.9. The use of a self-consistent ionisation profile again has a significant affect on the time lags (b) and absolute rms (c), with the self-consistent ionisation profile again leading to a more variable iron line (see magenta lines).

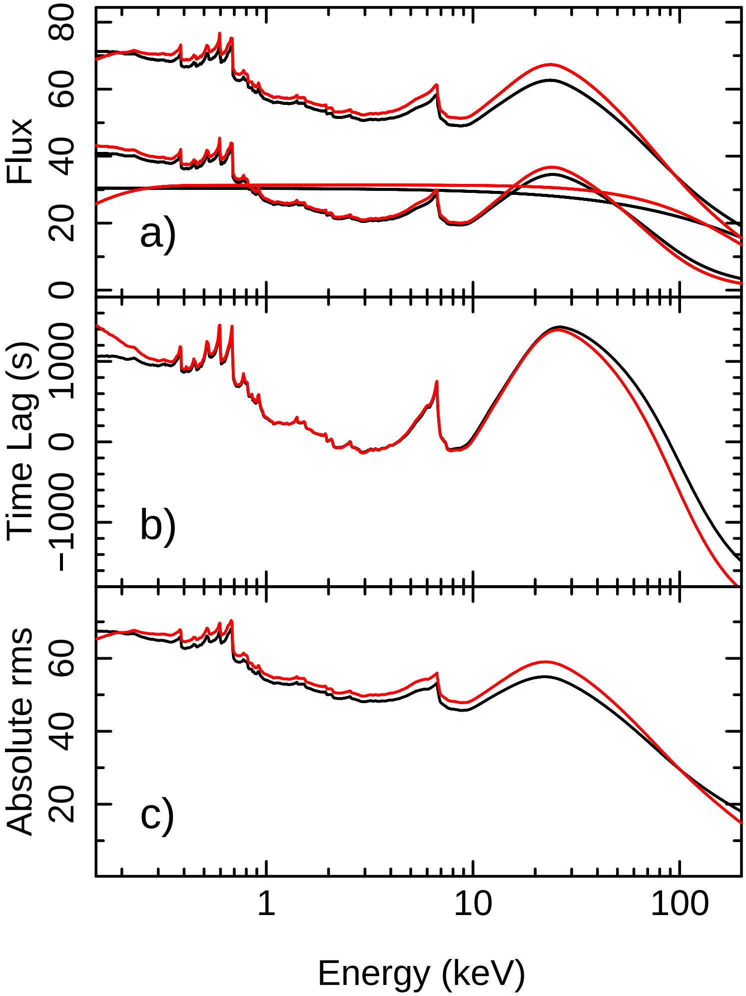

Figure 3.11: Time-averaged spectrum (a), time lags (b) and absolute variability amplitude calculated from the default parameters. The black lines represent the model RELTRANS (which assumes an exponentially cut-off power-law for the direct spectral component) and the red lines represent RELTRANSCp (which uses NTHCOMP for the direct spectrum). We see a significant difference in the time-averaged direct component. The time lags are largely unaffected for energies below ~ 20 keV, whereas the more physical model RELTRANSCp predicts a larger variability amplitude. Here we use default values for the environment variables, and the phase zero point is self-consistently calculated for a $2-10$ keV *XMM-Newton* pn timing mode reference band.

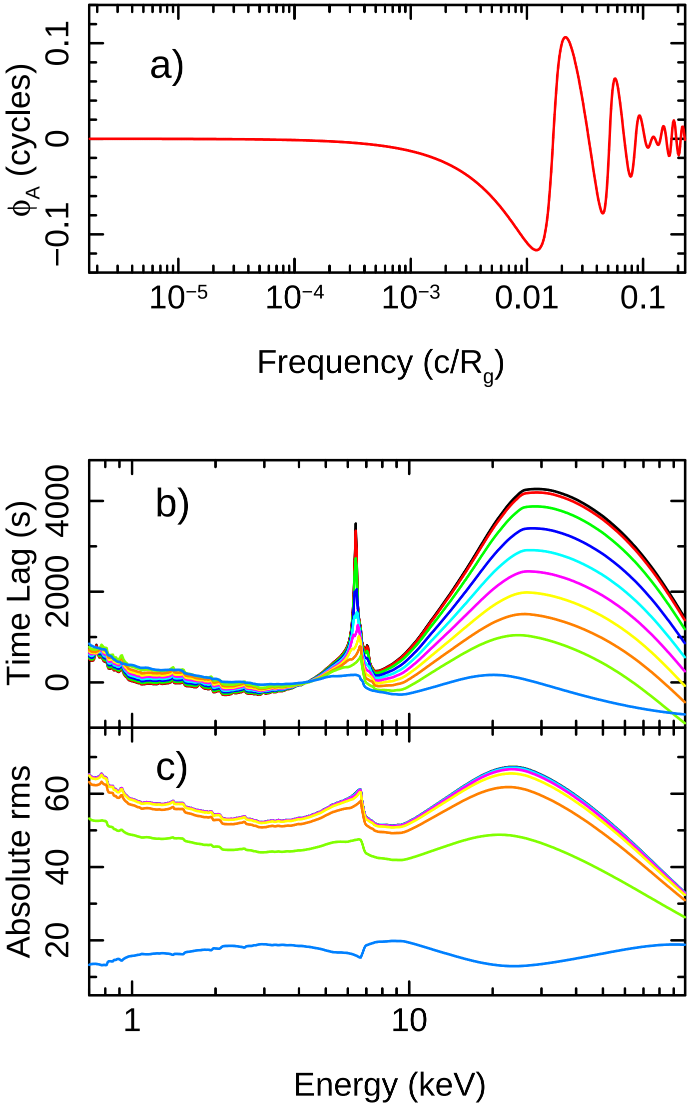

Figure 3.12: *a:* $\phi_A(\nu)$ calculated using the default model parameters of reltransCp (default environment variables), assuming that the reference band is the $2-10$ keV EPIC-pn flux. *b:* Time lag versus energy for the same parameters using the same calculation for $\phi_A(\nu)$. The black, red, green, blue, cyan, magenta, yellow, orange, light green and light blue lines (top to bottom) are calculated for different frequency ranges, which increase logarithmically from a minimum of 10^{-8} Hz to a maximum of 10^{-4} Hz (this range corresponds to $0.046-460$ Hz for a $10M_{\odot}$ black hole, or $\sim 2.26\times10^{-6}-10^{-2}$ c/R_g). *c:* The same calculation but for variability amplitude, setting $\alpha(\nu)=1$.

iron line feature gets broader with increasing frequency because the higher frequencies select reflection from smaller regions of the disc. Similarly, the line feature in the rms spectrum becomes weaker for higher frequencies as the fastest variability is washed out by path length differences introduced by reflection from different parts of the disc. At the highest frequency range plotted here, we see the effects of phase-wrapping, evidenced by the iron line and reflection hump becoming dips as opposed to excesses in the rms spectrum.

Our model calculates the energy dependent cross-spectrum for a given frequency range, rather than the cross-spectrum as a function of frequency for a given energy range. This feature is hardwired because we calculate the energy dependent transfer function in Fourier space (see equation 3.22) for a range of frequencies between ν_{min} and ν_{max}. This is much more computationally efficient than first calculating a 2D impulse-response function and Fourier transforming the time axis. All frequencies can be taken into account by fitting for many frequency ranges, as in Mastroserio et al. (2018). The public model does not currently include non-linear effects, but will soon be updated (description in Mastroserio et al submitted). Intrinsic hard lags can alternatively be produced by summing two model components. This is only possible when considering real and imaginary parts of the cross-spectrum, and the phase normalisations of the two component must be free parameters (i.e. not self-consistently calculated) and independent of one another. Using, for example, two RELTRANS components with different source heights and different spectral indices is the same as assuming the 'two blobs' geometry of Chainakun & Young (2017). The Fourier frequency dependent propagation time between the blobs is simply $|\phi_{A1}(\nu) - \phi_{A2}(\nu)|/(2\pi\nu)$.

3.4 Modelling biases

In this section, we explore two sources of bias in previous treatments of reflection and reverberation in the literature. The first is ignoring the instrument response matrix when analysing time lags. In section (3.4.1), we show that the value of the lag can be heavily biased in an energy range for which the instrument response is not diagonal and in which line-of-sight absorption is prominent. This is because such an energy range is *dominated* by photons from other energy bands that have been 'mis-classified'. The other source of bias is assuming a single disc ionisation parameter instead of accounting for a self-consistently calculated radial ionisation profile (section 3.4.2).

3.4.1 Bias caused by ignoring the telescope response

Our model provides two ways to properly account for the instrument response and line-of-sight absorption. The recommended option for the purposes of fitting to data

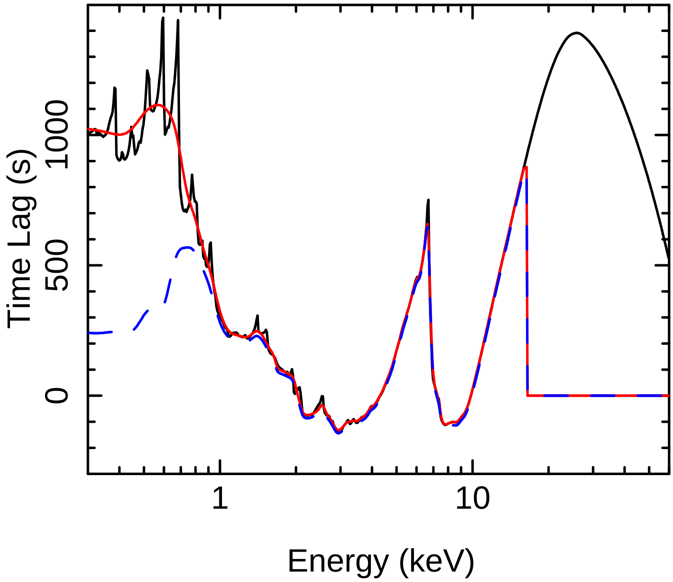

Figure 3.13: Time lags calculated for the default parameters. The black line is for the model only, and so does not account for a telescope response matrix. The red and blue lines assume the pn response and absorption column densities of $N_h = 0$ and $10^{22}\mathrm{cm}^{-2}$ respectively. We calculate ϕ_A for all three assuming the reference band is the $2-10$ keV band of the pn.

is to consider the real and imaginary parts of the cross-spectrum (`ReIm`=1 and 2). In this case, the fits files containing the data can be read into XSPEC in the normal way, with response files specified in the header, and the usual XSPEC operation of folding around the instrument response is appropriate. The user can then plot the best fitting cross-spectral model in terms of variability amplitude and time lags after the fit is complete (`ReIm`=3 and 4). However, the user may wish to instead fit for time lags and/or variability amplitude. In this case, the model cross-spectrum is folded around the instrument response within the code and the variability amplitude and time lags are calculated from this folded cross-spectrum (`ReIm`=5 and 6). Observationally constrained time lags and rms can be loaded into XSPEC with a diagonal dummy response matrix (using e.g. `flx2xsp`). The response files can be set through environment variables (`RMF_SET` and `ARF_SET`). If the environment variables are not set but the code is in a mode requiring a response, the user will instead be prompted at the terminal for input.

Fig 3.13 illustrates the importance of correctly accounting for the instrument response. The black line represents time lags for the model only, ignoring the instrument response (i.e. `ReIm`=4). In this case, the absorption model is not relevant because

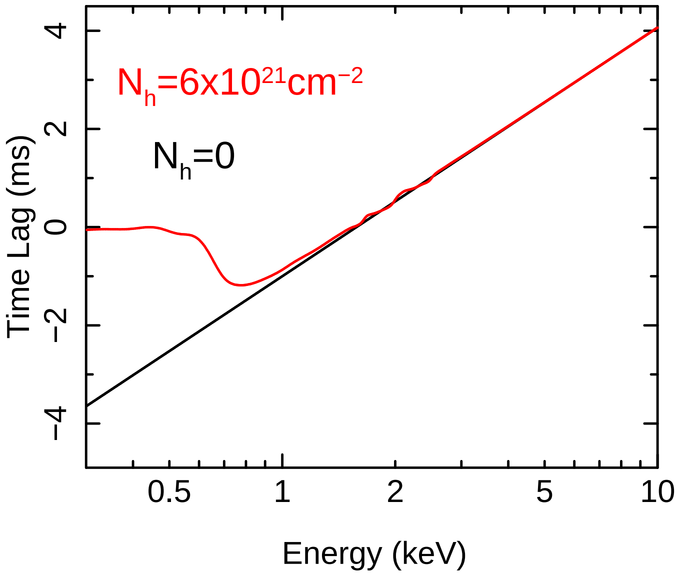

Figure 3.14: Log-linear time lag as a function of energy (black), with the parameters chosen to roughly match the $1-30$ Hz lag spectrum of GX 339−4 in observation 'O1' from De Marco et al. (2017) and Mahmoud et al. (2019). The red line is the time lag that would be observed by *XMM-Newton* assuming that the intrinsic lag-energy spectrum is given by the black (log-linear) line. To calculate this, we take the argument of the absorbed and folded model cross-spectrum. We see that an intrinsically log-linear lag spectrum appears to turn up at $E \lesssim 1$ keV in *XMM-Newton* observations.

it cancels out when the imaginary part of the cross-spectrum is divided by the real part. The red line represents the same model, but now the EPIC pn response has been used and we set the hydrogen column density to $N_h = 0$. The blue dashed line is the same again except that now we set $N_{\rm H} = 10^{22}{\rm cm}^{-2}$. We see very little differences in the $2-10$ keV region, whereas above ~ 15 keV the lags are completely undefined due to lack of effective area. The differences between the lines below ~ 1 keV occur because the response matrix is not diagonal in this energy range. For $N_h = 0$, the resulting ambiguity between soft photons and harder photons 'mis-classified' as soft simply smears out sharp features. When absorption is taken into account, the soft band instead becomes *dominated* by the mis-classified photons. This essentially introduces dilution: the lag between 0.5 keV and 1 keV is very small because most of the photons recored in the ~ 0.5 keV channel are actually ~ 1 keV photons.

Whereas Fig 3.13 is relevant for high frequencies at which the reverberation lags dominate over the intrinsic hard lags, the same effect is also potentially important for lower frequency ranges in which the intrinsic lags are still significant. In particular, signatures of thermal reverberation have been detected for a number of black hole X-ray binaries including GX 339−4 (Uttley et al. 2011; De Marco et al. 2017). In the 1−30 Hz frequency range, log-linear intrinsic lags are seen for $E \gtrsim 1$ keV and a turn up is seen for $E \lesssim 1$ keV, which is attributed to thermal reverberation (see top right of Fig 7 in De Marco et al. 2017). We investigate how this thermal reverberation signal may have been affected by the instrument response by first assuming that the intrinsic lag spectrum in the 1 − 30 Hz frequency range is simply log-linear for the full energy range (Fig 3.14, black line). From this, we calculate the energy dependent cross-spectrum. This additionally requires a model for the time-averaged spectrum and a model for the energy dependent fractional variability amplitude. We use TBABS*NTHCOMP ($N_h = 6 \times 10^{-21}\mathrm{cm}^{-2}$, $\Gamma = 1.9$, $kT_{bb} = 0.18$ keV) for the time-averaged spectrum and assume that the fractional rms increases linearly with energy ($rms \propto 0.024E + 0.043$, although our results only depend very weakly on this function). We then fold our model cross-spectrum around the *XMM-Newton* pn timing mode response matrix and calculate the 'folded' lag spectrum from the argument of this folded cross-spectrum (red line). We see a clear turn up in the 'folded' lag spectrum below ~ 1 keV that results from these energy channels being dominated by 'mis-classified' photons.

On first inspection, this looks worryingly like a spurious signature of thermal reverberation. However, the observation of GX 339−4 that our model is based upon has a number of characteristics that convincingly point to the presence of thermal reverberation. In particular, De Marco et al. (2017) present the 5 − 30 Hz lag energy spectrum in their Fig 7. That the ~ 0.5 keV lag increases as progressively higher frequency ranges are chosen is very suggestive of thermal reverberation. Moreover, the $E \sim 0.5$ keV lag is *larger* than the lag in the $\sim 1 - 6$ keV energy range, and so simply cannot be caused by the instrumental effect that we have explored here - which can only dilute the soft lags by averaging with the higher energy lags. We therefore conclude that the thermal reverberation interpretation of the data is sound. However, the *value* of the lag is very likely biased by the instrument response. In particular, Mahmoud et al. (2019) fit a transfer function model to the data that only accounts for the effective area curve of the instrument but not the redistribution matrix. This implies that the true reverberation lags are shorter than originally thought, and the measured disc inner radius of $\sim 20\ R_g$ may reduce once the correction is made.

We conclude that it is important to properly account for the telescope response matrix when modelling the $\lesssim 1$ keV region of *XMM-Newton* data, either by fitting for real and imaginary parts, or using the folding option. A similar effect is present in the *NICER* response, but not that of the *Nuclear Spectroscopic Telescope ARray* (*NuSTAR*; Harrison 2013).

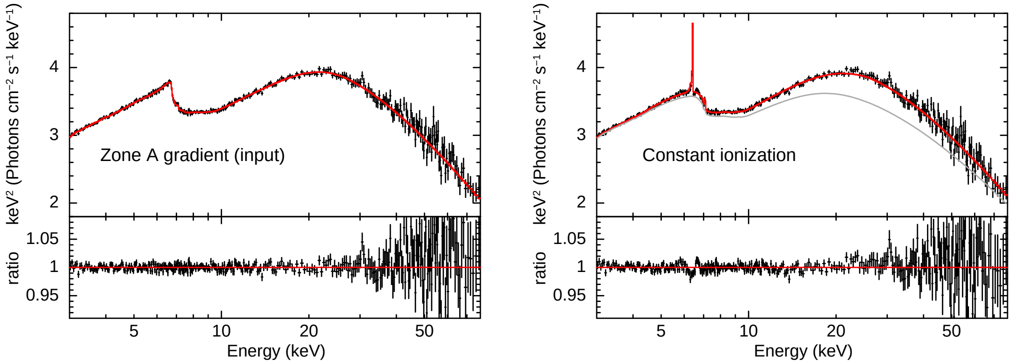

Figure 3.15: Unfolded fake data and model (top) and fake data to model ratio (bottom). The data were generated from a model with a radial ionisation profile calculated assuming a zone A Shakura-Sunyaev density profile. Left and right hand plots respectively show the results of fitting the input model and an alternative model with a single ionisation parameter (red) plus an extra xillver component (grey). Results are further detailed in Table 3.2. Spectra have been re-binned for plotting purposes (binned to a target signal to noise ratio of 150 but not co-adding more than 10 channels).

3.4.2 Bias caused by using a single ionisation

It is clear from the discussion in Section 3.3.3, and in particular Figs 3.9 and 3.10, that including a self-consistent radial ionisation profile can give very different model outputs to simply assuming a constant ionisation parameter. In this section, we create a fake *NuSTAR* time-averaged spectrum and fit back with a single ionisation parameter model in order to investigate biases that may have been introduced into the many spectral fitting studies that have used a single ionisation model.

Fake data

We simulate a 30 ks *NuSTAR* observation of a bright X-ray binary by inputing the model parameters listed in Table 3.2 into reltransCp, with the normalisation set to roughly match the observed flux of GX 339−4 when $\Gamma \approx 2$ (model $4-10$ keV flux $= 5 \times 10^{-9}$ erg cm^{-2} s^{-1}). We use fakeit to generate a fake 30 ks FMPA exposure, taking background into account. We ignore deadtime effects, but do not generate an FPMB exposure. Statistically, this is the same as taking both focal plane modules into account and assuming a deadtime correction factor of 1/2. Our fake observation therefore corresponds to a typical high quality observation used for the purposes of spectral fitting (e.g. Parker et al. 2015; Xu et al. 2018; Tomsick et al. 2018). We only simulate the time-averaged spectrum, since there have thus far only been a few studies fitting reverberation models to timing data.

Parameter	Input	Control Fit	Single Ion Fit
N_H (10^{22}cm^{-2})	1	1	1
h (R_g)	6	$5.48^{+0.616}_{-0.546}$	$2.45^{+0.26}_{p}$
a	0.9	$0.99^{p}_{-0.099}$	$0.778^{+0.0461}_{-0.0581}$
i (degrees)	30	$30.7^{+1.06}_{-1.72}$	$29.1^{+0.89}_{-1.12}$
Γ	2	$2.0^{+0.01}_{-0.01}$	$2.03^{+0.015}_{-0.009}$
$\log_{10}\xi^*$	3.75	$4.13^{+0.289}_{-0.587}$	$3.05^{+0.034}_{-0.034}$
A_{Fe}	1	$0.967^{+0.1926}_{-0.1259}$	$0.999^{+0.1198}_{-0.0599}$
$(kT_e)_{obs}$ (keV)	50	$46.1^{+15.0}_{-5.37}$	$50.8^{+11.81}_{-3.23}$
$1/\mathcal{B}$	0.5	$0.571^{+0.1694}_{-0.0743}$	$0.419^{+0.0511}_{-0.0188}$
norm (10^{-2})	10	$7.97^{+0.959}_{-0.621}$	$56.8^{+4.86}_{-12.51}$
xillverCp norm (10^{-3})	0	0	$6.32^{+0.08}_{-0.078}$
χ^2/d.o.f.		1540.68/1561	1505.89/1560**

Table 3.2: Input parameters and values measured by fitting back with the correct (control) model and a single ionisation model. Errors are 90% confidence limits, and p denotes that the parameter is pegged at a hard limit. *The ionisation parameter has different meanings in the two models (single value vs maximum value). ** A 0.5% systematic error was applied for the single ionisation model fit, as is commonly practiced in spectral fitting to account for calibration uncertainty and model systematics. Without the systematic error, the best fitting single ionisation model has a reduced χ^2 of 1626.38/1560, corresponding to a goodness of fit that is common for fits to real *NuSTAR* spectra (e.g. Miller et al. 2013).

Our input model assumes the Zone A Shakura-Sunyaev density profile. This is a reasonable assumption for the brightest hard / hard intermediate states of X-ray binaries. The bolometric luminosity of GX 339-4 is $L_x \sim 10^{38.5}$ erg s^{-1} when $\Gamma = 2$ (see Fig 5 of Plant et al. 2014). For $M \lesssim 10\ M_\odot$ (which is a reasonable upper limit: Heida et al. 2017) and a viscosity parameter $\alpha \gtrsim 0.01$, the zone A to B transition is therefore at $r_{ab} \gtrsim 200\ R_g$ (equation 2.17 in Shakura & Sunyaev 1973), indicating that the region of the disc that dominates the emissivity is radiation pressure and electron scattering dominated. Following the discussion in section 3.3.3 concluding that the disc coordinate dependence of μ_e and disc rest frame observed electron temperature are not important for low source inclinations, we use 100 ionisation zones for our input model, and only one for the emission angle and electron temperature.

Fit results

Fig 3.15 and Table 3.2 summarise the results of fitting the fake data with the input model (left) and a single ionisation model (right). We fix the hydrogen column density in both of the fits, assuming this to be constrained in some other way. We see that the single ionisation model under-predicts the source height with high statistical significance. This is consistent with Svoboda et al. (2012) and Kammoun et al. (2019), who found that using a single ionisation zone can produce artificially steep power-law emissivity profiles (and lower source height corresponds to steeper emissivity: Fig 3.4). Previous spectral fitting studies using lamppost models assuming a single ionisation parameter have therefore likely under-predicted the source height. The assumption of a single ionisation parameter seems to have introduced a small bias in the spin measurement, although we find that the spin is under-predicted here, whereas many observational studies, particularly for AGN, yield near-maximal spin values. We also note that the disc inner radius is fixed to the ISCO in our fake data, but is often observed to reduce as the spectrum softens in the real data (e.g. Plant et al. 2015; García et al. 2015). The large red wing of the iron line introduced by the ionisation gradient appears to have been compensated by a larger value of Γ instead of a smaller value of r_{in}.

Interestingly, the single ionisation fit includes a highly statistically significant (5.5 σ from an F-test) low-ionisation xillverCp component. Such a component is often required in fits to real spectra in order to account for enhanced distant reflection (e.g. from a flared outer disc, or from the companion star). Our experiment here implies that the often uncomfortably high flux required for the distant reflector may, in part, be due to a modelling systematic introduced by assuming a single ionisation parameter. The correct iron abundance is recovered for both fits, but we note that the best fitting single ionisation model with no distant reflection component includes a super-solar iron abundance ($A_{Fe} = 2.71^{+0.313}_{-0.229}$; errors are 90% confidence limits). This is interesting because super-solar iron abundances are now consistently measured in X-ray binaries, but it is not well understood why this should be the case (García et al. 2018). It is suspected that the iron abundance parameter is compensating for some missing physics in the models, such as higher electron density in the disc ($n_{\rm e} \sim 10^{20-22}{\rm cm}^{-3}$; Tomsick et al. 2018). The assumption of a single ionisation parameter may also contribute to the high measured iron abundance in some cases.

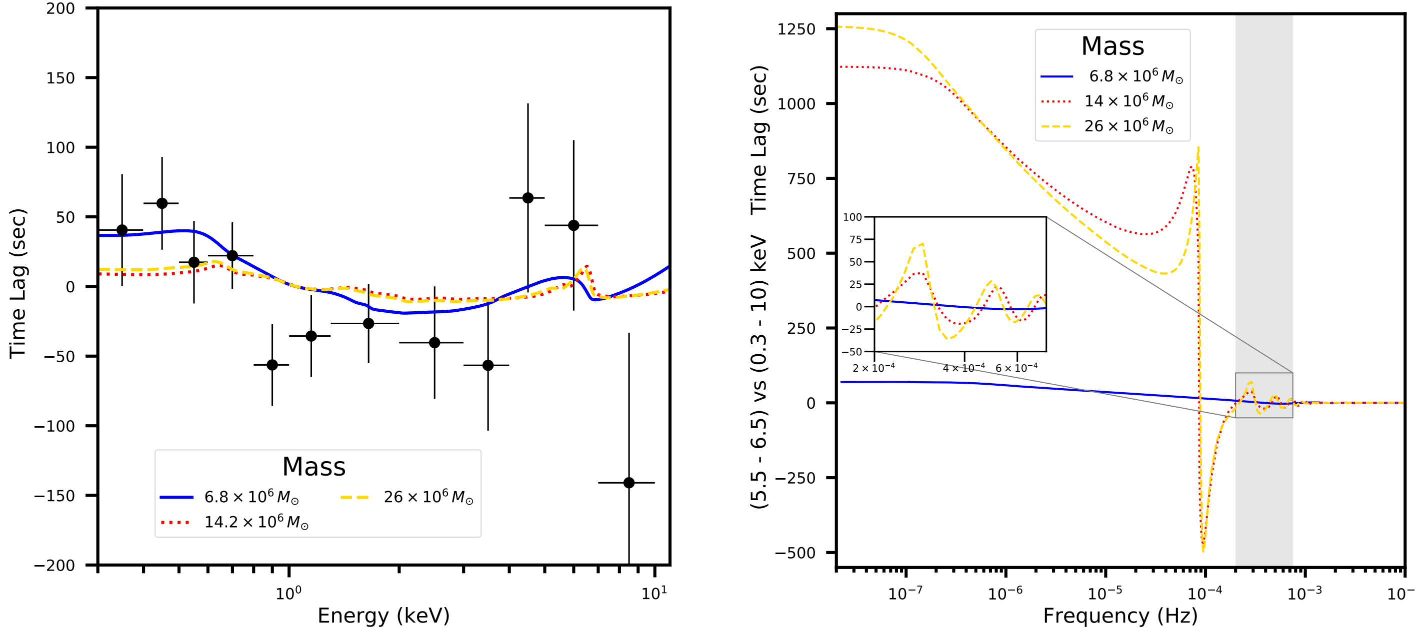

Figure 3.16: *Left:* Time lag as a function of energy in the frequency range $[2{-}7.5] \times 10^{-4}$ Hz for *XMM-Newton* data from Mrk 335 (black points), alongside three RELTRANS model fits (reference band: $0.3 - 10$ keV). For the blue solid line, the black hole mass is a free parameter, and for the red dotted and yellow dashed lines we fix it to two different optical reverberation values from the literature. *Right:* Time lag, averaged over the iron line region ($5.5 - 6.5$ keV), plotted against frequency for the same three models. We see that, in the frequency range used for the lag-energy spectrum (grey band), the models using the optical reverberation masses (red dotted and yellow dashed lines) are in the phase-wrapping regime whereas our best fitting model (blue solid line) is not.

3.5 Example fits for Mrk 335

As a proof of principle, we apply the RELTRANS model to an archival *XMM-Newton* observation of the AGN Mrk 335 for which an iron K feature has previously been identified in the lag-energy spectrum (Kara et al. 2013c). We choose this observation because it provides a good example of an iron K lag feature without the need for complications such as stacking multiple observations or dealing with photon pile-up (both of which are required for the Ark 564 lag-energy spectrum also featured in Kara et al. 2013c). We find that, even though this frequency range displays clear signs of reverberation, a statistically acceptable fit to the real and imaginary parts of the cross-spectrum could only be achieved by including non-linear variability of the direct spectrum, which is beyond the scope of this paper but is introduced for the RELTRANS model in a companion paper (Mastroserio et al. 2019). We therefore instead fit only the time lags in a single frequency range here, leaving a multi-frequency fit of real and imaginary parts of the cross-spectrum to a future paper.

3.5.1 Data

We consider the 133 ks *XMM-Newton* observation taken in 2006 (obs ID 0306870101) that was analysed by Kara et al. (2013c). Following Kara et al. (2013c), we consider only pn data, and reduce it using the *XMM-Newton* Science Analysis System (SAS v.11.0.0), applying the filters `PATTERN` ≤ 4 and `FLAG` $== 0$. We exclude background flares at the beginning and end of the observation (considering only times 252709714 to 252829414 seconds) and extract light curves with 10 second binning from 12 different energy bands, spaced roughly equally in the range $0.3-10$ keV, from a circular region with 35 arcsec radius centred on the maximum of the source emission. We apply the SAS task `epiclccorr` for background subtractions and various corrections.

Again following Kara et al. (2013c), we calculate the cross-spectrum between each of the 12 energy bands and a reference band that is the sum of all energy bands except for the current subject band (thereby ensuring statistical independence between the subject and reference bands; see e.g. Uttley et al. 2014). We average these 12 cross-spectra over the frequency range $[2-7.5] \times 10^{-4}$ Hz, since this is the range for which ‘soft lags’ are observed (De Marco et al. 2013b): i.e. fluctuations in the $0.3-0.8$ keV band lag behind those in the $1-4$ keV band (with the former assumed to be more reflection-dominated than the latter). We calculate energy dependent time lags by taking the argument of each frequency-averaged cross-spectrum and dividing by $2\pi\nu$, where $\nu = 4.75 \times 10^{-4}$ Hz is the centre of the frequency range. We calculate error bars using the analytic formula from Bendat & Piersol (2010, see also Nowak et al. 1999). Since the frequency resolution of the cross-spectra is $d\nu = 8.35 \times 10^{-6}$ Hz, the $[2-7.5] \times 10^{-4}$ Hz frequency range contains 65 frequency bins, meaning that the lag spectrum is Gaussian distributed and we can therefore fit models using the χ^2

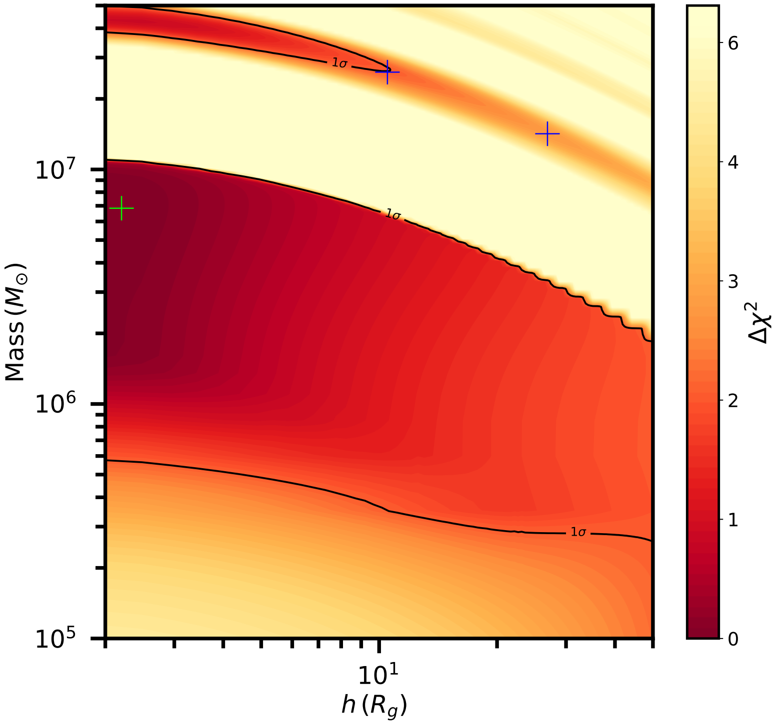

Figure 3.17: 2D χ^2 contour plot of black hole mass and source height resulting from fitting RELTRANS to the lag versus energy spectrum of Mrk 335 in the frequency range $[2-7.5]\times10^{-4}$ Hz. The green cross marks the best fit and the blue crosses mark the best fit for for the two optical reverberation masses.

statistic.

3.5.2 Fits to the lag-energy spectrum

Fig. 3.16 (left) shows the observed lag-energy spectrum of Mrk 335 (black points), which displays the iron K feature at $\sim$ 6.4 keV reported by Kara et al. (2013c)[5], alongside three RELTRANS model fits. A full treatment would employ a simultaneous fit to the time-averaged spectrum, which we will present in a future paper. For the purposes of this demonstration of the use of the model we instead fit only the lag spectrum, and avoid over-fitting by fixing most parameters to values constrained by a previous spectral analysis of these data (Keek & Ballantyne 2016). For the spin, disc inner radius, inclination angle, ionisation parameter, iron abundance, slope

---

[5] Although note that we use a slightly different frequency range, and so our results are consistent but not identical.

of the incident power-law and high energy cut-off, we use $a = 0.89$, r_{in} =ISCO, $i = 30°$, $\log_{10}\xi = 2.68$, $A_{\mathrm{Fe}} = 3.9$, $\Gamma = 1.95$ and $(E_{\mathrm{cut}})_{\mathrm{obs}} = 300$ keV (we assume a constant ionisation parameter for simplicity). Following Kalberla et al. (2005), we fix $N_h = 3.6 \times 10^{20}\,\mathrm{cm}^{-2}$. We use the model configuration that outputs time lags accounting for line-of-sight absorption and the instrument response (`ReIm`=6), and calculates ϕ_A self-consistently (`PHI_SET`=1). The remaining free parameters are black hole mass M, source height h and the boost parameter $1/\mathcal{B}$ (for which we set the hard ranges $> 2\ R_g$ and $0 - 3$ respectively).

The blue solid line represents our best-fitting model, which has parameters $M = 6.8^{+5.5}_{-5.9} \times 10^6 M_\odot$, $h = 2.2^{+34}_{-p}$ and $1/\mathcal{B} = 0.63^{+p}_{-0.48}$ (χ^2/d.o.f. $= 11.3/9$; errors are 1σ), where p indicates that a parameter is pegged at a hard limit. This value of mass is smaller than the optical reverberation measurements in the literature, with the two most recently published values being $M = [14.2 \pm 3.7] \times 10^6\ M_\odot$ (Peterson et al. 2004) and $M = [26 \pm 8] \times 10^6\ M_\odot$ (Grier et al. 2012). Chainakun et al. (2016b) recently also fit an X-ray reverberation model to the same lag spectrum and obtained a best fitting mass of $13.5 \times 10^6\ M_\odot$, albeit with poorly constrained errors due to the computational expense of their model. We investigate this apparent discrepancy by re-fitting our model with the mass fixed to the two optical reverberation values. The red dotted and yellow dashed lines in Fig. 3.16 (left) show the resulting best fits. The $M = 14.2 \times 10^6\ M_\odot$ fit has parameters $h = 26.9$ and $1/\mathcal{B} = 3$ (χ^2/d.o.f. $= 14.4/9$) and the $M = 26 \times 10^6\ M_\odot$ fit has parameters $h = 10.5\,R_g$ and $1/\mathcal{B} = 3$ (χ^2/d.o.f. $= 13.7/9$). We see that these two high mass fits have very similar lag-energy spectra. We note that the iron line feature in our model (and in the model of Chainakun et al. 2016b) is far less prominent than the Gaussian line feature in the empirical model plotted in Fig 8 of Kara et al. (2013c). However our best fitting model, which has one less free parameter than their linear plus Gaussian model, provides a better statistical description of the data (the empirical model has χ^2/d.o.f. $= 13.22/8$).

An F-test reveals that our best-fitting mass is preferred to the Peterson et al. (2004), Grier et al. (2012) and Chainakun et al. (2016b) mass values with only $\lesssim 1.5\ \sigma$ confidence. The reason why very different masses can give such simular χ^2 values is particularly fascinating, and serves to illustrate the importance of fitting to multiple frequency ranges instead of just one. Fig. 3.16 (right) shows the lag averaged over the iron line energy range plotted against frequency for the three models (colours and line styles have the same meaning as in the left hand plot). The grey band denotes the frequency range used for our fits. We see that, averaged over this frequency range, the three models give roughly the same time lag as each other (~ 10 s). However, the two high mass models diverge enormously from our best fitting model at lower frequencies. We see that the high mass models are actually in the phase-wrapping regime in the frequency range used for the fit. This happens when the time lag between the direct and reflected signals is greater than $\pi\nu$ or less than $-\pi\nu$, similar to the effect that leads to car wheels appearing to rotate backwards when viewed on film with a frame rate lower than the rotation frequency of the wheels. Note that the time lag between the two energy bands used for this figure is *not* greater than $\pi\nu$ when phase wrapping starts. This is because of dilution: the time lag between *direct* and *reflected* components is $> \pi\nu$, but both energy bands contain some direct and some reflected X-rays (see the discussion in Uttley et al. 2014). Fig 3.17 is a 2D χ^2 contour plot of black hole mass and source height that illustrates this point further. We see there are two dark stripes corresponding to regions of statistically acceptable mass (plus several lighter stripes in the top right hand corner). The two optical reverberation masses fall in the upper stripe (blue crosses), which therefore corresponds to our phase-wrapped regime. Our best fit falls in the lower stripe (green cross), and the error estimate quoted above of $\pm \sim 6 \times 10^6\ M_\odot$ only considers this lower stripe. We also see an anti-correlation between mass and source height. This occurs because the light-crossing time lag depends on $h \times R_g$, and therefore an increase in h can be offset to some extent by a decrease in M.

At lower frequencies ($\lesssim 10^{-5}$ Hz), the $5.5 - 6.5$ keV reverberation lag for the high mass models is *far* larger than for the low mass model. This is partly due to the larger mass itself (i.e. 1 R_g is a larger distance), and partly because the source height and boost parameter are both much larger in the high mass models (i.e. large h means the path-length difference is a greater number of gravitational radii, and large $1/\mathcal{B}$ means that the reflection fraction is still high even though h is large, thus reducing dilution). This means that, in the frequency range used for the fits, the phase-wrapped time lag in the high mass models is roughly similar to the time lag in the low mass model. The high mass models therefore predict that there should be a negative iron K lag feature at $\nu \sim 10^{-4}$ Hz and a very large positive lag at even lower frequencies, although these features will be heavily diluted by the intrinsic hard lags. Even though the lowest frequencies ($\nu \lesssim 10^{-5}$ Hz) cannot be probed with currently available data, it should be possible to test these predictions in future by fitting a modified version of the model that additionally models hard lags as fluctuations in the photon index for a number of frequency ranges, yielding a robust mass measurement in the process. Of the models we explore here, the low mass model is the more plausible, due to the very high boost parameter (pegged to its hard upper limit) required for the high mass models, although the parameters will likely change once hard lags are accounted for in this frequency range, which is necessary to also reproduce the observed variability amplitude. The results of Chainakun et al. (2016b) instead favour a higher mass, and their model included an ionisation profile and a simultaneous fit to the time-averaged spectrum. However, it is not clear whether or not their best fit was in the phase wrapping regime.

3.6 Discussion

We have presented a public XSPEC reverberation mapping model that can be fit to the energy dependent complex cross-spectrum of black hole X-ray binaries and AGN for a range of Fourier frequencies. It is now common to fit the time-averaged spectrum with sophisticated relativistic reflection models. Our model is designed to be comparably user-friendly to the spectral models, but with the considerable extra functionality of also modelling the timing properties. This provides the opportunity for better geometrical constraints and entirely new black hole mass constraints.

3.6.1 Comparison with previous work

We have compared our model extensively to the existing spectral model RELXILLLP, and find good agreement with the most recent version of that model. We did however find a very minor error in the Bardeen et al. (1972) expression for the Lorentz factor of a rotating disc element, which has propagated into the RELXILLLP model and likely somewhat further into the literature (see Appendix B.1). However, we find the discrepancy is small enough to be inconsequential. Further bench marking against other spectral models (e.g. Dovciak 2004; Wilkins & Fabian 2012) will be very useful.

Previous reverberation mapping modelling studies have mainly focused on AGN time lags (Cackett et al. 2014; Emmanoulopoulos et al. 2014; Chainakun & Young 2015; Caballero-García et al. 2018). Ours is the first public model to also consider variability amplitudes. Our model, similar to most previous studies, uses the lamppost geometry. There has been work to model more sophisticated geometries that self-consistently produce hard intrinsic lags through propagating mass accretion rate fluctuations (Wilkins & Fabian 2013; Wilkins et al. 2016), but these models are too computationally expensive for fitting to data. The two blobs model of Chainakun & Young (2017), consisting of two lamppost sources, allows a slightly more realistic geometry that also can produce hard intrinsic lags but without prohibitive computational expense. Such a geometry can be used in our model, as long as the user fits for real and imaginary parts of the cross-spectrum rather than amplitude and time lags. In this case, two RELTRANS model components with different source heights can simply be added together. Intrinsic lags are then produced if the amplitude and phase normalisations of the two components - $\alpha_1(\nu)$, $\alpha_2(\nu)$, $\phi_{A1}(\nu)$ and $\phi_{A1}(\nu)$ - are left as free parameters. This essentially models a lag between incident emission from the two lamppost sources, as in Chainakun & Young (2017).

3.6.2 ionisation profile

We include a self-consistently calculated radial disc ionisation profile in our model and find that this has a significant effect on the model outputs. There is some uncertainty over the radial disc density profile that should be used to calculate the ionisation profile. Our model considers both a Shakura-Sunyaev zone A (radiation pressure dominated) density profile, and a constant density. Even assuming the Shakura & Sunyaev (1973) model to be exact, we still expect the density profile to depend on mass accretion rate, black hole mass and the viscosity parameter. In particular, the discs of X-ray binaries in faint hard states likely do not have a radiation pressure dominated zone, especially given the weight of evidence for disc truncation in this state (e.g. Tomsick et al. 2009; Ingram et al. 2017). Interestingly though, this implies that there will be a point in the outburst at which the mass accretion rate has risen sufficiently for the inner disc to become radiation pressure dominated, leading to a change in ionisation profile. Perhaps with careful modelling, this may be detectable with high quality data from current observatories such as *NICER* and *NuSTAR*, or future observatories such as *ATHENA*, *STROBE-X* or *Colibrì* (Ray et al. 2019; Caiazzo et al. 2019). Constraining this transition would provide useful insights into disc physics, such as estimating the viscosity parameter in the inner disc. Fitting the cross-spectrum for a wide range of frequencies in addition to the time-averaged spectrum will be far more constraining in this respect than only considering the spectrum.

Although we account for the ionisation profile, we do not account for the dependence of the rest frame reflection spectrum on the density itself (García et al. 2016). We use the public XILLVER and XILLVERCP grids, that are hardwired for $n_e = 10^{15}$ cm^{-3}. This value is more appropriate for the most massive AGN than for X-ray binaries, whose discs are expected to be much denser ($n_e \propto 1/M$, assuming the disc to be radiation pressure dominated and in vertical hydrostatic equilibrium). The main difference is a much higher disc temperature and therefore much more thermal radiation in soft X-rays. The effect of radially stratified density has not yet been explored.

When we generate fake data from a model with a self-consistent ionisation profile and fit with a constant ionisation model, we find that a narrow (non-relativistically smeared) reflection component is required in the fit with high statistical significance (although we note that a more systematic parameter exploration would be required to make strong conclusions). This is interesting because fits to real data commonly require such a narrow reflection component, which can be attributed to a distant reflector (e.g. García et al. 2015; Ingram et al. 2017). This can either take the form of a flared outer disc, the companion star for X-ray binaries, or the torus for AGN. However, the flux of the best-fitting narrow reflection component is often uncomfortably high. Our result suggests that these high fluxes could actually be down to a modelling systematic that could be at least in part alleviated by using an ionisation profile. The timing-properties are also very sensitive to the ionisation profile. Indeed Chainakun et al. (2016b) found that the ~ 3 keV dip present in the lag spectrum of a number of AGN could only be explained by stratification of the disc ionisation parameter. We also note that, whereas a parameter combination can be found to allow a single ionisation model to mimick the time-averaged spectrum produced by a model with self-consistent ionisation, additionally considering the time lags and variability amplitude should break the degeneracy.

We also found from our fits to fake data that a constant ionisation model under-predicts the source height (consistent with the results of Svoboda et al. 2012 and Kammoun et al. 2019). Niedźwiecki et al. (2016) noted two problems associated with the very low source heights measured by many spectral fitting studies of AGN and X-ray binaries (e.g. Parker et al. 2014; Kara et al. 2015; Parker et al. 2015; Degenaar et al. 2015; Beuchert et al. 2017; Wang et al. 2017). First, the resulting surpression of the directly observed flux through gravitational redshift and lensing means that fits to bright sources such as Cygnus X-1 (e.g. Parker et al. 2015; Beuchert et al. 2017) require an intrinsic source flux as high as ~ 50 times the Eddington limit for a hard spectral state. Second, the intrinsic high energy cut-off implied by such a large source redshift is so high that runaway cooling should have long since been triggered by pair production (e.g. Poutanen & Svensson 1996; Fabian et al. 2012). The higher source heights yielded by accounting for a realistic ionisation profile alleviate both of these problems.

3.6.3 Time lags and instrument response

In Section 3.4.1, we show that failing to account for line-of-sight absorption and the instrument response matrix can significantly bias the predicted time lags. This bias is particularly prominent in the $\lesssim 1$ keV energy range of *XMM-Newton* data, but has little to no effect in the $\sim 2-10$ keV range. This may at least partly explain why studies of AGN that model the $\sim 0.3-1$ vs $\sim 1-10$ keV lags (e.g. Emmanoulopoulos et al. 2014) have returned lower source heights than those modeling the $\sim 5-7$ vs $\sim 2-4$ keV lags (Epitropakis et al. 2016). This is because ignoring the telescope response over-predicts the soft band lag for a given source height (see Fig 3.13), and so a very small source height is needed to still produce the fairly small lags present in the data. For frequency ranges in which the intrinsic hard lags are prominent, the response matrix bias can give rise to spurious features in the observed $E \lesssim 1$ keV lag spectrum that look worryingly like the features in X-ray binary data previously attributed to thermal reverberation (e.g. Uttley et al. 2011; De Marco et al. 2017). We conclude that the observation of GX 339$-$4 from De Marco et al. (2017) and Mahmoud et al. (2019) that we investigate does indeed contain a signature of thermal reverberation, but that the measured value of the lag may have been heavily biased by failure to account for the instrument response. Mahmoud et al. (2019) fit a transfer function model to the GX 339-4 data and measure a disc inner radius of $\sim 20\ R_g$. However, their model only accounts for the effective area curve of *XMM-Newton* and not the redistribution matrix. Their inner radius value may therefore be an over-estimate, since the intrinsic lags are likely shorter than what is inferred from their analysis.

3.6.4 Black hole mass

Our proof-of-principle fit to the lag-energy spectrum of Mrk 335 in a single frequency range (Section 3.5) favours a black hole mass of ~ 7 million $M_\odot$ to the optical reverberation values in the literature of ~ 14 million $M_\odot$ (Peterson et al. 2004) and ~ 26 million $M_\odot$ (Grier et al. 2012), and the previous X-ray reverberation value of ~ 13.5 million $M_\odot$ (Chainakun et al. 2016b), although the higher masses are only disfavoured with $\lesssim 1.5\ \sigma$ confidence. The confidence range on the mass is very large for such a fit to a single frequency range, partly because the size of the reverberation lag is degenerate with the reflection fraction. However, our findings here demonstrate very effectively that this degeneracy will be eliminated by a simultaneous fit to multiple frequency ranges, since our best-fitting $M = 6.8 \times 10^6\ M_\odot$ model predicts a wildly different time lag signature at lower frequencies to the two higher mass models that we also explore. For this it will be vital to additionally model the intrinsic hard lags. In fact, we find that intrinsic hard lags are required in order to explain the variability amplitude in addition to the lags even in the frequency range explored here. This may therefore bias the black hole mass yielded by our current analysis. We will conduct a full multi-frequency analysis on the Mrk 335 data in a future paper, also simultaneously considering the variability amplitude and time-averaged spectrum (Mastroserio et al in prep). The resulting constraints on the black hole mass may enable some of the uncertainties associated with optical reverberation mapping to be addressed, most notably the uncertain geometry of the broad line region (typically parameterised by the constant f). We note that the X-ray reverberation analysis of Emmanoulopoulos et al. (2014) returned a black hole mass estimate of $M = 19.8^{+11.8}_{-10.5} \times 10^6\ M_\odot$ for Mrk 335, which is again larger than our value. Their fit procedure was very different to ours and that of Chainakun et al. (2016b). They fit for time lags between two broad energy bands as a function of frequency, and employed simplified assumptions regarding the energy dependence of reflected X-rays.

X-ray reverberation mapping can also be used to measure the mass of stellar-mass black holes in X-ray binary systems. In a companion paper, we constrain the mass of the black hole in Cygnus X-1 (Mastroserio et al submitted). We do however note that care must be taken to avoid frequency ranges dominated by quasi-periodic oscillations, given strong evidence that these are driven by geometric oscillations that are not modelled here (Ingram et al. 2015, 2016).

3.6.5 Future modelling improvements

Our model is still very idealised, and there is much room for future improvement. We will in future extend our model to account for fluctuations in the power-law index of the illuminating spectrum (Mastroserio et al submitted). It will also be useful in future to include a non-zero disc scale height. Taylor & Reynolds (2018a) and Taylor & Reynolds (2018b) show that using the scale height expected for a radiation pressure dominated disc leads to steeper emissivity profiles, with spectral and timing properties consequently adjusted due to the signal being more dominated by the broader line and shorter time lags associated with the inner regions of the disc. Our calculation also assumes that the source is stationary, whereas emission would actually be boosted somewhat away from the disc if the source is actually a standing shock at the base of the outflowing jet, as is often suggested (Markoff et al. 2005; Dauser et al. 2013). We do however include a 'boosting parameter' that approximates this affect by reducing the reflection fraction. If the user takes the lamppost geometry seriously and finds that the boosting parameter is statistically required in the fit to be less than unity, they can conclude that the source is moving away from the disc. Niedźwiecki & Zdziarski (2018) recently pointed out that in a lamppost geometry, we should also sometimes see the other lamppost source on the underside of the disc and we should also see photons from the top lamppost who's trajectories have bent around the black hole and into our line of sight – particularly if the disc is truncated. We do not include these effects, which will presumably be blocked or significantly altered by material inside of the disc.

We use the models XILLVER and XILLVERCP to compute the rest frame reflection spectrum (García & Kallman 2010; García et al. 2013a), which are state-of-the-art, but still include approximations that can be addressed in future. A constant vertical density profile is assumed, which returns a very different $E \lesssim 1$ keV reflection spectrum from a calculation assuming vertical hydrostatic equilibrium (Nayakshin et al. 2000; Done & Nayakshin 2007; Różańska et al. 2011; Vincent et al. 2016). We note, however, that recent numerical simulations indicate that the vertical density profile of a magnetic pressure dominated disc is roughly constant near the surface (Jiang et al. 2019). The largest approximation of all is likely the lamppost model itself, and so it will be important to explore more realistic geometries in future (Zhang et al. 2019).

3.7 Conclusions

The X-ray reverberation models RELTRANS and RELTRANSCP are now publicly available for use in XSPEC. The source code and usage instructions can be downloaded from `https://adingram.bitbucket.io/`. The models can be used to simultaneously fit the real and imaginary parts of the energy-dependent cross-spectrum for a wide range of Fourier frequencies, plus the time-averaged spectrum. Intrinsic hard lags can be accounted for by using two model components added together. The model is designed to be user friendly for the beginner but flexible for the advanced user, with environment variables specifying model properties and advanced options. We find that modelling systematics have likely led to artificially low source heights being measured in the literature. We also find that bright distant reflection component often statistically required in spectral fits can at least partially be explained by the radial profile of the disc ionisation parameter. Our proof-of-principle fits to the lag-energy spectrum of the Seyfert galaxy Mrk 335 return a smaller mass for the central black hole than previous optical reverberation mapping analyses (~ 7 milion compared with $\sim 14 - 26$ million $M_{\odot}$), which we will investigate in more detail in future.

4

An X-ray reverberation mass measurement of Cygnus X-1

Guglielmo Mastroserio, Adam Ingram & Michiel van der Klis

Monthly Notices of the Royal Astronomical Society, 2019, 488, 348-361

Abstract

We present the first X-ray reverberation mass measurement of a stellar-mass black hole. Accreting stellar-mass and supermassive black holes display characteristic spectral features resulting from reprocessing of hard X-rays by the accretion disc, such as an Fe Kα line and a Compton hump. This emission probes of the innermost region of the accretion disc through general relativistic distortions to the line profile. However, these spectral distortions are insensitive to black hole mass, since they depend on disc geometry in units of gravitational radii. Measuring the reverberation lag resulting from the difference in path length between direct and reflected emission calibrates the absolute length of the gravitational radius. We use a relativistic model able to reproduce the behaviour of the lags as a function of energy for a wide range of variability timescales, addressing both the reverberation lags on short timescales and the intrinsic hard lags on longer timescales. We jointly fit the time-averaged spectrum and the real and imaginary parts of the cross-spectrum as a function of energy for a range of Fourier frequencies to *Rossi X-ray Timing Exporer* data from the X-ray binary Cygnus X-1. We also show that introducing a self-consistently calculated radial ionisation profile in the disc improves the fit, but requires us to impose an upper limit on ionisation profile peak to allow a plausible value of the accretion disc density. This limit leads to a mass value more consistent with the existing dynamical measurement.

4.1 Introduction

Black hole X-ray binary systems radiate a large X-ray flux due to accretion of matter from the companion star onto the black hole. When active, these sources display transitions between a hard state, when the hard ($\gtrsim 3$ keV) X-ray flux in the energy spectrum is higher than the soft X-ray flux, and a soft state when the situation is the opposite. The soft emission is dominated by radiation from the accretion disc, which is modelled with a multi-temperature black body (Shakura & Sunyaev 1973). The hard component of the spectrum is due to inverse-Compton emission, most likely coming from a cloud of hot electrons close to the black hole, often referred to as the 'corona' (Thorne & Price 1975). Radiation originating from the corona illuminates the accretion disc, where it is re-processed and then re-emitted. The resulting 'reflection' spectrum includes characteristic features such as a prominent iron Kα fluorescence line at ~ 6.4 keV and a Compton hump peaking at $\sim 20 - 30$ keV (e.g. George & Fabian 1991; Ross & Fabian 2005; García & Kallman 2010; Fabian & Ross 2010). Modelling the observed reflection spectrum provides a powerful tool for measuring the system parameters, because the emission is distorted by the strong gravity and rapid orbital motion of material close to the compact object. Whereas the restframe reflection spectrum depends on properties of the accretion disc such as ionisation state, the gravitational distortions depend strongly on geometrical parameters such as the disc inner radius and inclination angle. Time-averaged spectral analysis alone, however, is not at all sensitive to black hole mass, because the gravitational distortions depend on distances in units of gravitational radii ($R_g = GM/c^2$).

Besides the long term variability characterizing the state changes, accreting stellar mass black holes show rapid variability in the range of milliseconds to tens of seconds. Since the rays that reaches us via reflection follow a longer path length than those we observe directly, fluctuations in the inverse-Compton emission should be followed after a light-crossing delay by similar fluctuations in the reflected emission. The reflection signal is not only lagged with respect to the direct signal, but also smeared such that the fastest variability is washed out. This is because reflection from different parts of the disc is associated with different path lengths, such that a very short flash of X-rays from the corona would result in an extended flare of reflected emission. Whereas the spectral distortions depend on distances in mass scaled units, the reverberation lag between direct and reflected emission depends on distances in absolute units. Therefore measurement of a reverberation lag can calibrate the length of the gravitational radius for a system, providing a way to measure black hole mass (Stella 1990) that is orthogonal to other methods (e.g. Casares & Jonker 2014, and references therein).

A combined spectral and timing analysis can be achieved by calculating cross spectra between light curves in different energy bands (e.g. van der Klis et al. 1987; Nowak et al. 1999). This can be used to calculate time lag vs energy spectra for different timescale ranges (Mastroserio et al. 2018). The lag spectrum of long timescale variability (i.e. Fourier frequencies $\nu \lesssim 300 M_{\odot}/M$ Hz) is observed both in X-ray binaries and active galactic nuclei (AGN) to be featureless, with hard photons lagging soft photons (Miyamoto et al. 1988; Nowak et al. 1999; Papadakis et al. 2001; McHardy et al. 2004). These hard lags, which are far larger than the expected reverberation lags, are likely due to spectral variability of the directly observed coronal emission and they have been attributed to propagating mass accretion rate fluctuations in the accretion flow (Lyubarskii 1997; Kotov et al. 2001; Arévalo & Uttley 2006; Ingram & van der Klis 2013). In models considering an extended corona, fluctuations propagate from the soft X-ray emitting region further from the black hole to the hard X-ray emitting region closer to the black hole, giving rise to the hard lags. In alternative models considering a compact corona, propagating fluctuations in the disc instead cause variable heating and cooling of the corona, leading to hard lags driven by spectral pivoting of the inverse-Compton spectrum (Uttley & Malzac in prep). The propagating fluctuations mechanism has successfully explained the spectral-timing properties of a number of black hole X-ray binaries (Kotov et al. 2001), although questions remain (Rapisarda et al. 2016, 2017b; Veledina 2018).

The magnitude of the hard lags is observed to reduce with Fourier frequency, offering the possibility to detect reverberation signatures at high frequencies ($\nu \gtrsim 300 M_{\odot}/M$ Hz). Such signatures were first detected for AGN, first in the form of soft reflected X-rays lagging hard directly observed X-rays (Fabian et al. 2009) and later in the form of an iron Kα feature in the lag-energy spectrum (Zoghbi et al. 2011; Kara et al. 2016). Although alternative models have been proposed for the soft lags (e.g. Miller et al. 2010; Mizumoto et al. 2018), the iron K feature seems to provide clear evidence of reverberation. Detection of reverberation signatures has been more challenging in the case of Galactic black hole systems, owing to the much shorter associated light-crossing timescale. Soft lags attributed to thermally reprocessed photons lagging directly observed hard photons (thermal reverberation) were the first signature to be observed (Uttley et al. 2011; De Marco et al. 2015). Recently, Kara et al. (2019) reported on the first significant detection of iron Kα lags, using *NICER* data from MAXI J1820+070.

Still further information is contained in the frequency and energy dependent correlated variability amplitude, which can also be measured using the cross-spectrum. Modelling this in addition to the time-averaged spectrum and the frequency dependent lag energy spectrum can yield a better constraint on black hole mass. However, in order to probe the frequency dependence of the reverberation lags, we must additionally take account of the hard lags. In Mastroserio et al. (2018) we developed a formalism to model what we termed the *complex covariance* over a wide range of Fourier frequencies. We represented the observed hard lags in the coronal emission by a time dependent perturbation in the illuminating spectrum, and then self-consistently calculated the reverberation lags using a transfer function formalism (e.g. Reynolds et al. 1999; Wilkins & Fabian 2013). The formalism provides a solid mathematical framework to address the non-linear effects in the reverberation introduced by spectral changes in the coronal emission.

However, the analysis we presented in Mastroserio et al. (2018) did not include the effect of gravitational light bending, even though our best fitting model featured emission from very close to the black hole. In Ingram et al. (2019) we address this by incorporating a fully general-relativistic ray-tracing calculation for the transfer function, but without considering the non-linear effects. Here, for the first time, we include both the non-linear effects and general relativistic effects. We apply our model to *RXTE* data from Cygnus X-1 in order to place constraints on the mass of the central black hole. We explore a number of different assumptions for the radial dependence of the disc ionisation parameter, and find that the mass measurement is sensitive to which assumption we make.

In Section 4.2 we discuss how the non-linear effects of the complex covariance model are affected by the light bending calculation. In Section 4.3 we describe the data and in Section 4.4 we present the fits to the time averaged spectrum using models with three different ionisation profiles of the accretion disc. In Section 4.5 we perform joint fits to the complex covariance in 10 different frequency ranges and the time averaged spectrum. In Section 4.6 we discuss our results.

4.2 The non-linear model

We model the X-ray corona as a stationary point source located on the disc rotation axis at height h above the black hole (the lamppost model) and the disc as flat and geometrically thin, with its angular momentum axis aligned with the spin axis of the black hole. We consider two components of the X-ray spectrum. The first is the directly observed radiation from the point source (‘continuum’) and the second is radiation that has been re-processed and re-emitted by the disc before reaching the observer (‘reflection’). Both of these spectral components are distorted by the strong gravitational field in the vicinity of the black hole. We calculate the time-dependent energy spectrum observed by a distant observer by starting with the equations presented in Ingram et al. (2019) and introducing non-linear effects due to fluctuations in the slope of the continuum spectrum. In the following sub-sections we study the two components separately before combining them to provide an expression for the total radiation seen by the distant observer.

4.2.1 Direct Emission

We choose an exponentially cut-off power-law function to reproduce the shape of the inverse-Compton emission from the corona. Following Ingram et al. (2019) the directly observed specific flux seen by the distant observer is

$$F_o\left(E_o, t\right) = A(t')\, l\, g_{so}^{\Gamma-\beta\left(t'\right)} E_o^{1-\Gamma+\beta\left(t'\right)} e^{-E_o/(g_{so}E_{cut})} \tag{4.1}$$

where A is the normalisation, Γ and E_{cut} are respectively the power-law index and the high energy cut-off (the latter is related to the temperature of the corona) and l is the lensing factor due to light bending (see Ingram et al 2019, equation 10). $g_{so} = E_o/E_s$ is the blueshift experienced by photons travelling from the source to the observer, E_o and E_s are photon energy measured respectively in the observer and source restframe. Here, we have introduced fluctuations in the slope of the spectrum through the function $\beta(t)$, which depends on the time taken for the photons to travel from the source to the observer, τ_{so}, as $t' = t - \tau_{so}$. Eq. 4.1 is non-linear in time, though we can linearise the expression by Taylor expanding to the first order around $\beta = 0$ (see for details Mastroserio et al. 2018). The observed specific flux becomes

$$\begin{aligned} F_o\left(E_o, t\right) \approx\ & l\, g_{so}^{\Gamma} E_o^{1-\Gamma} e^{-E_o/(g_{so}E_{cut})} \\ & \left[A\left(t'\right) + B\left(t'\right)\left(\ln E_o - \ln g_{so}\right)\right] \end{aligned} \tag{4.2}$$

where we have defined $B(t) = A(t)\beta(t)$. For brevity let us define $D(E) = l\, g_{so}^{\Gamma} E^{1-\Gamma} e^{-E/(g_{so}E_{cut})}$.

4.2.2 Re-processed emission

Some of the photons emitted from the corona illuminate the accretion disc. They are re-processed and radiated an-isotropically. Again following Ingram et al. (2019) we can derive the expression for the reflected specific flux seen by the distant observer emitted from a patch of the disc which subtends a solid angle $d\Omega_d$ in the source restframe and has a surface area dA_d in its own rest frame. A disc patch with coordinates (r, ϕ) subtends a solid angle on the observer plane of $d\Omega = d\alpha_0\, d\beta_0/D^2$ where α_0 and β_0 are the impact parameters at infinity (Luminet 1979). The reflected flux from the disc patch is then

$$\begin{aligned} dR_o\left(E_o, t|\mu_e, r, \phi\right) = & A\left(t''\right) g_{do}^3 \epsilon(r, t'') \times \\ & \mathcal{R}\left(\frac{E_o}{g_{do}}|\Gamma - \beta(t''), g_{sd}E_{cut}\right) d\alpha_0\, d\beta_0 \end{aligned} \tag{4.3}$$

where

$$\epsilon(r, t) = \frac{g_{sd}^{\Gamma-\beta(t)}}{4\pi} \frac{d\Omega_d}{dA_d}. \tag{4.4}$$

is the radial emissivity profile and the two factors $g_{sd}(r)$ and $g_{do}(r, \phi)$ represent the blue-shift of the photons travelling from the source to the disc and from the disc to the observer respectively. $\mathcal{R}$ is the restframe reflection spectrum which depends on the incident radiation, μ_e is the cosine of the angle between the disc normal and the emergent trajectory of the reflected rays from the plane of the disc and β depends on the time taken from the photons to travel from the source to the disc, τ, as $t'' = t - \tau$. Note that oscillations in the illuminating power-law slope introduce non-linear effects in the emissivity profile *and* in the restframe reflection spectrum. We can again linearise Eq. 4.3 by Taylor expanding around $\beta = 0$:

$$dR(E,t) \approx dR(E|\beta=0) + \beta(t)\frac{\partial(dR)}{\partial\beta}(E|\beta=0). \tag{4.5}$$

Considering $\partial\mathcal{R}/\partial\beta = -\partial\mathcal{R}/\partial\Gamma$, Eq. 4.3 becomes

$$\begin{aligned} dR_o\left(E_o,t|r,\phi\right) = g_{do}^3\epsilon(r,\beta=0)\Bigg[& A\left(t-\tau\right)\mathcal{R}\left(\frac{E_o}{g_{do}}|\beta=0\right) \\ & -B\left(t-\tau\right)\mathcal{R}\left(\frac{E_o}{g_{do}}|\beta=0\right)\ln g_{sd} \\ & -B\left(t-\tau\right)\frac{\partial\mathcal{R}}{\partial\Gamma}\left(\frac{E_o}{g_{do}}|\beta=0\right)\Bigg]d\alpha_0\,d\beta_0. \end{aligned} \tag{4.6}$$

Here, we have left some dependencies implicit for brevity, such as the r and ϕ dependence of g_{do} and τ, and the dependence of $\mathcal{R}$ on the cosine of the emission angle, μ_e. Integrating Eq. 4.6 over all impact parameters corresponding to geodesic paths that intersect the accretion disc, we calculate the total reflection spectrum seen by the distant observer.

4.2.3 Total Emission

The total emission crossing the distant observer is simply the sum of the direct emission from the source and the re-processed emission from the disc. To use the transfer function formalism, we express the emission as a sum of convolutions. The total specific flux is

$$\begin{aligned} S(E_o,t) = D(E_o)\left[A(t') + B(t')\ln(E_o/g_{so}))\right] + \\ A(t')\otimes w_0(E_o,t'') - B(t')\otimes\left[w_1(E_o,t'') + w_2(E_o,t'')\right] \end{aligned} \tag{4.7}$$

where w_0, w_1 and w_2 are the three response functions associated with the three terms on the right hand side of Eq. 4.6 (see Appendix C.1 for the explicit expressions) and $\otimes$ denotes a convolution.

In the Fourier domain convolutions correspond to multiplications. The Fourier transform of the total observed specific flux is therefore

$$\begin{aligned} S(E_o,\nu) = A(\nu)\Big[D(E_o) + W_0(E_o,\nu)\Big] + \\ B(\nu)\left[D(E_o)\ln\left(\frac{E_o}{g_{so}}\right) - W_1(E_o,\nu) - W_2(E_o,\nu)\right] \end{aligned} \tag{4.8}$$

where W_0, W_1 and W_2 are the transfer functions (see Appendix C.1), which are the Fourier transforms of the response functions. Following Mastroserio et al. (2018), we calculate the complex covariance in order to fit not only to the time-average energy spectrum but also to the lags and covariance amplitude as a function of energy for different Fourier frequencies. Since this exploits more information in the signal than time-averaged spectroscopy alone, it enables better constraints of the system parameters. The model complex covariance is then $G(E_o,\nu) = S(E_o,\nu)\, e^{-i\phi_r(\nu)}$, where $\phi_r(\nu)$ is the phase of the reference band in our model. The complex covariance is therefore the cross-spectrum divided through by the modulus of the reference band. Following the notation of Mastroserio et al. (2018), this gives

$$\begin{aligned} G(E_o,\nu) = \alpha(\nu) \Bigg[& e^{i\phi_A(\nu)} D(E_o) + \gamma(\nu) e^{i\phi_B(\nu)} \ln\left(\frac{E_o}{g_{so}}\right) D(E_o) + \\ & e^{i\phi_A(\nu)} W_o(E_o,\nu) - e^{i\phi_B(\nu)} W_1(E_o,\nu) - e^{i\phi_B(\nu)} W_2(E_o,\nu) \Bigg], \end{aligned} \tag{4.9}$$

where $\gamma(\nu)$ is the relative amplitude $|B(\nu)|/|A(\nu)|$ and the phase of the reference band, $\phi_r(\nu)$, is swallowed up in the definitions of the phases $\phi_A(\nu)$ and $\phi_B(\nu)$, which are left as model parameters for a given frequency range, as are $\alpha(\nu)$ and $\gamma(\nu)$. This expression contains the non-linear effects considered in Mastroserio et al. (2018) and additionally all GR effects, as in Ingram et al (2019).

4.3 Data

As in Mastroserio et al. (2018), we consider archival *RXTE* observations of Cygnus X-1 from the proposal number P10238. We stack together the final five of the seven observations in this data set[1], since their spectra are very similar to one another in shape. We discard the first two observations because their spectra are clearly different to the rest. The total exposure is 56.2 ks for the time-average energy spectrum and 46.6 ks for the complex covariance. The difference in exposure time results from data discarded when selecting segments of contiguous data in order to perform ensemble averaging. It is worth mentioning this data set has been extensively used in the past (e.g. Revnivtsev et al. 1999; Kotov et al. 2001), and even recently (e.g. Mahmoud & Done 2018b), because it has high count rates, excellent timing resolution and adequate energy resolution.

Using only Proportional Counter Array (PCA) data, we extract a 2.84 - 3.74 keV reference band light curve and 28 'subject band' light curves in the energy range $4-20$ keV using the exact procedure described in Mastroserio et al. (2018). As in our previous work (Mastroserio et al. 2018), we calculate the cross-spectra between

---

[1] Observation IDs: 10238-01-06-00, 10238-01-07-00, 10238-01-07-000, 10238-01-08-00, 10238-01-08-000.

each subject band light curve and the reference band light curve, employing ensemble averaging as well as averaging over broad frequency ranges. We calculate the complex covariance by dividing the averaged cross-spectrum by the square root of the reference band (Poisson noise subtracted) power spectrum. The complex covariance is a complex quantity as a function of energy and frequency. Its modulus is related to the variability amplitude of the signal through the coherence (Vaughan & Nowak 1997) which we assume to be close to unity (Nowak et al. 1999). We use XSPEC version 12.10 (Arnaud 1996) to fit our model RELTRANS (Ingram et al 2019), modified from the publicly available version to additionally account for non-linear effects, simultaneously to the real and imaginary parts of the observed complex covariance for 10 frequency ranges and to the time-averaged spectrum. We add 0.1% systematics only to the time-average energy spectrum. Considering real and imaginary parts of the complex covariance instead of amplitude and phase allows us to extract the same information from the data and has many advantages, such as easily accounting for the telescope response within XSPEC (Mastroserio et al. 2018; Ingram et al 2019).

4.4 Fit to the time-averaged Spectrum

We start by fitting our model RELTRANS to the time-averaged spectrum alone. Line-of-sight absorption is accounted for within the RELTRANS model using the XSPEC intrinsic model TBABS. We assume the abundances of Wilms et al. (2000) throughout our analysis. We explore three different assumptions regarding the disc ionisation state within the RELTRANS model, which are described in the following sub-section.

4.4.1 Models

RELTRANS self-consistently calculates the normalisation of the reflected component of the observed spectrum relative to the direct component assuming a stationary lamppost source. Since in reality the source may be neither stationary nor point-like, the relative normalisation used in the model is equal to the self-consistently calculated value multiplied by the model parameter $1/\mathcal{B}$. Setting this boost parameter $1/\mathcal{B}$ to greater than (less than) unity mimics the effect of plasma moving towards (away) from the disc. The shape of the observed reflection spectrum can additionally be influenced by the spin of the black hole (Martocchia et al. 2000). We note that the model is computationally not very sensitive to the actual spin value (see also Dauser et al. 2013) and the leading order effect of the spin is to modify the innermost stable orbit (ISCO) of the accretion disc. In order to probe the full extent of the disc we fix the spin parameter to 0.998 throughout and allow r_{in} to be a free parameter.

The restframe spectrum, calculated using the model XILLVER (García & Kallman 2010; García et al. 2013a), depends on the disc ionisation parameter $\xi = 4\pi F_x/n_e$, where F_x is the 13.6 eV to 13.6 keV illuminating flux and n_e is the electron density

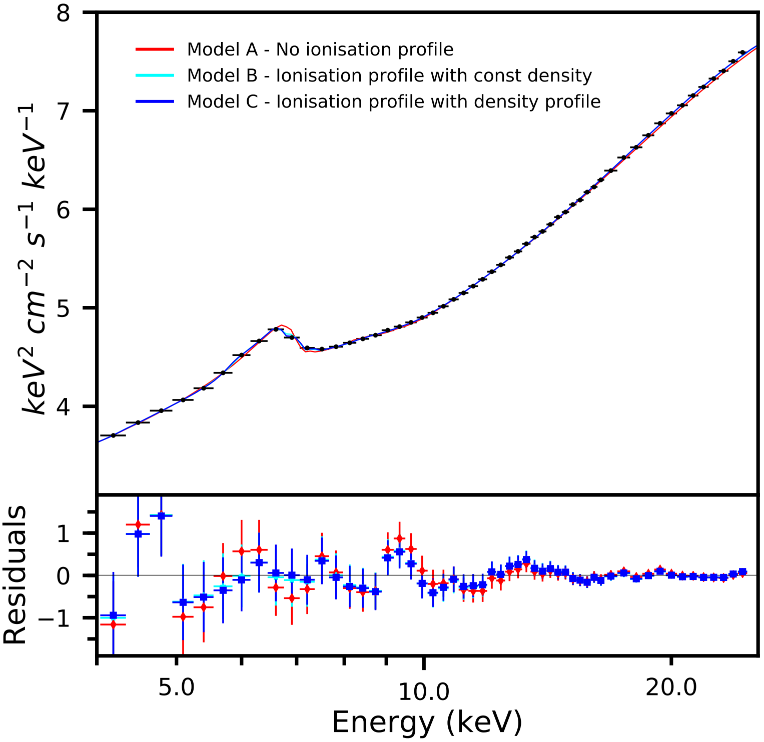

Figure 4.1: Unfolded spectrum (upper panel) and residuals (lower panel) of the time averaged energy spectrum fit. The three colours represent different models explained in the text (the data points are unfolded around the best fitting model C). 0.1% systematics have been added to the spectrum. A fit with no systematics added produces the same parameter values and residual shape.

of the disc (which is assumed to be vertically constant for the XILLVER calculation). This parameter sets the upper boundary condition of the XILLVER calculation for the vertical temperature and ionisation balance in the disc upper atmosphere. In most spectral studies, ξ is assumed to be constant over the entire disc extent. However, our model introduces an ionisation profile as a function of radius (following Svoboda et al. 2012; Chainakun et al. 2016a; Kammoun et al. 2019). Numerically, this involves discretizing the calculation into a number of ionisation zones. Throughout this paper we use 10 ionisation zones, which is found to provide adequate resolution (Ingram et al 2019).

We consider three different ionisation profiles. Model A uses the same ionisation parameter for the entire disc. This model is identical to the model RELXILLLP (Dauser et al. 2013; García et al. 2014; Ingram et al 2019). Model B uses an ionisation profile determined by self-consistently calculating $F_x(r)$ in the lamppost geometry and assuming n_e = constant (as in Svoboda et al. 2012). Model C again uses the

Table 4.1: Best fitting parameters obtained from fitting to the time-averaged energy spectrum with three different models. The models differ in the ionisation profile: Model A has a constant ionisation in the entire disc, Model B has a monotonic ionisation profile peaking at inner radius of the disc and Model C has a ionisation profile calculated assuming a density profile in the disc given by equation (4.10). The spin value is fixed to 0.998. Errors are all 90% confidence. Note that while we quote the observed high energy cut-off ($E_{\mathrm{cut,o}}$), the cut-off in the source restframe is $E_{\mathrm{cut}} = E_{\mathrm{cut,o}}/g_{so}$.

	$N_{\mathrm{H}}\ \left(10^{22}\ \mathrm{cm}^{-2}\right)$	$h\,(R_g)$	Incl (deg)	$r_{\mathrm{in}}\,(R_g)$	Γ
A)	$0.7^{+0.1}_{-0.1}$	$12.3^{+3.4}_{-5.0}$	$30.1^{+1.8}_{-2.1}$	$5.07^{+2.35}_{-(b)}$	$1.70^{+0.01}_{-0.02}$
B)	$0.9^{+?(c)}_{-0.2}$	$15.5^{+2.6}_{-1.8}$	$31.1^{+2.9}_{-3.1}$	$3.1^{+0.9}_{-1.2}$	$1.68^{+0.04}_{-0.04}$
C)	$0.9^{+?(c)}_{-0.3}$	$16.5^{+2.4}_{-4.7}$	$32.1^{+2.6}_{-2.5}$	$4.8^{+0.9}_{-0.5}$	$1.69^{+0.01}_{-0.02}$

	$\log\xi^{(a)}$	A_{Fe}	$E_{\mathrm{cut,o}}$ (keV)	$1/\mathcal{B}$	red χ^2
A)	$3.02^{+0.02}_{-0.02}$	$1.9^{+0.3}_{-0.2}$	774^{+156}_{-237}	$0.3^{+0.02}_{-0.02}$	46.67/44
B)	$4.7^{+0.5}_{-0.4}$	$1.6^{+0.5}_{-0.2}$	468^{+122}_{-41}	$0.45^{+0.02}_{-0.02}$	43.52/44
C)	$3.9^{+0.1}_{-0.6}$	$1.52^{+0.05}_{-0.22}$	431^{+49}_{-49}	$0.45^{+0.03}_{-0.02}$	41.37/44

[a] In Model B and C the parameter is the peak value of the ionisation profile.

[b] The lower bound is unconstrained.

[c] The uper bound is unconstrained.

same self-consistent calculation of $F_x(r)$, but assumes the following density profile

$$n_e \propto r^{3/2}\left[1-\left(\frac{r_{in}}{r}\right)^{1/2}\right]^{-2}. \tag{4.10}$$

This corresponds to zone A of a Shakura & Sunyaev (1973) accretion disc (where the pressure is dominated by radiation and the opacity is dominated by electron scattering; see in particular their Eq. 2.11), and assumes zero torque at the inner disc boundary. The ionisation profile in Model C is therefore not a monotonic function of radius: it has a maximum located a few R_g outside R_{in} (see Ingram et al. 2019). In all cases, we leave the normalisation of the ionisation profile as a free parameter in the fit.

4.4.2 Results

Figure 4.1 shows the all three models and the data points unfolded around the Model C best fit. The residuals, which are defined as the observed counts minus the folded model, shown in the lower panel are slightly larger in the case of Model A, and the χ^2 value for this model is correspondingly higher (see Table 4.1). Table 4.1 lists the best fitting parameter values for the different configurations of the model. We report all the parameter values in this paper with errors at 90% confidence.

For all three models, we measure an inclination similar to that inferred for the binary system (Orosz et al. 2011). The inner radius is close to the ISCO but it is found not to be pegged to it, as was the case for our previous work on Cygnus X-1 (Mastroserio et al. 2018). For Model A, we were not able to constrain a 90% confidence lower bound, while in the other two models r_{in} is well defined. In contrast with RELTRANS fits to the time-averaged spectrum of GRS 1915+105 (Shreeram & Ingram 2019), we do not find that including an ionisation profile systematically increases the best fitting value of r_{in}. The ionisation value reported in Table 4.1 is the *peak* ionisation value in the disc for the case of Models B and C, and thus the value presented in the table is much higher for these two models than for Model A. The relative iron abundance is mildly super-solar for all three models.

All three models have formally acceptable χ^2 values, although it is encouraging that the configurations featuring the more physical assumption of non-constant radial ionisation profile (Model B and C) have the lowest χ^2 values. All three fits are also similar in terms of residual systematics (Fig. 4.1), making it difficult to distinguish between them. We note that some parameters are nearly degenerate, for example, the absorption column density (N_h) and the high energy cut-off (E_{cut}), and the height of the point source (h) and the inner radius (r_{in}) are correlated in the fit.

4.5 Reverberation mapping and mass measurement

We now conduct joint fits, simultaneously considering the real and imaginary parts of the complex covariance across 10 frequency ranges and the time-averaged spectrum. We follow the approach of Mastroserio et al. (2018), except now we consider a broader range of frequencies (0.1 mHz to 32 Hz) and leave the black hole mass as a free model parameter in the fits. Fig. 4.2 shows the χ^2 curves of the mass for five different configurations of the model (described below). It is worth noting that all the curves constrain the mass to be between 5 and 50 $M_{\odot}$, which is reasonable for Cygnus X-1 (all the curves stop at 3σ likelihood). The shape of the curves demonstrates that the method can constrain the mass of the compact object even with archival *RXTE* data. The grey area in Fig. 4.2 represents the 3σ confidence interval of the existing dynamical mass measurement (Orosz et al. 2011). We see that all the curves intersect the grey box. All the configurations are described in the following subsections and the model parameters are listed in Table 4.2.

4.5.1 Model 1: constant ionisation profile

The first configuration has a constant ionisation profile (the same as Model A in the previous section). The hydrogen column density has a very low value compared to what was used in other works (Gilfanov et al. 2000; Tomsick et al. 2014) and its lower limit is not constrained by the fit, which is also the case for the disc inner radius.

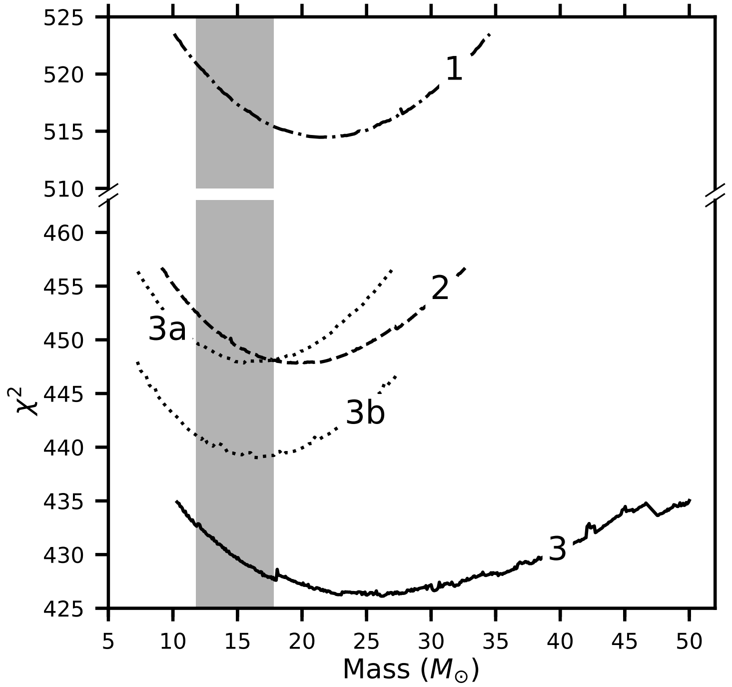

Figure 4.2: Chi-squared curves of black hole mass calculated for different assumptions on the degree of ionisation of the disc as a function of radius. The shaded region represents the 3σ confidence interval of the existing dynamical mass measurement.

Although the mass is formally compatible with the dynamical measurement, it is larger than the expected value.

4.5.2 Model 2: ionisation profile calculated assuming constant density

The second configuration calculates $\xi(r)$ assuming constant disc density (the same as Model B in the previous section), and the peak value of $\xi(r)$ is set as a free model parameter. In this configuration, $\xi(r)$ always peaks at r_{in}, and the ionisation value there indicates that the plasma is approximately fully ionised (complete ionisation occurs at $\log_{10}\xi \approx 4.7$). However, further out the ionisation decreases, so there is still a weak iron $K\alpha$ line feature in the XILLVER spectrum for $\log_{10}\xi = 4.5$, and the inner radius is still constrained by the overall shape of the iron line. The χ^2 is lower than for Model 1 and the mass is slightly closer to the dynamical value

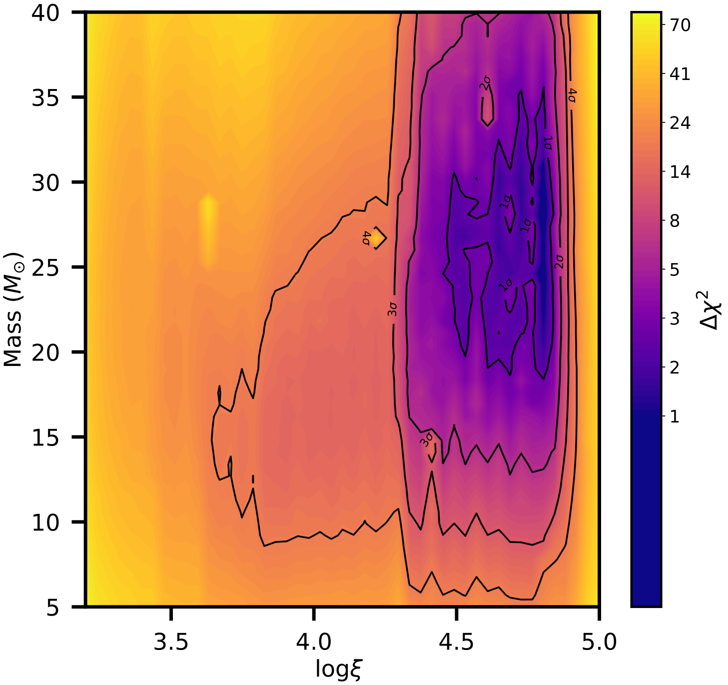

Figure 4.3: $\Delta\chi^2$ 2D contour plot between the black hole mass and the peak ionisation parameter. The ionisation profile is the one used in Model 3. The colour scale indicates the relative increase of χ^2 compared with the best fit of Model 3. The 4 black lines are the sigma contours corresponding to 2 degrees of freedom ($\Delta\chi^2 = 2.3$, 6.18, 11.83 and 19.33, corresponding to 1, 2, 3 and 4 σ).

4.5.3 Model 3: ionisation profile calculated assuming zone A density profile

The third configuration calculates $\xi(r)$ assuming that the electron density depends on radius following equation (4.10), which is appropriate for zone A of a Shakura & Sunyaev disc. The peak value of $\xi(r)$ is again a free model parameter, and the best-fitting value is again very high, but this peak is now at $r > r_{in}$ because the disc density becomes very high approaching r_{in} due to the boundary condition in Eq. 4.10. This model has the lowest χ^2 value, but the 90% lower bound of the best fitting mass is higher than the 90% upper bound of the dynamical measurement.

4.5.4 Model 3a and 3b: ionisation profile calculated assuming zone A density profile, peak ionisation parameter bounded

The very high peak values of the best fitting ionisation parameter for the previous two models may be implausible. Since we know the distance to Cygnus X-1, we can use the observed continuum flux and a reasonable estimate for the disc electron density in order to place the following upper limit on the ionisation parameter (see Appendix C.2 for a derivation)

$$\xi(r) = 5.77 \times 10^3 \text{ erg cm s}^{-1} \left(\frac{[1/\mathcal{B}]}{0.28}\right) \left(\frac{\epsilon(r) g_{sd}^{2-\Gamma}(r) g_{so}^{\Gamma-2}}{0.0014}\right)$$

$$\left(\frac{\mathcal{F}}{1.7 \times 10^3 \; keV cm^{-2}\mathrm{s}^{-1}}\right) \left(\frac{D}{2.5\mathrm{kpc}}\right)^2 \left(\frac{4 \times 10^{20}\mathrm{cm}^{-3}}{n_e}\right) \left(\frac{10 M_\odot}{M}\right)^2 . \qquad (4.11)$$

Here, $\mathcal{F}$ is the integral from 13.6 eV to 13.6 keV of the source flux (in the source rest frame) in our model (see Appendix C.2 for the exact definition). The values quoted in brackets are chosen as reasonable limits of each term that maximize $\xi(r)$. The first three terms on the right hand side of Eq. 4.11 can be derived directly from our fits. The values we use for these terms are derived from the Model 1 fit (which maximizes the estimate of $\xi(r)$, mostly due to the low source height). We estimate an upper limit for the distance to Cygnus X-1 from the *Gaia* second data release (2.17 ± 0.12 kpc; Gandhi et al. 2019). This is higher than the radio parallax distance of $1.86^{+0.12}_{-0.11}$ kpc (Reid et al. 2011). We choose the *Gaia* distance in order to get an upper limit. We consider a conservative lower limit for the mass of $10 M_\odot$. For our estimated lower limit of the electron density, we use the value of $\sim 4 \times 10^{20} cm^{-3}$ measured by Tomsick et al. (2018), which is lower than analytic estimates from disc theory (Svensson & Zdziarski 1994; García et al. 2016). We can therefore derive from Eq. 4.11 the highest physical upper limit on the peak ionisation parameter $\log_{10} \xi_{\max}$ of ≈ 3.76, implying that the best fitting values of this parameter for Models 2 and 3 are implausibly high. We therefore define Model 3a, which applies the same assumptions as Model 3 except now we set a sensible upper limit on $\log \xi_{\max}$ of 3.5. Although the minimum χ^2 for this new model is higher than for Model 3 (Fig. 4.2), the new model is more physical. It returns a mass value closer to the existing dynamical measurement. Finally, we define Model 3b, in which we relax the upper limit on the peak ionisation parameter to $\log \xi_{\max} \leq 4$. As expected, the χ^2 value is lower than for Model 3a and the best fitting mass increases slightly.

Fig. 4.3 shows the correlation between black hole mass and peak ionisation parameter in more detail in the form of a 2D χ^2 contour plot for Model 3. In line with Fig. 4.2, we see that the minimum χ^2 value corresponds to a very high ionisation and a black hole mass of $\sim 25 M_\odot$. For lower (more realistic) values of peak ionisation, a lower mass ($\sim 15 M_\odot$) is preferred. Very low peak ionisation values are strongly ruled out.

Table 4.2: Best fitting parameters obtained from our simultaneous fit to the complex covariance in 10 frequency ranges ($0.98mHz - 32$ Hz) and the time-average spectrum. The spin value is fixed to 0.998. The models listed in the table have different ionisation profiles. Model 1 has a constant ionisation profile and ξ is the ionisation value throughout the disc. Model 2 has an ionisation profile calculated assuming constant density and self-consistently calculated illuminating flux. Model 3 has an ionisation profile calculated assuming a 'Zone A' density profile and self-consistently calculated illuminating flux. Models 3a and 3b have the same ionisation profile as Model 3, except the peak ionisation is pegged to an upper limit of 3.5 and 4.0 respectively. Errors are all 90% confidence. Note that while we quote the observed high energy cut-off ($E_{\mathrm{cut,o}}$), the cut-off in the source restframe is $E_{\mathrm{cut}} = E_{\mathrm{cut,obs}}/g_{so}$.

	N_{H} $(10^{22}\mathrm{cm}^{-2})$	h (R_g)	Incl (deg)	r_{in} (R_g)	Γ	$\log\xi^{(a)}$	A_{Fe}	$E_{\mathrm{cut,o}}$ (keV)	Boost	Mass	red χ^2
1)	$0.13^{+0.08}_{-?(b)}$	$6.2^{+0.6}_{-0.8}$	$32.4^{+0.6}_{-1.0}$	$1.8^{+0.4}_{-(c)}$	$1.60^{+0.01}_{-0.01}$	$3.08^{+0.02}_{-0.01}$	$3.7^{+0.1}_{-0.1}$	218^{+13}_{-9}	$0.28^{+0.01}_{-0.01}$	$21.6^{+6.8}_{-6.6}$	515/563
2)	$0.7^{+0.2}_{-0.1}$	$9.7^{+1.9}_{-1.4}$	$33.8^{+1.4}_{-1.5}$	$2.2^{+0.9}_{-1.0}$	$1.65^{+0.02}_{-0.02}$	$4.5^{+0.6}_{-0.7}$	$2.0^{+0.4}_{-0.2}$	371^{+55}_{-63}	$0.50^{+0.05}_{-0.04}$	$19.7^{+5.3}_{-5.4}$	448/563
3)	$0.6^{+0.1}_{-0.1}$	$9.0^{+1.4}_{-1.7}$	$35.0^{+1.2}_{-1.2}$	$1.3^{+0.7}_{-(c)}$	$1.67^{+0.01}_{-0.01}$	$4.7^{+0.7}_{-0.6}$	$1.7^{+0.2}_{-0.3}$	712^{+82}_{-97}	$1.1^{+0.2}_{-0.1}$	$26.0^{+9.6}_{-8.6}$	426/563
3a)	$0.79^{+0.04}_{-0.10}$	$9.5^{+2.7}_{-3.9}$	$35.1^{+1.4}_{-1.0}$	$5.9^{+0.7}_{-0.7}$	$1.67^{+0.01}_{-0.02}$	$3.5^{(d)}$	$1.8^{+0.2}_{-0.1}$	377^{+36}_{-36}	$0.46^{+0.02}_{-0.03}$	$16.5^{+5.0}_{-5.0}$	447/563
3b)	$0.75^{+0.09}_{-0.24}$	$10.8^{+1.9}_{-1.2}$	$35.0^{+0.8}_{-1.8}$	$3.1^{+0.4}_{-0.4}$	$1.66^{+0.02}_{-0.02}$	$4.0^{(d)}$	$1.7^{+0.5}_{-0.3}$	355^{+54}_{-96}	$0.60^{+0.04}_{-0.03}$	$16.5^{+6.1}_{-5.2}$	439/563

[a] Besides Model 1 the parameter is the peak value of the ionisation profile.

[b] The lower limit of the hydrogen column density is not constrained below 0.2

[c] The lower limit of the inner radius is the ISCO ($1.237\,R_g$).

[d] The ionisation peak is pegged to the upper limit.

4.5.5 Other Model Parameters

Table 4.2 lists best fit parameter values for the different configurations of the model. For all models except Model 1, the hydrogen column density agrees with the value of $N_h \approx 0.6 \times 10^{22}\,\mathrm{cm}^{-2}$ previously used for this data set (Gilfanov et al. 2000; Grinberg et al. 2014; Tomsick et al. 2018). Model 1 again differs from the others with regard to the iron abundance, which is twice solar or less for all models with an ionisation profile. Previous time-averaged spectral fitting studies have returned much higher iron abundances for Cygnus X-1 (up to ~ 5 times solar Parker et al. 2015; Walton et al. 2016) and other sources (e.g. GX 339-4 García et al. 2015; Parker et al. 2016), as did our previous spectral-timing analysis that included neither light bending nor a radial ionisation profile (Mastroserio et al. 2018). Our fits to the complex covariance all return slightly higher values of disc inclination angle than our fits to the time-averaged spectrum alone (see Table 4.1), which are in turn all larger than the inclination angle of the binary system (Orosz et al. 2011). However, our fits return lower inclinations than some previous time-averaged spectral fitting studies in both the soft ($> 38°$ Walton et al. 2013; Tomsick et al. 2014) and hard ($> 42°$ Parker et al. 2015) spectral states. This discrepancy is not down to differences in the fitted models, since our single ionisation model for the time-averaged spectrum is identical to RELXILLLP, which was used for the other studies, yet our Model A fit to the time-averaged spectrum returns a low inclination. The previous studies used different data sets, some from other instruments. Interestingly, we find that fitting for the complex covariance *without* also considering the time-averaged spectrum returns still higher inclination values (between 39°and 45°).

When expressed in units of R_g, the disc inner radius r_{in} is very small for the first three configurations, and becomes larger for the final two models with limits on the peak ionisation. We find that the same happens when we place an upper limit on the peak ionisation parameter for Model 2.

There is clearly an anti-correlation between the ionisation parameter and the inner radius of the disc that can be seen by comparing different fits and confirmed by the error contour plot (see Appendix C.3). The data can not accommodate a strong contribution from the innermost part of the disc. Either this innermost part is mostly ionised, or, if the ionisation is forced to be lower, the data requires a slightly truncated disc to exclude the contribution from the innermost region of the disc.

The source height for all our models is significantly larger than the very small value ($h \lesssim 2\ R_g$) reported by Parker et al. (2015). Niedźwiecki et al. (2016) pointed out that such a small source height implies an intrinsic source luminosity many times the Eddington limit due to the large gravitational redshift experienced by source photons. Our models do not suffer from such a problem, with the intrinsic source flux only being a factor ~ 1.33 times the observed source flux. We note that our previous analysis in which we ignored light bending and fixed the mass to $14.8 M_\odot$ instead needed $h < 2.5\, R_g$ (Mastroserio et al. 2018). The larger source height returned by our current analysis is not down to the mass being a free parameter, since a larger black hole mass would require a *lower* source height to reproduce the same reverberation lag. Instead, the higher source height is well explained by the inclusion of light bending, since this leads to an increased reverberation lag for a given geometry. We therefore now need a higher source height to explain the same data. The source heights we measure here are similar to those found by e.g. Basak et al. (2017) and Tomsick et al. (2018), although direct comparison is difficult since these studies employed different model assumptions.

Introducing an ionisation profile seems to increase the high energy cut-off returned by the fit, particularly for Model 3. The values returned here are higher than for previous studies (e.g. Wilms et al. 2006; Mastroserio et al. 2018).

In order to further explore correlations between parameters, we run a Markov Chain Monte Carlo (MCMC) parameter exploration on Model 3. The setup and results of this analysis are presented in Appendix C.3.

4.5.6 Model comparison

Of the models we tested, Model 3 has the lowest χ^2 value. We note that some of the parameter values for this model differ from the other models. In particular the boost parameter is close to unity for this model, consistent with a steady point source, but $\lesssim 0.5$ for the other models, consistent with the coronal plasma moving away from the black hole. Moreover both the high energy cut-off and the mass are much higher for Model 3. Interestingly if we fix the boost parameter to 0.5 in Model 3, the best fit requires an energy cut-off of ~ 356 keV, a mass of $\sim 15 M_{\odot}$, the inner radius increases to $\sim 3.7 R_g$ and the ionisation peak decreases to ~ 3.8[2]. It seems that forcing the boost parameter to 0.5 aligns Model 3 to Model 3a and 3b, with a similar reduced χ^2 of 440/564.

Fig. 4.4 shows the real (a) and imaginary (b) parts of the complex covariance in the frequency range 0.1 mHz to 32 Hz. The lines are Model 3 calculated with the best fitting parameters and the points are the data unfolded around the best fitting model. The lower panels in both plots show the residuals of the fit. Our current analysis considers three additional low frequency ranges compared with Mastroserio et al. (2018), which improves the overall signal to noise. However, we do not expect this to have changed the best fitting parameters, since the reverberation time lag does not change its value significantly below the lowest frequency considered in Mastroserio et al. (2018) (e.g. see Emmanoulopoulos et al. 2014). We note that around the iron Kα line energy range the model slightly overestimates the width of the line. Similar residuals were found in Mastroserio et al. (2018), although implementation of light

---

[2] When the boost is fixed to 0.5 the parameters not mentioned in the text are similar to the ones of the other configurations.

bending and an ionisation profile has made the new residuals around the iron line less prominent than in the previous model. For the purposes of clarity, this figure does not show the time-averaged spectrum, whose residuals are shown instead in Fig. 4.5. The black stars are the energy spectrum residuals of Model 3 and they show a different structure compared with Fig. 4.1, which represents the fit only to the time-average spectrum. It seems that adding the complex covariance to our analysis requires the iron line to be broader. This is also indicated by the best fitting value for the disc inner radius, which becomes smaller when we include the complex covariance in the fit (compare Models A, B and C with Models 1, 2 and 3). Fig. 4.5 also includes the energy spectrum residuals for Model 3a (blue squares) and Model 3b (red diamonds). These residuals are again very similar to Model 3. Fig. 4.6 shows the complex covariance residuals for Model 3a, which are similar to the Model 3 residuals (see Fig. 4.4). Model 3b has an almost identical complex covariance residual plot, which is not shown here. Therefore, although setting an upper limit for the peak ionisation parameter increases the overall χ^2, it does not introduce any new features into the residuals.

Although we fit for real and imaginary parts of the complex covariance in order to simply account for the telescope response, we can also plot the time lags and variability amplitude associated with our model, which is more intuitive. Fig.4.7 shows the lags and amplitude for Model 3, with the data points derived from the unfolded complex covariance. For clarity, the model curves are shown with a higher resolution than the data, and the data and the model lags for the frequency ranges $1-5$ mHz, $5-17$ mHz and $17-50$ mHz are not plotted due to their large error bars. Fig. 4.8 shows the continuum parameters as a function of Fourier frequency for Model 3. The behaviour of all three parameters resembles that reported in Mastroserio et al. (2018), except for ϕ_A dropping to slightly lower values than before at high frequency. These parameters set the power-law pivoting variations. They are defined in the Fourier domain as the relative phase difference between the reference band light curve and each narrow energy band light curve (ϕ_A, ϕ_B), and as the ratio between the power-law index amplitude and normalisation amplitude (γ). Although their physical meaning is not immediately clear, it can still be useful to compare them with more physical models.

4.6 Discussion

We have, for the first time, estimated the mass of a Galactic black hole through X-ray reverberation mapping. We use the model RELTRANS (Ingram et al 2019) which uses a lamppost geometry in full GR to predict complex covariances, modified to include the non-linear effects resulting from fluctuations in the slope of the irradiating spectrum. The source is located on the black hole spin axis irradiating a razor thin accretion

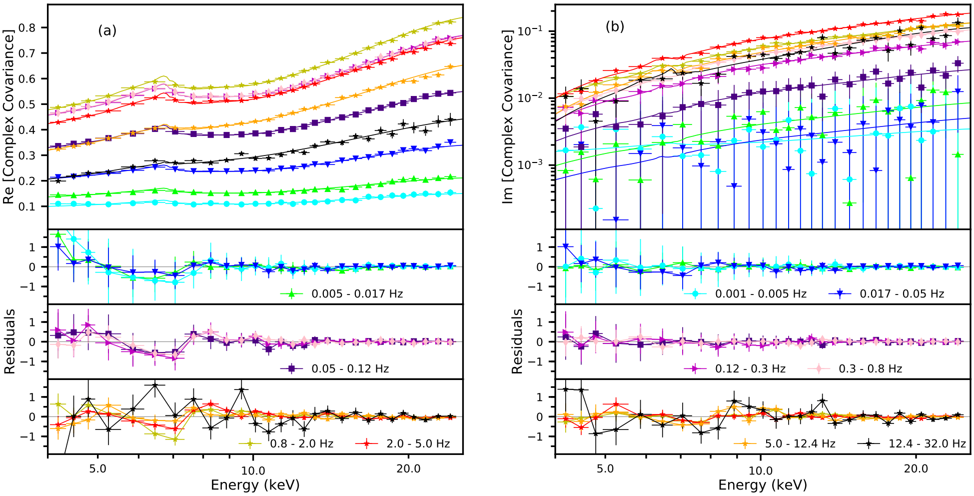

Figure 4.4: Top panels show the fit of real (a) and imaginary (b) part of the Cygnus X-1 complex covariance spectrum with Model 3. The fit also includes the time-averaged energy spectrum which is not shown in this plot. The dots are the data and the lines in the top panels are the model which has a much higher energy resolution than the data for clarity. The bottom panels show the data minus the folded model (command `plot rediduals` in XSPEC).

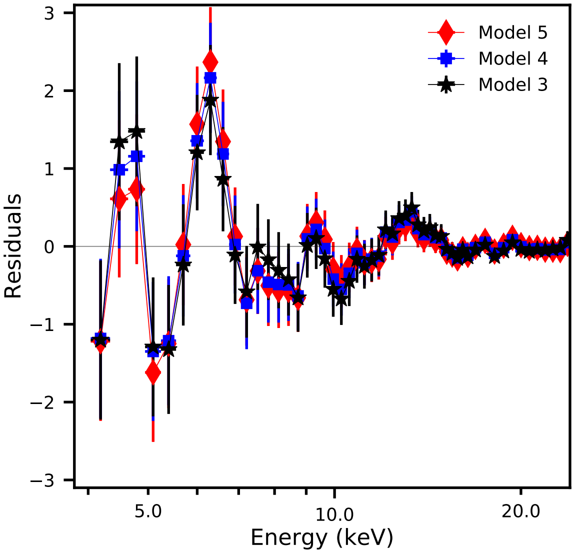

Figure 4.5: Residuals (data minus the folded model) of the time-average energy spectrum of Model 3 (black stars), Model 3a (blue squares) and Model 3b (red diamonds). Here the residual plot shows only the time-averaged energy spectrum contribution for clarity, however this a joint fit with the complex covariance.

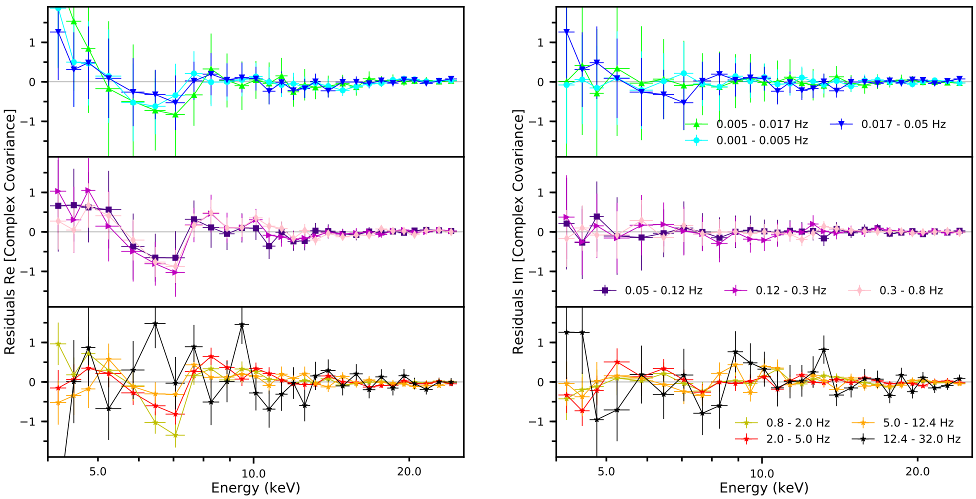

Figure 4.6: Residuals (data minus the folded model in units of normalised counts per second per keV) of the complex covariance spectra (real and imaginary part) for Model 3a. The fit also includes the time-average energy spectrum which is not shown in this plot.

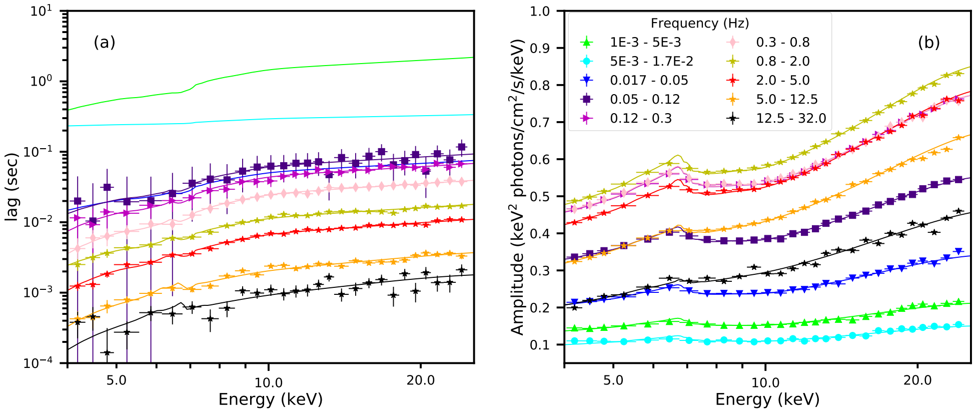

Figure 4.7: Lags (a) and variability amplitude (b) as a function of energy for different Fourier frequency ranges. The dots are the data and the lines are calculated from the best fitting parameters of Model 3. The data points for the lowest three frequency ranges are not plotted in the lag energy spectrum because their very large error bars. Only the model lines are plotted for these frequency ranges.

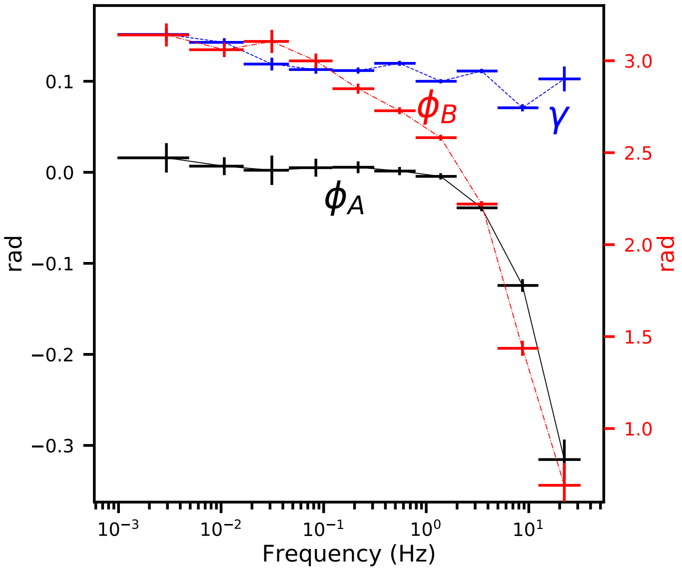

Figure 4.8: Best fit parameters which control the spectral power-law slope variability, as function of Fourier frequency for Model 3. The ϕ_A line and the γ line (black solid and blue dashed) refer to the left y-axis. The ϕ_B line (red dotted) refers to the right yaxis. Every group of three parameters in the same frequency range has been used to fit the complex covariance.

disc in the black hole equatorial plane.

We test a number of models, each employing a different assumption regarding the radial dependence of the disc ionisation parameter $\xi(r)$. Model 1 assumes constant ξ and yields a mass of $M = 21.6^{+6.8}_{-6.6}\ M_{\odot}$ (errors are 90% confidence). Model 2 self-consistently calculates $\xi(r)$ from the radial dependence of the illuminating flux and additionally assuming the electron density in the disc to be constant with radius, yielding a mass of $M = 19.7^{+5.3}_{-5.4}\ M_{\odot}$. Model 3 self-consistently calculates $\xi(r)$ assuming the radial density profile in zone A of the Shakura & Sunyaev (1973) accretion disc model, and yields a mass of $M = 26.0^{+9.6}_{-8.6}\ M_{\odot}$. Zone A (radiation dominated pressure and electron scattering dominated opacity), for a source with luminosity of 1.6% the Eddington limit, $\alpha = 0.01$ and mass of $14.8\,M_{\odot}$ extends to around $15\,R_g$. Since the region inside of this dominates the reflection emissivity, the assumption of a zone A density profile is reasonable. Moreover, for radii larger than this, the ionisation is low so that its assumed profile is less important. Model 3 has the lowest χ^2, but we find that the best fitting peak value of $\xi(r)$ is implausibly high. By combining the known distance to Cygnus X-1 with our model parameters and a reasonable estimate for the electron density in the disc atmosphere, we place the highest possible physical upper limit on the peak ionisation parameter $\log_{10}\xi_{\rm max}$ of 3.76. We therefore define Model 3a, which employs the same assumptions as Model 3 but the peak of the ionisation parameter is now bound by the reasonable upper limit on $\log_{10} \xi_{\rm max}$ of 3.5. This is our most physical model and yields a mass of $M = 16.5 \pm 5\ M_\odot$, which is consistent with the existing dynamical mass measurement ($M = 14.8 \pm 1\ M_\odot$ Reid et al. 2011). The correlation between the mass and peak ionisation is illustrated clearly by the 2D χ^2 contour plot in Fig 4.3.

We note that adding the complex covariance to the fit creates structures in the residuals of the time-average energy spectrum (Fig. 4.5) that are not present in the fit to the time-averaged spectrum alone (Fig. 4.1). When we fit Model 2 to the complex covariance only (i.e. ignoring the time-averaged spectrum), the best fit ionisation peak and inner disc radius are compatible with the joint fit, but the mass is larger ($31^{+13}_{-12}\, M_\odot$). For Model 3, the same experiment instead yields the same mass of the joint fit with larger error bars ($M = 25.6^{+13}_{-10}\ M_\odot$), but lower ionisation peak ($4.0^{+0.3}_{-0.1}$) and slightly larger disc inner radius ($2.6^{+1.1}_{-1.0}\, R_g$) (all other parameters are similar to the joint fit). This, in addition to the Model 3a and 3b fit results, implies an anti-correlation between the inner radius and peak ionisation that is confirmed by an MCMC simulation (see Appendix C). This anti-correlation occurs because the inner disc does not contribute to the iron line for the highest peak ionisation values. Such over-ionisation therefore has a similar effect to disc truncation.

Our analysis is sensitive to black hole mass because reverberation lags give distances in units of km and spectral distortions give distances in units of gravitational radii. This means that the width of the iron line feature in the time-averaged spectrum *and* in the complex covariance jointly sets geometrical parameters such as the disc inner radius and the source height. Reverberation lags give rise to an iron line feature in the lag-energy spectrum, but this feature is not well constrained for the data set we explore here (see Fig. 4.7 left). Still, geometries that would give rise to very large or very small reverberation lags are ruled out, since they would result in lag spectra with respectively a large excess or dip in their lag spectra. The energy and frequency dependent correlated variability amplitude on the other hand is very constraining. We can clearly see in Fig. 4.7 (right) that the reflection features become weaker for higher Fourier frequencies. This is because the fastest continuum variability is washed out in the reflected emission by the finite size of the reflector (i.e. destructive interference between rays reflecting from different parts of the disc; Revnivtsev et al. 1999; Gilfanov et al. 2000). The larger the path length differences, the more steeply the amplitude of the reflection features will drop off with Fourier frequency. This can be achieved in the model either by increasing the black hole mass, which would not affect the width of the line, or by increasing geometrical parameters such as h or $r_{\rm in}$, which would reduce the width of the line. The model therefore depends on black hole mass in a very different way to any of the geometrical parameters.

4.6.1 Future modelling improvements

Although it is encouraging that our most physical model returns a sensible black hole mass estimate, there are still many improvements that can be made to our reverberation model in future. We assume that the disc is infinitely thin whereas in reality the disc has a finite thickness, particularly in the zone A regime (Shakura & Sunyaev 1973). Including a realistic disc scale height leads to a more centrally peaked emissivity profile (Taylor & Reynolds 2018a,b) leading to shorter time lags and a broader iron line for a given disc inner radius. We may therefore expect the future inclusion of a realistic disc height to push the best fitting disc inner radius to larger values, although it is difficult to confidently predict since the new emissivity profile will also effect the ionisation profile. It has also been suggested that Cygnus X-1's accretion disc is warped, since some reflection spectroscopy results (Tomsick et al. 2014; Walton et al. 2016) suggest that the inner disc has a different inclination angle to the binary system (Orosz et al. 2011). Such a warp would again change the reflection emissivity profile if included in the model. However, in other suggestions Cygnus X-1 is an aligned system since it has no peculiar velocity with respect to its association of O stars, perhaps indicating that there was no natal supernova kick to mis-align the black hole spin axis at birth (and maybe even that the black hole was formed via direct gravitational collapse; e.g. Mirabel & Rodrigues 2003). This would also explain the absence of strong low frequency quasi-periodic oscillations (QPOs) in the source in the context of the Lense-Thirring precession model (e.g. Ingram et al. 2009; Rapisarda et al. 2017b). We note that our fits here return inner disc inclination angles only slightly discrepant with the binary inclination ($\sim 35^\circ$ vs $\sim 27^\circ$).

Also, although XILLVER is state-of-the-art, it will be possible in future to include more realistic disc physics in the calculation of the rest frame reflection spectrum. We currently calculate the disc ionisation parameter using a reasonable function for the electron density, $n_e(r)$, but we use the publicly available XILLVER grid in order to calculate the restframe spectrum, which assumes $n_e = 10^{15}$ cm^{-3}. We therefore use the correct value of the ionisation parameter for our calculation, but the radiative processes and atomic physics are always calculated in a low density environment, whereas X-ray binary discs are thought to have much higher densities ($n_e \sim 10^{20}\text{cm}^{-3}$). Fixing this issue is challenging, since the atomic data used for the XILLVER calculation is not currently tabulated for the high densities of Galactic black hole discs (Shakura & Sunyaev 1973; Svensson & Zdziarski 1994; Tomsick et al. 2018). The leading order effect of increasing n_e is on the < 3 keV spectrum, but the importance of using a realistic value has recently been demonstrated (García et al. 2016; Tomsick et al. 2018; Jiang et al. 2019). Finally, we assume a point-like stationary corona. Alternatively including an extended corona may change our results, although it is difficult to judge in which way without performing the necessary calculations. Properly including a plasma velocity vector may also change our results by adjusting the radial dependence of the illuminating flux as well as just the normalisation (Dauser et al. 2013). Our formalism will enable us in future to test our assumptions about the accretion geometry using the known black hole mass and distance for Cygnus X-1, calibrating our model for future use on other sources.

4.6.2 Implications

Our models return a range of values for the disc inner radius, some compatible with earlier claims of near maximal black hole spin (Fabian et al. 2012; Parker et al. 2015) and some (including our most physical model, Model 3a) with $r_{\rm in}$ as large as $\sim 6\ R_g$. Whether or not the disc truncates outside of the ISCO in the hard state is still debated. Generally, time-averaged reflection spectroscopy tends to indicate smaller disc inner radii than does timing analysis (e.g. Rapisarda et al. 2017b). We note that a number of the future improvements to our model discussed in the previous subsection could have the effect of pushing the best fitting $r_{\rm in}$ further out, although the parameter space will be rather complex. We also note that including a radial ionisation profile does not systematically push r_{in} to larger values, in contrast with the findings of Shreeram & Ingram (in prep) for GRS 1915+105.

In our model, we account for the hard 'continuum' lags that dominate at low Fourier frequencies with a pivoting power-law model, and this provides good fits to the data. If the corona is indeed quite compact, then such lags could well be produced by varying cooling and heating of the corona. Disc photons cool the corona before the propagating accretion rate fluctuations arrive into the corona and heat it (Uttley & Malzac in prep). The same type of lags would also be present for the case of an extended corona but propagating fluctuations *within* the corona (both radially and vertically, in the case of a veritical struncture) would need to be taken into account in our reverberation model (e.g. Wilkins et al. 2016; Chainakun & Young 2017).

The geometry of our best fitting models is compatible with a compact source within which the plasma is moving away from the black hole, perhaps the base of the jet (e.g. Markoff et al. 2005; Kara et al. 2019). In all cases, our best fitting source height is sufficiently large so as not to require the intrinsic source flux to be super-Eddington after the application of relativistic corrections. However, our fits do return high values of the high energy cut-off. If the corona is stationary, this implies that it must be very extended ($\gg 100\ R_g$) in order to be in $\mathrm{e}^{\pm}$ pair equilibrium (e.g. Fabian et al. 2015). However, if it is outflowing, then its radiation as we observe it will be Doppler blue shifted due to the fairly low inclination angle, meaning that the rest frame temperature is lower and thus allowing for a more compact corona. More insight into the true rest frame electron temperature can be gained in future by using a continuum model more sophisticated than an exponentially cut-off power-law and by considering data in the > 25 keV energy range, as would be provided by *NuSTAR*. We plan to carry out further calibration of the model on well-studied sources such as

Cygnus X-1, which will introduce the prospect of using X-ray reverberation mapping to measure the mass of black holes that have no existing dynamical mass measurement. This will be particularly useful for systems that suffer from heavy extinction, and will cut down on systematic errors in cases where the binary inclination angle is poorly constrained. The extra constraints on the Galactic black hole mass function provided by a new mass measurement technique will enhance studies of the mass gap between black holes and neutron stars, and comparison with the mass function of coalescing black hole systems. We note that our method is also applicable to AGN.

4.7 Conclusions

We performed a mass measurement of Cygnus X-1 through X-ray reverberation analysis. Our most physical model (Model 3a) requires a black hole mass of $16.5 \pm 5\,M_\odot$ consistent with the dynamical measurement. The model uses an accretion disc ionisation profile limited to not exceed the highest ionisation that is physically plausible. Removing this upper bound (Model 3), leads to a fit that has a lower χ^2 but includes physically implausible peak ionisation values, implying either a very low density disc atmosphere or a much greater distance to the system than is inferred from parallax. We performed our analysis with *RXTE* data. Using telescopes with much higher energy resolution such as *NICER* and *NuSTAR* would improve our results in terms of constraining the shape of the spectral features and disentangle the degeneracy among some of the model parameters. We plan to use this model in future on such data sets, both for Galactic black holes and AGNs.

5

Multi-timescale reverberation mapping of Mrk 335

Guglielmo Mastroserio, Adam Ingram & Michiel van der Klis

Submitted to Monthly Notices of the Royal Astronomical Society

Abstract

Time lags due to X-ray reverberation have been detected in several Seyfert galaxies. The different travel time between reflected and directly observed rays naturally cause this type of lag, which depend directly on the size of the system, and hence on the mass of the central black hole. A different type of lag occurs at longer timescales, which are likely dominated by propagating fluctuations in mass accretion rate. We use the RELTRANS model to self-consistently account for both these types of lags in order to fit simultaneously to the time-averaged energy spectrum and the lag energy spectra of Mrk 335 over multiple timescales. The resulting mass estimate is a few million Solar masses which is significantly lower than the mass measured with the optical reverberation mapping technique ($14 - 26$ million $M_{\odot}$). When we add the correlated variability amplitudes to the time lags by fitting the full complex cross-spectra, the model is unable to describe the characteristic reverberation Fe Kα line and cannot constrain the black hole mass. This may be due to the assumption of unity coherence in the model which is not consistent with the data on short timescales.

5.1 Introduction

Active Galactic Nuclei (AGN) are thought to be powered by the accretion of matter onto supermassive black holes ($10^6 - 10^9 M_\odot$). The gas forms an accretion disc and emits a multi-temperature blackbody spectrum which peaks in the UV band (Shields 1978; Malkan 1983). Some of these photons act as seed photons for inverse Compton up-scattering in a hot electron ‘corona’ (Eardley et al. 1975; Thorne & Price 1975). The resulting *direct* Comptonised emission is often simply modelled as a power-law with a high energy cut-off, where the power-law index and the cut-off energy are related to the optical depth and the electron temperature, respectively.

Part of this radiation illuminates the disc and is re-emitted, producing the *reflection* component in the spectrum (e.g., Lightman & White 1988). The shape of the overall time-averaged energy spectrum depends on the properties of both the corona, such as optical depth and temperature, and the accretion disc, including both its physical characteristics (e.g., ionisation and iron abundance) and its geometry (e.g., inclination and radius of the inner edge). One of the most prominent features in the reflection spectrum is an iron $K\alpha$ line emitted at 6.4 keV and broadened by the effects of orbital motion in the disc and relativistic redshift (Fabian et al. 1989). The black hole drags space-time around it further modifying the emission line profile (Fabian et al. 2000), making it possible to measure the spin of the black hole (see Reynolds 2014 for a review).

Although this approach of time-averaged spectral fitting led to very interesting results, there are several aspects that have remained unclear, in particular, the exact geometry of the system. For example, the extent of the corona is under debate. It might be either a compact cloud of gas that could reasonably (compared to the accretion disc dimensions) be modelled as a point source (Haardt & Maraschi 1991), or a more extended structure, with various geometries being considered for it (e.g. Eardley et al. 1975; Haardt & Maraschi 1993). One of the reasons for this ambiguity is that in time averaged spectral fitting, degeneracies among the model parameters can often not be avoided. In order to help break such degeneracies, it is possible to additionally study the time variability of the spectrum. One effective way to study the spectral variability is to measure the time lags observed in both supermassive and stellar mass black holes between the variability in different photon energy bands. Two types of lag are observed in AGN, the ‘hard lag’ that is intrinsic to the direct emission (intrinsic lags) and the ‘soft lag’ that is due to the differences in light crossing time from corona to observer between the direct and the reflected emission (the reverberation lags). The intrinsic lags are thought to be generated by mass accretion rate fluctuations propagating through the accretion disc towards the black hole (e.g. Lyubarskii 1997; Arévalo & Uttley 2006; Ingram & van der Klis 2013). The timescales of the fluctuations depend on the viscosity of the gas, thus long timescales arise in the outer part of the accretion flow and short timescales closer to the black hole. The fluctuations reach the corona causing variations in the electron temperature. At each radius the variability is due to the product of local fluctuations and the generally slower fluctuations that propagated in from larger radii. Conversely, the reverberation lags are due to the different path lengths of the variability signals to reach the observer. Hence, the variability in the energy band dominated by the reflected emission lags behind the variability of the direct, inverse Compton emission.

The hard lags dominate at long timescales, and hence in many sources the lags as a function of Fourier frequency computed between $\simeq 0.3 - 1.0$ keV (soft energy band) and $\simeq 2.0 - 4.0$ (hard energy band) are positive (i.e., hard flux lags soft flux) at Fourier frequencies $\nu \leq 300 M_\odot/M$ Hz. The lag spectrum as a function of photon energy calculated in this frequency range is featureless and lag depends approximately linearly on $\log E$. At higher frequencies the hard intrinsic lags are smaller, and soft (negative) reverberation lags have been detected, which in the lag vs energy spectrum exhibit a broad iron line feature in the $6 - 7$ keV range. Detecting this Fe line reverberation feature in the lag energy spectrum is easier in AGN than in stellar mass black holes because they are much bigger systems and so the timescales involved are consequently longer. However, because of their distance, AGN are usually fainter than stellar mass black holes, so they are often characterized by a worse signal to noise. For that reason, we need to use as wide as possible a frequency range to calculate the lag energy spectrum, and analyse it together with the time-averaged energy spectrum in order to constrain the system parameters.

Looking only at the time lags means considering only a limited part of the information in the data, as the correlated variability amplitude as a function of energy and frequency is ignored in this approach. Lags and amplitudes have been considered together in only a few cases (e.g. Uttley et al. 2011; Kara et al. 2013b; Rapisarda et al. 2016), however, joint modelling of both has not yet been performed for AGN. So, progress could be made by jointly modelling the time-averaged and variability (time lag and correlated amplitude) spectra taking into account both the effects of mass accretion rate propagating fluctuations and reverberation lags. The best way to consider time lags and correlated amplitudes together is by explicitly modeling the real and imaginary parts of the complex cross spectra (van der Klis et al. 1987; Rapisarda et al. 2016; Ingram et al. 2016; Mastroserio et al. 2018), and that is the approach taken in this paper.

We have developed the fully relativistic reverberation mapping model RELTRANS (Ingram et al. 2019) that, using a transfer function formalism (e.g. Campana & Stella 1995; Reynolds et al. 1999; Cackett et al. 2014), computes the complex cross-spectrum for a range of Fourier frequencies and the time-averaged energy spectrum in a prescription based on a ‘lamppost’ coronal geometry (e.g. Matt et al. 1991), assuming isotropic emission and a flat thin accretion disc. In the configuration of RELTRANS that we use, the disc radial ionisation profile is self-consistently calculated from the radial density profile corresponding to a Shakura & Sunyaev (1973) zone A accretion disc. The model computes the reverberation lags and accounts for the different light crossing times of the photons using proper relativistic ray-tracing both between corona and each point on the disc and from each point on the disc to the observer. We use here a further improved version of RELTRANS which accounts for the hard lags through the pivoting of the continuum spectrum by allowing fluctuations in the index and normalisation of the power law (Mastroserio et al. 2019). This serves as a proxy for the cooling and heating of the corona by the fluctuations in the rate of seed photons coming from the disc and the mass accretion rate fluctuations propagating into the corona. Each patch of the disc sees a different hardness of the incident emission coming from the corona due to the effects of orbital motion and redshift which are properly evaluated taking into account the different paths of the photons (Mastroserio et al. 2018). This causes non-linear effects in the fluctuations of the reflected emission (i.e., not just the strength but also the shape of the reflection spectrum fluctuates) which are taken into account in the model. RELTRANS has been successfully tested on Cygnus X-1 (Mastroserio et al. 2019) and previously used for a proof of principle of the method (fitting only the reverberation lags) in Mrk 335 (Ingram et al. 2019).

In this paper we present a full exploration of the model with XMM-Newton observations of Mrk 335. The Seyfert 1 galaxy Mrk 335 has been extensively studied both in terms of time-averaged spectrum (e.g. Wilkins & Gallo 2015; Keek & Ballantyne 2016) and lag spectrum, which shows both hard and soft lags (e.g., Kara et al. 2013a; De Marco et al. 2013a; Chainakun et al. 2016a). The source has been observed at different flux levels (defining 'flux epochs') (Wilkins & Fabian 2013) with XMM-Newton from 2006 to 2009. Reverberation lags are detected only in the highest-flux epoch (Kara et al. 2013a) although the reflection component in the spectrum is weaker then than in the low flux epochs (Keek & Ballantyne 2016). We therefore select the high flux epoch and use RELTRANS to simultaneously fit the time-averaged energy spectrum and the complex cross-spectra as a function of energy in multiple Fourier frequency ranges.

5.2 Data reduction

We analyse a 133 ks observation of Mrk 335 performed with *XMM-Newton* in 2006 (obs ID 0306870101). During the observation the source was in the high-flux epoch (Wilkins & Gallo 2015) with a $0.5 - 10$ keV flux of 4.08×10^{-11} erg cm^{-2} s^{-1} (Grupe et al. 2007). We follow the data reduction procedure described in Ingram et al. (2019), considering only the EPIC-pn data and discarding the EPIC-MOS data (following Kara et al. 2013a). We use the Science Analysis System (SAS) v11.0.0 to extract the signal from a circular region with 35 arcsec radius centred on the maximum of the source emission. We apply the filters PATTERN ≤ 4 and FLAG $== 0$ and discard background flares at the beginning and at the end of the observation (considering only times 252709714 to 252829414 seconds telescope time). We extract the time-averaged source and background energy spectrum and also extract light curves with 10 second binning from 12 different energy bands with the same energy resolution as used by Kara et al. (2013a). The SAS task EPICLCCORR performs various corrections including subtracting the background signal, which is extracted from a circular region of 35 arcsec radius at some distance from the source. We compute the cross-spectrum between the light curve for each energy band and the reference light curve which is the sum of all the light curves except the subject one (Uttley et al. 2014). In order to Fourier transform the light curves we fill the small gaps (less than 100 seconds) by randomly extracting the missing count rates from a Poisson distribution centered on the value interpolated between the previous and the next bin of the gap. We divide the cross-spectrum into four frequency ranges: $0.02-0.2$ mHz, $0.2-0.7$ mHz, $0.7-2$ mHz and $2-10$ mHz. For the first and the second frequency ranges we are roughly in the regimes dominated by the hard and soft lags, respectively, as found by De Marco et al. 2013a. Since the Fourier frequency resolution of the cross-spectrum is 8.35×10^{-6} Hz, the first frequency range contains 21 Fourier frequencies, and the other three frequency ranges contain more. The cross-spectral amplitudes averaged over these four frequency ranges are therefore sufficiently close to Gaussian-distributed that we can use the χ^2 statistic for the purposes of fitting models (Nowak et al. 1999).

5.3 Spectral timing analysis

5.3.1 Time-averaged energy spectrum

Fitting the $2-10$ keV time-averaged spectrum with an absorbed power-law model reveals evident residuals in the iron Kα line energy range (see Fig. 5.1), consistent with previous analyses (Keek & Ballantyne 2016; Wilkins & Gallo 2015). We also see the emission line at 7.01 keV in the rest frame of the host galaxy (the cosmological redshift to Mrk 335 is $z = 0.025785$; Huchra et al. 1999) that was reported by Keek & Ballantyne (2016). Throughout this paper, we model this line in the time-averaged spectrum with a narrow Gaussian function with fixed centroid. Including a XILLVER (García et al. 2013a) component in the model to account for distant reflection leads to a reduced χ^2 of $\chi^2/\mathrm{dof} = 167.6/127$ (Model [A] in Table 5.2). This poor fit implies that a relativistic reflection component is also required, for which we use the model RELTRANS (Ingram et al. 2019). The full expression for our model (Model [B]) is

$$\textsc{tbabs} \times (\textsc{xillver} + \textsc{reltrans} + \textsc{zgauss}), \tag{5.1}$$

where the direct continuum emission is included in the RELTRANS model as an exponentially cut-off power-law. We fix the hydrogen column density to $N_\mathrm{H} = 3.6 \times$

$10^{20}\mathrm{cm}^{-2}$ following Kalberla et al. (2005) and assume the relative elemental abundances of Wilms et al. (2000). We fix the ionisation parameter of the distant reflector to $\log \xi = 0$. In contrast, we model the radial profile of the disc ionisation parameter using a self-consistent calculation of the irradiating flux in a lamppost geometry and assuming the radial density profile that corresponds to 'zone A' in the Shakura & Sunyaev (1973) disc model. In RELTRANS, this configuration is chosen by setting the environment variable `A_DENSITY`$= 1$ (see Table 5.1 for a full list of RELTRANS environment variables used for all of our fits). The peak ionisation parameter in the disc (the highest value attained by $\log \xi$) is a model parameter that we leave free in the fit. We choose to only model the $2.0 - 10$ keV energy range of the spectrum because the $0.3 - 2.0$ keV energy range can only be adequately described by including a complicated 3 layer warm absorber model (Longinotti et al. 2013), which is beyond the scope of this paper.

Fig. 5.2 shows the best fitting model together with the unfolded data (upper panel). The residuals (bottom panel) do not present any particular structure and the reduced χ^2 is $\chi^2/\mathrm{dof} = 115/123$. Here, and throughout this paper, we have fixed the high energy cut-off, as this quantity cannot be constrained in the < 10 keV energy range of *XMM-Newton*, to $E_{\mathrm{cut}} = 300$ keV (in the observer frame), and we have also fixed the inclination angle to $i = 30^{\circ}$ (following for both of these parameters Keek & Ballantyne 2016). We fix the dimensionless black hole spin parameter to $a = 0.998$ and allow the disc inner radius to be a free parameter.

The best fitting model parameters are listed in Table 5.2. We obtain a larger disc inner radius than the fit of Keek & Ballantyne (2016) to the same data, and a smaller (more plausible) relative iron abundance. Since they used RELXILL (Dauser et al. 2013; García et al. 2014), the two differences between our model and theirs is that we assume a lamppost geometry as opposed to parameterizing the reflection emissivity profile with a broken power-law, and we self-consistently account for a radial disc ionisation profile instead of assuming a single value of the ionisation parameter. Our fit requires a large value of the 'boost' parameter, $1/\mathcal{B}$. This sets the normalization of the relativistic reflection spectrum relative to the direct emission. For $1/\mathcal{B} = 1$, the relative normalization of the reflection component is set entirely by the lamppost geometry and general relativistic light bending, whereas $1/\mathcal{B} > 1$ returns a stronger reflection component than expected in the lamppost geometry and $1/\mathcal{B} < 1$ corresponds to a weaker than expected reflection (see Ingram et al. 2019 for more details). A deviation from the expected isotropic lamppost emission can be due to the true source geometry being something other than point-like and/or an intrinsic velocity of the plasma in the corona that beams the emission. Since the physical assumptions of RELTRANS are only valid for a boost parameter reasonably close to unity, we impose a hard upper limit in our fits of $1/\mathcal{B} = 3$ to avoid unrealistic values. We see that the best fitting value in our fit is close to this upper limit.

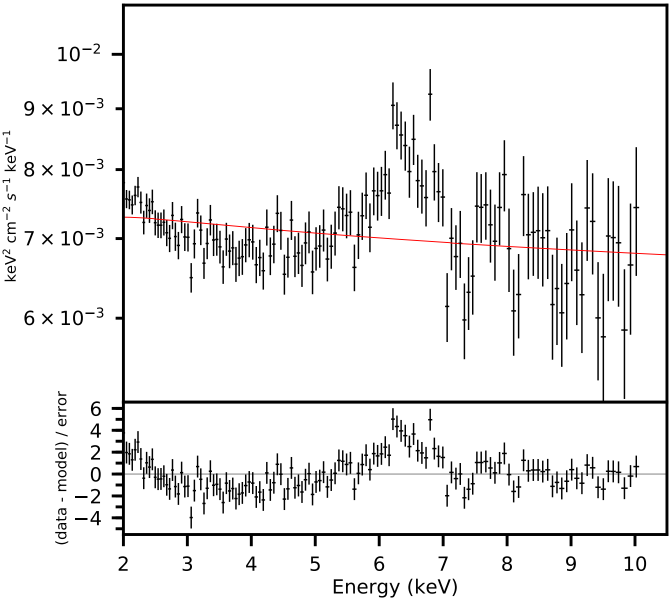

Figure 5.1: Upper panel Time-averaged energy spectrum unfolded with an absorbed power-law model. Lower panel: residuals of this model. Clear residuals around the iron line energy range can be seen.

Table 5.1: List of the environment variables for each of the models used in the analysis. M [#] stands for Model number #

Variables	M [B]	M [0]	M [1]	M [2]	M [3]	M [4]
MU_ZONES	1	1	1	1	1	1
ECUT_ZONES	1	1	1	1	1	1
ION_ZONES	10	10	10	10	10	1
A_DENSITY	1	1	1	1	1	1
PHI_SET	0	1	1	0	0	0

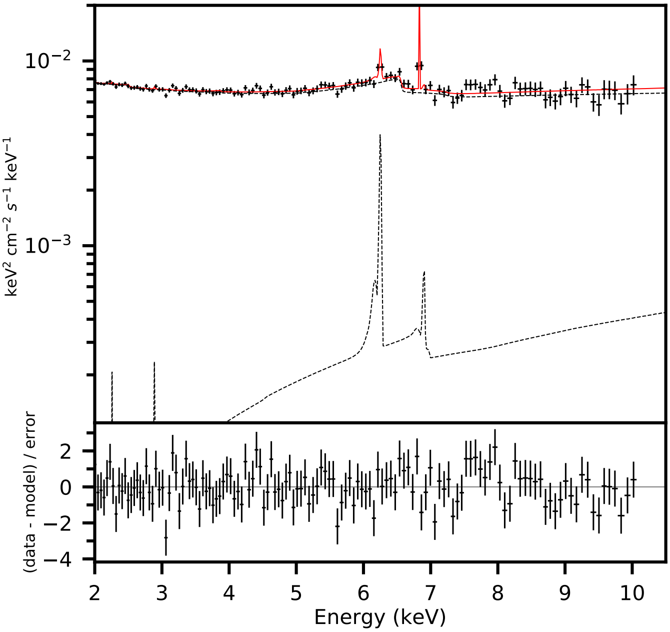

Figure 5.2: Upper panel: Time-averaged energy spectrum unfolded with the best fitting model accounting for direct emission and relativistic component (RELTRANS) and the distant reflector (XILLVER). The narrow emission line at 7.01 keV in the source restframe is modelled with a Gaussian component. Lower panel: Residuals of the best fit model.

Table 5.2: Best fitting parameters for the different models in the paper. First column lists the free parameters in the model; a dash in the model column indicates that the parameter is not part of that model. All models include Galactic absorption with hydrogen column density fixed to $n_H = 3.6 \times 10^{20}\mathrm{cm}^{-2}$, a high energy cut-off fixed to 300 keV, and a narrow Gaussian line in the time-averaged spectrum fixed at 7.01 keV in the galaxy rest frame, with cosmological redshift $z = 0.025785$. The black hole is considered maximally spinning ($a = 0.998$) in all relativistic models. Models [A] and [B] fit to the time-averaged spectrum only. Model [A] does not include the relativistic reflection component, Model [B] does. Models [0]–[4] simultaneously fit the time-averaged spectrum and different selections of lag-spectra or cross-spectra. Model [0] fits one lag spectrum in the frequency range $0.2 - 0.7$ mHz where the reverberation is thought to dominate, whereas Models [1] and [2] fit multiple lag spectra in the $0.2 - 10$ mHz and $0.02 - 10$ mHz frequency ranges, respectively. Models [3] and [4] fit the complex cross-spectra in these same frequency ranges. Errors are all 90% confidence.

	Time-ave spectrum		Time-ave + Lag spec (1 Freq - 3 Freq - 4 Freq)			Time-ave + Cross-spec (3 Freq - 4 Freq)	
Parameter / Model	PW + XIL [A]	REL + XIL [B]	MODEL [0] –	[1] –	[2]	MODEL [3] –	[4]
$h\,[R_g]$	-	13^{+13}_{-7}	22^{+31}_{-18}	$20.5^{+27.7}_{-10.0}$	$1.9^{+0.2}_{-0.2}$	21.5^{+34}_{-20}	$21.1^{+2.3}_{-5.3}$
$r_{\mathrm{in}}[ISCO]$	-	14^{+5}_{-5}	8.5^{+14}_{-a}	$1.7^{+15.1}_{-a}$	$5.8^{+1.3}_{-0.7}$	$9.5^{+13.5}_{-a}$	4^{+3}_{-2}
Γ_{pl}	$2.19^{+0.02}_{-0.03}$	$3.00^{+0.02}_{-0.08}$	$2.3^{+0.06}_{-0.10}$	$2.30^{+0.08}_{-0.04}$	$2.15^{+0.02}_{-0.02}$	$2.2^{+0.1}_{-0.1}$	$2.10^{+0.02}_{-0.02}$
$\log \xi$	0 (XIL)	$1.7^{+0.3}_{-0.4}$	$1.9^{+1.3}_{-1.2}$	$2.25^{+1.3}_{-1.3}$	$2.9^{+0.2}_{-0.1}$	$1.9^{+1.4}_{-0.7}$	$4.2^{+b}_{-0.1}$
A_{Fe}	$0.5^{+0.1}_{c}$	$0.6^{+0.1}_{-0.1}$	$0.65^{+0.2}_{-c}$	$0.65^{+0.17}_{-c}$	$0.5^{+0.15}_{-c}$	$0.7^{+0.2}_{-0.2}$	$0.5^{+0.1}_{-c}$
$1/\mathcal{B}$	-	$2.6^{+d}_{-1.4}$	$1.6^{+d}_{-0.5}$	$1.6^{+1.1}_{-0.4}$	$3^{+d}_{-0.4}$	$1.6^{+d}_{-0.8}$	8.5^{+1}_{-1}
Mass $[10^6 M_\odot]$	-	-	$1.0^{+3.0}_{-0.7}$	$1.77^{+3.00}_{-0.95}$	$2.7^{+0.3}_{-0.1}$	$e^{+0.6}_{-e}$	$53.2^{+18.8}_{-7.6}$
χ^2/dof	167.6/127	116/123	124/134	196/157	166/157	142/149	144.4/145

[a] The lower limit of the inner radius is the ISCO ($1.237R_g$).

[b] The upper limit of the ionisation is 4.7.

[c] The lower and upper limit of the iron abundance are 0.5 and 10 respectively.

[d] The upper limit of the boost parameter is 3

[e] The mass is pegged to $1M_\odot$

5.3.2 Time-averaged and lag spectrum

We now model the lag-energy jointly with the time-averaged spectrum, again using RELTRANS. We again ignore energies < 2 keV in the time-averaged spectrum because of the complicated structure of the warm absorber. For the lags, we instead consider the extended energy range $0.3 - 10.0$ keV. Although soft lags can be caused by the response of the warm absorber to changes in the ionising flux (Silva et al. 2016) which is not accounted for in our model, these lags should only be relevant for variability on longer timescales than the Fourier frequency ranges considered in our analysis. We therefore choose to model the reverberation lags down to 0.3 keV in order to maximize the signal to noise of the data.

Model [0]

The first model we explore, Model [0], considers the time-averaged spectrum and only lags calculated in the Fourier frequency range $0.2 - 0.7$ mHz, following Chainakun et al. (2016a) and Ingram et al. (2019). This is the frequency range in which an iron K feature indicative of reverberation was discovered by Kara et al. (2013a). Since the lags in this frequency range are thought to be dominated by reverberation lags (e.g., De Marco et al. 2013c), we do not include intrinsic hard lags in our model. For this model, we self-consistently calculate the zero level of the lag spectrum by specifying that the phase lag between the reference band and itself must be zero (`PHI_SET`$= 1$; see Table 5.1).

Fig. 5.3 shows the unfolded time-averaged spectrum (panel B) and the lag spectrum (panel A) alongside the best fitting Model [0] (for clarity, we plot the model with a finer energy resolution than the data). We confirm that in the $0.2 - 0.7$ mHz frequency range the lag energy spectrum shows the iron line feature (Kara et al. 2013a). The fit is statistically acceptable (reduced χ^2 of $\chi^2/\mathrm{dof} = 124/134$) and no clear structure can be seen in the residuals (top and bottom panels). The best fitting Model [0] parameters listed in Table 5.2 are similar to those from the fit to only the time-averaged spectrum. The most obvious differences are the photon index, Γ_{pl}, and the boost parameter, $1/\mathcal{B}$, which are both smaller in the Model [0] fit. This indicates that the direct spectrum is harder and this is balanced out by the reflection component (which is harder than the direct component) being weaker. In this respect, Model [0] is more physically self-consistent, since the model assumptions are only valid for $1/\mathcal{B} \sim 1$. We note, however, that the model upper limit of 3 on the boost parameter prevents us from constraining its 90% confidence level. The source height is slightly larger than before and the disc inner radius slightly smaller, although still larger than that found by Keek & Ballantyne (2016). The best fitting black hole mass is roughly $1 \times 10^6\ M_{\odot}$. This is similar to the result of Ingram et al. (2019), who fit only the lag spectrum in this frequency range without jointly fitting the time-averaged spectrum and ignored the radial dependence of the ionisation parameter. They fixed all spec-

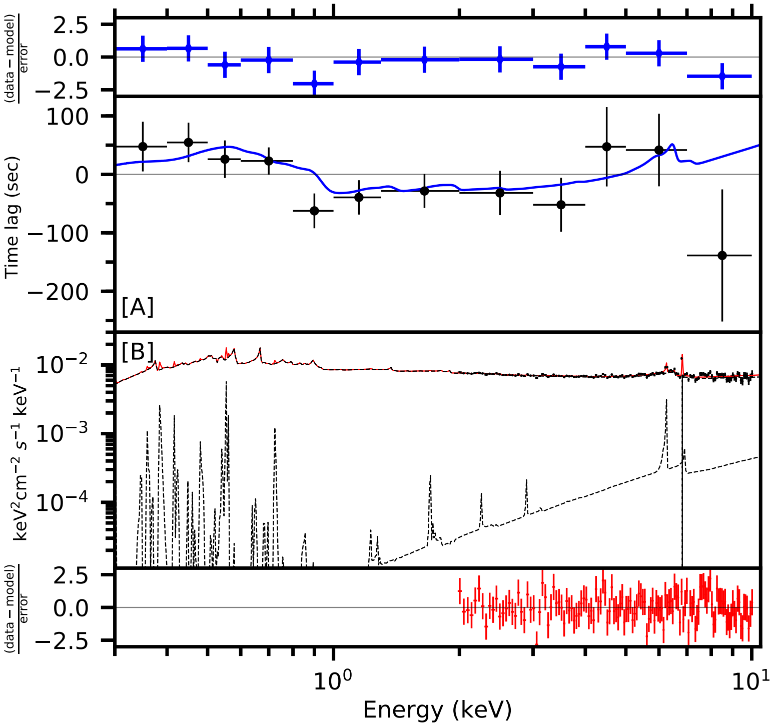

Figure 5.3: Bottom panels: Time-averaged unfolded energy spectrum and residuals of the best fit of Model [0]. The total model (red solid curve) and its components (dashed curves) were fitted to the spectrum in the $2-10$ keV energy range, even though the model curves continue down to 0.3 keV. Upper panels: Time lag energy spectrum in the $0.2-0.7$ mHz Fourier frequency range and the residuals of the best fit model. The model has been drawn with higher energy resolution than the data for clarity.

tral parameters except for h and $1/\mathcal{B}$ to the values measured by Keek & Ballantyne (2016). Our fit here features a larger source height and larger boost parameter (the increased boost parameter acts to offset the reduction in reflection fraction caused by the increased source height) than the Ingram et al. (2019) fit.

Model [1]

We now extend our analysis by additionally modelling the lag spectrum in the two higher frequency ranges ($0.7-2$ mHz and $2-10$ mHz), which we also assume to be dominated by reverberation lags. The best fitting parameters of this model, hereafter Model [1], are listed in Table 5.2, and the best fitting lag spectra and time-averaged energy spectrum are shown as the dashed curves in panels B, C, D and E in Fig. 5.4 alongside the data. The reduced χ^2 of $\chi^2/\mathrm{dof} = 196/157$ is still formally acceptable within 3σ confidence, but the goodness of fit is worse than for Model [0]. We see that, as before, this model includes an iron line feature in the $0.2-0.7$ mHz frequency range (panel B). The observed lag spectrum in the highest frequency range (panel D) shows hints of a dip at the iron line energy, that may potentially be interpreted as a phase-wrapped reverberation feature (see Section 5.4.1). However, the signal to noise is too low to confirm this speculation, and the model lags are very small in both of the higher frequency ranges (dashed curves in panels C and D). The best fitting parameters are similar to those of Model [0] except the disc inner radius is smaller and the ionisation parameter is larger. The best fitting black hole mass is similar to the previous model (a few million Solar masses).

Model [2]

We now also include the lowest frequency range ($0.02-0.2$ mHz) in our fit. At these timescales, the reverberation mechanism is not sufficient to describe the lags. Therefore for this model, hereafter Model [2], we account for the hard intrinsic lags with fluctuations in the hardness of the direct emission. We use the analytic prescription for a pivoting power law photon energy spectrum described in Mastroserio et al. (2018) and Mastroserio et al. (2019). The lags produced by this prescription in the continuum emission have a featureless monotonic energy dependence (see Mastroserio et al. 2018 for details). The non-linear effects in the reflection spectrum caused by the assumed spectral pivoting are accounted for self-consistently. In this case the model cannot currently calculate the zero level of the lag spectrum, so the parameter ϕ_A is a free parameter of the fit (`PHI_SET`$=0$).

The best fitting Model [2] parameters are listed in Table 5.2, and the best fitting lag spectra and time-averaged energy spectrum are shown as the solid curves in panels A, B, C, D and E in Fig. 5.4. The residuals are shown in the right hand column. The reduced χ^2 of $\chi^2/\mathrm{dof} = 166/157$ is again formally acceptable (the null-hypothesis probability is higher than for Model [1]). However, we see in Fig. 5.4 (panel B) that Model [2] does not describe the iron line feature in the observed $0.2-0.7$ mHz lag spectrum as well as Model [1] does. This is largely because the Model [2] has weaker observer's reflection fraction (as defined in Ingram et al. 2019) than Model [1] (1.99 for Model [2] and 2.68 for Model [1]) which dilutes the reverberation lags. Some parameters have changed from the Model [1] fit: the source height is lower, the disc inner radius is larger, and the boost parameter is also larger (pegged to the maximum allowed value). However, we note that the black hole mass is similar to Model [1].

5.3.3 Time-averaged and complex cross-spectrum

We finally account for the variability amplitude of the reflection component in addition to the time lags by simultaneously fitting the complex cross-spectrum as a function of energy jointly with the time-averaged spectrum. We now only fit in the $2-10$

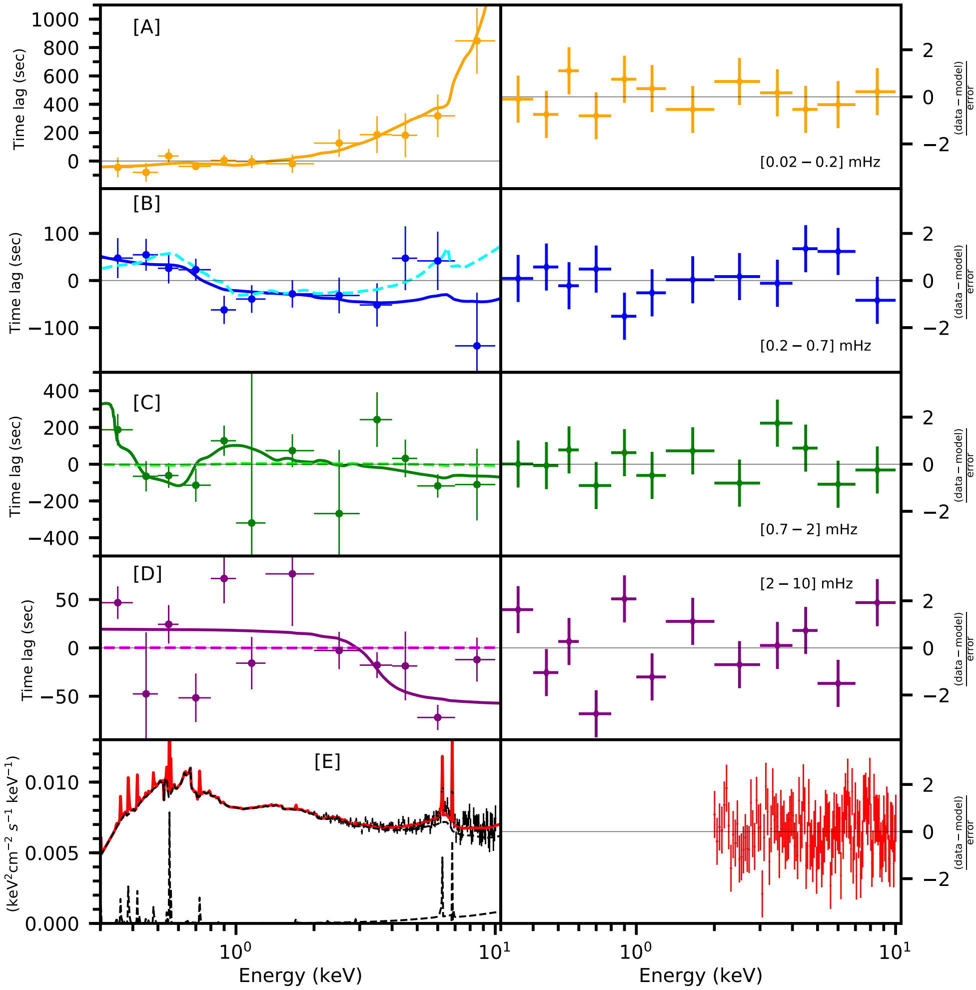

Figure 5.4: Joint fit of the time-averaged energy spectrum and the lag energy spectra in different Fourier frequency ranges (specified in the panels). Left panels: data and best fitting Models 1 and 2, right panels: residuals of Model 2 (residuals of Model 1 are not shown). Panels A–D: time lag spectra; panel E: unfolded time-averaged spectrum. Time-averaged Models 1 and 2 are very similar, so panel E shows only Model 2; the dashed curves in panel E are the model components. The time-averaged spectrum is fitted in the $2-10$ keV energy range, the time lag spectra in $0.3-10$ keV. The solid curves in panels A–D represent Model 2 and the dashed curves in panels B–D Model 1 (which does not consider the first frequency range). Model curves are plotted with higher resolution than the data for clarity.

keV energy range, since the warm absorber will affect the energy dependence of the cross-spectrum even if it does not contribute to the time lags.

Model [3]

We fit simultaneously to the time-averaged spectrum and the complex cross-spectrum in the three highest frequency ranges, ignoring intrinsic hard lags. This model, hereafter Model [3], is therefore the same as Model [1], except the variability amplitude is considered in addition to the time lags and the time-averaged spectrum. The best fitting model is shown as dashed curves in panels B, C, D and E of Fig. 5.5, where the upper panels show the unfolded real and imaginary parts of the cross-spectrum and the bottom panel the unfolded time-averaged spectrum. However, we note that some model parameters are very poorly constrained, particularly the height of the source and the inner radius of the disc. The 90% confidence range of the former ranges from $1.5\,R_g$ (very close to the event horizon of the black hole) to more than $50\,R_g$. The latter is consistent with the ISCO within 90% confidence, but also with $28.5\ R_g$. The boost parameter is very similar to Model [1], even though its upper limit is not constrained. The black hole mass is the most poorly constrained, with only an upper limit of $0.6 \times 10^6 M_\odot$. This is likely because this model does not reproduce the reverberation feature in the lag spectrum, which provides the best mass constraint.

Model [4]

We now additionally model the cross-spectrum of the lowest frequency range, requiring us to again account for hard intrinsic lags with a pivoting power-law prescription. As we noticed in the previous fit, the model in panels B and D does not follow the shape of the data around the iron line range. Interestingly, the lowest frequency range (panel A) shows clear evidence of the reflection component in the real part of the cross-spectrum. This may indicate that the model can constrain the reflection component in the variability amplitude at low frequency even though the lags are dominated by the intrinsic continuum variability, although the same does not happen in any of the higher frequency ranges. Nevertheless the reduced χ^2 of $\chi^2/\mathrm{dof} = 144.4/145$ indicates an acceptable fit. The black hole mass is $53^{+19}_{-8} \times 10^6 M_\odot$ which is different from the other models. However, in order to achieve this fit, it was necessary to relax our hard upper limit of 3 on the boost parameter. With this limit in place, almost all of the parameters are poorly constrained and the mass has an upper limit of $1.5 \times 10^6 M_\odot$ and a best fitting value of $\sim 1\ M_\odot$. When allowed to vary freely, the boost parameter becomes very large ($1/\mathcal{B} = 8.5^{+1}_{-1}$). The inner radius is close to the black hole, suggesting a contribution from the inner part of the disc, although the peak of the ionisation increases drastically. This is due to the broad iron line showing up in the real part of the low frequency range cross-spectrum that is not evident in the lag spectrum at the same frequency.

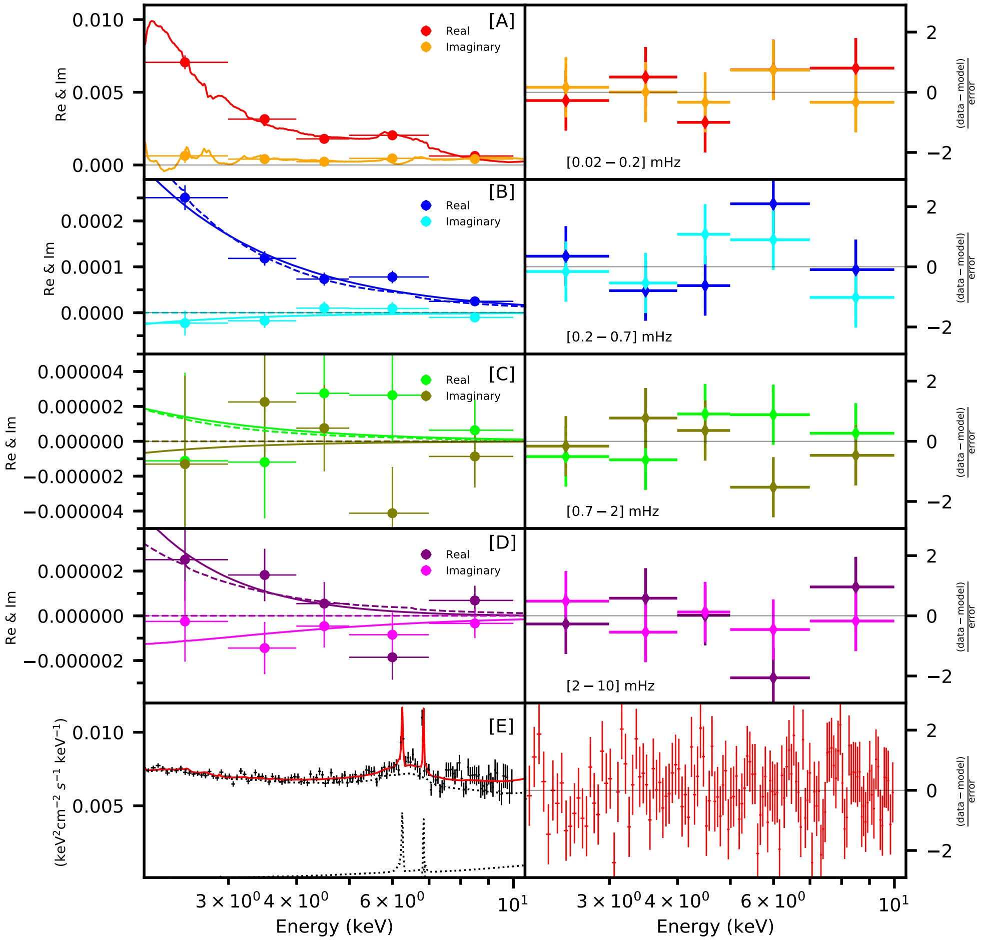

Figure 5.5: Left panels: unfolded spectra of the real and imaginary part of the cross-spectrum and the time-averaged energy spectrum with the best fitting Model 3 (dashed lines) and Model 4 (solid lines). Right panels: residuals of the best fitting Model 4. Panel E shows the time-averaged spectrum of Model 4 (not Model 3) and the different components (dotted lines). The time-averaged spectrum of Model 3 is very similar to Model 4. Panels from A to D show the complex cross-spectrum in 4 ranges of frequencies (specified in the panels). Model 4 fits all the ranges, whereas Model 3 does not consider the first one.

5.4 Discussion

In this work we have jointly modelled the time-averaged X-ray spectrum and the short timescale X-ray variability of the Seyfert galaxy Mrk 335 using our relativistic reflection model RELTRANS. We considered the high-flux *XMM-Newton* observation from 2006, in which Kara et al. (2013a) found evidence of reverberation lags the $\sim 0.2-0.7$ mHz Fourier frequency range. We first modelled the time-averaged energy spectrum alone (Model [B]), before additionally modelling the lag-energy spectrum in the frequency ranges (> 0.2 mHz) thought to be dominated by reverberation lags (Models [0] and [1]). We then included a prescription to account for the intrinsic hard lags seen at low frequencies (Mastroserio et al. 2018, 2019) in order to additionally model the $0.02-0.2$ mHz frequency range (Model [2]). Finally, we extended our analysis to model the complex cross-spectrum for the reverberation dominated frequency ranges (Model [3]) and the full range of frequencies (Model [4]).

5.4.1 Model comparison

All of our fits have acceptable reduced χ^2. However, some of the model fits do not reproduce the observed iron K feature in the $0.2-0.7$ mHz lag-energy spectrum (see Fig. 5.6). In these cases (Models [3] and [4]), it is likely that the model does not adequately describe the data, but the χ^2 statistic is dominated by the time-averaged spectrum and so ends up overall being statistically acceptable. The best-fitting[1] timing model is Model [0]. This simultaneously describes the time-averaged spectrum and the $0.2-0.7$ mHz lag-energy spectrum. The model predicts an iron K feature of moderate strength in the lag spectrum (Fig. 5.6), and provides an excellent statistical description of the data.

Model [1] additionally models the time lags for two higher frequency ranges ($0.7-2$ and $2-10$ mHz) only accounting for the reverberation lags. Whilst this fit is statistically acceptable, its null-hypothesis probability is worse than that for Model [0]. Indeed, the $2-10$ mHz lag spectrum includes a dip around the iron line that the model does not reproduce. This could be a phase-wrapped reverberation feature. Phase-wrapping occurs when the time lag is greater than half a cycle of the considered Fourier frequency, and is a direct result of the periodicity in the phase range $-\pi$ to π of the cosines forming the Fourier basis functions. Therefore, if the time lag at Fourier frequency ν is $t_{\rm lag} > (2\nu)^{-1}$, phase-wrapping will occur every $(2\nu)^{-1}+n(\nu)^{-1}$ where n is an integer number. Similar to car wheels appearing to be stationary when viewed on low frame-rate film, the first phase wrap induces a jump by 2π in phase (between π and $-\pi$, so reversing the sign), the next phase-wrap (i.e. $3/2\nu$ or $-1/2\nu$) does the same, and so on. The time lags that we estimate from the observations (by multiplying phase

---

[1] i.e. the model with the highest null-hypothesis probability, defined as the probability that the χ^2 would be at least this large if the model were exactly correct.

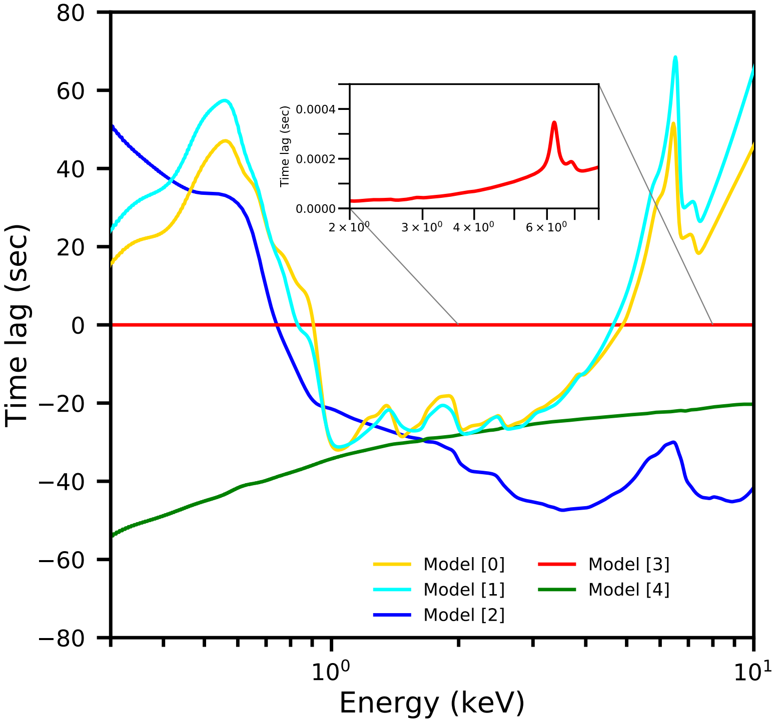

Figure 5.6: Lag energy spectra in the frequency range $0.2 - 0.7$ mHz for Model [0]-[4]. The inset plot shows that in Model [3] the reverberation lag is present but it contributes less than a millisecond.

lag by $1/(2\pi\nu)$) in the $2-10$ mHz frequency range ($t_{\rm lag} \sim 50$ s; Fig. 5.4D) correspond to phase lags of ~ 0.3 cycles, and so some of the jumps from one energy channel to the next may result from phase-wrapping. If the model describes the observation perfectly, then phase-wrapping features can be very constraining. However, we clearly see that Model [1] does not reproduce any features in the highest frequency lag spectrum. This may be due to some of the simplistic model assumptions we employ (e.g. the lamppost geometry) preventing the model from being accurate enough to intricately reproduce any phase-wrapping features in the data. We do, however, note that the error bars on the lag spectrum are slightly under-estimated in this plot. This is for two reasons. First, whenever an error bar extends above a phase lag of 0.5 cycles (i.e. π radians), the top part of the error bar should also appear at the bottom of the plot. Similarly, the bottom part of error bars that extend below -0.5 cycles should also appear at the top of the plot. Second, the standard error formula we use for the time lags (Bendat & Piersol 2000) is derived from the theoretical error on the real and imaginary parts of the cross-spectrum *assuming* that the phase lag error is $\ll \pi$. This assumption begins to break down for the highest frequency range explored here.

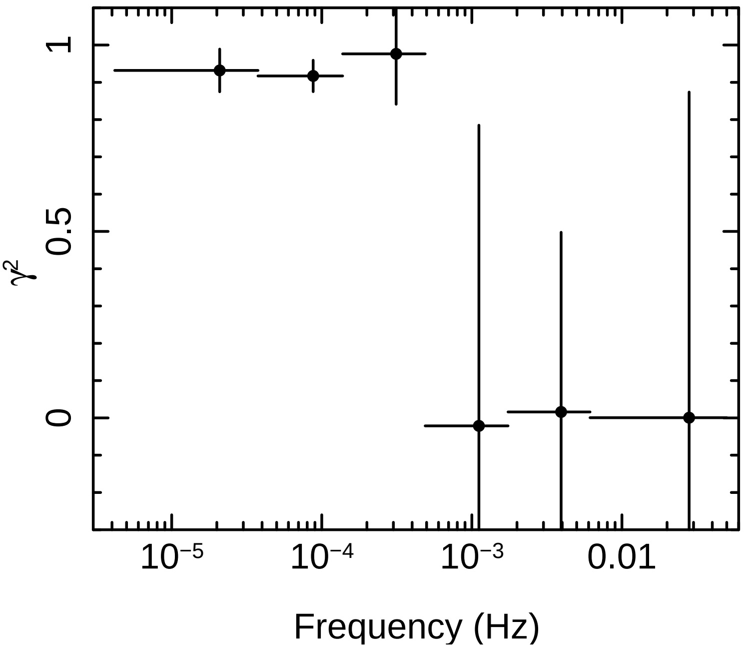

Figure 5.7: Intrinsic squared coherence (see equation 8 in Vaughan & Nowak 1997) between the iron line energy band ($5-7$ keV) and the continuum dominated $1-4$ keV energy band.

Therefore, the poorer fit quality associated with Model [1] may potentially simply be explained by under-estimated error bars. In Model [2] we also consider the lowest frequency range ($0.02-0.2$ mHz) introducing hard intrinsic lags into the model, and we obtain a higher quality fit. This is mostly due to the additional freedom afforded by the additional parameters of the intrinsic lag mechanism that enable the model to naturally reproduce the shape of the lowest frequency lag spectrum and also make the model sufficiently flexible to also affect the higher frequencies. Nevertheless, it is encouraging that Models [0-2] have fairly similar parameters, particularly the black hole mass.

The issue of underestimating the time lag error bars due to the periodicity of the phase does not occur for the cross-spectrum. However, although the reduced χ^2 is statistically acceptable for the two fits to the cross-spectrum, Models [3] and [4] miss the reverberation feature , and in particular the black hole mass of Model [3] is implausible. Fig. 5.6 shows the 0.2-0.7 mHz lag spectrum for each model. We see that the lags are very small for Model [3], with the iron K feature peaking at less than a millisecond (see inset). Since we can fit the lag and not the cross-spectrum, we conclude that our model is failing to reproduce the modulus of the cross-spectrum. A direct consequence is that the fit prioritizes the modulus, because of its smaller error bars, and so this leads to the implausible Model [3] mass value and no reverberation features. The reason why the model fails to fit the correlated variability amplitude could be the below unity coherence of Mrk 335, which our model does not account for. Fig. 5.7 shows that the intrinsic coherence between the iron line energy band and the continuum dominated energy band becomes consistent with zero around 0.5 mHz. The RELTRANS model assumes unity coherence at all frequencies (Mastroserio et al. 2018; Ingram et al. 2019).

5.4.2 Disc inner radius and black hole spin

For most of the models explored here, the best fitting disc inner radius is larger than that found by Keek & Ballantyne (2016), who fixed $r_{\rm in}$ to the ISCO and inferred a black hole spin of $a = 0.89 \pm 0.05$ from the time-averaged spectrum of the same observation that we consider here. Since they used RELXILL for their fit, as noted in Section 5.3.1, the configuration of RELTRANS we use here is different in two ways: it uses an emissivity profile calculated in the lamppost geometry instead of parameterizing it with a broken power-law function, and it considers a radial ionisation profile instead of a constant ionisation parameter. These changes appear to increase the inferred disc inner radius, and therefore decrease the inferred black hole spin parameter if $r_{\rm in}$ is assumed to be at the ISCO. In fact, for our fit to the time-averaged spectrum alone (Model [B]), the 90% lower limit on $r_{\rm in}$ is larger than the largest possible value of the ISCO (9 R_g for a maximally retrograde spin), indicating that the disc may be truncated by some physical process other than general relativity, as is often claimed for black hole X-ray binary discs in the hard state (e.g. Esin et al. 1997; Done et al. 2007). The disc inner radius is slightly smaller for our best fitting model (Model [0]), which considers both the time-averaged spectrum and the $0.2-0.7$ mHz lag spectrum. The best fitting $r_{\rm in}$ value for this model is larger than the ISCO of a Schwarzschild black hole (6 R_g), implying either a truncated disc or a retrograde spin. However, $r_{\rm in}$ is also consistent with the ISCO of a maximally spinning black hole within 90% confidence. Chainakun et al. (2016a) also carried out a joint fit to the time-averaged spectrum and $0.2-0.7$ mHz lag spectrum for the data set we consider here, but they fixed $r_{\rm in}$ to the ISCO and the spin to $a = 0.998$ in their fit, and so we cannot compare our results in this respect.

It is also notable that the iron abundance yielded by our models, $A_{\rm Fe} \sim 0.5-0.7$, differs significantly from the large value of $A_{\rm Fe} = 3.9 \pm 0.7$ returned by the fits of Keek & Ballantyne (2016). It is common for X-ray reflection modelling to measure significantly super-solar iron abundances both for AGN and black hole X-ray binaries (e.g. Dauser et al. 2012; Parker et al. 2015; García et al. 2015; see García et al. 2018 for a brief review). It is possible that including a radial ionisation profile, as we have done here, goes some way to reducing the inferred iron abundance, as speculated by Ingram et al. (2019). Chainakun et al. (2016a) included an ionisation profile in their model, albeit of a different form, and they found $A_{\mathrm{Fe}} = 2^{+3}_{-1}$.

5.4.3 Black hole mass

Our fits that consider timing properties are sensitive to black hole mass. Fig. 5.8 (top) shows the $\Delta\chi^2$ versus mass curves for each of these models. Fig. 5.8 (bottom) shows another representation of this. Instead of $\Delta\chi^2$, which gives no indication of the relative goodness of fit of each model, we plot a probability derived from the χ^2 and the number of degrees of freedom, n, for each model. The peak of each distribution is equal to the null-hypothesis probability; i.e. the probability that χ^2 would be at least as big as the minimum χ^2 of the model, χ^2_{min}, under the assumption that this model is exactly correct. The shape of each distribution is set by $\Delta\chi^2 = \chi^2 - \chi^2_{\mathrm{min}}$, such that the probability plotted on the y-axis is $p = P(n/2, \chi^2_{\mathrm{min}}/2)P(1/2, \Delta\chi^2/2)$, where $P(a, x)$ is the incomplete gamma function. This way, we can see for example that Model [0] has the best goodness of fit, whereas the Model [1] fit is comparatively poor.

We see that the models considering the time-averaged spectrum jointly with the time lags (Models [0]-[2]) all return similar best fitting values of black hole mass, $M \sim [1-3] \times 10^6\ M_\odot$, whereas the models that consider the time-averaged spectrum and the entire cross-spectrum give different values. The best-fitting mass value of $M \sim 1\, M_\odot$ for Model [3] is completely implausible, whereas the Model [4] best fit of $M \sim 50 \times 10^6\ M_\odot$ is reasonable. However, as discussed in Section 5.4.1, the fits to the cross-spectrum do not seem to adequately reproduce the properties of the data, which we suggest to be due to our model effectively assuming unity coherence in tension with the data. Furthermore, the fit requires an unrealistically large boost parameter ($1/\mathcal{B} \sim 8$), suggesting a different geometry than the lamppost, which is inconsistent with the reverberation calculation in the model. Similarly to the Ingram et al. (2019) value of $M = 6.8^{+5.5}_{-5.9} \times 10^6 M_\odot$, our mass is a good bit smaller than the optical reverberation mass measurements ($M = 14.2 \pm 3.7 \times 10^6 M_\odot$; Peterson et al. 2004 and $26 \pm 8 \times 10^6 M_\odot$; Grier et al. 2012). The Ingram et al. (2019) model was also consistent with these higher masses, as long as $0.2 - 0.7$ mHz is actually in the phase-wrapping regime (see their Figure 16). However, this is no longer the case now that we jointly fit to the time-averaged spectrum. Chainakun et al. (2016a) use a similar procedure to us and get a higher mass. It is not clear why our results are so different, although we have a different assumption for the radial dependence of the ionisation profile and we let r_{in} be free instead of fixing it to the smallest possible value. Moreover, they fit the time-averaged energy spectrum in a larger energy range $0.3 - 10$ keV than ours and model the time lag with a reverberation model and a phenomenological power-law to account for the intrinsic lags. Emmanoulopoulos et al. (2014) also get a higher black hole mass. Although they use the transfer function approach to model the reverberation lag, they use a different procedure than ours,

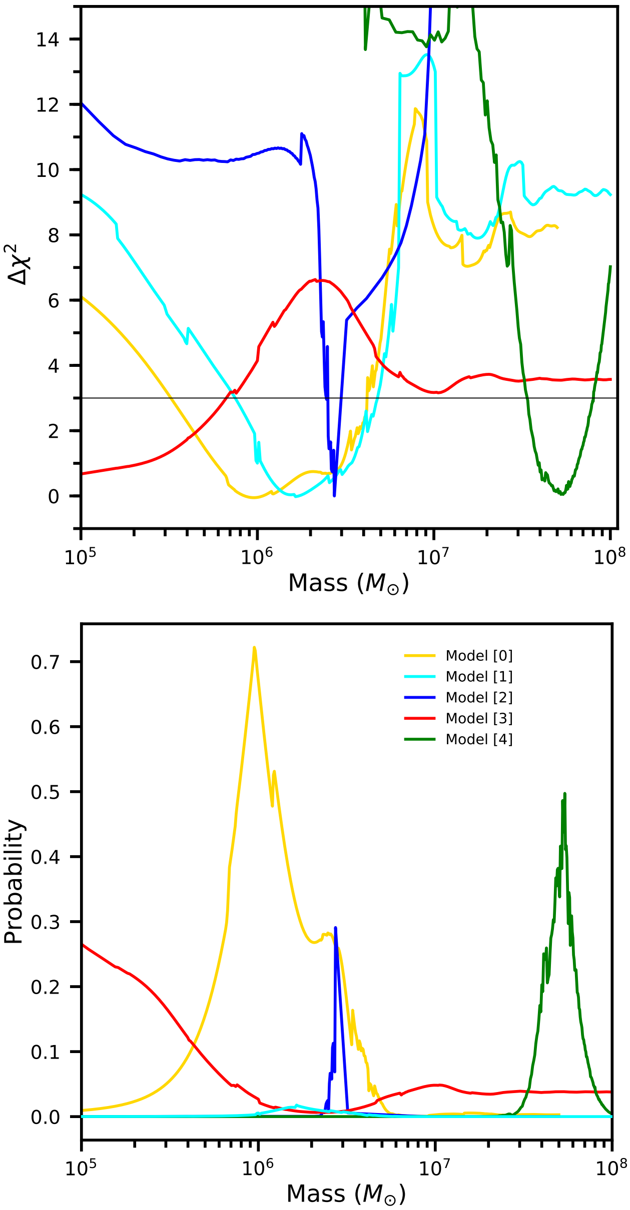

Figure 5.8: Top panel: $\Delta\chi^2$ as function of mass for 5 models considered in the paper. For every value of the mass we perform a new fit (with the mass value fixed) and calculate the difference of the new χ^2 with the best fit χ^2. This is done for every model. This procedure does not account for the different degrees of freedom of each model. The black line is the 1 σ level. Bottom panel: null-hypothesis probability as a function of mass value for 5 Models. This representation makes it possible to compare the goodness of fit for different models and their mass values. See the text for a detailed explanation of the probability calculation.

fitting the only the lag as a function of frequency (lag between 0.31 keV and 1.54 keV X-ray energy bands) and modelling the positive hard lags with a power-law.

5.4.4 Assumptions

In order to calculate a radial ionisation profile, our model assumes the density profile corresponding to zone A of the Shakura & Sunyaev (1973) disc model, in which the dominant sources of pressure and opacity are, respectively, radiation and electron scattering. The maximum value of the ionisation parameter in the disc is left as a model parameter. In the case of zone A, the maximum ionisation does not occur at the inner radius, because the stress-free inner boundary condition leads to the density becoming very high at $r_{\rm in}$, and consequently to the ionisation parameter dropping. According to Shakura & Sunyaev (1973) the outer limit of zone A in an AGN with luminosity 5×10^{43} erg/s (as is measured in the $0.5-10$ keV range for this observation; Grupe et al. 2007) and assuming viscosity parameter $\alpha = 0.01$ and black hole mass 10^6 or 50×10^6 $M_\odot$ is $R_{\rm ab} \sim 1000$ R_g or $\sim$ $72R_g$ (increasing α increases $R_{\rm ab}$). Thus we can comfortably consider most of the emission to come from a zone A density profile accretion disc.

We assume the lamppost geometry and account for hard intrinsic lags with an analytic pivoting power-law prescription, enabling the model to be fast enough to fit to data. However, Wilkins & Gallo (2015) inferred that the corona is radially extended (to around $26R_g$) over the disc during the high-flux epoch that we consider, and then contracts when the flux decreases. In such an extended corona, intrinsic hard lags may arise due to inward propagation of accretion rate fluctuations (Wilkins et al. 2016). It seems likely that our simple model does not provide an adequate approximation of such a geometry, which may explain why we were unable to find a physically plausible fit to the cross-spectrum. Indeed, below-unity coherence, as is observed here, is naturally expected from propagation across an extended corona (e.g. Rapisarda et al. 2017b), but much harder to explain for a very compact corona. Including a more realistic coronal and disc (e.g. Taylor & Reynolds 2018b) geometry in future may therefore enable us to find a more satisfactory fit, and may also go some way to relieving the tension that our black hole mass measurements have with the existing optical reverberation measurements. It is interesting to note that our model seems to work much better for the black hole X-ray binary Cygnus X-1 (Mastroserio et al. 2019). We cannot currently rule out this being due to the two systems having different coronal geometries. However, we note that observations of AGN probe much faster timescales (in terms of R_g/c) in the system, and so it could simply be that the model is accurate for long timescales in the system but less so for the shortest timescales.

5.5 Conclusions

We have modelled the X-ray spectral and timing properties of an observation of Mrk 335. Our model provides a good description of the time-averaged spectrum and lag spectrum. The best fitting disc inner radius for most of the models we fit is larger than that found by previous analyses (e.g. Keek & Ballantyne 2016), implying a lower black hole spin than previously thought (even retrograde) or a truncated disc. Indeed, for our best fitting model (Model [0]), the best fitting value of disc inner radius is 10.5 R_g, although the 90% lower bound is still consistent with the ISCO of a maximally spinning black hole. We also find a smaller (more plausible) value for the iron abundance than the previous spectral analysis by Keek & Ballantyne (2016). Our joint fits to the time-averaged spectrum and lag spectrum all return a black hole mass of $\sim 10^6\ M_\odot$ ($1.0^{+3.0}_{-0.7} \times 10^6 M_\odot$ for our best fitting model), which is lower than that measured by optical reverberation mapping ($M = 14.2 \pm 3.7 \times 10^6 M_\odot$; Peterson et al. 2004 and $26 \pm 8 \times 10^6 M_\odot$; Grier et al. 2012).

However, our joint fits to the time-averaged spectrum and the cross-spectrum, although statistically acceptable, are not physically plausible. The fit that ignores the Fourier frequency range dominated by intrinsic hard lags yields an implausibly low black hole mass, and the fit that accounts for intrinsic hard lags, although returning a reasonable black hole mass ($M \sim 50 \times 10^6\ M_\odot$), requires a reflection fraction that is inconsistent with the assumed geometry. This indicates that, whilst our model can explain the time lags, it fails to adequately describe the variability amplitude of the reflected emission as a function of energy. This could be because the intrinsic coherence for this observation drops significantly below unity for frequencies above ~ 1 mHz, whereas the model assumes unity coherence. Incorporating a more sophisticated geometry into the model in future may help with this.

A

Appendices to Chapter 2

A.1 Complex covariance analysis

Analysing real and imaginary parts means that any linearity of the signal in the time domain is preserved in the frequency domain. This is not the case for amplitude and phase. Here we consider two simple explicit examples to illustrate the superiority of considering real and imaginary parts instead of amplitude and phase. The first concerns the response matrix of the instrument and the second concerns scenarios when multiple variable spectral components are present. We assume unity coherence and infinite ensemble averaging, allowing us to drop angle the brackets notation.

A.1.1 Instrument Response

It is often assumed that the instrument response can be applied to the cross-spectral amplitude (or covariance/rms), giving

$$|G_{\rm o}\left(I,\nu\right)| = \int_0^{+\infty} R_{\rm t}\left(E,I\right)|G\left(E,\nu\right)|dE \tag{A.1}$$

where $G_{\rm o}\left(I,\nu\right)$ is the observed complex covariance in the specific energy channel I and $R_{\rm t}\left(I,E\right)$ is the instrument response. Here, $G\left(E,\nu\right)$ is in units of photons per second per cm^2 per keV, and $G_{\rm o}$ is in units of counts per second. However, this expression is not correct in general. The correct expression is

$$G\left(I,\nu\right) = \int_0^{+\infty} R_{\rm t}\left(E,I\right)\, G\left(E,\nu\right)dE. \tag{A.2}$$

The amplitude of the complex covariance for channel I is then

$$|G_{\mathrm{o}}(I,\nu)| = \sqrt{\begin{array}{l}\left[\int_0^{+\infty} R_{\mathrm{t}}(E,I)\,\mathrm{Re}\left[G(E,\nu)\right]dE\right]^2 + \\ \left[\int_0^{+\infty} R_{\mathrm{t}}(E,I)\,\mathrm{Im}\left[G(E,\nu)\right]dE\right]^2\end{array}}\,. \tag{A.3}$$

where Re and Im respectively denote the real and the imaginary part. For $Re\left[G(E,\nu)\right] \neq 0$ and $Im\left[G(E,\nu)\right] \neq 0$, Eq. A.1 is therefore incorrect. In the special case where $Re\left[G(E,\nu)\right] = 0$ or $Im\left[G(E,\nu)\right] = 0$, Eq. A.3 does reduce to Eq. A.1.

Since the observed phase lags are often fairly small, Eq. A.1 is, in practice, often fairly close to true. However, using our formalism of treating real and imaginary parts separately introduces no mathematical errors, and is no more difficult to implement than considering the amplitude and the phase. It is clear the instrument response cannot be applied to the phase in a manner analogous to Eq. A.1.

A.1.2 Multiple Components Fitting

Consider a signal $s_1(E,t) = p(E)\,a(t)$ and another signal $s_2 = q(E)\,b(t)$, with Fourier transforms $p(E)\,A(\nu)$ and $q(E)\,B(\nu)$. Using Eq. 2.1 it follows from the linearity of the Fourier transform that the cross-spectrum of $s_1(E,t) + s_2(E,t)$ is

$$C(E,\nu) = A(\nu)\,p(E)\,F^*(\nu) + B(\nu)\,q(E)\,F^*(\nu)\,; \tag{A.4}$$

i.e. simply the sum of the two individual cross-spectra. However, this linearity is lost for the amplitude and the phase lag. Setting, for simplicity, the amplitude and phase of the reference band to $|F(E_{\mathrm{r}}\nu)| = 1$ and $\phi_F(\nu) = 0$ respectively, the amplitude and phase lag of the cross-spectrum are

$$\begin{aligned} |C(E,\nu)| &= \sqrt{p^2|A|^2 + q^2|B|^2 + 2pq\mathrm{Re}\left[A\,B^*\right]} \\ \tan\phi_C(E,\nu) &= \left[\frac{p\,\mathrm{Im}\left[A\right] + q\,\mathrm{Im}\left[B\right]}{p\,\mathrm{Re}\left[A\right] + q\,\mathrm{Re}\left[B\right]}\right], \end{aligned} \tag{A.5}$$

In both expressions we have dropped the energy and frequency dependence of the components so as not to weigh the notation. We see that the expression of the amplitude has a cross term that would not appear if we simply added the amplitude of the two components. The exception is if the two components are in phase with each other, since in this case the amplitude of two vectors added in the complex plane is equal to the sum of the two amplitudes. Kotov et al. (2001) considered the case where the contribution of one component (e.g. $q(E)B(\nu)$) is small compared to the total spectrum ($q << p$), in that case a binomial expansion gives

$$\begin{aligned} |C(E,\nu)| \simeq & p\,|A|\sqrt{1+2\frac{q\,Re\,[A\,B^{*}]}{p\,|A|^{2}}} \\ \simeq & p\,|A| + q\,\frac{Re\,[A\,B]}{|A|} = p|A| + q|B|\cos\phi_{AB}, \end{aligned} \tag{A.6}$$

where ϕ_{AB} is the phase difference between A and B. Therefore, the contribution from the cross-terms in this case is small, but the normalisation of the second component is modified by a factor $\cos\phi_{AB}$. From Eq. A.5, it is clear that summing lags of two additive spectral components is not appropriate.

A.2 Response function

Eq. 2.7 in the text refers to emission from a specific patch of the accretion disc area. If the we consider flat space the area is expressed by $r\,dr\,d\phi$ and the total observed reflection spectrum varying in time is calculated by integrating the specific flux over the entire disc

$$R(E,t) = \int_{r_{\mathrm{in}}}^{r_{\mathrm{out}}}\int_{0}^{2\pi} K(r) g^{3} A(t-\tau)\,\mathscr{R}(E/g)\,r\,dr\,d\phi, \tag{A.7}$$

where we have not specified the r and ϕ dependence of g and τ for brevity. As defined in the main text, E is the observed energy and $\mathscr{R}$ is the restframe reflection spectrum. The factor $K(r)$ accounts for geometrical dilution of radiation from the the point source incident on the disc patch, and is given by

$$K(r) = \varepsilon(r)\,\frac{\cos i}{D^{2}} = \frac{h\,\cos i}{\left(h^{2}+r^{2}\right)^{3/2}\,D^{2}}. \tag{A.8}$$

The blue shift $g(r,\phi)$ is given by

$$g(r,\phi) = \frac{\sqrt{-g_{tt} - 2g_{t\phi}\omega - g_{\phi\phi}\omega^{2}}}{1+\omega r\sin\phi\sin i}, \tag{A.9}$$

where $\omega = 1/\left(r^{3/2}+a\right)$ is the angular velocity in the dimensionless units, and we have again ignored light-bending (see Ingram et al. 2015, 2017). Finally light-crossing lag, $\tau(r,\phi)$, (i.e. the difference between the path of the light traveling directly from the point source to the observer and the light reflecting from the disc divided over the speed of light $\tau = l/c$) is given by

$$\tau c = \sqrt{r^{2}+h^{2}} - r\sin i\cos\phi + h\cos i, \tag{A.10}$$

when light-bending is ignored.

A.3 Linearization

Taylor expanding Eq 2.7 around $\beta = 0$ gives

$$\begin{aligned} dR\left(r,\phi|E,t\right) \simeq & A\left[t-\tau(r,\phi)\right]\Bigg[\mathscr{R}\left(E/g(r,\phi)|\Gamma\right) - \beta\left(t-\tau(r,\phi)\right) \\ & \frac{\partial\mathscr{R}}{\partial\Gamma}\left(E/g\left(r,\phi\right),\Gamma\right)\Bigg] K(r)\, g^3\left(r,\phi\right) r\, \mathrm{d}r\, \mathrm{d}\phi. \end{aligned} \tag{A.11}$$

Setting $B\left(t\right) \equiv A\left(t\right)\beta\left(t\right)$, the reflected flux integrated over the entire disc is

$$\begin{aligned} R\left(E,t\right) \simeq & \int_{t'=0}^{t'=\infty}\int_{\phi=0}^{\phi=2\pi}\int_{r=r_{\text{in}}}^{r_{\text{out}}} A\left(t'\right)\delta\left(t-\tau-t'\right) \\ & \mathscr{R}\left(E/g\left(r,\phi\right)|\Gamma\right) K\left(r\right) g^3\left(r,\phi\right) r\,\mathrm{d}r\,\mathrm{d}\phi\, dt' - \\ & \int_{t'=0}^{t'=\infty}\int_{\phi=0}^{\phi=2\pi}\int_{r=r_{\text{in}}}^{r_{\text{out}}} A\left(t'\right)\delta\left(t-\tau-t'\right) \\ & \frac{\partial\mathscr{R}}{\partial\Gamma}\left(E/g\left(r,\phi\right)|\Gamma\right) K\left(r\right) g^3\left(r,\phi\right) r\,\mathrm{d}r\,\mathrm{d}\phi\, dt'. \end{aligned} \tag{A.12}$$

From the definition of a convolution

$$A(t)\otimes z\left(E,t\right) \equiv \int_0^\infty z\left(E,t-t'\right) A(t')\,\mathrm{d}t', \tag{A.13}$$

where $z\left(E,t\right)$ is an arbitrary function of energy and time. We can simplify to

$$R\left(E,t\right) = A(t)\otimes w\left(E,t\right) - B(t)\otimes w_1\left(E,t\right), \tag{A.14}$$

where $w\left(E,t\right)$ and $w_1\left(E,t\right)$ are defined in the main text. For the continuum, it is clear from Eq. 2.10 that

$$D\left(E,t\right) \simeq \left[A\left(t\right) + B\left(t\right)\ln E\right] E^{-\Gamma}\mathrm{e}^{-E/E_{\text{cut}}}. \tag{A.15}$$

Summing direct and reflected components, and using the convolution theorem gives Eq. 2.13 in the main text. The transfer functions can be written analytically as

$$\begin{aligned} W\left(E,\nu\right) &= \int_{r_{\text{in}}}^{r_{\text{out}}}\int_0^{2\pi} \mathrm{e}^{i2\pi\nu\tau} K(r) g^3 \mathscr{R}\left(E/g|\Gamma\right) r\,\mathrm{d}r\,\mathrm{d}\phi \\ W_1\left(E,\nu\right) &= \int_{r_{\text{in}}}^{r_{\text{out}}}\int_0^{2\pi} \mathrm{e}^{i2\pi\nu\tau} K(r) g^3 \frac{\partial\mathscr{R}}{\partial\Gamma}\left(E/g|\Gamma\right) r\,\mathrm{d}r\,\mathrm{d}\phi, \end{aligned} \tag{A.16}$$

where we neglected the r and ϕ dependency of g and τ for brevity. In our code, we first calculate transfer functions for $\mathscr{R} = \delta\left(E - 1\text{keV}\right)$ and $\frac{\partial\mathscr{R}}{\partial\Gamma} = \delta\left(E - 1\text{keV}\right)$ and then perform convolution operations in the energy variable with $\mathscr{R}\left(E|\Gamma\right)$ and $\frac{\partial\mathscr{R}}{\partial\Gamma}\left(E|\Gamma\right)$ for obtaining W and W_1 respectively.

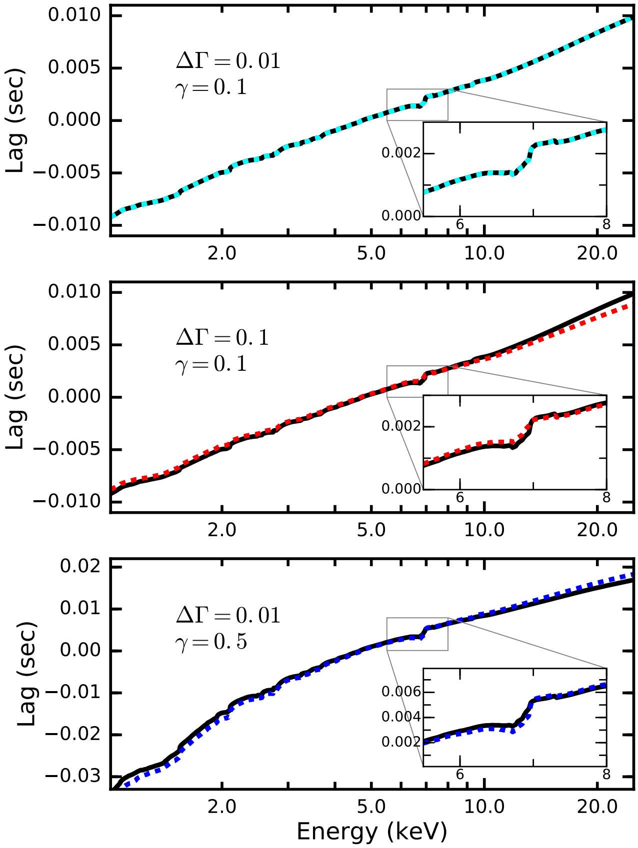

Figure A.1: Predicted time lags as a function of energy for 2.5Hz. For all the panels the solid curves are the exact prediction (made in the time domain without Taylor expansion) and the dashed curves are calculated using the Eq. 2.10 and 2.11 (first-order Taylor expansion). For all the panels, $\phi_A = 0\,\text{rad}$ and $\phi_B = 0.2\,\text{rad}$. In all panels we use the parameters: $\Gamma = 2$, $i = 30°$, $r_{\text{in}} = 10$, $r_{\text{out}} = 100$, $h = 10\,R_{\text{g}}$, $a = 0.998$, $M = 10M_{\odot}$, $\log_{10}\xi = 3.1$, $A_{\text{Fe}} = 1$

We checked under which conditions the linearisation of both the continuum and reflection expression is valid. Fig. A.1 shows the lag-energy spectrum at 2.5 Hz calculated in the time domain without Taylor expanding either the continuum or the reflection expressions (solid lines) and analytically using first order linearisation (dashed lines). We used a single frequency sine wave as input of the exact calculation of the lags, i.e. $A\,(t) \propto 1 + \sin\left(2\pi\nu t - \phi_{\text{A}}\right)$ and $B\,(t) \propto \sin\left(2\pi\nu t - \phi_{\text{B}}\right)$. The top panel (a) shows that for a reasonable choice of $\Delta\Gamma$ and a value of γ similar to what we found from the fitting procedure the two curves match. However, if we decided to increase one of the two parameters (central and bottom panel) the Taylor expansion is less accurate.

A.4 Convolution of the theoretical model with the instrument response

Our model for the Fourier transform of the spectrum, $S(E,\nu)$, is given by Eq. 2.13 in the main text. Setting $Z(E,\nu) = E^{-\Gamma}\mathrm{e}^{-E/E_{\mathrm{cut}}} + W(E,\nu)$ and $Z_1(E,\nu) = E^{-\Gamma}$ $\mathrm{e}^{-E/E_{\mathrm{cut}}} \ln E - W_1(E,\nu)$ gives the simplified form

$$S(E,\nu) = A(\nu)Z(E,\nu) + B(\nu)Z_1(E,\nu). \tag{A.17}$$

Note that Z and Z_1 are complex in general, due to the phase lags introduced by the transfer functions W and W_1. Convolving this around the instrument response (using the same procedure explained in Eq. A.2 in Appendix A.1) gives the Fourier transform of the observed spectrum

$$S(I,\nu) = A(\nu)Z(I,\nu) + B(\nu)Z_1(I,\nu), \tag{A.18}$$

where I indicates the I^{th} energy channel. The Fourier transform of reference band flux is $F(\nu)$, and therefore our model for the complex covariance of the I^{th} energy channel is

$$G(I,\nu) = \frac{A(\nu)F^*(\nu)Z(I,\nu) + B(\nu)F^*(\nu)Z_1(I,\nu)}{|F(\nu)|}. \tag{A.19}$$

To simplify further, we can simply set

$$\alpha(\nu)\mathrm{e}^{i\phi_A(\nu)} = \frac{A(\nu)F^*(\nu)}{|F(\nu)|} \tag{A.20}$$

$$\alpha(\nu)\gamma(\nu)\mathrm{e}^{i\phi_B(\nu)} = \frac{B(\nu)F^*(\nu)}{|F(\nu)|} \tag{A.21}$$

to get

$$G(I,\nu) = \alpha(\nu)\left[\mathrm{e}^{i\phi_A(\nu)}Z(I,\nu) + \gamma(\nu)\mathrm{e}^{i\phi_B(\nu)}Z_1(I,\nu)\right]. \tag{A.22}$$

This expression is identical to Eq. 2.15 that we derived in the main text convolving the final complex covariance model (Eq. 2.14) with the instrument response.

A.5 Reference band

Following Revnivtsev et al. (1999) and Gilfanov et al. (2000), who analysed the observations considered here, we choose channels $5-7$ ($2.84-3.74$ keV) as our reference band. This choice is motivated by these channels having high count rates and being disjunct from the 'science' channels (and thus ensuring statistical independence between the reference band and all of the science channels). Moreover the $2.84-3.74$

keV range does not contain any of the reflection features that we are interested in observing. When the complex covariance is calculated (for the data) in the reference band energy range, the imaginary part is identically zero because the complex covariance of the reference band with itself has zero phase by definition. This could, in principle, impose an additional constraint that involves all the continuum parameters of the model:

$$\sum_{I=I_1}^{I_2} \mathrm{Im}\left[G(I,\nu)\right] = 0, \tag{A.23}$$

where I indicates the I^{th} energy channel, I_1 to I_2 set the reference band channel range and $G(I,\nu)$ is defined in Eq. A.2. In our case it is not possible to apply this extra condition because the available instrument response $R'_{\mathrm{t}}(E,I)$ is poorly calibrated in the energy range of the reference band, while the relation between $G(E,\nu)$ and $G(I,\nu)$ is of course always defined by the *true* instrument response $R_{\mathrm{t}}(E,I)$. A mathematical way of looking at it is that we construct a model for the Fourier frequency dependent spectrum $S(E,\nu)$, which we cross with the Fourier transform of a model reference band, $F(\nu)$, to get the predicted complex covariance

$$G(E,\nu) = \frac{S(E,\nu)F^*(\nu)}{|F(\nu)|}. \tag{A.24}$$

If we had a response matrix that were well calibrated for the reference band energy channels, we could self-consistently calculate the reference band Fourier transform from our spectral model

$$F(\nu) = \int_0^{\infty} \sum_{I_1}^{I_2} R_t(E,I)S(E,\nu)dE. \tag{A.25}$$

However, we do not know the true response $R_{\mathrm{t}}(E,I)$, and so we simply leave the phase angle of the unity magnitude complex number $F(\nu)/|F(\nu)|$ as a model parameter that gets swallowed up into the definition of the parameters $\phi_A(\nu)$ and $\phi_B(\nu)$. In order to calculate $G(I,\nu)$ to fit to the data, we convolve $G(E,\nu)$ with the *available* response $R'_t(E,I)$. This response is actually well calibrated in the range where we fit it to the data, so assuming the model is correct we obtain the correct values for the fit parameters and hence correctly recover $G(E,\nu)$. If we could convolve this $G(E,\nu)$ with the true response $R_{\mathrm{t}}(E,I)$, the $G(I,\nu)$ obtained from this operation would satisfy condition A.23. However, if we convolve $G(E,\nu)$ with the available response $R'_{\mathrm{t}}(E,I)$ which is poorly calibrated and hence differs from $R_{\mathrm{t}}(E,I)$ between I_1 and I_2, we obtain

$$\frac{\int_0^{\infty} \sum_{I_1}^{I_2} R'_{\mathrm{t}}(E,I)S(E,\nu)dE \ F^*(\nu)}{|F(\nu)|} = \frac{F'(\nu)F^*(\nu)}{|F(\nu)|}, \tag{A.26}$$

whose imaginary part is not identically zero. For this reason, using the available response, condition A.23 is not expected to apply to our chosen reference band. Indeed, when we perform this experiment this turns out to be the case, although the discrepancy is not very large, indicating the calibration, while poor, is still passable even in the energy range of the reference band. It is worth noting that the poor calibration of the reference band does not affect our measurements of $G(E, \nu)$. Since we divide through by the modulus of $F(\nu)$, all that is affected is the phase of our reference band model $F(\nu)$. At any given frequency this only introduces a phase offset that is the same at each energy, not affecting the physically meaningful phase differences between energy bands. In the absence of a physical time series model, however, the phase differences between Fourier frequencies in a given energy band can not be used to constrain the physical parameters.

B

Appendices to Chapter 3

B.1 Area of a disk ring

The proper area of a disk annulus of width dr as measured by a stationary observer is given by $d^2x = 2\pi\sqrt{g_{rr}g_{\phi\phi}}dr$ (see e.g. Wilkins & Fabian 2012). The disk area element we are after for our calculation is measured in the disk frame, bringing in a factor of γ^{ϕ}, which is the Lorentz factor of the orbiting disk element. Substituting in the components of the Kerr metric gives

$$\frac{dA_{\rm ring}}{dr} = 2\pi\gamma^{\phi}\sqrt{\frac{r^4 + a^2r^2 + 2a^2r}{r^2 - 2r + a^2}}. \tag{B.1}$$

This equation agrees with the formula derived by Wilkins & Fabian (2012) and Dauser et al. (2013), except for a small typographical error in Dauser et al. (2013). We see that, in the limit $r >> 2$, this reduces to $2\pi r$, as we would expect.

Formulae for the Lorentz factor are presented in Bardeen et al. (1972) (hereafter BPT72) and Dauser et al. (2013). However, a very small error in BPT72 has propagated into the later literature. We therefore present a derivation here. In order to do this, we must first define a local non-rotating frame (LNRF) in which $r =$constant, $\theta =$constant and $\phi = \omega t+$constant. Here, $\omega = -g_{t\phi}/g_{\phi\phi}$ is the term that allows the reference frame to rotate with inertial frames (i.e. the frame dragging effect). For any stationary, axisymmetric, asymptotically flat spacetime, we can write the line element $ds^2 = g_{\mu\nu}dx^{\mu}dx^{\nu}$ as

$$ds^2 = -{\rm e}^{2\nu}dt^2 + {\rm e}^{2\psi}(d\phi - \omega dt)^2 + {\rm e}^{2\mu_1}dr^2 + {\rm e}^{2\mu_2}d\theta^2, \tag{B.2}$$

where the exponentials are defined in equations 2.3 and 2.5 of BPT72 for the case of the Kerr metric. Setting $M = 1$ in the BPT72 equations gives the dimensionless units we employ here.

We can represent the 4-velocity in the LNRF as $u^{(a)} = u^{\mu} e^{(a)}_{\mu}$, where the components of the tetrad of basis vectors are given by $e^{(i)} = e^{(i)}_{\mu} dx^{\mu}$. The (covariant) tetrad of basis vectors for the LNRF is (BPT72 equation 3.2)

$$e^{(t)} = \mathrm{e}^{\nu} dt, \quad \mathrm{e}^{(r)} = \mathrm{e}^{\mu_1} dr, \quad \mathrm{e}^{(\theta)} = \mathrm{e}^{\mu_2} d\theta, \quad \mathrm{e}^{(\phi)} = -\omega \mathrm{e}^{\psi} dt + \mathrm{e}^{\psi} d\phi, \tag{B.3}$$

where it is a long-standing travesty that the letter e is used both for the basis vectors and as the exponential number (we try to clear this up by using an italicised font for the basis vectors). This gives

$$\begin{aligned} \mathbf{e^{(t)}}_{\mu} &= (\mathrm{e}^{\nu}, 0, 0, 0), \quad & \mathbf{e^{(r)}}_{\mu} &= (0, \mathrm{e}^{\mu_1}, 0, 0), \\ \mathbf{e}^{(\theta)}{}_{\mu} &= (0, 0, \mathrm{e}^{\mu_2}, 0), \quad & \mathbf{e}^{(\phi)}{}_{\mu} &= (-\omega^{\psi}, 0, 0, \mathrm{e}^{\psi}). \end{aligned} \tag{B.4}$$

The covariant tetrad can be derived from the definition $e^{(a)}_{\mu} e^{(b)}_{\nu} g^{\mu\nu} = \eta^{(a)(b)}$, and the contravariant tetrad from $e^{\mu}_{(a)} e^{\nu}_{(b)} g_{\mu\nu} = \eta_{(a)(b)}$, where η is the Minkowski metric.

The 3-velocity is $v^{(i)} = u^{(i)}/u^{t}$. For circular, equatorial orbits, the only non-zero component of the 3-velocity is the ϕ component, which is given by

$$v^{(\phi)} = (\Omega_{\phi} - \omega)\mathrm{e}^{\psi - \nu} \tag{B.5}$$

where $\Omega_{\phi} = u^{\phi}/u^{t}$ is the angular velocity of the disk element. In the Kerr metric, this is $\Omega_{\phi} = \pm 1/(r^{3/2} \pm a)$, where the top and bottom signs are respectively for prograde and retrograde spin. Equation (B.5) is the same as equation 3.10 in BPT72 except for a small typographical error in the index of the exponential in the BPT72 version. Subbing in the Kerr metric gives

$$v^{(\phi)} = \frac{r^2 + a^2 - 2ar^{1/2} + 2r^{-1}(a^2 \pm a^2)}{\Delta^{1/2}(r^{3/2} \pm a)}, \tag{B.6}$$

where $\Delta = r^2 - 2r + a^2$. The Lorentz factor is then simply given by $\gamma^{\phi} = [1 - (v^{(\phi)})^2]^{-1/2}$. Equation (B.6) agrees with equation 3.11a in BPT72 for prograde spin but not for retrograde. Equation 10 in Dauser et al. (2013) can be reproduced by taking equation 3.11a from BPT72 and dropping the ± and ∓ signs. Therefore, our equation (B.6) is valid for prograde and retrograde spins, whereas the equivalent equations from BPT72 and Dauser et al. (2013) (and potentially many other references) are only strictly accurate for prograde spin. In practice, the inaccuracy introduced by these mistakes is very small and need not be worried about.

B.2 Blueshift factors and angles

Here we present the formulae used to calculate the various blueshift factors and angles. The covariant form of the tangent 4-vector of photons following geodesics in the Kerr metric is (see e.g. Bardeen et al. 1972; Dauser et al. 2013)

$$(\mathbf{k})_\mu = (-1, \pm\sqrt{V_r}/\Delta, \pm|q|, 0), \tag{B.7}$$

where q is Carter's constant (Carter 1968) and

$$\Delta = r^2 - 2r + a^2; \qquad V_r = (r^2 + a^2)^2 - \Delta(q^2 + a^2). \tag{B.8}$$

Carter's constant for 'incident' photons propagating from source to disk is (e.g. Dovciak 2004)

$$q_i^2 = \frac{\sin\delta(h^2 + a^2)^2}{h^2 - 2h + a^2} - a^2, \tag{B.9}$$

and Carter's constant for 'emergent' photons propagating from a disk element to the observer is (e.g. Dovciak 2004; Ingram et al. 2015)

$$q_e^2 = \beta^2 + \cos^2 i\ (\alpha^2 - a^2). \tag{B.10}$$

4-velocity can be expressed as

$$\mathbf{u}^\mu = \frac{\boldsymbol{\Omega}^\mu}{\sqrt{-g_{\alpha\beta}\Omega^\alpha\Omega^\beta}}, \quad \text{where} \quad \boldsymbol{\Omega}^\mu \equiv \frac{d\mathbf{x}^\mu}{dt}. \tag{B.11}$$

The 4-velocity of the disk element is therefore

$$\begin{aligned} (\mathbf{u_d})^\mu &= u_d^t(1, 0, 0, \Omega_\phi); \qquad \Omega_\phi = \frac{\pm 1}{r^{3/2} \pm a}; \\ u_d^t &= \left\{1 - \frac{2}{r} + \frac{4a\Omega_\phi}{r} - \left[r^2 + a^2\left(1 + \frac{2}{r}\right)\right]\Omega_\phi^2\right\}^{-1/2}, \end{aligned} \tag{B.12}$$

and the 4-velocity of the stationary source is

$$(\mathbf{u_s})^\mu = \frac{1}{\sqrt{-g_{tt}}}(1, 0, 0, 0) = \sqrt{\frac{h^2 + a^2}{h^2 - 2h + a^2}}(1, 0, 0, 0). \tag{B.13}$$

The blueshift seen by an observer on the disk patch is therefore

$$\begin{aligned} g_{sd}(r) =& \frac{(k_i)_\mu (u_d)^\mu}{(k_i)_\nu (u_s)^\nu} = \frac{(u_d)^t}{(u_s)^t} = \\ =& \sqrt{\frac{h^2 - 2h + a^2}{h^2 + a^2}}\left\{1 - \frac{2}{r} + \frac{4a\Omega_\phi}{r} - \left[r^2 + a^2\left(1 + \frac{2}{r}\right)\right]\Omega_\phi^2\right\}^{-1/2}. \end{aligned} \tag{B.14}$$

It follows that the blueshift experienced by photons propagating from the stationary lamppost source to a distant stationary observer is

$$g_{so} = \frac{1}{u_s^t} = \sqrt{\frac{h^2 - 2h + a^2}{h^2 + a^2}}. \tag{B.15}$$

The cosine of the incidence angle is given by

$$\mu_i = -\frac{(k_i)_\mu e^\mu_{(\theta)}}{(k_i)_\nu (u_d)^\nu} = \frac{(k_i)_\theta e^\theta_{(\theta)}}{(u_d)^t} = \frac{(q_i/r)}{(u_d)^t}, \tag{B.16}$$

because the θ component of the contravariant tetrad of basis vectors is $e^\theta_{(\theta)} = 1/r$. For the blueshift experienced by emergent photons propagating from disk element to observer, $g_{do}(r, \phi)$, we use equation (4) from Ingram et al. (2017). This is accurate for a razor thin disk in the black hole equatorial plane. The cosine of the emission angle is

$$\mu_e = \frac{(k_e)_\mu e^\mu_{(\theta)}}{(k_e)_\nu (u_d)^\nu} = g_{do}(r, \phi)(k_e)_\theta e^\theta_{(\theta)} = g_{do}(r, \phi)\frac{q_e}{r}. \tag{B.17}$$

B.3 Environment variables

The environment variables used by the model as listed in Table B.1. All have sensible default values that the user can override, for example to change the model resolution or explore different radial ionization profiles.

Name	Function	Possible values	Default value
`REV_VERB`	Sets the verbose level.	0-1	0
`PHI_SET`	Sets whether ϕ_A is calculated self-consistently (1) using equation 3.25 or set by the model parameter `phiA` (0).	0-1	0
`RMF_SET`	Name (including path) of the instrument response file. If the code is in a mode requiring an instrument response, the user is prompted for this.	string	none
`ARF_SET`	Name (including path) of the instrument ancillary response file. This is not required if a .rsp file is entered.	string	none
`MU_ZONES`	Sets how many bins of $\mu_e(r,\phi)$ are used for the calculation. If this is set to 1, $\mu_e = \cos i$ is assumed.	1-10	5
`ECUT_ZONES`	Sets how many bins of $g_{sd}(r)$ are used for the calculation. If this is set to 1, it is assumed that the high energy cut-off seen by each disk ring is equal to E_{cut} rather than $g_{sd}(r)E_{cut}$.	1-10	5
`ION_ZONES`	Sets how many bins of $\log_{10}\xi(r)$ are used for the calculation. If this is set to 1, the ionization is assumed to be constant and determined by the input model parameter `logxi`. Otherwise, a radial ionization profile is used, with `logxi` setting the normalisation of the profile.	1-100	10
`A_DENSITY`	Sets whether the radial ionization profile is calculated assuming a constant disk density (0), or assuming a zone A Shakura-Sunyaev disk density profile (1). The parameter `logxi` respectively sets exactly or roughly the peak value of $\log_{10}\xi(r)$ for the former and latter cases.	0-1	1
`GRID`	Name of geodesics grid (with full path). If a value is given, the grid is used to calculate an interpolated transfer function. Otherwise, all geodesics are calculated on the fly. Use of the grid is faster if a and i are free parameters, and the on the fly calculation is faster if they are fixed.	string	null
`RELXILL_TABLE_PATH`	RELXILL variable: points to the directory containing the XILLVER tables.	string	null

Table B.1: Environment variables. The default variables are used if the user does not set any of the above variables.

C

Appendices to Chapter 4

C.1 Transfer functions

In the text we derived the expression of the total observed specific flux as a function of time (equation 4.8). Here we write down explicitly the expressions of the three response functions and their Fourier transform.

$$\begin{split} w_0(E_o, t) = \int_{\alpha_0} \int_{\beta_0} & g_{do}^3 \epsilon(r)\, \delta(t - \tau) \\ & \mathcal{R}\left(E_o | \mu_e, \Gamma, g_{sd} E_{cut}\right) d\alpha_0\, d\beta_0, \end{split} \tag{C.1}$$

$$\begin{split} w_1(E_o, t) = \int_{\alpha_0} \int_{\beta_0} & g_{do}^3 \epsilon(r)\, \delta(t - \tau) \\ & \ln g_{sd} \mathcal{R}\left(E_o | \mu_e, \Gamma, g_{sd} E_{cut}\right) d\alpha_0,\, d\beta_0 \end{split} \tag{C.2}$$

$$\begin{split} w_2(E_o, t) = \int_{\alpha_0} \int_{\beta_0} & g_{do}^3 \epsilon(r)\, \delta(t - \tau) \\ & \frac{\partial \mathcal{R}\left(E_o | \mu_e, \Gamma, g_{sd} E_{cut}\right)}{\partial \Gamma} d\alpha_0\, d\beta_0. \end{split} \tag{C.3}$$

In the Fourier transform of these expressions the delta function ($\delta(t - \tau)$) becomes $e^{2\pi\tau\nu}$.

C.2 Ionization calculation

In order to estimate the upper limit of the ionisation parameter, we do not consider the time dependence of the direct emission and we use the definitions of Ingram et al (2019). Let us start from the definition of the ionisation parameter in the disc at radial coordinate r (see e.g. Eq. 10 in García et al. 2013a)

$$\xi(r) = 4\pi \frac{F_{d,in}(r)}{n_e(r)}, \tag{C.4}$$

where

$$F_{d,in}(r) \equiv \frac{C}{2}\epsilon(r) \int_{13.6\mathrm{eV}}^{13.6\mathrm{keV}} E_d^{1-\Gamma} \mathrm{e}^{-E_d/(g_{sd}E_{\mathrm{cut}})} dE_d, \tag{C.5}$$

is the incident flux from the source to the disc in the disc restframe. However, the model for the direct emission that we use to fit to the data is in the observer restframe

$$F_o(E_o) = A\, l\, g_{so}^{\Gamma} E_o^{1-\Gamma} \mathrm{e}^{-E_o/(g_{so}E_{\mathrm{cut}})}, \tag{C.6}$$

where the normalization A of RELTRANS model (the XSPEC model parameter 'norm') absorbes the distance (D) to the source and the normalisation of the direct emission with $A = C/(4\pi D^2)$. Here, E_{cut} is defined in the source restframe. We can define $\mathcal{F}$

$$\mathcal{F} \equiv A \int_{13.6\mathrm{eV}}^{13.6\mathrm{keV}} E_o^{1-\Gamma} \mathrm{e}^{-E_o/(g_{so}E_{\mathrm{cut}})} dE_o, \tag{C.7}$$

because it comes directly from the model that we fit to the data. In order to express the ionisation parameter in terms of observed flux we can start from Eq. C.5 and apply coordinate transforms from E_d to E_s and then from E_s to E_o using the blueshift definitions $g_{so} = E_o/E_s$ and $g_{sd} = E_d/E_s$. We obtain

$$F_{d,in}(r) = 2\pi\, D^2\, \epsilon(r)\, g_{sd}^{2-\Gamma}\, g_{so}^{\Gamma-2}\, \mathcal{F}. \tag{C.8}$$

The emissivity as defined in Ingram et al (2019) is in units of R_g^{-2}. Keeping this definition, we can express the ionisation parameter in units of $[erg\, cm\, s^{-1}]$ as

$$\xi(r) = \frac{8\pi\, D_{\mathrm{cm}}^2}{n_{e,\mathrm{cm}^{-3}}} \frac{\epsilon(r)\, g_{sd}^{2-\Gamma}\, g_{so}^{\Gamma-2}}{R_{g,\mathrm{cm}}^2} \mathcal{F}_{\mathrm{erg\,cm^{-2}\,s^{-1}}}. \tag{C.9}$$

Finally, Eq C.9 assumes isotropic radiation from the source. We should multiply by the boost parameter ($1/\mathcal{B}$). Eq 4.11 in the text follows from subbing in sensible values for the parameters.

C.3 MCMC analysis

In order to further probe the parameter space we run multiple MCMC simulations for Model 3 using the Goodman-Weare algorithm. We run 4 chains using the XSPEC routine CHAIN. The total length is 10^5 for the first 3 and 2×10^5 for the final chain. We use 200, 400, 800 and 200 walkers for the 4 chains. All the walkers start from the best fit of Model 3 and we set the burn-in period to 4000 steps in the first three chains and 2000 steps for the last one. We test the length of the burn-in period with the Geweke convergence measure, finding this to be in the range -0.2 to 0.2 for each parameter in each chain[1], indicating that convergence has been achieved.

We jointly fit 21 spectra (real and imaginary parts of the complex covariance for 10 frequency ranges plus the time-average energy spectrum) so we have 51 free parameters. The continuum phase (ϕ_A and ϕ_B) and amplitude (α and γ) parameters are tied between real and imaginary parts for a given frequency, but all depend on frequency. They therefore contribute 40 free parameters. The normalization of the time-average spectrum (which is effectively $\alpha(\nu = 0)$), and the hydrogen column density of the absorption model contribute a further two free parameters. This leaves 9 remaining parameters: Γ, $E_{\rm cut}$ and the 7 key parameters that we explore in detail: M, $1/\mathcal{B}$ (Boost in the model), $A_{\rm Fe}$, $\log \xi$, $r_{\rm in}$, Incl and h.

Fig. C.1 is the integrated probability distribution exploring the correlations between these 7 key parameters using the MCMC. The inner radius is negative in order for it to be expressed in units of ISCOs in the RELTRANS model (following the RELXILL convention). The inner radius and peak ionization parameter appear to have bi-modal distributions, and anti-correlate with one another. The correlation between mass and peak ionization parameter revealed by the contour plot in Fig. 4.3 does not show up here, since the MCMC does not explore the high χ^2 regions of parameter space as comprehensively as a brute-force grid search. For each parameter that we consider in the plot, the Rubin-Gelman convergence measure (Gelman & Rubin 1992) for the first three chains[2] is < 1.05 (with values close to unity indicating convergence). We find that integrated probability distribution plots computed for each of the 4 individual chains all look very similar to Fig. C.1, indicating that the 4 chains sample similar distributions. In particular, this shows that the bi-modal behaviour of the $r_{\rm in}$ and $\log \xi$ parameters does not result from different chains returning different distributions.

---

[1] The Geweke convergence measure compares two intervals of the chain, one shortly after the burn-in period and one towards the end of the chain. For each parameter, Geweke's statistic measures the difference between the mean parameter value in these two intervals, and therefore if convergence is achieved it will have an expectation value of zero and follow the standard normal distribution (Geweke 1992).

[2] The Rubin-Gelman convergence measure only compares chains of the same length

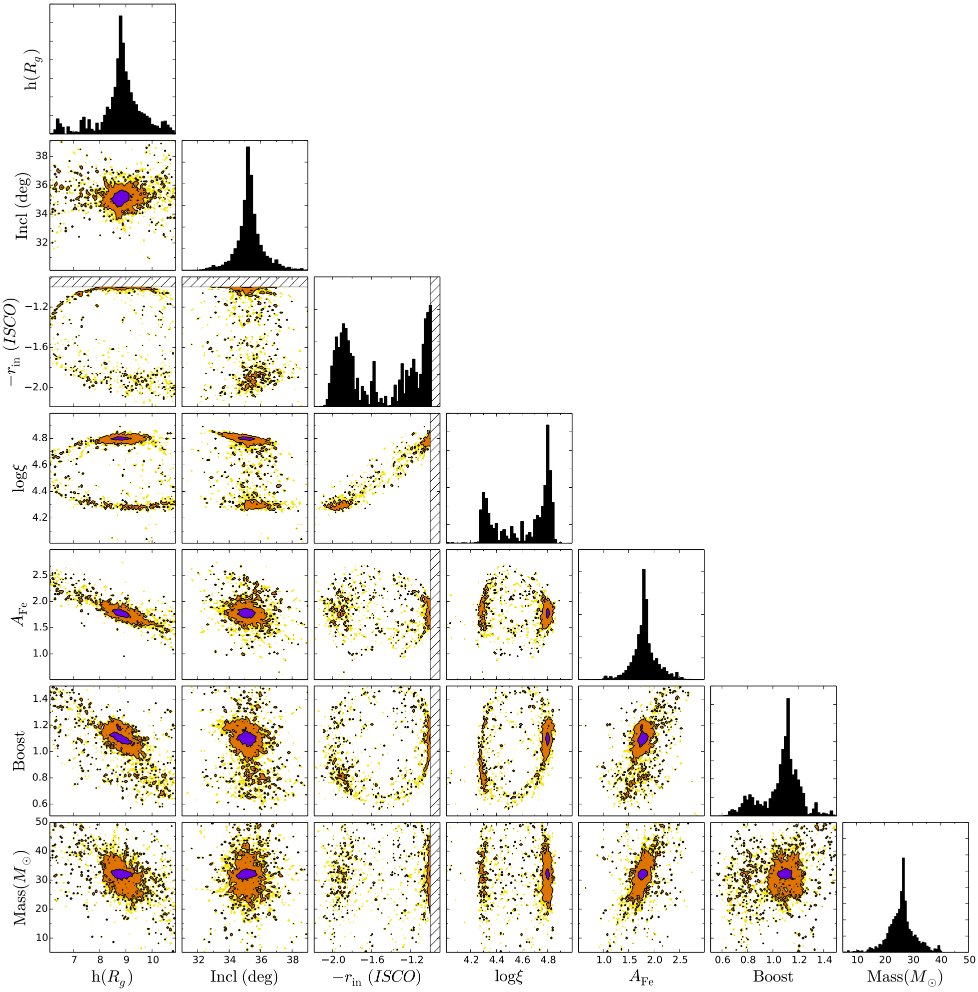

Figure C.1: Output distributions from the MCMC simulation of Model 3. The purple, orange and yellow regions are 1σ, 2σ and 3σ contours respectively. The inner radius is presented as negative following the RELTRANS convention and hatched regions indicate forbidden values. The y-axes for the histograms are in arbitrary units.

Bibliography

Arévalo, P., & Uttley, P. 2006, MNRAS, 367, 801

Arnaud, K. A. 1996, in Astronomical Society of the Pacific Conference Series, Vol. 101, Astronomical Data Analysis Software and Systems V, ed. G. H. Jacoby & J. Barnes, 17

Axelsson, M., Hjalmarsdotter, L., & Done, C. 2013, MNRAS, 431, 1987

Bambi, C. 2017, Black Holes: A Laboratory for Testing Strong Gravity, doi:10.1007/978-981-10-4524-0

Bardeen, J. M., Press, W. H., & Teukolsky, S. A. 1972, ApJ, 178, 347

Basak, R., Zdziarski, A. A., Parker, M., & Islam, N. 2017, MNRAS, 472, 4220

Basko, M. M., Sunyaev, R. A., & Titarchuk, L. G. 1974, A&A, 31, 249

Belczynski, K., Bulik, T., Fryer, C. L., et al. 2010, ApJ, 714, 1217

Bendat, J. S., & Piersol, A. G. 2000, Measurement Science and Technology, 11, 1825

—. 2010, Random Data: Analysis and measurement procedures; 4th edition (Wiley, 2010)

Beuchert, T., Markowitz, A. G., Dauser, T., et al. 2017, A&A, 603, A50

Blumenthal, G. R., & Gould, R. J. 1970, Reviews of Modern Physics, 42, 237

Caballero-García, M. D., Papadakis, I. E., Dovčiak, M., et al. 2018, MNRAS, 480, 2650

Cackett, E. M., Zoghbi, A., Reynolds, C., et al. 2014, MNRAS, 438, 2980

Caiazzo, I., Heyl, J., Ingram, A. R., et al. 2019, BAAS, 51, 516

Campana, S., & Stella, L. 1995, MNRAS, 272, 585

Carter, B. 1968, Phys. Rev., 174, 1559

Casares, J., & Jonker, P. G. 2014, Space Sci. Rev., 183, 223

Chainakun, P., & Young, A. J. 2015, MNRAS, 452, 333

—. 2017, MNRAS, 465, 3965

Chainakun, P., Young, A. J., & Kara, E. 2016a, MNRAS, 460, 3076

—. 2016b, MNRAS, 460, 3076

Chan, C., Müller, B., Heger, A., Pakmor, R., & Springel, V. 2018, ApJ, 852, L19

Coppi, P. S. 1999, in Astronomical Society of the Pacific Conference Series, Vol. 161, High Energy Processes in Accreting Black Holes, ed. J. Poutanen & R. Svensson, 375

Dauser, T., García, J., Parker, M. L., Fabian, A. C., & Wilms, J. 2014, MNRAS, 444, L100
Dauser, T., García, J., Walton, D. J., et al. 2016, A&A, 590, A76
Dauser, T., Garcia, J., Wilms, J., et al. 2013, MNRAS, 430, 1694
Dauser, T., Svoboda, J., Schartel, N., et al. 2012, MNRAS, 422, 1914
De Marco, B., & Ponti, G. 2016, ApJ, 826, 70
De Marco, B., Ponti, G., Cappi, M., et al. 2013a, MNRAS, 431, 2441
—. 2013b, MNRAS, 431, 2441
De Marco, B., Ponti, G., Miniutti, G., et al. 2013c, MNRAS, 436, 3782
De Marco, B., Ponti, G., Muñoz-Darias, T., & Nandra, K. 2015, ApJ, 814, 50
De Marco, B., Ponti, G., Petrucci, P. O., et al. 2017, MNRAS, 471, 1475
Degenaar, N., Miller, J. M., Chakrabarty, D., et al. 2015, MNRAS, 451, L85
Dexter, J., & Agol, E. 2009, ApJ, 696, 1616
Done, C. 2010, arXiv e-prints, arXiv:1008.2287
Done, C., Davis, S. W., Jin, C., Blaes, O., & Ward, M. 2012, MNRAS, 420, 1848
Done, C., Gierliński, M., & Kubota, A. 2007, A&A Rev., 15, 1
Done, C., & Nayakshin, S. 2007, MNRAS, 377, L59
Dovciak, M. 2004, PhD thesis
Dove, J. B., Wilms, J., & Begelman, M. C. 1997, ApJ, 487, 747
Duro, R., Dauser, T., Wilms, J., et al. 2011, A&A, 533, L3
Duro, R., Dauser, T., Grinberg, V., et al. 2016, A&A, 589, A14
Eardley, D. M., Lightman, A. P., & Shapiro, S. L. 1975, ApJ, 199, L153
Ellis, G. F. R. 2007, General Relativity and Gravitation, 39, 1047
—. 2009, General Relativity and Gravitation, 41, 581
Emmanoulopoulos, D., Papadakis, I. E., Dovčiak, M., & McHardy, I. M. 2014, MNRAS, 439, 3931
Epitropakis, A., & Papadakis, I. E. 2017, MNRAS, 468, 3568
Epitropakis, A., Papadakis, I. E., Dovčiak, M., et al. 2016, A&A, 594, A71
Esin, A. A., McClintock, J. E., & Narayan, R. 1997, ApJ, 489, 865
Etherington, I. M. H. 1933, Philosophical Magazine, 15
Fabian, A. C., Iwasawa, K., Reynolds, C. S., & Young, A. J. 2000, PASP, 112, 1145
Fabian, A. C., Lohfink, A., Kara, E., et al. 2015, MNRAS, 451, 4375
Fabian, A. C., Miniutti, G., Gallo, L., et al. 2004, MNRAS, 353, 1071
Fabian, A. C., Rees, M. J., Stella, L., & White, N. E. 1989, MNRAS, 238, 729
Fabian, A. C., & Ross, R. R. 2010, Space Sci. Rev., 157, 167
Fabian, A. C., Zoghbi, A., Ross, R. R., et al. 2009, Nature, 459, 540
Fabian, A. C., Wilkins, D. R., Miller, J. M., et al. 2012, MNRAS, 424, 217
Fender, R. 2010, 'Disc-Jet' Coupling in Black Hole X-Ray Binaries and Active Galactic Nuclei, Vol. 794, 115
Fender, R., Corbel, S., Tzioumis, T., et al. 1999, ApJ, 519, L165
Field, G. B., & Rogers, R. D. 1993, ApJ, 403, 94

Galeev, A. A., Rosner, R., & Vaiana, G. S. 1979, ApJ, 229, 318

Gandhi, P., Rao, A., Johnson, M. A. C., Paice, J. A., & Maccarone, T. J. 2019, MNRAS, 485, 2642

García, J., Dauser, T., Reynolds, C. S., et al. 2013a, ApJ, 768, 146

García, J., Elhoussieny, E. E., Bautista, M. A., & Kallman, T. R. 2013b, ApJ, 775, 8

García, J., & Kallman, T. R. 2010, ApJ, 718, 695

García, J., Dauser, T., Lohfink, A., et al. 2014, ApJ, 782, 76

García, J. A., Fabian, A. C., Kallman, T. R., et al. 2016, MNRAS, 462, 751

García, J. A., Kallman, T. R., Bautista, M., et al. 2018, in Astronomical Society of the Pacific Conference Series, Vol. 515, Workshop on Astrophysical Opacities, 282

García, J. A., Steiner, J. F., McClintock, J. E., et al. 2015, ApJ, 813, 84

Gelman, A., & Rubin, D. B. 1992, Statistical Science, 7, 457

Gendreau, K. C., Arzoumanian, Z., Adkins, P. W., et al. 2016, in Proc. SPIE, Vol. 9905, Space Telescopes and Instrumentation 2016: Ultraviolet to Gamma Ray, 99051H

George, I. M., & Fabian, A. C. 1991, MNRAS, 249, 352

Geweke, J. 1992, in Bayesian Statistics (University Press), 169–193

Ghisellini, G. 2013, Radiative Processes in High Energy Astrophysics, Vol. 873, doi:10.1007/978-3-319-00612-3

Gilfanov, M., Churazov, E., & Revnivtsev, M. 2000, MNRAS, 316, 923

Grier, C. J., Peterson, B. M., Pogge, R. W., et al. 2012, ApJ, 744, L4

Grinberg, V., Pottschmidt, K., Böck, M., et al. 2014, A&A, 565, A1

Grinberg, V., Leutenegger, M. A., Hell, N., et al. 2015, A&A, 576, A117

Grupe, D., Komossa, S., & Gallo, L. C. 2007, ApJ, 668, L111

Guilbert, P. W., & Rees, M. J. 1988, MNRAS, 233, 475

Haardt, F., & Maraschi, L. 1991, ApJ, 380, L51

—. 1993, ApJ, 413, 507

Haardt, F., Maraschi, L., & Ghisellini, G. 1994, ApJ, 432, L95

Harrison, F. A. e. a. 2013, ApJ, 770, 103

Heida, M., Jonker, P. G., Torres, M. A. P., & Chiavassa, A. 2017, ApJ, 846, 132

Heil, L. M., Uttley, P., & Klein-Wolt, M. 2015, MNRAS, 448, 3348

Huchra, J. P., Vogeley, M. S., & Geller, M. J. 1999, ApJS, 121, 287

Ichimaru, S. 1977, ApJ, 214, 840

Ingram, A., Done, C., & Fragile, P. C. 2009, MNRAS, 397, L101

Ingram, A., Maccarone, T. J., Poutanen, J., & Krawczynski, H. 2015, ApJ, 807, 53

Ingram, A., Mastroserio, G., Dauser, T., et al. 2019, MNRAS, 1677

Ingram, A., & van der Klis, M. 2013, MNRAS, 434, 1476

Ingram, A., van der Klis, M., Middleton, M., Altamirano, D., & Uttley, P. 2017, MNRAS, 464, 2979

Ingram, A., van der Klis, M., Middleton, M., et al. 2016, MNRAS, 461, 1967

Janka, H.-T. 2012, Annual Review of Nuclear and Particle Science, 62, 407

Jansen, F., Lumb, D., Altieri, B., et al. 2001, A&A, 365, L1

Jiang, J., Fabian, A. C., Wang, J., et al. 2019, MNRAS, 484, 1972

Kalberla, P. M. W., Burton, W. B., Hartmann, D., et al. 2005, A&A, 440, 775

Kammoun, E. S., Domček, V., Svoboda, J., Dovčiak, M., & Matt, G. 2019, MNRAS, 485, 239

Kara, E., Alston, W. N., Fabian, A. C., et al. 2016, MNRAS, 462, 511

Kara, E., Fabian, A. C., Cackett, E. M., Miniutti, G., & Uttley, P. 2013a, MNRAS, 430, 1408

Kara, E., Fabian, A. C., Cackett, E. M., et al. 2013b, MNRAS, 428, 2795

—. 2013c, MNRAS, 434, 1129

Kara, E., Fabian, A. C., Lohfink, A. M., et al. 2015, MNRAS, 449, 234

Kara, E., Steiner, J. F., Fabian, A. C., et al. 2019, Nature, 565, 198

Keek, L., & Ballantyne, D. R. 2016, MNRAS, 456, 2722

King, A. R., & Pringle, J. E. 2006, MNRAS, 373, L90

King, A. R., Pringle, J. E., & Hofmann, J. A. 2008, MNRAS, 385, 1621

Kolehmainen, M., Done, C., & Díaz Trigo, M. 2014, MNRAS, 437, 316

Körding, E., & Falcke, H. 2004, A&A, 414, 795

Kotov, O., Churazov, E., & Gilfanov, M. 2001, MNRAS, 327, 799

Kubota, A., Ebisawa, K., Makishima, K., & Nakazawa, K. 2005, ApJ, 631, 1062

Laor, A. 1990, MNRAS, 246, 369

—. 1991, ApJ, 376, 90

Lightman, A. P., & Rybicki, G. B. 1980, ApJ, 236, 928

Lightman, A. P., & White, T. R. 1988, ApJ, 335, 57

Lindquist, R. W. 1966, Annals of Physics, 37, 487

Longinotti, A. L., Krongold, Y., Kriss, G. A., et al. 2013, ApJ, 766, 104

Luminet, J.-P. 1979, A&A, 75, 228

Lyubarskii, Y. E. 1997, MNRAS, 292, 679

Mahmoud, R. D., & Done, C. 2018a, MNRAS, 480, 4040

—. 2018b, MNRAS, 473, 2084

Mahmoud, R. D., Done, C., & De Marco, B. 2019, MNRAS, 486, 2137

Makishima, K., Maejima, Y., Mitsuda, K., et al. 1986, ApJ, 308, 635

Malkan, M. A. 1983, ApJ, 268, 582

Markoff, S., Nowak, M. A., & Wilms, J. 2005, ApJ, 635, 1203

Martocchia, A., Karas, V., & Matt, G. 2000, MNRAS, 312, 817

Martocchia, A., & Matt, G. 1996, MNRAS, 282, L53

Mastroserio, G., Ingram, A., & van der Klis, M. 2018, MNRAS, 475, 4027

—. 2019, MNRAS, 1682

Matt, G., Perola, G. C., & Piro, L. 1991, A&A, 247, 25

Matt, G., Perola, G. C., Piro, L., & Stella, L. 1992, A&A, 257, 63

McHardy, I. M., Arévalo, P., Uttley, P., et al. 2007, MNRAS, 382, 985

McHardy, I. M., Papadakis, I. E., Uttley, P., Page, M. J., & Mason, K. O. 2004, MNRAS, 348, 783

Meyer, F., & Meyer-Hofmeister, E. 1994, A&A, 288, 175

Middleton, M. 2016, in Astrophysics and Space Science Library, Vol. 440, Astrophysics of Black Holes: From Fundamental Aspects to Latest Developments, ed. C. Bambi, 99

Miller, J. M. 2007, ARA&A, 45, 441

Miller, J. M., Parker, M. L., Fuerst, F., et al. 2013, ApJ, 775, L45

Miller, L., Turner, T. J., & Reeves, J. N. 2008, A&A, 483, 437

Miller, L., Turner, T. J., Reeves, J. N., & Braito, V. 2010, MNRAS, 408, 1928

Mirabel, I. F., & Rodrigues, I. 2003, Science, 300, 1119

Misner, C. W., Thorne, K. S., & Wheeler, J. A. 1973, Gravitation (San Francisco: W.H. Freeman and Co., 1973)

Misra, R., & Mandal, S. 2013, ApJ, 779, 71

Mitsuda, K., & Dotani, T. 1989, PASJ, 41, 557

Mitsuda, K., Inoue, H., Koyama, K., et al. 1984, PASJ, 36, 741

Miyamoto, S., & Kitamoto, S. 1989, Nature, 342, 773

—. 1991, ApJ, 374, 741

Miyamoto, S., Kitamoto, S., Mitsuda, K., & Dotani, T. 1988, Nature, 336, 450

Mizumoto, M., Done, C., Hagino, K., et al. 2018, MNRAS, 478, 971

Montgomery, C., Orchiston, W., & Whittingham, I. 2009, Journal of Astronomical History and Heritage, 12, 90

Motta, S. E., Casella, P., Henze, M., et al. 2015, MNRAS, 447, 2059

Mushtukov, A. A., Ingram, A., & van der Klis, M. 2018, MNRAS, 474, 2259

Nayakshin, S., Kazanas, D., & Kallman, T. R. 2000, ApJ, 537, 833

Niedźwiecki, A., & Zdziarski, A. A. 2018, MNRAS, 477, 4269

Niedźwiecki, A., Zdziarski, A. A., & Szanecki, M. 2016, ApJ, 821, L1

Novikov, I. D., & Thorne, K. S. 1973, in Black Holes (Les Astres Occlus), 343–450

Nowak, M. A., Vaughan, B. A., Wilms, J., Dove, J. B., & Begelman, M. C. 1999, ApJ, 510, 874

O'Connor, E., & Ott, C. D. 2011, ApJ, 730, 70

Oppenheim, A. V., & Schafer, R. W. 1975, Digital signal processing

Orosz, J. A., McClintock, J. E., Aufdenberg, J. P., et al. 2011, ApJ, 742, 84

Page, K. L., Schartel, N., Turner, M. J. L., & O'Brien, P. T. 2004, MNRAS, 352, 523

Papadakis, I. E., Nandra, K., & Kazanas, D. 2001, ApJ, 554, L133

Parker, M. L., Wilkins, D. R., Fabian, A. C., et al. 2014, MNRAS, 443, 1723

Parker, M. L., Tomsick, J. A., Miller, J. M., et al. 2015, ApJ, 808, 9

Parker, M. L., Tomsick, J. A., Kennea, J. A., et al. 2016, ApJ, 821, L6

Patrick, A. R., Reeves, J. N., Porquet, D., et al. 2012, MNRAS, 426, 2522

Peterson, B. M. 1997, An Introduction to Active Galactic Nuclei

Peterson, B. M., Ferrarese, L., Gilbert, K. M., et al. 2004, ApJ, 613, 682

Plant, D. S., Fender, R. P., Ponti, G., Muñoz-Darias, T., & Coriat, M. 2014, MNRAS,

442, 1767
—. 2015, A&A, 573, A120
Potter, W. J., & Balbus, S. A. 2017, MNRAS, 472, 3021
Poutanen, J. 1998, in Theory of Black Hole Accretion Disks, ed. M. A. Abramowicz, G. Björnsson, & J. E. Pringle, 100–122
Poutanen, J. 2002, MNRAS, 332, 257
Poutanen, J., & Fabian, A. C. 1999, MNRAS, 306, L31
Poutanen, J., & Svensson, R. 1996, ApJ, 470, 249
Rapisarda, S., Ingram, A., Kalamkar, M., & van der Klis, M. 2016, MNRAS, 462, 4078
Rapisarda, S., Ingram, A., & van der Klis, M. 2017a, MNRAS, 469, 2011
—. 2017b, MNRAS, 472, 3821
Ray, P. S., Arzoumanian, Z., Ballantyne, D., et al. 2019, arXiv e-prints, arXiv:1903.03035
Rees, M. J. 1984, ARA&A, 22, 471
Reid, M. J., McClintock, J. E., Narayan, R., et al. 2011, ApJ, 742, 83
Reis, R. C., Fabian, A. C., Ross, R. R., & Miller, J. M. 2009, MNRAS, 395, 1257
Remillard, R. A., & McClintock, J. E. 2006, ARA&A, 44, 49
Revnivtsev, M., Gilfanov, M., & Churazov, E. 1999, A&A, 347, L23
Reynolds, C. S. 2014, Space Sci. Rev., 183, 277
—. 2019, Nature Astronomy, 3, 41
Reynolds, C. S., & Nowak, M. A. 2003, Phys. Rep., 377, 389
Reynolds, C. S., Young, A. J., Begelman, M. C., & Fabian, A. C. 1999, ApJ, 514, 164
Risaliti, G., Harrison, F. A., Madsen, K. K., et al. 2013, Nature, 494, 449
Ross, R. R., & Fabian, A. C. 1993, MNRAS, 261, 74
—. 2005, MNRAS, 358, 211
Różańska, A., Madej, J., Konorski, P., & SaĐowski, A. 2011, A&A, 527, A47
Rybicki, G. B., & Lightman, A. P. 1979, Radiative processes in astrophysics
Salpeter, E. E. 1964, ApJ, 140, 796
Shakura, N. I., & Sunyaev, R. A. 1973, A&A, 24, 337
Shapiro, S. L., Lightman, A. P., & Eardley, D. M. 1976, ApJ, 204, 187
Shaposhnikov, N. 2012, ApJ, 752, L25
Shields, G. A. 1978, Nature, 272, 706
Silva, C. V., Uttley, P., & Costantini, E. 2016, A&A, 596, A79
Stella, L. 1990, Nature, 344, 747
Stern, B. E., Poutanen, J., Svensson, R., Sikora, M., & Begelman, M. C. 1995, ApJ, 449, L13
Sunyaev, R. A., & Truemper, J. 1979, Nature, 279, 506
Svensson, R., & Zdziarski, A. A. 1994, ApJ, 436, 599
Svoboda, J., Dovčiak, M., Goosmann, R. W., et al. 2012, A&A, 545, A106
Tanaka, Y., Nandra, K., Fabian, A. C., et al. 1995, Nature, 375, 659

Taylor, C., & Reynolds, C. S. 2018a, ApJ, 855, 120

—. 2018b, ApJ, 868, 109

Thorne, K. S. 1974, ApJ, 191, 507

Thorne, K. S., & Price, R. H. 1975, ApJ, 195, L101

Titarchuk, L. 1994, ApJ, 434, 570

Tomsick, J. A., Yamaoka, K., Corbel, S., et al. 2009, ApJ, 707, L87

Tomsick, J. A., Nowak, M. A., Parker, M., et al. 2014, ApJ, 780, 78

Tomsick, J. A., Parker, M. L., García, J. A., et al. 2018, ApJ, 855, 3

Uttley, P., Cackett, E. M., Fabian, A. C., Kara, E., & Wilkins, D. R. 2014, A&A Rev., 22, 72

Uttley, P., McHardy, I. M., & Vaughan, S. 2005, MNRAS, 359, 345

Uttley, P., Wilkinson, T., Cassatella, P., et al. 2011, MNRAS, 414, L60

van den Eijnden, J., Ingram, A., Uttley, P., et al. 2017, MNRAS, 464, 2643

van der Klis, M. 1989, in NATO Advanced Science Institutes (ASI) Series C, ed. H. Ögelman & E. P. J. van den Heuvel, Vol. 262, 27

van der Klis, M., Hasinger, G., Stella, L., et al. 1987, ApJ, 319, L13

Vaughan, B. A., & Nowak, M. A. 1997, ApJ, 474, L43

Veledina, A. 2018, MNRAS, 481, 4236

Vincent, F. H., Różańska, A., Zdziarski, A. A., & Madej, J. 2016, A&A, 590, A132

Walton, D. J., Zoghbi, A., Cackett, E. M., et al. 2013, ApJ, 777, L23

Walton, D. J., Tomsick, J. A., Madsen, K. K., et al. 2016, ApJ, 826, 87

Wang, Y., Méndez, M., Sanna, A., Altamirano, D., & Belloni, T. M. 2017, MNRAS, 468, 2256

Wilkins, D. R., Cackett, E. M., Fabian, A. C., & Reynolds, C. S. 2016, MNRAS, 458, 200

Wilkins, D. R., & Fabian, A. C. 2011, MNRAS, 414, 1269

—. 2012, MNRAS, 424, 1284

—. 2013, MNRAS, 430, 247

Wilkins, D. R., & Gallo, L. C. 2015, MNRAS, 449, 129

Wilkinson, T., & Uttley, P. 2009, MNRAS, 397, 666

Wilms, J., Allen, A., & McCray, R. 2000, ApJ, 542, 914

Wilms, J., Nowak, M. A., Pottschmidt, K., Pooley, G. G., & Fritz, S. 2006, A&A, 447, 245

Xu, Y., Harrison, F. A., García, J. A., et al. 2018, ApJ, 852, L34

Yang, X., & Wang, J. 2013, ApJS, 207, 6

Zdziarski, A. A., Johnson, W. N., & Magdziarz, P. 1996, MNRAS, 283, 193

Zdziarski, A. A., Lubiński, P., Gilfanov, M., & Revnivtsev, M. 2003, MNRAS, 342, 355

Zhang, W., Dovčiak, M., & Bursa, M. 2019, ApJ, 875, 148

Zoghbi, A., Fabian, A. C., Reynolds, C. S., & Cackett, E. M. 2012, MNRAS, 422, 129

Zoghbi, A., Uttley, P., & Fabian, A. C. 2011, MNRAS, 412, 59

Życki, P. T., Done, C., & Smith, D. A. 1999, MNRAS, 309, 561

Contribution from co-authors

Here I list the bibliographic information of the papers included in this thesis. The position in the author list reflects the importance of the contribution of each co-author.

Chapter 2: Multi-timescale X-ray reverberation mapping of accreting black holes
G. Mastroserio, A. Ingram & M. van der Klis
Monthly Notices of the Royal Astronomical Society, 2018, 475, 4027-4042

Chapter 3: A public relativistic transfer function model for X-ray reverberation mapping of accreting black holes
A. Ingram, **G. Mastroserio**, T. Dauser , P. Hovenkamp, M. van der Klis & J. A. García
Monthly Notices of the Royal Astronomical Society, 2019, 488, 324-347

Together with AI, GM wrote the public version of the RELTRANS code. GM further contributed by reducing the Mrk 335 data, fitting the model to it and partly writing the corresponding section of the paper.

Chapter 4: An X-ray reverberation mass measurement of Cygnus X-1
G. Mastroserio, A. Ingram & M. van der Klis
Monthly Notices of the Royal Astronomical Society, 2019, 488, 348-361

Chapter 5: Multi-timescale reverberation mapping of Mrk 335
G. Mastroserio, A. Ingram & M. van der Klis
Submitted to Monthly Notices of the Royal Astronomical Society

Samenvatting

Zwarte gaten met accretie vertonen karakteristieke componenten in hun gemiddelde energiespectrum en ook hun tijdsvariaties hebben opvallende kenmerken. Met de juiste modellen kunnen deze diagnostieken een inzicht geven in de geometrie van deze systemen en de eigenschappen van het zwarte gat. Door de energie- en tijdsafhankelijkheid van de röntgenemissie van deze zwarte gaten in hun samenhang te analyseren kunnen we gebruik maken van de volledige informatie in de waarnemingen. In dit proefschrift kijken we naar de variabiliteit en de energie-afhankelijkheid van de reflectie-component. Dit is de emissie die ontstaat wanneer fotonen, die oorspronkelijk door de corona (een heet, optisch dun plasma vlakbij het zwarte gat) naar de accretieschijf worden uitgestraald, in de atmosfeer van de schijf worden omgezet, en opnieuw uitgestraald. Er zijn aanwijzingen dat dit proces in zowel zwart-gat röntgendubbelsteren als in actieve kernen van melkwegstelsels optreedt. Belangwekkend genoeg is de energie- en tijdsafhankelijke respons voor elk stukje van de accretieschijf verschillend. Dit is een gevolg van verschillen in de sterkte van de relativistische effecten die de energie van de fotonen verschuiven tijdens het traject van bron naar waarnemer, en van de verschillen in reistijd van de invallende en de gereflecteerde straling. De reflectiecomponent is daarom geschikt om de kansen te benutten die worden geboden door het combineren van de energie- en tijdsafhankelijkheid van de emissie. Een van de beste manieren om dit te doen is de tijdsvertraging te bestuderen van de variaties in de reflectiecomponent ten opzichte van de variaties in de continuumcomponent, die rechtstreeks naar de waarnemer wordt uitgezonden en daardoor eerder arriveert. Deze ‘lichtecho’-vertragingen worden waargenomen op relatief korte tijdschalen (Fourierfrequenties $> 300 M_\odot/M$ Hz). Op langere tijdschalen wordt het tijdsvertragings-energiespectrum gedomineerd door een ander proces, vermoedelijk gerelateerd aan het voortbewegen van fluctuaties in de massa-accretiesnelheid door de accretiestroom. Deze bewegende accretiesnelheidsfluctuaties produceren stochastische variaties in de electrontemperatuur van de corona door hun effect op zowel het vrijmaken van gravitationele energie als de snelheid van de Compton koeling in de corona, hetgeen resulteert in kleine fluctuaties in de helling van het coronale emissiespectrum (‘kantelen’) die tijdsvertragingen kunnen opleveren.

In dit proefschrift presenteer ik een nieuw model dat deze twee vormen van tijdsvertraging gezamenlijk beschrijft. Hoofdstuk 2 behandelt het wiskundig formalisme dat het kantelen van het coronale spectrum en de resulterende vertragingen beschrijft. Gezien vanuit elk punt op de schijf is het invallende spectrum anders. Dit beinvloedt het reflectiespectrum dat elk stukje schijf uitzendt en daarom niet alleen de intensiteit, maar ook de vorm, van het lichtecho-energiespectrum. De gevolgen van deze niet-lineaire effecten voor de tijdsvertraging-energiespectra worden berekend onder aanname van een compacte corona op de draaiingsas van het zwarte gat, zodat de helling van het invallende spectrum afhangt van de straal in de schijf maar niet het azimuth. Hoewel het formalisme van Hoofdstuk 2 geen volledige algemeen-relativistische berekening van de fotonpaden van corona naar schijf en van schijf naar waarnemer omvat, laten we zien dat de methode in principe werkt met een analyse van Rossi X-ray Timing Explorer data van Cygnus X-1 die een statistisch acceptabele fit oplevert, weliswaar met residuele structuur rond de ijzer Kα-emissielijn.

Hoofdstuk 3 behandelt het nieuwe model reltrans, dat het model van Hoofdstuk 2 verbetert door de exacte geodetische paden in de Kerr metriek van de fotonen te berekenen met behulp van een ‘ray tracing’ techniek. Het model neemt zowel de energie- als de tijdsrespons van de accretieschijf in aanmerking, en berekent daarom zowel het tijdgemiddelde energiespectrum, dat met bestaande relativistische reflectiemodellen kan worden vergeleken, als de tijdsvertraging als functie van de energie. De relativistische correcties in het lichtecho-mechanisme worden berekend met een overdrachtsfunctie-formalisme.

In Hoofdstuk 4 wordt reltrans uitgebreid met de niet-lineaire effecten veroorzaakt door de fluctuaties in spectrale hardheid die we aanvankelijk onderzochten in Hoofdstuk 2. De Cygnus X-1 fit van Hoofdstuk 2 suggereerde dat de binnenrand van de schijf en de corona zich beide zeer dicht bij het zwarte gat bevonden. Echter, onder deze omstandigheden zijn relativistische effecten belangrijk, zodat onze nieuwe volledig relativistische versie van het model vereist is om de data goed te beschrijven. De nieuwe analyse van de Cygnus X-1 gegevens levert inderdaad een betere fit op, en door een gezamenlijke fit van het gemiddelde energiespectrum en energieafhankelijke complexe kruisspectra voor meerdere Fourierfrequenties zijn we in staat om voor het eerst een rÃűntgenecho-massabepaling te doen van een zwart gat van stellaire massa. We vinden bovendien dat modellen met een radiÃńel ionisatieprofiel in de accretieschijf statistisch geprefereerd worden boven modellen die de fysisch minder waarschijnlijke aanname maken van een constante ionisatie. De verschillende massa’s die we meten met verschillende ionisatieprofielen komen allemaal binnen 3σ overeen met de dynamische massabepalingen van Cygnus X-1, waarbij een meer realistisch ionisatieprofiel een lichtecho-massa oplevert die dichter bij de dynamische waarde ligt.

Tenslotte bekeken we de toepasbaarheid van het model op een superzwaar zwart gat, Markarian 335, door eerst alleen de lichtecho-vertragingen te fitten (Hoofdstuk 3) en later de gecorreleerde variabiliteits-amplitudes en -vertragingen op verschillende tijdschalen (Hoofdstuk 5). De resultaten van Hoofdstuk 3 laten al zien dat het model een bruikbare meting van de massa oplevert. Ze laten echter ook duidelijk zien dat het fitten van slechts één frequentiegebied enige ontaarding tussen parameters laat bestaan, zoals tussen bronhoogte en massa. Om die reden bevat Hoofdstuk 5 experimenten met een meer verfijnde analyse van de tijdsvertragingen en variabiliteitsamplitudes van Markarian 335, waarbij zowel de lichtecho-vertragingen als de intrinsieke tijdsvertragingen ten gevolge van het spectrale kantelen worden bestudeerd. De fit aan de tijdsvertragingen lijkt lagere waardes van de massa van het zwarte gat te prefereren (een paar miljoen zonsmassa's) dan de optische lichtecho-metingen ($\sim$ 10 - 20 miljoen zonsmassa's). Als we echter ons model ook fitten aan de gecorreleerde variabiliteits-amplitudes, is het niet in staat om sommige karakteristieke lichtecho-effecten te beschrijven die in de data waarneembaar zijn, en levert het geen bruikbare metingen van de massa op, hetgeen suggereert dat er fysische processen in het spel zijn die niet in het model voorkomen. Een aanwijzing hiervoor is dat de gemeten coherentie tussen de energiebanden niet gelijk is aan één, zoals wel in het model wordt verondersteld.

De conclusie van dit werk is dat Fourier-tijdsvariatieanalyse als functie van fotonenergie in zwarte gaten met accretie een krachtig hulpmiddel vormt om informatie te verkrijgen uit spectrale variabiliteitsgegevens die niet op andere wijze toegankelijk is.

Summary

Accreting black holes show characteristic components in the time-averaged energy spectrum and distinctive features in their time variability. When properly modelled, these diagnostics can constrain the geometry of the systems and the parameters of the black hole. Jointly accounting for both the energy and the time dependence of the X-ray radiation from accreting black holes exploits the complete information provided by the observations. This thesis focuses on studying the variability and energy dependence of the reflection component. This is the emission due to photons originally radiated from the corona (hot optically thin plasma close to the black hole) that illuminate the accretion disc, are re-processed in the disc atmosphere and are re-emitted before reaching the observer. There is evidence that this process occurs both in black hole X-ray binaries and active galactic nuclei (AGN). Interestingly, the energy and timing response of the accretion disc is different for every patch of the disc, because of the different strength of the relativistic effects that shift the energy of photons as they travel from source to observer, and the different light crossing times of the illuminating and reflected radiation. Therefore the reflection is a useful spectral component with which to exploit the possibilities afforded by combining the energy and timing aspects of the emission. One of the best ways to do this is to study the time lags of variations in the reflection component compared to those in the continuum component, which is emitted directly towards the observer and whose variations therefore arrive earlier. These *reverberation lags* are observed at relatively short timescales (Fourier frequencies $> 300 M_{\odot}/M$ Hz). At longer timescales, the lag energy spectrum is instead dominated by another process, thought to be associated with mass accretion rate fluctuations propagating through the accretion flow. These propagating mass accretion rate fluctuations lead to stochastic variations in the electron temperature of the corona by varying both the release of gravitational energy and the Compton cooling rate in the corona, which results in small fluctuations in the slope of the coronal emission ('pivoting') that can show up as time lags.

In this thesis, I present a new model that jointly addresses these two types of lag. Chapter 2 presents the mathematical formalism that describes this pivoting of the coronal spectrum and the lags that it produces. The illuminating spectrum seen at each point on the disc is different. This affects the reflection spectrum re-emitted by each disc patch and therefore the shape, and not just the strength, of the

reverberation energy spectrum. The consequences of these non-linear effects for the lag energy spectra are calculated assuming a compact corona located on the black hole spin axis, so that the slope of the illuminating spectrum depends on disc radius but not azimuth. Although the formalism of Chapter 2 does not include a full General Relativistic calculation of the photon trajectories from the corona to the disc and from the disc to the observer, we present a proof-of-principle analysis of *Rossi X-ray Timing Explorer* data of Cygnus X-1 and achieve an acceptable fit, albeit with some residual structure around the iron Kα emission line.

Chapter 3 presents the new model RELTRANS, which improves upon the model explored in Chapter 2 by calculating the exact geodesic trajectories of the photons in the Kerr metric with a 'ray tracing' technique. The model accounts for both the energy and the timing response of the accretion disc, and so computes both the time-averaged spectrum, which can be compared with existing relativistic reflection models,and the time lag as a function of energy. The relativistic corrections to the reverberation mechanism are calculated using a transfer function formalism.

In Chapter 4 RELTRANS is extended by now also including the non-linear effects due to the hardness fluctuations first explored in Chapter 2. The proof-of-principle Cygnus X-1 fit presented in Chapter 2 suggested an inner radius of the disc and a position of the illuminating source both very close to the black hole. However, in these conditions the relativistic effects are important, and thus our new fully relativistic version of the model is required to accurately describe the data. Indeed, the new Cygnus X-1 analysis improves the fit to the data, and by jointly fitting the time-averaged energy spectrum and the complex cross-spectrum as a function of energy for multiple Fourier frequencies we are able to accomplish the first X-ray reverberation mass measurement of a stellar mass black hole. Moreover, we find that model configurations that account for a radial ionization profile in the disc are statistically preferred over configurations that make the less physical assumption of constant ionization. The different masses measured using different ionisation profiles are all compatible with the dynamical mass measurement of Cygnus X-1 within 3σ, with a more realistic ionisation profile producing a reverberation mass value closer to the dynamical value.

Finally we also considered the applicability of the model to a supermassive black hole, Markarian 335, first fitting only the reverberation lags (Chapter 3) and later the correlated variability amplitudes and the time lags at different timescales (Chapter 5). The results in Chapter 3 already show that the model produces a useful constraint on mass. However, they also make clear that fitting only a single frequency range leaves some degeneracy among parameters, such as source height and black hole mass. Therefore, Chapter 5 provides experiments towards a more sophisticated analysis of the time lags and the variability amplitude of Markarian 335 studying both the reverberation lags and the intrinsic lags due to the pivoting. The fit to the time lags seems to favour lower values of the black hole mass (a few million Solar masses) than the optical reverberation mapping measurements ($\sim$ 10 - 20 million Solar masses).

However, when we fit our model also to the correlated variability amplitudes, the model is unable to describe some characteristic reverberation features present in the data, and can not provide useful constraints to the black hole mass, suggesting the presence of physical processes not addressed by the model. In fact the coherence between energy bands is not unity at all the timescales as assumed in the model.

The conclusion of the work is that energy-resolved Fourier timing analysis of accreting black holes is a powerful tool for inferring information from spectral variability data not otherwise accessible. In this thesis we modelled the spectral timing behaviour by creating and exploring a mathematical formalism that enables the reverberation lags to be self-consistently modelled for a large range of variability timescales in an analytic model suitable to fit to real-world data.

Acknowledgements

Michiel, Adam, ‘thank you’ is not enough to express what I feel. I couldn’t ask for better supervisors. I’m immensely glad you decided to start this journey with me, I learnt so much from you and not only from a scientific point of view. You were always available to give the right advice or to explain one more time the same concept that didn’t stick to my mind. You are my scientific parents. The main reason I want to continue this job is because I hope there are people like you out there.

Thanks to the API, because if you haven’t experienced such environment it’s difficult to imagine a place like this. People try always their best to integrate everybody and from the first day I immediately felt part of the community. A very special thank goes to all the people that are part of this amazing institute, all the stuff, the amazing secretaries, Postdocs and PhDs who make this place unique, I’m honoured to have been a part of it. I leave here more than just four years of my life.

I promised myself I wouldn’t have written any name, everybody helped me to grow up in a certain way, however, I want to reserve few lines for few folks. Thanks to the spine(s) of the institute because your role is (and I hope will always be) to glue these people together. All the APIs (me included) know that they can count on you; it doesn’t matter if it’s only a joke, a beer or a complain that nobody wants to hear. Thanks to the Bata teams, because I didn’t believe a group of astronomers could do 160km relay across two countries, but we did it! Twice!! Thanks to my (marathon) running mates, one because you never forget your first time, the other because the duration it’s important too. Thanks to my swimming partner, for all the cycling therapy. Thanks to my first friend(s), the weekends at the institute are better with some company. Thanks to my older scientific brother, because your pessimistic view of the world balanced my naive and childish belief. You helped me to discover the dark side of the moon. Thanks to my friend ‘oltre-manica’, because you put an effort in this thesis too. Thanks to my neighbour, because at a certain point of our long discussions I just wanted to be quiet and listen to what you were explaining to me. You opened my eyes and taught me to observe from a different point of view. I always felt enriched after a chat with you. Thanks Plasmisti, because we know where everything started and we were there together. Lorentz, sono stato davvero felice quando ho saputo che saresti arrivato, nell’ultimo periodo mi hai letteralmente accudito, grazie di cuore. Bel, non ci sono parole, non riesco a trovarle. Voglio solo dire che non riesco neanche a immaginare il mio percorso senza il tuo sostegno e i tuoi consigli. Sei semplicemente unico.

Grazie alla mia famiglia, perché quello che sono lo devo a loro. Grazie per aver sempre creduto in me e perché so di poter contare sempre su di voi in qualsiasi momento.

And finally thanks to you, because we belong to the same species. There is nobody like you. Sarai per sempre una parte di me.

Guglielmo,
September 2019

“I know, I know nothing”

Plato, Apology of Socrates

ISBN 978-94-6323-880-9

Printed by Gildeprint

contact email: guglielmo.mastroserio@gmail.com

Cover credits Jeremy Perkins.